Dimpled channel flows

An experimental investigation into the drag performance of dimpled surfaces in turbulent channel flows

J.M.A (Joost) van der Voort Maarschalk

TU Delft

DIMPLE

Dimpled channel flows

An experimental investigation into the drag performance of dimpled surfaces in turbulent channel flows

Master of Science Thesis

to obtain the degree of Master of Science at Delft University of Technology

J.M.A. (Joost) van der Voort Maarschalk

to be defended publicly on Friday January 29, 2021 at 10:00 AM

Faculty of Civil Engineering and Geosciences · Delft University of Technology

The picture on the cover was taken at the High Speed Lab at Delft University of Technology in August 2020. The black area at the bottom of the picture marks the entrance of the DC-40, a wind tunnel that was designed, constructed, and used in this research. In the top center of the picture, the tunnel's ceiling wall is removed, and dimpled test plates can be observed.

DELFT UNIVERSITY OF TECHNOLOGY

Faculty of Civil Engineering and Geosciences
Department of Geo-engineering

The undersigned hereby certify that they have read and recommend to the Faculty of Civil Engineering and Geo-Sciences for acceptance a Thesis entitled **Dimpled channel flows: An experimental investigation into the drag performance of dimpled surfaces in turbulent channel flows** by **J.M.A (Joost) van der Voort Maarschalk** in partial fulfillment of the requirements for the degree of Master of Science in Geo Engineering.

Dated: January 29, 2021

Chair of supervisor committee: _____

W. (Wout) Broere, Dr. ir.
Assistant Professor in the Department of Geo-Engineering (CEG)

Supervisor: _____

C. (Cees) van Rhee, Prof. dr. ir.
Professor in the Department of Hydraulic Engineering (CEG)

Supervisor: _____

F.F.J. (Ferry) Schrijer, Dr. ir.
Assistant Professor in the Department of the Aerodynamics (AE)

Daily supervisor: _____

O.W.G (Olaf) van Campenhout, Drs. ir.
Business Develepment at Dimple Aerospace B.V.

Preface

As a child, I loved to build things. This love evolved in the past nine months when I designed and built a wind tunnel at Delft University of Technology. Following the design and construction, I performed various tests on a dimpled surface in this new wind tunnel.

First and foremost, I owe a debt of gratitude to Drs. Olaf van Campenhout. With his entrepreneurial mindset, he assisted me wherever he could but simultaneously encouraged me to push my boundaries. His enormous amount of energy and enthusiasm reduced the number of bad days at the office to zero. From the Aerodynamics department, I am most thankful to Dr. Ferry Schrijer. He was very involved throughout the entire project, and with his expertise, he managed to challenge intermediary results every single meeting.

I want to thank the chair of my committee, Dr. Wout Broere, professor at the faculty of Civil Engineering and Geosciences. Wout was involved from the very beginning and always supported this project. From the same faculty, I thank Prof. Cees van Rhee who I was lucky to have as my fourth supervisor. Both Wout and Cees reminded me to perform this research from a civil engineering perspective. Without their cooperation in letting me fulfill my experiments at the High Speed Lab at the faculty of Aerodynamics Engineering, this project would never have kicked-off in the first place.

Thanks go out to Ir. Michiel van Nesselrooij. As Olaf's thoughtful partner, he assured to keep both feet on the ground during exciting times and offered a helping hand every now and then.

Finally, I would like to thank the technical staff at the High Speed Lab. I mainly owe thanks to Peter Duyndam and Dennis Bruikman. They taught me plenty of practical skills, and without their help, the new wind tunnel would never have seen the light of day.

Dedication

I dedicate this thesis to my two grandfathers.

My first grandfather started his Electrical Engineering studies at Delft University of Technology, precisely 60 years before I attended my first lecture. Throughout my youth, he shared his unconditioned love for technology, engineering, and space with me. This undoubtedly contributed to the passion I have for technology today. He would have been truly captivated by this research, and I hope that somehow, he witnessed this project from above.

With my other grandfather, I share a great deal of enthusiasm for languages and, since recently, aerodynamics. Combining his broad interest in science, having flown himself some decades ago, and being present when the first foundations of this project were set, made my grandfather extremely fascinated with this research. I owe him tremendous gratitude for pre-reading various reports throughout my studies, including part of this thesis, and always encouraging me to improve my writing.

To my granddads Willem and Louk, I thank you both.

Abstract

Drag in pipelines is composed almost solely of skin friction drag. The most common technique to achieve drag reduction (DR) is by adding drag-reducing agents. However, in the aerospace industry, various impressive passive drag-reducing techniques have been suggested to reduce skin friction drag in the past decades. Among these techniques, dimpled surfaces form a relatively unexplored terrain. Research into reducing skin friction drag in the turbulent regime by using dimples has been performed in the aviation industry since the '80s. The excessive amount of skin friction drag in pipelines forms an intriguing challenge to break new grounds. Several researchers investigated the potential of DR of turbulent flows using dimpled channels. Even though most of these studies that found DR are disputed, studies published at the National University of Singapore (NUS) obtained positive results time and again.

NUS's exact test setup was reconstructed at Delft University of Technology, which has not been done yet as far as the author of this report is aware. Identical pressure measurements were performed, yielding an absolute DR of $\approx 5\%$, which is slightly less than what was obtained at NUS ($>7\%$). Flat plates return a DR between 8-15%, dimpled test plates returned at DR between 12-20%. The test plates were covered for 99.5% with diamond-shaped dimples of 100 mm long and 50 mm wide. In total, 29 pressure taps were used to determine the change in drag in an 8 m long channel of 20 mm in height. Tests were done at Reynolds numbers, based on half channel width and centerline velocity, between 6,000 and 40,000. Accurate results were perceived up to a Reynolds number of 21,000, likely due to test-setup limitations.

Multiple verifications such as two-dimensionality of the flow, comparison of theoretical and experimental skin friction coefficients, and instantaneous pressure tests were used to allow for an objective analysis. The pressure measurements were also supported by 1D hotwire anemometry (HWA) tests and surface oil flow visualizations (SOFV). The majority of the investigated boundary layers were absent of anomalies. It should be mentioned that the viscous sublayer could not be captured, neither a quantitative momentum analysis was performed. However, a shift in the velocity profile, acquired at the same test location, for different test plates was observed. Furthermore, an increased velocity near the wall was observed for dimpled test plates. Surface oil flow measurements did show similar flow patterns to what was recorded at NUS. However, the actual behavior is not investigated through HWA. Hence, it cannot be confirmed nor denied if the change in drag is a consequence of these near-wall flow mechanisms. SOFV did not show irregular flow structures such as flow reversal.

Finally, tests were performed with a correction for test volume increase caused by the dimples. After this correction, the drag over dimpled plates increased instead of reduced. Considering other studies on dimpled surfaces that also found an increase in drag, it is strongly believed that the positive effect of dimples in turbulent channel flows does not stem from skin friction drag but rather from the increase in channel volume.

Although the precision of the results was relatively high, the accuracy of the wind tunnel was insufficient. Additional research is required to narrow down the 8-15% error that was obtained while testing flat plates.

Contents

List of Figures

List of Tables

Nomenclature

Abbreviations and acronyms

API	American Petroleum Institute
BTU	British Thermal Units
CA	Contact Angle
CCA	Constant Current Anemometry
CEPA	Canadian Energy Pipeline Association
CR	Coverage Ratio
CTA	Constant Temperature Anemometry
DA	Dimple Aerospace
DNS	Direct Numerical Simulation
DR	Drag Reduction
DRA	Drag Reducing Agent
DRT	Drag Reducing Technique
EIA	Energy Information Administration
HDD	Horizontal Directional Drilling
LDC	Local Distribution Companies
MAPE	Mean Absolute Percentage Error
MC	Measurement campaign
NGL	Natural Gas Liquids
NTP	Normal temperature and pressure
NUS	National University of Singapore
OCW	Open Course Ware
PHMSA	Pipeline and Hazardous Materials Safety Administration
POM	Polyoxymethylene
PST	Pipelines Safety Trust
SG	Specific gravity
SOFV	Surface Oil Flow Visualization
SPS	Solid Particle Suspension

TBL	Turbulent Boundary Layer	
TRL	Technology Readiness Level	
TUD	Delft University of Technology	

Dimensionless numbers

ϵ_s	Strain	[−]
κ	Von Kármán constant constant	[−]
Π	Wake parameter	[−]
A_H	First constant in King's law	[−]
B	Additive constant in the logarithmic law of the wall	[−]
B_H	Second constant in King's law	[−]
$C_{\mathrm{f},e}$	Experimental skin friction coefficient	[−]
$C_{\mathrm{f},t}$	Theoretical skin friction coefficient	[−]
e_v	Disturbance factor	[−]
e_v	Disturbance factor	[−]
f_1	Fraction of solid surface in contact with water	[−]
f_D	Darcy friction factor	[−]
H	Shape factor	[−]
K	Consistency index	[−]
K_x	Skewness	[−]
n	Flow index	[−]
R_f	Roughening factor	[−]
Re	Reynolds number	[−]
u^+	Dimensionless velocity	[−]
y^+	Dimensionless wall coordinate	[−]

English symbols

A	Area	[m^2]
D	Dimple diameter	[mm]
d	Dimple depth	[mm]
D_h	Hydraulic diameter	[mm]
d_s	Diameter orifice	[mm]
E	Voltage	[V]
E_Y	Young's modulus	[GPa]
g	Gravitational constant	[$\mathrm{m/s}^2$]
h	Channel height/pipeline diameter	[mm]
$h_{1,2}$	Entrance/exit height of pipe	[m]

I	Moment of inertia	[mm^4]
K	Consistency index	[$Pa \cdot s^n$]
L	Characteristic length	[m]
l_*	Viscous lengthscale	[μm]
l_s	Length orifice	[mm]
M_{air}	Molecular weight of air	[g/mol]
M_{gas}	Molecular weight of gas	[g/mol]
P	Wetted perimeter	[m]
p_g	Pressure gradient	[Pa/m]
$p_{1,2}$	Pressure at inlet/outlet	[Pa]
u	Fluid velocity	[m/s]
u_c	Centerline velocity	[m/s]
u_d	Deflection	[mm]
u_τ	Friction velocity	[m/s]
$v_{1,2}$	Inlet/outlet velocity	[m/s]

Greek Symbols

δ	Boundary layer thickness	[mm]
δ^*	Displacement thickness	[mm]
$\dot{\gamma}$	Shear rate	[1/s]
ϵ	Absolute roughness	[mm]
ϵ_b	Burr height	[mm]
γ	Specific gravity	[kN/m^3]
μ	Dynamic viscosity	[$Pa \cdot s$]
ν	Kinematic viscosity	[$Pa \cdot s$]
ρ	Density	[kg/m^3]
σ	Principle stress	[N/m^2]
τ	Shear stress	[N/m^2]
τ_0	Yield stress	[N/m^2]
θ	Momentum thickness	[mm]
θ_W	Angle of contact water droplet with surface according Wenzel	[°]
θ_Y	Contact angle water droplet with smooth surface	[°]
θ_{CB}	Angle of contact water droplet with surface according Cassie-Baxter	[°]
ξ	Dilatational viscosity	[$Pa \cdot s$]

Chapter 1

Introduction

The motion of an object through the air was first described by Aristotle 350 B.C. Anderson (1997) remarked in his book that Aristotle reasoned that an object moving through a continuum continuously encounters a certain resistance to continue its motion. Around 1500, Leonardo Da Vinci was the first to recognize various flow patterns and studied the motion of fluids rounding a static object. His sketches showed detailed flow fields over objects in a stream that form an accurate representation of reality. With a sketch from *Codex Atlanticus* illustrated in Figure 1.1, one of the first visual distinctions between pressure drag and skin friction drag was made. While Aristotle philosophized about resistance in ancient times, resistance (or drag) of trains, vessels, and airplanes is still nowadays a widely discussed topic. Drag is present everywhere, and the reduction of skin friction drag has a huge potential for energy-savings in various industries.

Figure 1.1: Sketches by Leonardo Da Vinci of flow fields over objects in a flowing stream (Da Vinci, 1509).

1.1 Importance of drag reduction in pipelines

Over the past few decades, worldwide energy consumption has become a widely discussed topic. The International Energy Outlook published by the U.S. Energy Information Administration (2019) (EIA) provides an illustrative overview of worldwide energy consumption ranging from 2010 with projections to 2050. At the moment of writing, petroleum and natural gas account for over 58% of the primary energy consumption. EIA foresees that renewable energy is on the rise with a projected increase of 3.0% per year while natural gas and liquids will increase as well with an annual gain of 1.1% and 0.6%, respectively. Even though renewable energy will strengthen its position in the primary energy consumption, fossil fuels remain inevitable in the near future. Therefore, it is vital to reduce the energy demand of current energy sources instead of merely focusing on renewable energy itself.

For example, hydrocarbons are transported in various ways. Comparing several transporting methods based on cost, see Figure 1.2, and energy consumption, Table 1.1, pipelines turn out to be one of the most efficient transport methods (Papavinasam, 2014). Even more so, considering the transport of crude oil in the USA

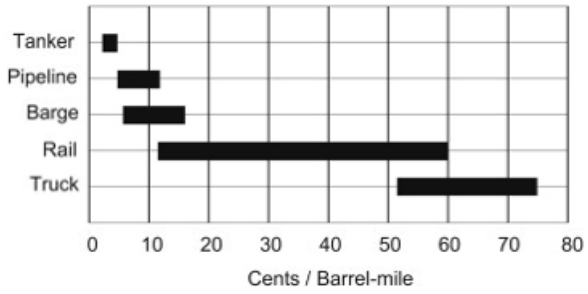

Figure 1.2: Average cost (USD) various transport methods of oil and gas.

Mode of Transportation	Energy Consumption (BTU/Ton-mile)
Airplane	37,000
Truck	2,300
Railroad	680
Waterway (barge)	540
Oil pipeline	450

Table 1.1: Energy consumption of different transportation methods of oil and gas.

depicted in Figure 1.3, pipeline transport is the most frequently used method. On top of that, it is the safest method to transport the product. It has relatively the least accidents, does the smallest environmental damages, and has the lowest clean-up cost per ton-mile (Luong, 2019). As such, it is of major significance to investigate possibilities to enhance this transport method by reducing the required energy consumption considering oil and gas are still transported by 2050, according to EIA. Moreover, once the transition to fully sustainable energy

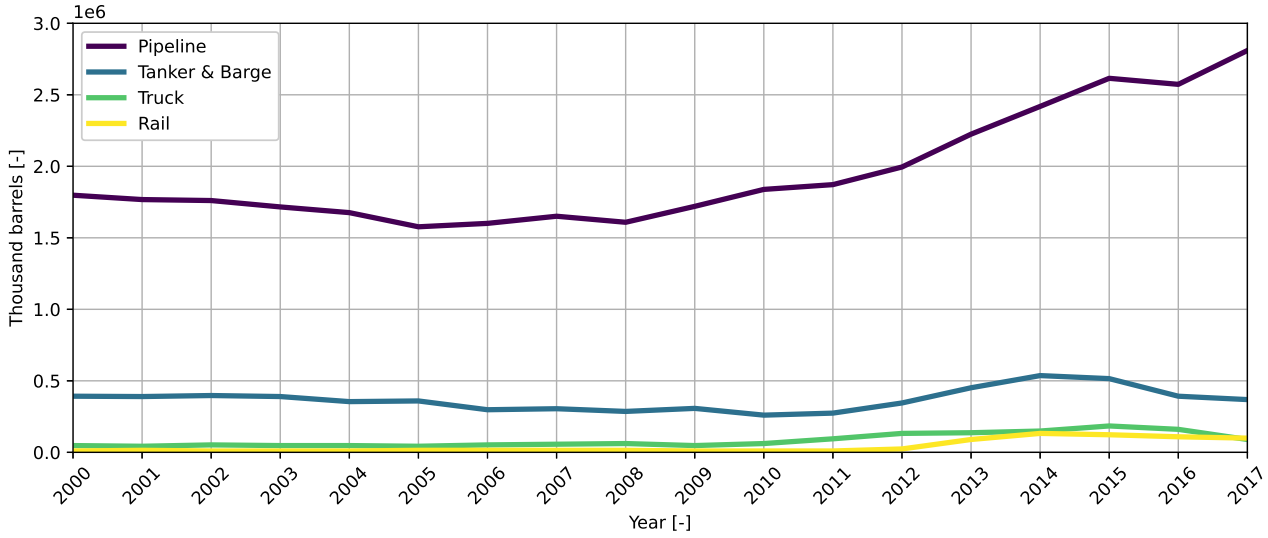

Figure 1.3: Methods of transporting crude oil in the USA (Luong, 2019).

is made, the high demand for pipelines will remain considering their efficient way of transporting energy. E.g., there will always be a demand for water supply. In 2002, the Congressional Budget Office estimated that the water pipeline network in the USA extends over approximately 2.1 million km, involving water- as well as wastewater pipelines (Beider and Tawil, 2002). In other words, the relevance of pipelines will not decay.

In light of the above, this research will focus on the drag caused by a product within pipelines and how this drag could potentially be diminished.

1.2 Drag components

Total drag in pipelines is composed of form drag and skin friction drag. In a pipeline with a smooth inner surface, i.e., without structures, there exists exclusively skin friction drag. To put this into perspective, the skin friction drag component in transmission pipelines (long straight tubes absent of strong bends) accounts for approximately 98% of the total drag according to Yunqing et al. (2017). Bird et al. (2006) even state that the only contribution of drag is skin friction drag in the case of perfectly smooth pipes.

More recent research has also demonstrated that 3D structures on the pipeline's inner surface positively influence the skin friction drag caused by the wall on the flow. An example is micro-structures of a sinusoidal shape (Charron et al., 2009). Once 3D structures are implemented, not only skin friction drag but also the form drag component should be taken into account. Note that from now on, drag will be referred to as reduction of total drag unless indicated otherwise.

Flow in a tube can be described in terms of the Reynolds number (Re). This dimensionless quantity is a ratio of inertial forces over viscous forces. It includes the density ρ, the viscosity μ, the velocity u, and a characteristic length, which is the pipeline diameter h in this case:

$$Re = \frac{\rho u h}{\mu} = \frac{u h}{\nu} \tag{1.1}$$

Alternatively, the ratio of μ/ρ can also be denoted as ν, the kinematic viscosity of the fluid. *Laminar* flow can generally be identified for Re's lower than 1800 while Re's higher than 2300 are linked to *turbulent* flow. For flow within tubes where the only contribution of drag is skin friction drag, i.e., smooth walls, and no boundary layer separation takes place, the transition from laminar to turbulent flow is in the range of $1800 < \text{Re} < 2300$ (Bird et al. (2006); Darbyshire and Mullin (1995)). In other words, for higher flow rates, the flow becomes turbulent. Turbulence in the flow translates into more friction, which will cause more drag. If it would be possible to suppress the turbulence without lowering the flow rate, then this will result in a drag reduction (DR). Note: the length scale and type of velocity used to compute the Reynolds number might vary for different research.

1.3 Dimpled surfaces

Over the years, various techniques have been discovered, examined, and improved to reduce skin friction drag as much as possible. This will be touched upon later in this report. One of the techniques is the application of dimpled surfaces. The initial purpose of dimpled surfaces was the enhancement of heat transfer (Kiknadze et al., 1984). Over the years, more interest has been roused regarding a second purpose: reducing skin friction drag. The exact functioning of this technique remains unclear as there has not been done extensive research yet. However, the main consensus seems to be that alternating spanwise velocity interacts with turbulent

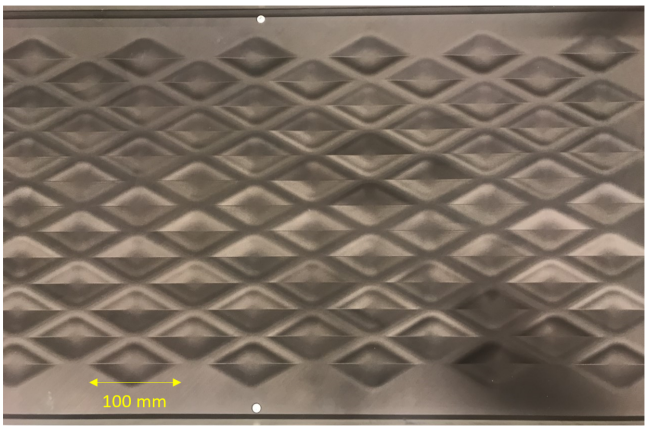

Figure 1.4: Example of a test plate with diamond-shaped dimples.

structures in the boundary layer (Van Nesselrooij et al., 2016). In addition to that, the streamwise vorticity contributes to decreasing the skin friction drag (Tay et al., 2015). It is believed that dimples have the same result as oscillating walls in terms of drag reduction. Research that has been performed on dimpled surfaces has a history of ranging results containing positive as well as negative outcomes with regards to drag reduction (e.g., Veldhuis and Vervoort (2009); Lienhart et al. (2008); Van Nesselrooij et al. (2016)). However, various researches performed at the National University of Singapore (NUS) have shown drag reduction time and again (e.g., Tay (2011); Tay et al. (2015); Tay et al. (2019)). An 8 m long conduit with a slim wind tunnel height of 20 mm and a width of 400 mm is used continuously throughout the years. The relevance of reducing skin friction drag within pipelines, combined with the promising results obtained at NUS by using dimpled surfaces, forms an interesting research topic. An example of a dimpled plate is depicted in Figure 1.4.

1.4 Scope

Objectives.
The introduction of this report points out that skin friction drag is almost the only source of drag within pipelines. Also, pipelines are one of the most efficient techniques to transport fluids. A rather undiscovered technique involving dimpled surfaces is postulated in the aviation industry. Potentially, this could also be beneficial for turbulent fluid flows in pipelines. Hence, the main objective is established:

Investigate the potential of drag reduction caused by a dimpled surface in turbulent channel flows.

This objective has a one on one correlation with the main research question. The main objective can be subdivided into several smaller objectives that support the main objective. Section 3.2 of this report points out that multiple studies done at NUS show consistent drag reduction caused by dimpled surfaces exposed to a channel flow. Therefore, sub-research question 1-4 are related to validating research performed at NUS:

1. **Verify channel configuration.** Determine if channel configuration as proposed by NUS leads to a zero pressure gradient boundary layer with a linear pressure drop.
2. **Investigate the turbulent boundary layer above a flat as well as a dimpled surface.** Once drag reduction is found, it is extremely relevant to see which flow structures can be identified and if flow patterns can be predicted.
3. **Determine the influence of the volume increase of the channel due to the dimpled surface.** This is something that does not seem to have been done at NUS. Nevertheless, due to the relatively slim wind tunnel, dimples possibly significantly impact the volume of the channel and, thereby, on the change in drag.
4. **Analyze flow structures near the wall.** Surface flow measurements are easy to apply and might give additional information about the flow close to the surface for a larger area.
5. **Correlation between performed experiments and actual pipelines.** Draw a verdict on where in the pipeline industry dimpled surfaces could be theoretically applied.

The supporting objectives also have one on one correlations with the subsequent sub-research questions, which are listed below.

Research questions.
In line with the main objective, the following research question is elaborated:

Can drag reduction be observed for turbulent channel flows employing a dimpled surface?

In conjunction with the sub-objectives, various research questions are formulated:

1. *Can a zero pressure gradient boundary layer with a linear pressure gradient be obtained? Which verifications are required to confirm this?*
2. *What momentum difference in the turbulent boundary layer can be observed between flat- and dimpled test plates?*
3. *Does a correction for the increased channel volume abate encountered drag reduction? If so, by how much?*
4. *Does flow reversal occur in the diamond-shaped dimples used at NUS?*
5. *Do dimpled surfaces have the potential to be applied in existing pipelines?*

Report overview. This report contains eight more chapters. Following the introduction, relevant fluid dynamics and drag within pipelines are discussed. Chapter 3 expands on various drag-reducing techniques with a particular interest in dimpled surfaces. In chapter 4, the experimental considerations are addressed. Chapters 5-7 elaborate on three measurement techniques used in this research to answer the research questions. Each chapter involves a methodology section, results, and a discussion. In chapter 8, a conclusion is drawn, and the report is finalized with some recommendations.

Chapter 2

Fundamental principles

This chapter discusses the fundamental concepts required to answer the aforementioned research questions. The first section elaborates on the principles of boundary layers in turbulent flows. The second section aims to gain information about the flow behavior of various fluids in different pipeline types and where drag arises in pipeline systems.

2.1 Relevant fluid dynamics

This section discusses the fundamental principles of relevant fluid dynamics. This knowledge will prove useful throughout the rest of the report.

2.1.1 Types of fluid flow

It is convenient to shed some light on different fluid flow types briefly. Newtonian, non-Newtonian, Bingham plastic, and time-dependent flows will be discussed.

Newtonian fluid flows. These type of flows are clearly described by Newton's law of viscosity (White, 2006):

$$\tau = \mu \left(\frac{\partial u}{\partial y} + \frac{\partial v}{\partial x} \right) \tag{2.1}$$

which is the shear force at any point in the flow τ expressed in the viscosity μ and the velocity gradients in x- and y-direction. The term $\partial v/\partial x$ can often be neglected as it is two orders of magnitude smaller than the first term. From Figure 2.1, one can conclude that for a Newtonian fluid the shear stress is linear dependent on the shear rate. According to Bird et al. (2006), it has been found that the resistance to flow of all liquids

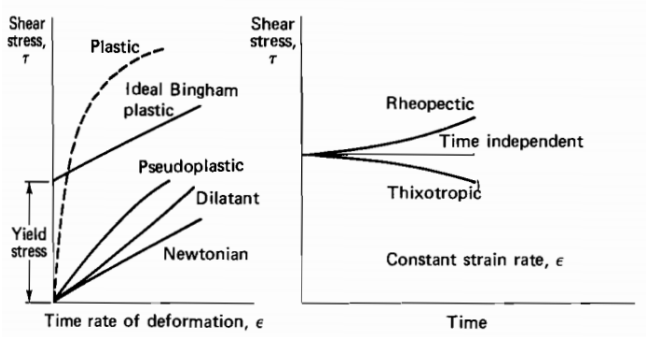

Figure 2.1: Viscous behaviour of various fluids (White, 2006).

and gases with a total molecular weight < 5000 behaves according Equation 2.1 and are classified as *Newtonian fluids*. The Newtonian fluids requires two parameters, μ and the dilatational viscosity ξ which are dependent on

the temperature, pressure and composition. The dilational viscosity is often ignored for gases with low density (Bird et al., 2006).

Non-Newtonian fluid flows. These type of fluids that do not follow Newton's law of viscosity as is described in Equation 2.1. They often have a molecular weight > 5000. For *non-Newtonian* fluids, the shear stress is non-linear dependent on the shear rate. The flow can be either shear thickening, a local increase in viscosity, referred to as *dilatant* or shear thinning, a local decrease of viscosity, which is referred to as *pseudo-plastic*. In case the fluid viscosity shrinks significantly, the 'fluid' can also be classified as plastic, indicated with the dashed line in Figure 2.1. Examples of *non-Newtonian* fluids are polymer solutions, suspensions, emulsions, and pastes.

For the left chart in Figure 2.1, the behavior is time-independent. Another complication of Non-Newtonian fluids is that they may be dependent on time. If the shear stress is held constant, the strain rate may vary, and vice versa (White, 2006). Thixotropic fluids are fluids that become less viscous with time. In other words, at a standstill, the viscosity is higher than during flow conditions.

Bingham plastic fluid. Bingham (1916) discovered that certain fluids behave differently depending on the amount of stress they experience. He stated that certain materials behave as solid under low stress and start behaving like a liquid once exposed to higher stresses. An *Ideal Bingham* plastic fluid behaves linear shear rate dependent, similar to a *Newtonian* fluid. However, to transform the solid into a fluid and set the material in motion, a certain 'yield stress' needs to be overcome.

The viscous behavior of different fluids can be described by the comprehensive three-parameter Hershel-Bulkley model, which is widely used. It involves yield stress τ_0, consistency index K, and flow index n. The shear rate is denoted by $\dot{\gamma}$.

$$\tau = \tau_0 + K\dot{\gamma}^n \tag{2.2}$$

The focus in this research is on incompressible *Newtonian* fluid flows. In case other types of fluids are considered, this will be pointed out.

2.1.2 Different flow regimes in pipelines

The different flow regimes mentioned briefly in chapter 1 are elaborated in this section. Firstly, laminar- and turbulent flow will be described. Furthermore, it is examined how the boundary layer responds to different flow regimes in pipelines. Lastly, hydraulic turbulent regimes are discussed.

Laminar-, transition- and turbulent flow

Figure 2.2 provides a visible representation of the laminar and turbulent flow in the form of the Moody diagram. Capital D in Figure 2.2 is the pipeline inner diameter which is denoted as h in this report. The straight line on the left and multiple lines on the right, which depend on the surface roughness, indicate laminar and turbulent flow. The end of the laminar curve and the beginning of the turbulent curves are dotted, illustrating transitional flow. Furthermore, as the laminar flow is a straight line, the friction factor can be expressed by a linear equation (Bird et al., 2006):

$$f_D = \frac{64}{Re} \tag{2.3}$$

where f_D is the (Darcy) friction factor. The relative roughness does not influence the friction factor for low Reynolds numbers and is only dependent on the Reynolds number. On the contrary, at very high Reynolds numbers, the Reynolds number is independent of the friction factor and is only dependent on the roughness, see Figure 2.2. The adverse regimes are bridged by the transitional regime and the first part of the turbulent regime. In this range, the friction factor depends both on the roughness as well as the Reynolds number. For turbulent flows, many empirical relations are put forth by researchers to solve for the Darcy friction factor (Mohsenabadi, 2014). One of the more often suggested correlations is the Colebrook White equation (Shashi Menon, 2015):

$$\frac{1}{\sqrt{f_D}} = -2\log\left(\frac{\varepsilon/D_\mathrm{h}}{3.7} + \frac{2.51}{\mathrm{Re}\sqrt{f_D}}\right) \tag{2.4}$$

Where ϵ is the absolute roughness and D_h the hydraulic diameter. The Colebrook White formula is an implicit equation, both left, and right terms contain the friction factor, that requires an iteration process to solve it

(Brkic, 2011). It can be argued that the Colebrook White equation is only valid for pipe flows. For a rectangular duct with a sufficiently large width-height ratio, two-dimensional flow can be observed. Therefore, this equation is used for two-dimensional flows. Zanoun et al. (2003) used a 12:1 width-height ratio to ensure two-dimensional flow. Dean (1974) reports that for a 12:1 ratio, the centerline velocity rises about 2% over a distance of $100h$. Dean (1978) concludes that a threshold ratio of 7:1 is required to allow for a neglectable impact of the duct's sidewalls. In this research, a channel with a width-height ratio of 20:1 will be used because considering other researches can be validated (Tay et al., 2015).

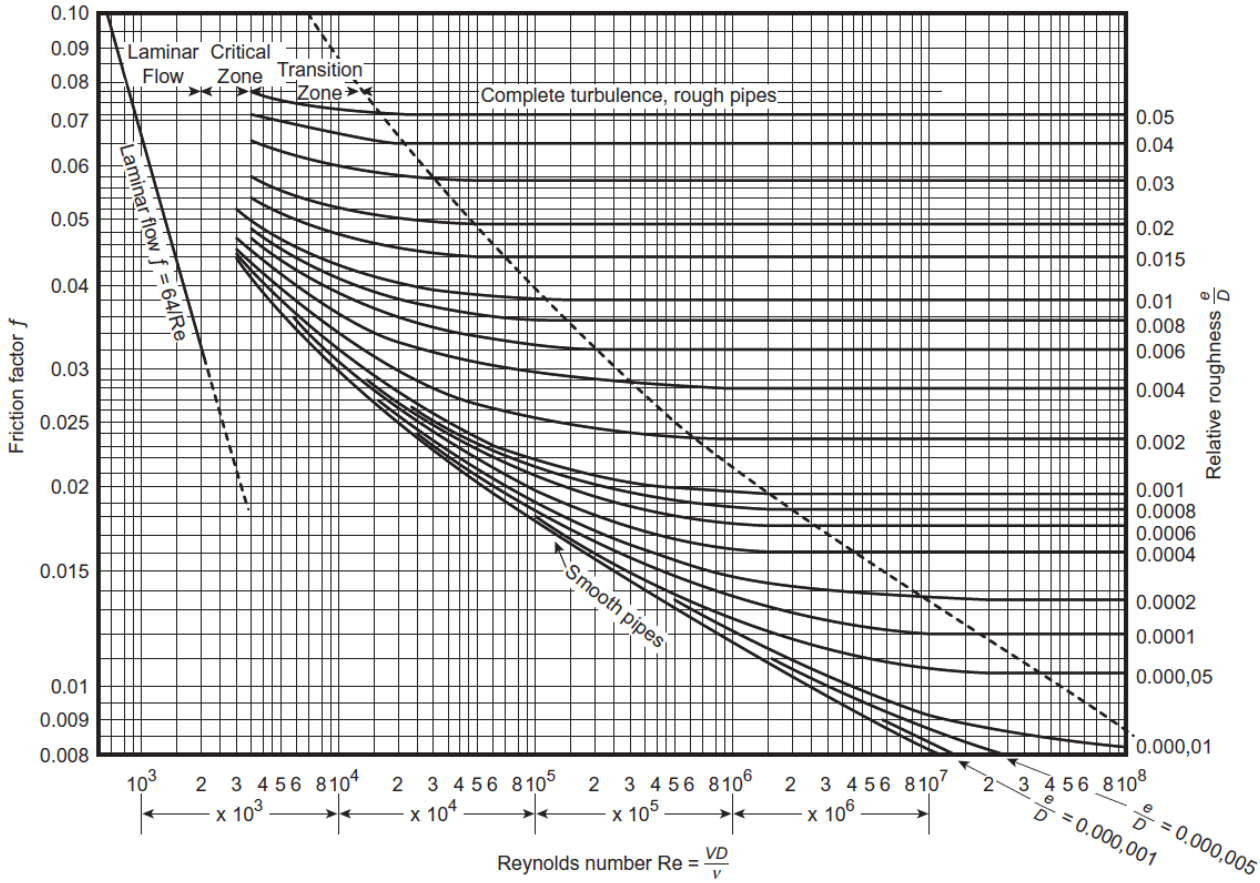

Figure 2.2: Moody diagram: Reynolds number versus friction factor and roughness (Shashi Menon, 2015).

Flow regimes in pipelines

There is a difference between the boundary layers that form over airfoils and boundary layers within pipelines. Airfoils have one boundary layer starting at the wall, i.e., the airfoil's surface, where a no-slip condition applies. Further away from the wall, the velocity increases until the free stream velocity is reached; the undeflected flow characterizes this. On the other hand, for pipe flows, a sole boundary layer exists as the circular wall forms a closed system. The centerline velocity of the pipe flow designates the highest velocity in the tube. This is represented in Figure 2.3. The two red converging lines indicate how long it takes before the flow is fully developed. In other words, how long it takes for the maximum velocity to be reached. A flow is said to be *fully developed* when the velocity at each point on the cross-section is within 1% of its ultimate value. For turbulent flows, a distance of 50 times the pipeline diameter h suffices to reach fully developed flow (Widden, 1996). It is convenient to distinguish four regions in the boundary layer as depicted in Figure 2.4. The first layer is the layer closest to the wall, where viscosity has a prominent role. In the buffer layer, the transition between the viscous and the inertial sublayer occurs. The third layer is the beginning of the main turbulent stream, followed by the turbulent stream itself. The three regions closest to the wall are the most interesting in light of this research. Hence, these will be discussed further in subsection 2.1.3. In the fully developed region of Figure 2.3, laminar and turbulent flow can be distinguished. As aforementioned, this is correlated with the Reynolds number. The turbulent boundary layer can be identified as a thicker layer with a lower centerline velocity. In Figure 2.4,

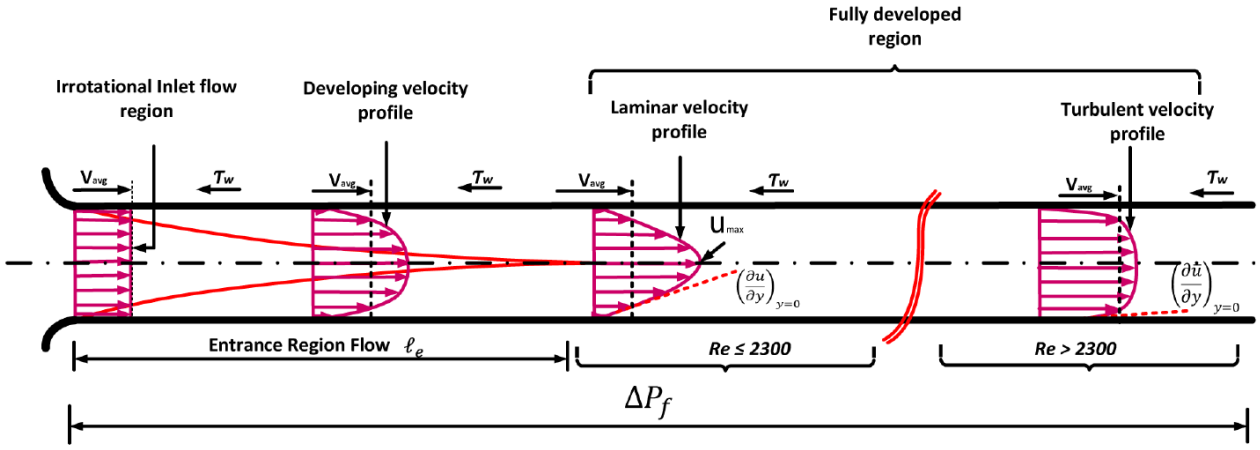

Figure 2.3: Development boundary layer pipe flow (Makwashi et al., 2019).

Δx denotes the intersection of the BL curve with the viscous sublayer height. It can be concluded that Δx is larger for turbulent boundary layers, resulting in larger viscous forces. The boundary layer can be in the order of several mm, whereas the viscous sublayer is in the order of μm. A chart with logarithmic axes is required to make further analyses on flow behavior close to the wall, which is explained in subsection 2.1.3.

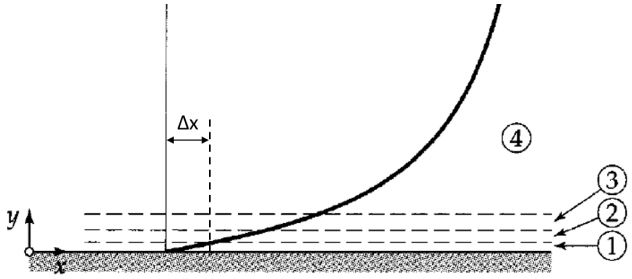

Figure 2.4: Four boundary layer regions for describing turbulent flow near a wall. 1: viscous sublayer, 2: buffer layer, 3: intertial buffer layer, 4: main turbulent stream (Bird et al., 2006).

Hydraulic turbulent regimes

Turbulent flow within pipelines can typically be subdivided into three types of flow: hydraulically smooth turbulent, partially turbulent, or rough turbulent flow regime. This is illustrated in Figure 2.5. The difference is clearly explained by Brkic (2011; 2018). Pipes are classified as hydraulically smooth when the laminar sublayer thickness close to the wall is larger than the absolute roughness ϵ of the wall itself. A turbulent flow propagating through a pipe covered by a thin laminar viscous layer at the wall is called partially turbulent flow. As the Reynolds number increases, the thickness of this laminar viscous layer diminishes, and the pipe roughness becomes more important until a fully turbulent regime is reached. The laminar viscous sublayer has now also become turbulent, which only occurs at Re >100,000 (Brkic et al., 2018). In pipelines with smaller pressures and diameters, the flow regime will be partially turbulent. The hydraulic turbulent regimes should not be confused with the flow regime described earlier.

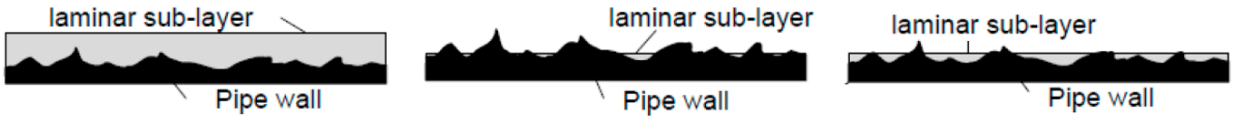

(a) Hydraulically smooth. **(b)** Partially non-fully developed. **(c)** Rough.

Figure 2.5: Different hydraulic turbulent regimes for pipe flow (Brkic et al., 2018).

2.1.3 Turbulent boundary layers

In this research, experimental investigations near the wall are performed. Therefore, it is relevant to understand the principles, available in the book by White (2006), that were used to examine a turbulent boundary layer (TBL). Equations 2.5 and 2.6 express the distance to the wall and the velocity in a dimensionless number:

$$y^+ = \frac{y u_\tau}{\nu} \tag{2.5}$$

$$u^+ = \frac{u}{u_\tau} \tag{2.6}$$

where y is the actual distance from the wall, u_τ is the friction velocity or shear velocity and y^+ and u^+ are the dimensionless wall unit and the dimensionless velocity, respectively. The shear velocity can be computed by using the earlier defined shear stress:

$$\tau = \sqrt{\frac{u_\tau}{\rho}} \tag{2.7}$$

where ρ is the density of the fluid. As mentioned above, TBL's can be subdivided into four regions: the viscous sublayer, the buffer layer, the overlap layer to free stream velocity, and the free stream velocity itself. The viscous sublayer is only exposed to viscous forces, and turbulent forces are damped. In this region, there exists a linear relation between y^+ and u^+. The buffer layer is a smooth curve that connects the viscous sublayer with the overlap layer. The overlapping layer is dependent on logarithmic law constants κ (Von Kármán constant) and B (addative constant in the logarithmic velocity law), which are commonly suggested to be $\kappa = 0.40 - 0.41$ and $B = 5.0 - 5.5$. In short:

$$\begin{array}{rlll} 0 \leq & \mathrm{y}^+ & \leq 5 & \text{Viscous sublayer} \quad \mathrm{u}^+ = \mathrm{y}^+ \\ 5 \leq & \mathrm{y}^+ & \leq 30 & \text{Buffer layer} \\ 30 \leq & \mathrm{y}^+ & \leq 350 & \text{Overlap layer} \quad \mathrm{u}^+ = \frac{1}{\kappa} \ln \mathrm{y}^+ + \mathrm{B} \end{array} \tag{2.8}$$

The three regions closeset to the wall are elegantly expressed in one equation by Spaldings law of the wall. The equation is valid up to the point where the outer layer starts to rise above the logarithmic curve.

$$\mathrm{y}^+ = \mathrm{u}^+ + e^{-\kappa \mathrm{B}} \left[e^{\kappa \mathrm{u}^+} - 1 - \kappa \mathrm{u}^+ - \frac{(\kappa \mathrm{u}^+)^2}{2} - \frac{(\kappa \mathrm{u}^+)^3}{6} \right] \tag{2.9}$$

To analyze the boundary layer further, various parameters can be considered. Firstly, the boundary layer thickness is defined as δ. In aerodynamics the boundary layer thickness is the distance from the wall where the velocity has reached 99% of its 'free stream' velocity. When the diameter h is less than the viscous boundary layer thickness, the maximum velocity is the centerline velocity and the velocity profile takes on a parabolic shape, see Figure 2.3. Subsequently, the boundary layer thickness is defined as the radius of the tube:

$$\delta = \frac{h}{2} \tag{2.10}$$

Equation 2.10 does imply that the roughness of the channel walls is the same at each location. Different roughnesses can lead to a skewed parabolic velocity profile. Secondly, the value of the displacement thickness is how much the outer inviscid layer is 'displaced' by the viscous forces at the wall. For incompressible flows Equation 2.11 applies:

$$\delta^* = \int_0^{y \to h} \left(1 - \frac{u}{u_c} \right) dy \tag{2.11}$$

where u_c is the centerline velocity. Similar to the function of the displacement thickness, the momentum thickness is a function of 'x' only.

$$\theta = \int_0^{y \to h} \frac{u}{u_c} \left(1 - \frac{u}{u_c} \right) dy \tag{2.12}$$

the ratio of the displacement thickness and the momentum thickness is called the *Shape factor* which is denoted by H:

$$H = \frac{\delta^*}{\theta} > 1 \tag{2.13}$$

which will also be used later to analyse the BL. Put forward by Blasius, the $Shape factor$ has a value of 2.59 for laminar flows while for turbulent flows H is in the order of 1.3-1.4 (White, 2006).

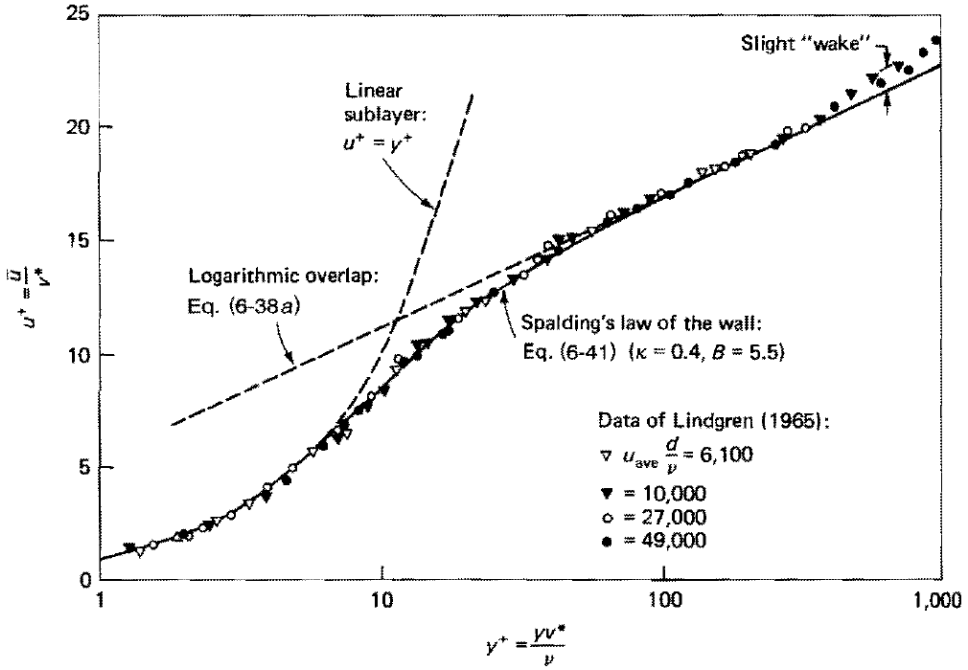

Figure 2.6: Spaldings law of the wall (White, 2006).

2.2 Drag in pipelines

In this section, different pipeline types will be discussed, and the flow behavior of different fluids. For each discussed fluid, the operating flow regime at various conditions is established. Complementary to this, the author seeks to give some perspective on the importance of reducing skin friction drag by enacting a comparison between drag formed by friction and drag formed by obstacles in a pipeline system.

2.2.1 Pipeline types

In the first three subsections, types of flows, flow regimes, and relevant physics of turbulent boundary layers were touched upon. In this subsection, different types of pipelines will be discussed. By using the physics described earlier, a deliberate judgment can be made on which sort of pipeline would be suitable for drag-reducing techniques (DRT's) to be applied. The different types of pipelines that are compared form part of natural gas- and oil pipeline systems. Nevertheless, pipelines that transport (waste)water, NGL's, hydrogen, or other liquids are equally relevant when it comes to potential DRT's.

Three main categories of pipelines can be recognized: gathering-, transmission-, and distribution pipelines. In addition to this, other pipelines complete the system. In Table 2.1, a clear overview is depicted. Considering the liquids and gases that are moved through pipeline systems, the transportation of two products is amplified: gas and oil. The distribution and service lines are smaller pipelines with lower pressures. Nevertheless, they have the largest share in total pipeline mileage in the U.S. and Canada, see Table 2.2. Furthermore, they are only used for the transportation of gas to domestic areas and businesses. The distribution pipelines in the USA, depicted in Table 2.2, consist of mainlines and service lines. The flow- and the service pipelines are not depicted in Figure 2.7. However, they respectively form the first and the last part of the system as is described in Table 2.1. Other clear flowcharts can be found on the website of PHMSA (2020).

Offshore Technology (2020) state that the total length of the global transmission pipeline network surpasses 2 million km, which involves the transportation of oil, gas, and NGL (Natural Gas Liquids). It is described that North-America has a >40% share in this, although data of non-Western countries such as China is not reported. In Table 2.1, six variations of pipelines are depicted forming the whole pipeline network. Each type of pipeline has its own properties in terms of pressure and pipeline diameter. The transmission pipelines operate under the highest pressure of almost 10 MPa. Other researches such as Chaczykowski (2010) mention pipeline pressures of up to 25 MPa for natural gas.

Table 2.1: Different pipeline types. NDF = No data found.

Pipeline type	Description	Diameter [mm]	Pressure [bar]	Product	Source
Flow	Connected to a single wellhead in the producing field. Move product to gathering pipelines	<305	41.37-82.74	Unodorized natural gas	Guo et al. (2007); Enerpac (2017)
Gathering	Connect multiple flow lines and move product from site to oil batteries or natural gas processing facilities	101-304	49.30	Natural gas, crude oil (sometimes mixed with water, NGL's	CEPA (2015); PHMSA (2020),
Feeder	Carry the product from the gathering points to the long distance transmission pipelines	152-304	NDF	Crude oil, NGL's, natural gas	CEPA (2015); PHMSA (2020)
Transmission	Move the product from the gathering point to refining, storage- and processing facilities	101-1212	13.79-96.53	Refined petroleum products, crude oil, NGL's, natural gas	CEPA (2015); PHMSA (2020)
Distribution	Network used by Local Distribution Companies (LDC) that deliver product to commercial and residential end-users	13-152	13.79	Odorized natural gas	CEPA (2015), PHMSA (2020)
Service	Connected to a meter that delivers natural gas to individual customers	<50	<0.69	Odorized natural gas	PST (2015)

Table 2.2: Data of different pipeline types in the US and Canada (Papavinasam (2014), PHMSA (2020) and CEPA (2015); Canadian Energy Pipeline Association). NDF = No data found.

Country	Gathering (km)	Feeder (km)	Transmission (km)	Distribution (km)	Total (km)
USA	79,000	NDF	700,000	2,785,000 (gas only)	>3,500,000
Canada	250,000	25,000	117,000	450,000	>840,000

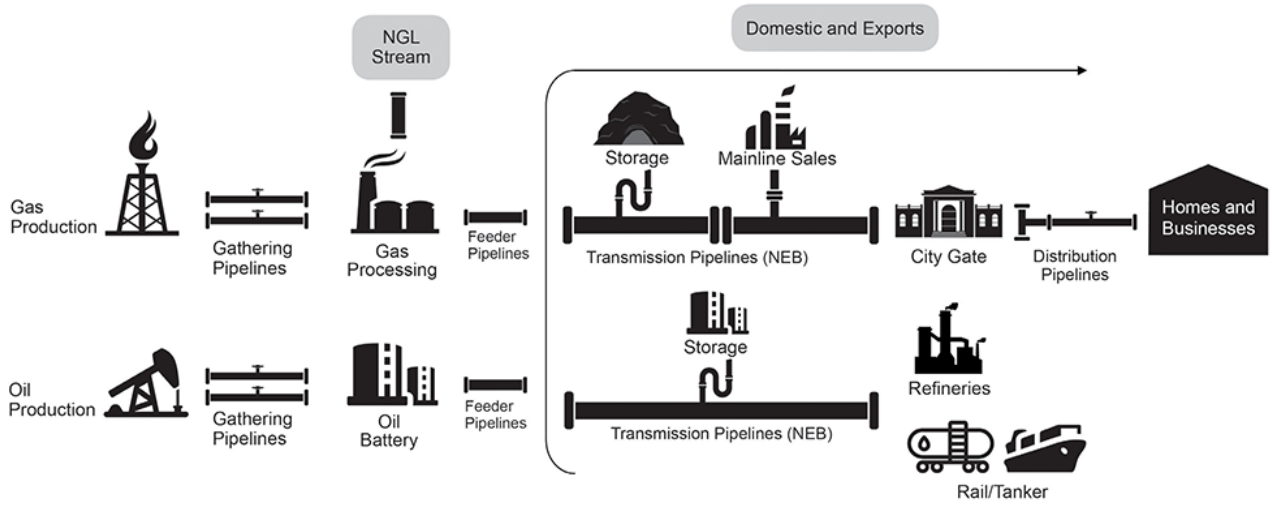

Figure 2.7: Pipeline stages.

2.2.2 Different fluids

Considering Table 2.1 in conjunction with gas or fluid properties and flow velocities, the type of flow regime for different products in various pipeline types can be expressed in terms of Reynolds number. By consulting the Moody diagram, see Figure 2.2, it can be determined if the flow is laminar, transitional, or turbulent. In this subsection, natural gas, crude oil, slurries, and drilling fluids are benchmarked for different viscosities, densities, pipelines diameters, and flow velocities. Tables 2.3-2.6 depict the results. The computed Reynolds numbers are based on a range of velocities and a range of pipeline diameters.

Natural gas flow

For natural gas, the pressure and temperature under which is operated have a large influence on the density and viscosity which is depicted in Figure 2.8a. In addition to that, the specific gravity (SG) also has a role. The SG of gas can be determined by Equation 2.14 below:

$$\gamma = \frac{M_{gas}}{M_{air}} \tag{2.14}$$

where M_{gas} is the molecular weight of the gas and M_{air} the molecular weight of air at standard temperatures (i.e., 15.6°C and 1 atm). Based here-on, the SG, often denoted as γ, for natural gas is ≈ 0.65. The dependency of temperature, SG and pressure on the viscosity of natural gas is illustrated clearly by Beal (1946) in Figure 2.8a. Some basic calculations are performed based on standard conditions, referred to as normal temperature

Table 2.3: Flow regime in different pipeline types for **natural gas**.

Pipeline Type	u [m/s]	h [m]	Re_h[1][-]	Regime
Flow	2-4	0.10-0.30	$1.49{\cdot}10^4$-$8.92{\cdot}10^4$	Turbulent
Gather	4-15	0.10-0.30	$2.97{\cdot}10^4$-$3.34{\cdot}10^5$	Turbulent
Transmission	15-25	0.10-1.21	$1.11{\cdot}10^5$-$2.25{\cdot}10^6$	Turbulent

[1] The density is for natural gas is assumed to be 0.65 kg/m^3, the viscosity $1.0758 * 10^{-5} Pa \cdot s$ (Civan, 1989)

Table 2.4: Flow regimes for **oil** flow in gathering pipelines. Water density is set at 1000 kg/m^3. Viscosity is based on information in Figure 2.8b.

API	ρ_{oil} [kg/m^3]	h [m]	u [m/s]	μ_{oil} [Pa·s]	Re_h [-]	Flow regime
15	966	0.1	1	0.700	138	Laminar
15	966	0.3	3	0.700	1242	Laminar
25	904	0.1	1	0.023	3931	Turbulent
25	904	0.3	3	0.023	$3.538{\cdot}10^4$	Turbulent
35	850	0.1	1	0.005	$1.697{\cdot}10^4$	Turbulent
35	850	0.3	3	0.005	$1.530{\cdot}10^5$	Turbulent

Table 2.5: Flow regimes for **slurries** at fixed pipeline diameter of 500 mm and water density at 1000 kg/m3.

C_v	ρ_{oil} [kg/m^3]	u [m/s]	μ_m [mPa · s]	Reynolds number [-]	Flow regime
0.1	1165	0.5	1.4	2,08E+05	Turbulent
0.1	1165	2	1.4	8,32E+05	Turbulent
0.1	1165	4	1.4	1,66E+06	Turbulent
0.3	1495	0.5	3.0	1,25E+05	Turbulent
0.3	1495	2	3.0	4,98E+05	Turbulent
0.3	1495	4	3.0	9,97E+05	Turbulent
0.5	1825	0.5	15.6	2,92E+04	Turbulent
0.5	1825	2	15.6	1,17E+05	Turbulent
0.5	1825	4	15.6	2,34E+05	Turbulent

Table 2.6: Flow regimes for **drilling fluids**. Expanded table used in the study by Kong et al. (2019).

Parameters	Values				
Inlet flow rate (L·s^{-1})	0.5	1	2	3	5
(Out)flow rate of the central hole in the inner drill pipe (m·s^{-1})	0.17	0.34	0.68	1.02	1.7
Reynolds-number in the inner drill pipe	345	690	1380	2070	3450
Flow regime	Laminar	Laminar	Laminar	Laminar	Turbulent
(In)flow rate of the annulus between the inner and outer drill pipe (m·s^{-1})	0.18	0.36	0.72	1.08	1.8
Reynolds-number between inner and outer drill pipes	126	252	504	756	1260
Flow regime	Laminar	Laminar	Laminar	Laminar	Laminar

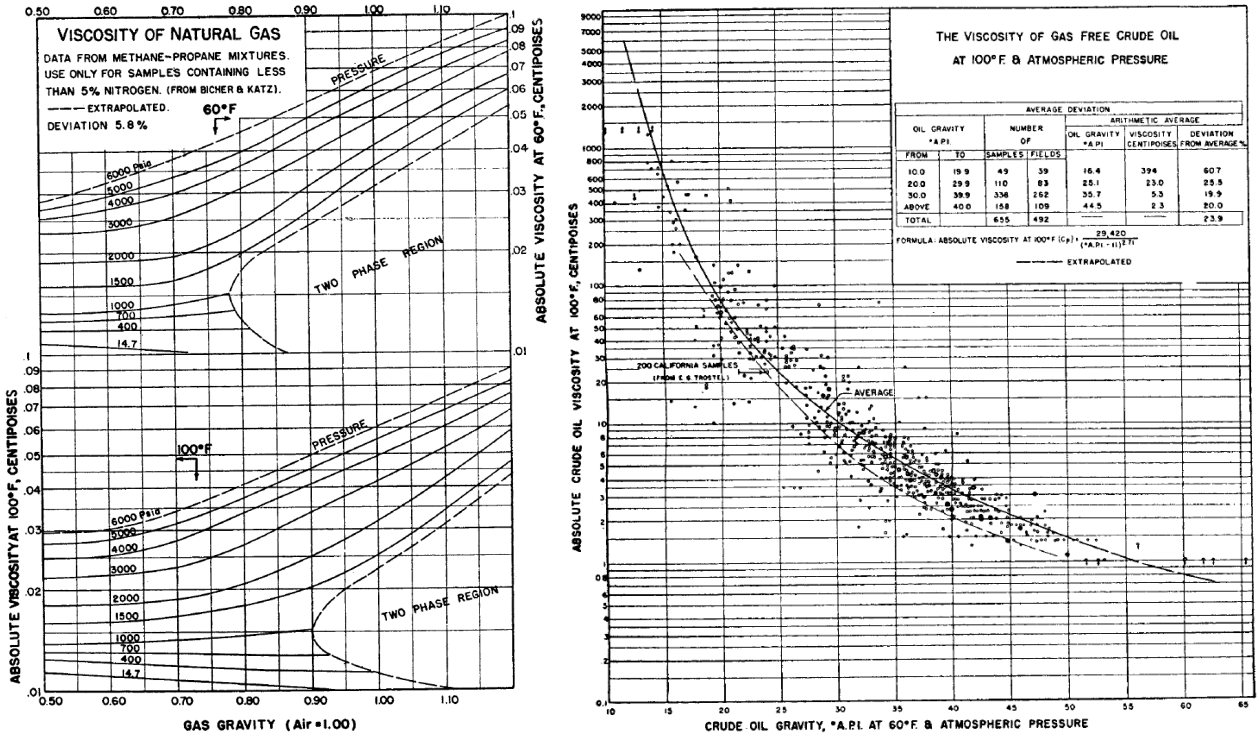

(a) Viscosity of natural gas (Beal, 1946). Standard conditions: 60° F (15.6° C) and 14.7 psia (1 atm).

(b) Viscosity of oil at 100° F (37.8° C) and atmospheric pressure (Beal, 1946).

Figure 2.8: Viscosity of gas and oil.

and pressure (NTP). In order to obtain a Reynolds number, the velocity within the pipeline is essential. For now, we classify flow velocities at the natural draft, low pressure, and high-pressure (INTECH GmbH, 2020). In correspondence with these pressures, flow pipelines (natural draft), gathering pipelines (low pressure), and transmission pipelines (high pressure) are investigated.

Oil flow

While the density of gas increases significantly under higher pressure and temperature, oil density ranges mainly due to its specific gravity. The density of oil is often expressed in API (named after the institution that created this measure: American Petroleum Institute). The SG of crude oil can be deduced according the following formula by Gerez and Pick (1996):

$$SG = \frac{\gamma_{oil}}{\gamma_{water}} = \frac{141.5}{API + 131.5} \quad (\text{at } 15.6°C) \tag{2.15}$$

The SG is referenced against the density of water which is approximately 1000 kg/m^3, although salty water might indicate a slightly higher density value. Crude oils with a API-value of 10 or lower are usually classified as extra heavy oils as they have a higher density than water. Oils ranging from 10-20 API are referred to as heavy oils and 20-30 API as medium. There are various opinions but anything above 35 API can be classified as a light crude oil (Azubuike and Ikiensikimama (2013); et al. Martinez-Palou (2011)). An API range of 10-40 results in a crude oil density spectrum between 825 and 1000 kg/m^3, assuming a water density of 1000 kg/m^3.

Similar to gas, oil viscosity is also dependent on pressure and temperature. This is visualized in a graph by Beal (1946) in Figure 2.8b. Although it portrays viscosity at field temperatures and field pressures, which are both relatively high, it indicates the temperature and pressure dependency.

The third and fourth parameters are the diameter of the oil pipeline and the velocity. Davis and Michaelides (2009) used an abandoned oil well of $h = 0.3$ m in Texas for geothermal power production while Renpu (2011) carefully analyses oil production wells and identifies production casing diameters of approximately 0.1-0.3 m. For Reynolds number computations depicted in Table 2.4, an oil viscosity at 100° F and atmospheric pressure, see Figure 2.8b, is used in combination with oil production rates of 1-3 m/s (Guo, 2019). It can be concluded that thick oils with a low API have a much lower viscosity, resulting in $Re < 2000$ and laminar flow. On the other hand, oils with a high API are more viscous and often operate in the turbulent flow regime.

Slurries

The slurry density depends on the density of the solids present in the mixture, the water density, and the concentration. For example, a concentration of 0.3, a water density of 1000 kg/m^3 and a solid density of 2650 kg/m^3 result in a slurry density of ≈ 1.5 kg/m^3.

The velocity of slurries is a relevant parameter within pipelines. Firstly, the critical velocity is defined, which denotes the minimum required velocity within a particular pipeline necessary to transport materials without sedimentation. Put concretely, if the velocity drops below this threshold, the particles within the slurry will settle, form a stationary bed, and eventually might lead to clogging (Jin and Randall, 2018). On the other hand, high velocities of mixtures in pipelines might cause cavitation, which is also not conducive for pipe flow (TUD OCW (2016), Open Course Ware). During dredging operations, it is more critical to avoid cavitation than the formation of a stationary bed, considering the relatively shorter suction pipelines. The opposite is true for longer pipelines, often tubes used for discharge of the dredged material. This occurs by default considering a longer pipeline will result in lower flow velocity towards the pipe's end.

When the pump has a higher capacity, longer pipelines can be used for discharge. Furthermore, the maximum pipe length is dependent on the characteristics of the mixture that is transported. E.g., slurries with a high density required more energy to be put in motion. The same holds for slurries with a higher viscosity. To compute the mixture viscosity, the equation by Thomas (1965) can be used:

$$\mu_m = \mu_w(1 + 2.5 \cdot C_v + 10.05 \cdot {C_v}^2 + 0.00273 \cdot \mathrm{e}^{16.6 \cdot C_v}) \tag{2.16}$$

where μ_m is the mixture's viscosity, μ the viscosity of water, and C_v the spatial volumetric concentration. The viscosity of water at 20°, an ambient pressure of 1 atm, and a spatial volumetric concentration of 0.3 results in a μ_m of approximately 3 mPa·s.

Van Eeten (2011) reports typical slurry densities between 1200 and 1800 kg/m^3. To give an indication in terms of Reynolds numbers, an overview is given in Table 2.5 assuming a pipeline diameter of 500 mm, a constant water viscosity, and a velocity in the range of 0.5-4.0 m/s. Reynolds numbers indicate turbulent flow, although, for much thicker slurries with higher C_v-values, the Reynolds number drops.

Drilling fluids

During horizontal directional drilling (HDD), drilling fluids form a critical aspect of the operation. In short, HDD is a trenchless technology where a pipe is installed underground with its entry and exit location at surface level. A drill pipe with a drill bit is used to create the first passage, see Figure 2.9. This is followed by reaming tools that enlarge the passage and a pullback operation of the pipeline. A water and bentonite mixture, referred to as drilling fluid, is pumped through the drill pipe until it reaches the drill bit. It has various functions, such as returning the cuttings from the drill bit to the passage entrance, keeping the cuttings in suspension, and cooling

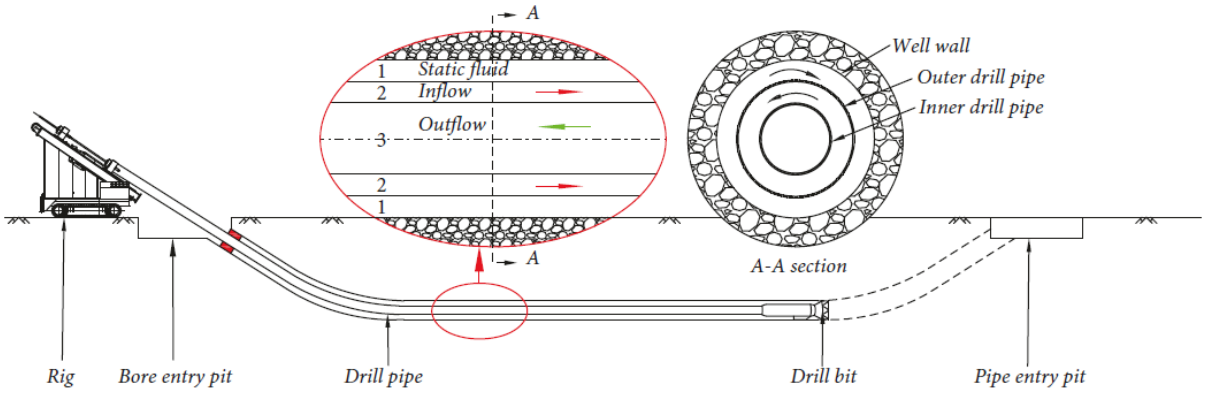

Figure 2.9: HDD operation. Modified cross-section of the pipe with in- and outflow within the pipe Kong et al. (2019).

the drill bit. Drag reducing technologies such as additives can enhance the flow of the drilling fluid on the inside of the drill pipe. Generally, cuttings are returned on the outside of the pipe as where they lubricate the drill pipe. However, Kong et al. (2019) investigated drilling fluids for a dual drill pipe system that is used during an HDD operation. This means that the inflow, as well as the outflow, occurs within the pipe. In his research, glass balls of density 2540 kg/m^3 acted as dredged material. The fluid is transported through an annulus to the drill bit that has an inner diameter of 92 mm and an outer diameter of 102 mm. Outflow, including the glass balls that act as 'dredged' material, is through the inner drill pipe, which has an inner diameter of 61 mm. The velocity ranged from 0.17 m/s to 1.71 m/s. The Reynolds is 2,000 for a flow velocity of $\approx$ 1 m/s. When the flow becomes turbulent, the volume fraction of cuttings that are displaced shrinks. Hence, turbulent flow is not conducive to the transport efficiency of drilling fluids.

2.2.3 Estimation of pressure losses

In this subsection, it is identified where pressure drop is observed due to friction in a pipeline network. For straight sections, the Darcy Weisbach formula can be applied (Kundu et al., 2016):

$$\Delta P = f_D \cdot \rho \cdot \frac{L}{D_h} \cdot \frac{u^2}{2} \tag{2.17}$$

where ΔP is the pressure drop in Pa, f_D is the Darcy friction factor, D_h the hydraulic diameter, u the fluid velocity, and L the length of the pipeline. The hydraulic diameter is denoted as four times the cross-sectional area A of the channel over the wetted perimeter P:

$$D_h = \frac{4A}{P} \tag{2.18}$$

When transporting liquid product, most likely, only part of the entire perimeter will be wetted. In the case of a rectangular channel, three of the four sides will be wetted. Liquids will therefore cause a relatively high hydraulic diameter value and hence smaller pressure drop.

Self evidently, pipelines are not infinite straight tubes. As illustrated earlier in Table 2.1, most of the pipelines in the US and Canada are distribution pipelines. They involve bends, valves, contractions, and expansions, which positively influence the amount of friction. This has been briefly summarized by Bird et al. (2006) in Table 2.7.

Combining Equation 2.17, the pressure loss of disturbances described in Table 2.7 and Bernoulli's principle results in the following equation:

$$\frac{1}{2}\rho\left(v_1^2 - v_2^2\right) + g\rho\left(h_1 - h_2\right) + \int_{p_1}^{p_2} \frac{1}{\rho} dp = \sum_i \left(f_D \cdot \rho \cdot \frac{L}{D_h} \cdot \frac{u^2}{2}\right)_i + \sum_i \left(e_v \rho \frac{u^2}{2}\right)_i \tag{2.19}$$

where h_1 and h_2 are the height of the entrance and the exit of the pipe, v_1 and v_2 are the inlet- and outlet velocity, p_1 and p_2 are the pressure at inlet and outlet, respectively. The parameter e_v is the disturbance factor which is dependent on the type of disturbance depicted in Table 2.7. Considering the right side of Equation

2.19, it can be established that the factor e_v is equivalent to the ratio of $f_D \cdot L/D_h$. Based on this, it can be established how large the impact is of corners, valves, contractions and expansions with respect to straight sections of pipelines.

Blasius formula can be used to determine the Darcy friction factor based on Reynolds number for turbulent flow (White, 2006):

$$f_D = \frac{0.316}{Re^{0.25}} \quad 2.1 \times 10^3 < Re < 10^5 \tag{2.20}$$

While this formula does not include a term for pipe roughness, it is sometimes use in non-hydraulically smooth pipe computations for simplicity. It is valid for Reynolds numbers up to $Re < 10^5$. An implicit variation on this formula is the *Prandtl formula* (Bird et al., 2006).

Table 2.7: Brief summary of friction loss factors that can be used in combination with Equation 2.19 (Approximate values for turbulent flow)[1] (Bird et al., 2006).

Disturbances	e_v
Sudden changes in cross-sectional area[2]	
Rounded entrance to pipe	0.05
Sudden contraction	$0.45(1-\beta)$
Sudden expansion[3]	$\left(\frac{1}{\beta}-1\right)^2$
Orifice (sharp-edged)	$2.71(1-\beta)\left(1-\beta^2\right)\frac{1}{\beta^2}$
Fittings and valves	
90° elbows (rounded)	$0.4-0.9$
90° elbows (square)	$1.3-1.9$
45° elbows	$0.3-0.4$
Globe valve (open)	$6-10$
Gate valve (open)	0.2

[1] Taken from H. Kramers , Technische Hogeschool, Holland (1958), pp 53-54
[2] Here β = (smaller cross sectional area)/(larger cross sectional area)
[3] See derivation from macrosopic balances in example 7.6-1 Bird et al. (2006). If β=0, then $\hat{E}_v = \frac{1}{2}v^2$, where v is the velocity *upstream* from the enlargement.

Consider an example of a pipe flow with a Reynolds number of 25,000, which is in the order of magnitude for distribution pipelines where many valves, contractions, and elbows are present. The friction factor based on the *Blasius equation* is $f_D = 0.0251$. consulting Equation 2.18, the ratio L/D_h can be simplified to $L/2R$ assuming a fully wetted perimeter for circular gas pipelines. By using Table 2.1 and considering a distribution pipeline radius of 70 mm, it results that a length of approximately 2 m distribution pipeline generates the same pressure loss as a rounded elbow bend of 45°($e_v = 0.35$) of the same pipeline type. In other words, the pressure loss due to friction forces is generally much more than the pressure loss caused by bends, swivels, and pipe joints. Pressure loss due to friction is therefore often referred to as the major loss, and the other losses are categorized as minor losses (TUD OCW (2016); Jin and Randall (2018)).

It should be mentioned that elbows, contractions, valves, and other sudden changes in the cross-sectional area directly contribute to the total drag, which consists of form- and skin friction drag. The straight pipeline sections, on the other hand, exclusively generate skin friction drag.

2.3 Conclusion fundamental principles

Hereby the conclusions of chapter 2 are summarized:

- Relevant fluid dynamics were discussed at the beginning of this chapter. The provided formulas and charts will prove to be of use throughout the report.

- There is a large spectrum of pipelines ranging from small diameters and low pressures to large diameters and high pressures. Among these pipelines, there exist long straight tubes such as transmission pipelines to transport product over long distances and pipeline networks, which are common in urban areas.
- For several fluids, the flow regime in which it is operates was investigated. This is challenging as regards the various amount of parameters on which the flow regime is dependent. Hence, a range of operating flow regimes for natural gas, oil, slurries, and drilling fluids was constructed. The bulk of the fluids are transported in the turbulent flow regime, although transport of thick oils and specifically drilling fluids can also operate in the laminar flow regime.
- Straight pipelines without bends are mainly exposed to skin friction drag. Also, pressure is lost in distribution pipeline networks due to valves, contractions, and elbows. A comparison between pressure loss due to skin friction drag and pressure loss due to form drag is constituted. It is concluded that 2 m of distribution pipeline generates the same amount of pressure loss as a 45° elbow. Therefore, long and relatively straight pipelines combined with high flow rates and considerable pressure (e.g., transmission pipelines) form the ideal circumstances for skin friction drag-reducing techniques to be applied. In the following chapter, drag-reducing techniques that can be used to reduce skin friction drag are amplified.

Chapter 3

Drag reducing techniques

This chapter considers two conventional drag-reducing techniques, one active and one passive. It is followed by a section on dimpled surfaces, a relatively undiscovered drag-reducing technique that could reduce skin friction drag in pipelines.

3.1 Active and passive flow control

In this section, one active and one passive drag-reducing technique will be discussed to put the dimple technology mentioned in chapter 1 into perspective. In terms of active flow control, the addition of drag-reducing agents (DRA) is a highly lucrative method. The application of riblets is a widely acknowledged passive drag reduction technology that will be reviewed.

3.1.1 Active flow control - DRA

The presence of DRA in the pipeline industry is so apparent that this technique must be addressed. A few examples will be touched upon in the upcoming paragraphs.

The direct impact of DRA on DR was discovered in the early '30s of the last century. The presence of certain additives in a fluid-flow achieved astonishing results in terms of drag reduction. It was only shortly after the Second World War that Toms (1948) not only discovered but also recognized the phenomenon of drag reduction after the addition of small amounts of linear macromolecules to a flowing fluid (Shenoy, 2020). Around the same time Toms (1948) published his findings, a similar discovery on the positive influence of DRA was made. Mysels (1949) claimed that the drag of oil flow could be reduced by converting gasoline into a thixotropic gel by adding an aluminum soap. The gasoline would experience less drag resistance than the unthickened gasoline for the same flow rate. Over the years, various techniques involving DRA have been researched. A few examples are given below.

Polymers

The first and foremost type of DRA is the addition of polymers, compositions of large molecules called macromolecules, which are multiples of simpler chemical units called monomers. It is widely acknowledged that polymers are primarily active in the TBL (Virk (1971); Fontaine et al. (1992)). The presence of the polymers activates a deceleration in streamwise velocity near the wall. With increasing distance from the injection point, this deficit diminishes. A second effect of injecting polymers is a reduction of wall-normal root-mean-square velocity. These reductions are substantially larger than the decrease in streamwise velocity and involve an abatement in Reynolds shear stress, making them a good DRA. The third and final result of injecting polymers is that they eventually reach Virk's asymptotic condition (Virk, 1971) which rules as a maximum possible drag reduction. As the polymers most affect the region near the wall, experiments including rough surfaces are of particular interest (e.g., Petrie et al. (2003)).

Injection
Polymers are brought into flow by injection. It is important to maintain the wall as intact as possible during this procedure, considering that any discrepancy might generate more drag instead of less. Figure 3.1 demonstrates a clear representation of how polymers can be launched into a flow. The vortex chamber has the function to relieve the no-slip condition of the polymer wall jet that is generated by the narrow inlets. The downstream wall below the knife-edge smoothly guides the polymer along the flat surface over the flat plate downstream of the injection slot (Petrie et al., 2003). This results in a uniform spanwise polymer flow. Bear in mind that this merely describes one of the various injection designs.

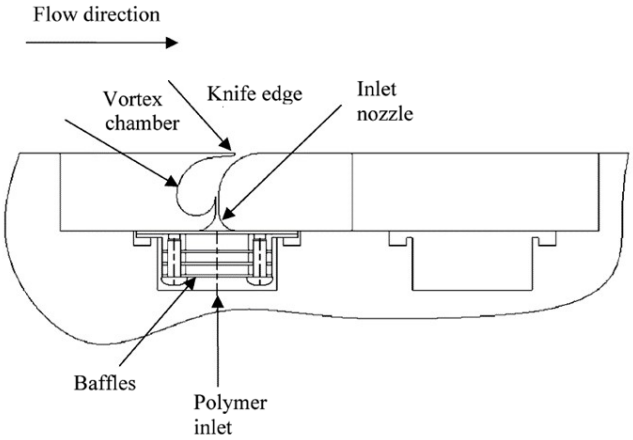

Figure 3.1: Side view of setup to inject polymers Petrie et al. (2003)

Properties
Polymers require a large molecular weight in order to have a positive effect on drag reduction. Debatable is the threshold of the molecular weight $\overline{M}_w$ of a polymer to ensure it positively influences the drag. For example, Virk et al. mentioned in their study from 1967 a minimum threshold of 80,000 g/mol while in his research of 1975 he is referring to a $\overline{M}_w$ of 570,000 g/mol. Paterson and Abernathy (1970) conducted their experiments with molecular weights between 250,000 and 8,000,000 g/mol while Agarwal and Porter (1980) used a poly(vinyl acetate) of $\overline{M}_w$ 750,000 g/mol. Generally speaking, polymers with a molecular weight >500,000 g/mol show positive effects. The preference of macromolecular conformations in the flow comes forth from the polymers' mechanical degradation with flow time. The polymers are not as prone to degradation as other additives, making them a favorable agent for higher drag reduction rates (Brostow, 1983). Eventually, the polymers do break downstream and degrade.

In addition to their considerable molecular weight, the polymers' concentration in the solvent is of importance. It is interesting that for polymers, an infinitesimal amount is needed in order to be lucrative. E.g., Toms added 10 ppm of PMMA (polymethylmethacrylate), resulting in a drag reduction of 80% (Abdulbari et al., 2014).

Advantages and drawbacks
As described above, adding polymers is a very effective technique that can significantly reduce the turbulence near the wall. Various researchers report drag reductions up to 60-80% (Ptasinski et al. (2001); White and Mungal (2008); Abdulbari et al. (2014)). A downside of the polymers is that certain types can be highly toxic, causing a disproportionate environmental impact (Abdulbari et al., 2014). The toxicity makes it impossible to use DRA by adding polymers to fluids directly used by humans, such as drinking water.

Surfactants

Properties
Polymers have particularly been applied in non-closed systems as the large molecule polymers degrade rapidly to polymers of lower molecular weight, eliminating their functioning when applied in closed-loop systems (Ohlendorf et al., 1986). However, surfactants (surface-active-agents) are a perfect substitute for this issue. Comparable to polymers, surfactants also involve macrostructures. They operate at the surfaces between solid-liquid, liquid-liquid, or liquid-gas interfaces. One of the most important properties is aggregation or self reassembling, making them excellent for closed systems. A major disadvantage is that most surfactants are syntactic (Clint, 1992).

Practical applicability
The first commercial application of surfactants was the injection of a few ppm in the Trans-Alaska pipeline. Carrying crude oil from North to South Alaska resulted in a 30% drag reduction (Abdulbari et al., 2014). However, their practical applicability remains low due to mechanical degradation (Shenoy, 1984).

Solid particle suspensions

Although the scientists were not aware that they discovered the first DRA, they noticed a pressure drop in turbulent pipe flow of paper pulp suspensions in water (Shenoy, 2020). This additive was insoluble and can thereby be classified as a solid particle suspension (SPS).

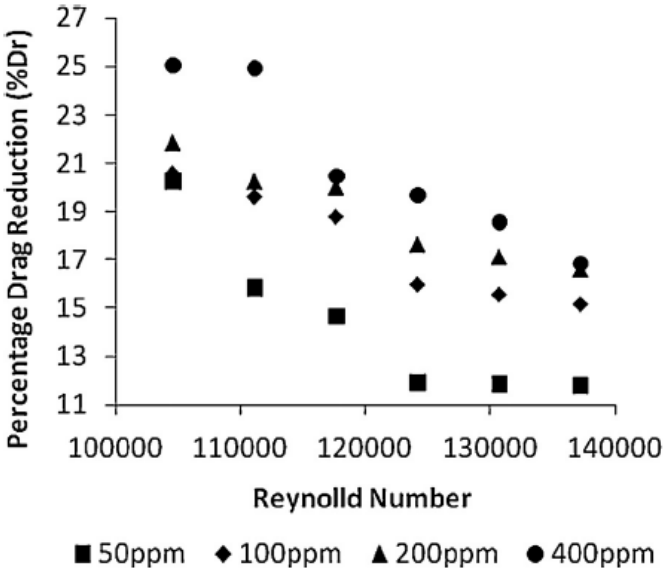

Figure 3.2: Drag reduction in 2.0 m, 0.0381 m inner diameter pipeline for different Reynolds numbers (Abdulbari, 2012).

Properties
There are two types of suspensions; granular particles that approach spherical particles and fibers (Shenoy, 2020). Similar to polymers, SPS mitigate the velocities fluctuations perpendicular to the wall, whereby the streamwise turbulence is enhanced. The concentration of the suspensions is typically in the order of a few hundred ppm. Abdulbari (2012) demonstrated an optimal drag reduction for 400 ppm, see Figure 3.2, while A.A.B. Hayder, A.H. Nour and Abdalia (2011) used a solution of 500 ppm to obtain a DR of 46%. Despite positive results concerning drag reduction, other studies found less promising results. Zhao et al. (2010) found a bulk velocity increase of 14% in his flow rate in his DNS study. A. Kartushinsky, A. Mulgi and Michaelides (2005) performed experimental research by inserting particles of different sizes in a gaseous pipe flow. Only for small particle diameters, a slight DR was encountered.

Advantages and drawbacks
First of all, suspended solids do not suffer from mechanical degradation. Secondly, in comparison with the aforementioned polymers, suspensions are easier to add and remove from the flow (Shenoy, 2020). On the other hand, there is a chance that this comes with a major disadvantage in the form of possible clogging and residues that are left behind in the pipeline at lower flow velocities (Abdulbari, 2012).

Practical applicability
Albeit some results are promising in terms of DR, this form of DRA has not been implemented. Arguments are that results are too far apart to convincingly state that this method works. Secondly, the settling of particles forms a great risk of clogging and thereby outage the pipeline.

3.1.2 Passive flow control - Riblets

From the previous subsection, it can be concluded that DRA's generally positively affect reducing skin friction drag. On the other hand, various complications such as removing the DRA, contamination by the DRA, or complex injection systems have to be considered. Contrarily to the DRA, a passive DRT does not come in conjunction with the challenges mentioned above. The conventional wisdom of fluid friction has been that a

Table 3.1: Overview of studies done on riblets in closed channels (Bixler and Bhushan, 2013a).

Fluid	Riblet design	Riblet configuration	Riblet material	Maximum turbulent pressure drop/drag reduction	Reference
Water	Blade	Aligned segmented	Acrylic	23%	Jung and Bhushan (2009)
	Blade & sawtooth	Aligned, segmented & continuous	Vinyl & acrylic	22%	Bixler and Bhushan (2013b)
	Sawtooth	Continous	Vinyl	9%	Rohr et al. (1992)
	Sawtooth	Continous	Polymer	28%	Reidy and Anderson (1988)
	Sawtooth	Continous	Vinyl	7%	Liu et al. (1990)
Oil	Blade	Aligned, segmented & continuous	Acrylic	7%	Bixler and Bhushan (2013c)
Air	Blade	Continous	Polymer	3%	Nitschke (1983)
	Blade & sawtooth	Aligned, segmented & continuous	Vinyl & acrylic	11%[1]	Bixler and Bhushan (2013b)
	Sawtooth	Continous	Epoxy	7%	Enyutin et al. (1995)

[1] Microsized tunnel.

supersmooth surface results in the least DR (Yee, 1992). This idea comes forth from the comparison between a smooth surface and a surface with random roughness. However, evidence found in nature unequivocally contradicts this theory. Bhushan (2009) offers a broad overview of unique surfaces with extraordinary characteristics that have evolved and optimized over time by Darwin's evolution theory. The most noteworthy technique are riblets which will be discussed in this subsection. In Appendix A, two more passive DRT's (compliant coatings and super-hydrophobic surfaces) are discussed.

Riblets are a direct copy of the microstructures present on shark skin. They are longitudinal ribbed structures in the streamwise direction. When the structures are continuous in the streamwise direction, they are referred to as 2D riblets. This is in contrast with actual shark skin, which is composed of 3D structures, i.e., a variation of structures in streamwise direction (Dean and Bhushan, 2010) Various structures have been studied, although sawtooth, scalloped, and blade riblets are the most common geometries (Bilinksky (2017); Abdulbari et al. (2013)). It is well known that riblets rearrange the turbulent structures only near the wall. The restriction of spanwise movement of longitudinal vortices is the main reason for turbulent drag reduction (Abdulbari et al. (2015); Choi (1989)). This technique originally comes forth from the airline industry. Walsh (1982; 1984;

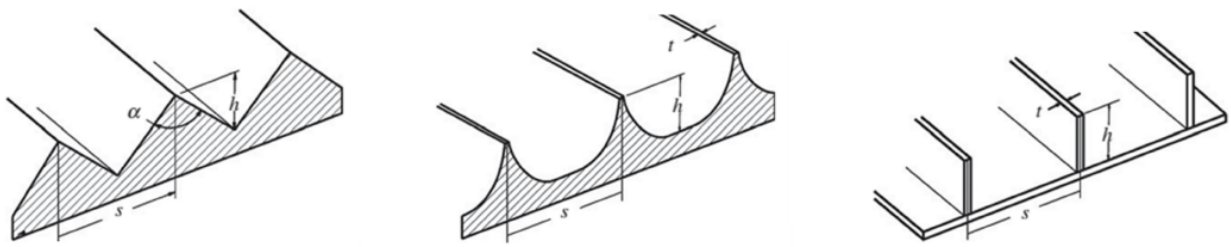

Figure 3.3: Common riblet structures. Fltr: sawtooth, scalloped, and blade (Bilinksky, 2017).

1986; 1988) did extensive research on riblets in the '80s of the last century at NASA Langley research facility (Hampton, VA). Apart from the aviation industry, riblet trends have also been studied for pipe flows. Dean and Bhushan (2010) showed a DR of 7% for riblets in pipe flows. The optimized spacing for these riblets is larger than for riblets on a flat surface as the ribs are pointed towards each other instead of parallel to each other.

It is no mystery that fabricating riblets and preventing clogging of the microstructures form the main challenges for this technique (Bilinksky (2017); Dean and Bhushan (2010)). Structures for the aerodynamic purpose have a typical size of 30-70 μm (García-Mayoral and Jiménez, 2011). A few examples of absolute roughnesses of commercial pipes are given by White (2006), which are in the order of 1-250 μm. Concluding, the 'roughness' of riblets has the same order of magnitude as the roughness used in the Moody diagram. Nevertheless, similar to dimples, riblets are composed in a particular pattern while the roughness on conventional pipelines' inner surface is random.

Despite the fact that the technology readiness level (TRL) of this technique is rather high (e.g., a test flight with riblets was already performed in 1989 (Robert, 1992)), the degradation of the material, maintenance of the surface, and high fabrication costs remain a bottleneck (Lienhart et al., 2008). A clear overview of studies that encountered a drag reduction due to riblets in closed channels is given by Bixler and Bhushan (2013a). Table 3.1 not only contains studies on air but also on water and oil. The different configurations that are mentioned are depicted in Figure 3.4.

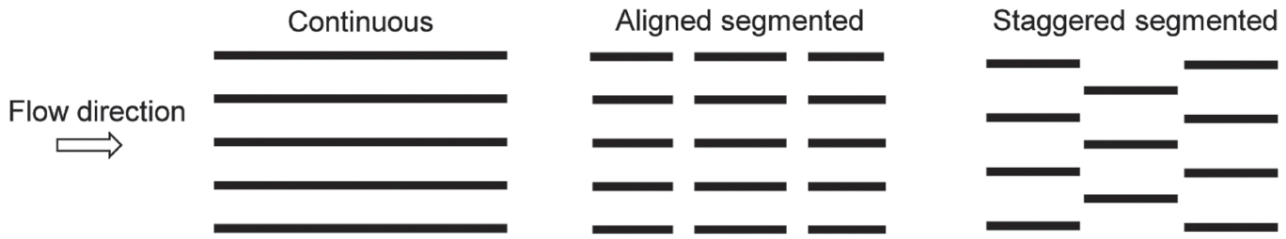

Figure 3.4: Different riblet configurations (Bixler and Bhushan, 2013a).

3.2 Studies on dimpled surfaces

In this section, a selection of interesting studies will be reviewed concerning dimpled surfaces with a focus on the application in channels. Dimpled surfaces is also an example of a passive DRT. However, in contrast with riblets, dimpled surfaces do not cope with degradation, fabrication challenges, and clogging. The technology is still in its infancy compared to other technologies, but it does have a promising prospect. Not many cross-validations of studies on dimples seem to have been done. Hence, enacting an analysis that clarifies which results of dimpled surfaces have been validated by other researchers and which studies show interesting results but are still to be reviewed is the key focus of this section.

As described at the beginning of subsection 3.1.2, it is concluded that skin friction drag reduces as a surface becomes smooth. If machining dimpled patterns into a flat surface enhances turbulent flow, it contradicts Moody's chart depicted in Figure 2.2. With this in mind, dimples' functioning is elucidated in subsection 3.2.2 in paragraph 'Results measurements NUS'.

3.2.1 Overview

In order to have a better sense of what studies have been done on flow through dimpled channels in the past decades, an overview is depicted in Table 3.2. It denotes which studies have been reviewed by other researches and what was concluded. The first researchers discovering the positive effect of dimples were Russian scientists in 1977. The focal point of their research was on increased heat transfer of dimpled surfaces rather than on drag reduction. The first person to publish about this discovery was Kiknadze et al. (1984). It marks an important event in the history of the dimple technology. Studies that have been published in the past decades about dimple technology can be separated in two groups: one that aims to increase the heat transfer and a second group that aspires to find drag reduction. Although the increase of heat transfer due to dimpled surfaces is not the primary objective of this research, the considered flow structures observed in these studies can be helpful.

Table 3.2: Overview publications on dimples between 2006-2020. Numbers in red indicate studies with DR that have not been validaded yet.

Research	Methodology	Notes	Change in drag	Disputed
Alekseev et al. (2006)	Experiment	No clear setup available	-17%	✓
Lienhart et al. (2008)	Experiment/ Numeric	Channel dimensions similar to Tay	+1%	
Veldhuis and Vervoort (2009)	Experiment/ Numeric	Contradicting Exp. and Num. results	-15%	✓
Tay (2011)	Experiment		-2%	
Tay et al. (2015)	Experiment		-3%	
Van Nesselrooij et al. (2016)[1]	Experiment	Disputed Alekseev et al., Veldhuis and Vervoort and Tay	-4%	✓
Van Campenhout et al. (2018)	Experiment	Disputed Van Nesselrooij et al.	+1%	
Spalart et al. (2019)	Experiment/ Numeric	Disputed Van Nesselrooij et al.	+1-2%	
Tay et al. (2019)	Experiment		-7.3%	
Ng et al. (2020)	Numeric		-7.4% <drag <+6.4%	

[1] Mentions that deviation with the results of Tay (2011) is possible due to channel design.

Investigations before 2000 are mainly concerned with the increase in heat transfer. At this point, the dimple technology is not as commonly known yet as other drag-reducing technologies such as riblets. However, a patent filed by Yee (1992) shows innovative applications for dimpled surfaces in the early '90s. Yee invented a reduction of skin friction drag by applying a plurality of depressions on the surface of a body moving through a fluid. The depressions are 20 times wider than they are deep, which seems to be in line with studies performed some 20 years later by Tay (2011). Figure 3.5 depicts examples of potential applications. The findings by Yee (1992)

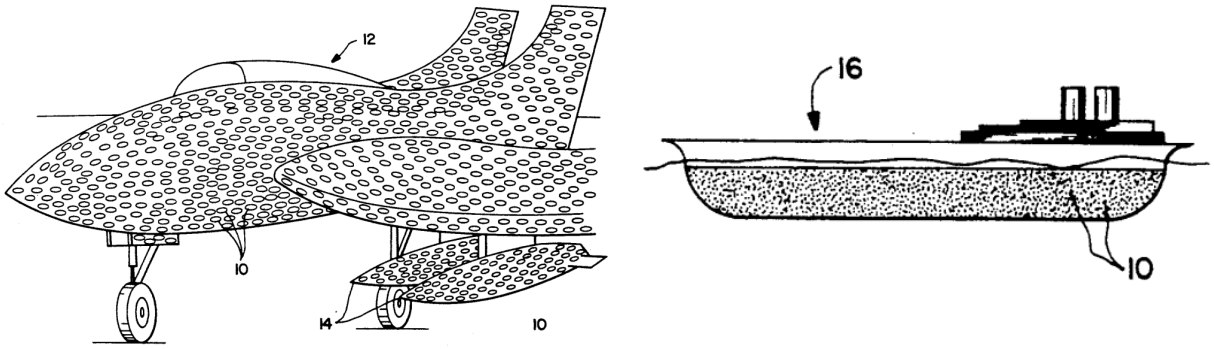

(a) Plural depressions on an aeroplane

(b) Plural depressions on a vessel

Figure 3.5: Plural depressions applied on different body surfaces (Yee, 1992).

are in line with the patent filed by Vida (2004) who also mentions dimples of $d/D \leq 0.1$, where d is the dimple depth, and D the dimple diameter. Vida provides a more detailed description of his patent. He states that the curvature of the dimples continuously connects the dimples to the surrounding surface. In other words, the indentation of the dimple has no sharp edges with respect to the wall. Similar to Yee, he also recognizes the potential of application for locomotion and other transportation devices.

In 2000, Moon et al. investigated the effect of channel height h on heat transfer and friction in a dimpled passage. He concluded that the channel height and Reynolds number were relatively independent of the Darcy friction factor. Moon et al. (2000) used dimple diameter of $D = 17.1$ mm, and h/D ratios $0.37 \leq h/D < 1.49$, i.e. channel heights of 6.33 - 25.48 mm. The ratio $d/D = 0.19$ is rather large in comparison with ratios found in earlier mentioned patents by Yee (1992) and Vida (2004).
A study in the early '00s (Mahmood et al., 2001) used a wind tunnel with channel dimensions 1219 by 50.8

by 411 mm (x-, y- and z-direction). Reynolds number is based on the channel height and ranges from 1,250 to 61,500. The d/D ratio in this is study is 0.1 where $D = 50.8$ mm. The facility used for this research is the same that was used later in Mahmood and Ligrani (2002), Burgess N. K. and Ligrani (2003) and Ligrani et al. (2005). Although the key point of attention in the experiments completed at the University of Utah was the increase of heat transfer, it is briefly mentioned that there are appreciable pressure losses.

In 2006, Alekseev et al. focuses on how tornado-like jets interact with a 3D-surface, i.e., a dimpled surface. Although drag reduction is mentioned, no exact experimental setup or explanation of pressure measurements is described. Another interesting publication in terms of dimpled channels is written by Lienhart et al. (2008). He performed a DNS as well as experimental measurements. The experimental measurements were done in a wind tunnel of dimensions 6000 by 50 by 600 mm. Tests involved dimples of $D = 15$ mm and $D = 47$ mm. The smaller dimples had a depth of $d = 0.75$ mm while the larger dimples were machined $d = 2$ mm into the surface. He concluded that the dimples slightly reduced the friction drag but that the total drag showed some increase. Measurements were done at a Reynolds number, based on half channel width and bulk velocity, of $Re \approx 11,000$. For the undimpled surface experiments, he perceived results coinciding perfectly with the DNS study results ten years earlier by Moser R.D. and Mansour (1999). All in all, Lienhart et al. concludes that dimples give a slight increase in drag.

At TUD, notable researches on drag reduction due to dimpled surfaces by Veldhuis and Vervoort (2009), Van Nesselrooij et al. (2016) and Van Campenhout et al. (2018) have been performed. Van Nesselrooij et al. disputed researches done by Alekseev et al. (2006), Veldhuis and Vervoort (2009) and Tay (2011). Research done by Van Campenhout et al. marks one of the few studies that repeated measurements with the same test conditions as in an earlier study, i.e.Van Nesselrooij et al. (2016). It is remarkable that the results of both studies do not coincide, which indicates the complexity of performing unbiased measurements.

In 2019, Spalart et al. reviewed the research done by Van Nesselrooij et al. (2016) and disputed this research by finding a 1-2% drag increase, which is in the same ballpark as research done by Van Campenhout et al. (2018) and Lienhart et al. (2008). Discussions between the authors of these researches did not result in detecting flaws in the study by Van Nesselrooij et al. and the deviating results remain unresolved.

Research has been done on dimpled surfaces in general, yet the studies done on dimpled surfaces in channel flows are scarce. Researchers at NUS have published various articles on this specific topic. Over the last decade, they did numerical as well as experimental research in this field (e.g., 2011; 2015; 2020). Moreover, they tested multiple dimple patterns alternated with different dimple geometries. Although some dimple patterns and geometries returned more DR for a larger spectrum of Reynolds numbers than others, all researches were concluded with some form of a drag reduction.

Tay et al. (2015) already pointed out that it is difficult to compare his results with other literature as outcomes of the measurements are highly dependent on parameters such as dimple geometry, which often remain unreported. The author of this document acknowledges this dilemma. Although the main consensus tends towards dimpled surface have a negative impact on the change in drag, see Table 3.2, researchers at NUS continue to publish articles with promising results for channeled flows that have not or only partially been validated. This forms a gap for new research.

3.2.2 Experiments at NUS

Based on the previous subsection it is interested to look further into experiments done at NUS by Tay and others. Albeit there is overlap between the articles, the findings are promising. In this subsection, a selection of the published articles will be discussed. An overview is depicted in Table 3.3.

Experimental details

The majority of the experimental details used in research done at NUS have been consistent. Both the repeating designs and the varying parts of the experiments conducted will be shown. The test setup is rather straightforward and does not seem to have been adapted over the years. The dimple geometry has been ameliorated many times and plausibly will be extended even more based on one of the latest findings at NUS (Tay et al., 2019).

Table 3.3: Change in drag for different dimple patterns after studies performed at NUS. ND = No data.

Research	Pattern + max drag						Max Re-number	Coverage Ratio	Remarks
	Spherical	Triangle	ellipse	Teardrop (up)	Teardrop (down)	Diamond			
2009	ND								Only surface flow visualization by HWA, $D = 40$ mm
2011	-2%						40,000	40% and 90%	Re based on channel height
2014	ND						28,000		Re based on D, only flow visualization
2015	-3%						35,000	40% and 90%	
2016	-4%	+3%					65,000	90%	Re based on half channel height, triangle width not described
2017	-4%						34,000	90%	Max drag obtained by shifting deepest point $0.1D$ downstream
2018	-3.5%			-6%	-5%		50,000	84%	CR for teardrops
2019						-7.3%	50,000	99%	CR for diamonds
2020	+6.4%		-4.9%	-3.1%	+0.1%	-7.4%	2,800	90.7%/84.4%/ 99.5%	DNS, Re based on bulk stream velocity

Test setup. The dimensions of the test setup used by Tay et al. have not been changed over the last few years (Tay (2011); Tay (2011); Tay et al. (2015); Tay and Lim (2017); Tay and Lim (2018); Tay et al. (2019)). The height of the channel (y-direction and normal to the wall) is 20 mm and is denoted by h. The other dimensions are generally expressed in terms of channel height and, therefore, dimensionless. The streamwise length of the test section is $120h$, i.e., 2.4 m. The test section is preceded by a 3.2 m entrance section ($160h$) in the upstream direction and followed by a 2.4 m exit section ($120h$) in the downstream direction. The downstream part of the test setup is connected to a suction fan, responsible for creating a channel flow. Before entering the inlet of the test setup, the flow is converged and straightened by a bellmouth. The bellmouth is equipped with a honeycomb and screens. The channel is $20h$ in the spanwise direction. A clear representation of the side- and front view of the test setup is shown in Figure 3.6.

The motivation of Tay et al. (2015) to opt for a relatively long entrance, exit, and test section is to reduce the error as much as possible. It allows the flow to fully develop three times along the channel: once at the entrance section, once at the test section, and once at the exit section. The long test section provides sufficient time for the flow to adjust to the dimpled surface and for drag reduction to occur (Tay, 2011). The top of the test section, covered with a dimpled pattern, can be removed and replaced by a flat plate to perform baseline measurements or a dimple plate with another pattern. Tay et al. (2015) describe that the channel comprises 17 identical channel wall pieces that can be assembled as top or bottom of the channel and 22 sidewall pieces, of which 18 are identical and can be put together in any configuration. It is not mentioned if the channel wall pieces involve the test section pieces or not. The bellmouth has a constriction of 16:1, which most likely results in an extended bellmouth, particularly in the y-direction. The channel is constructed out of aluminum, which restricts optical access.

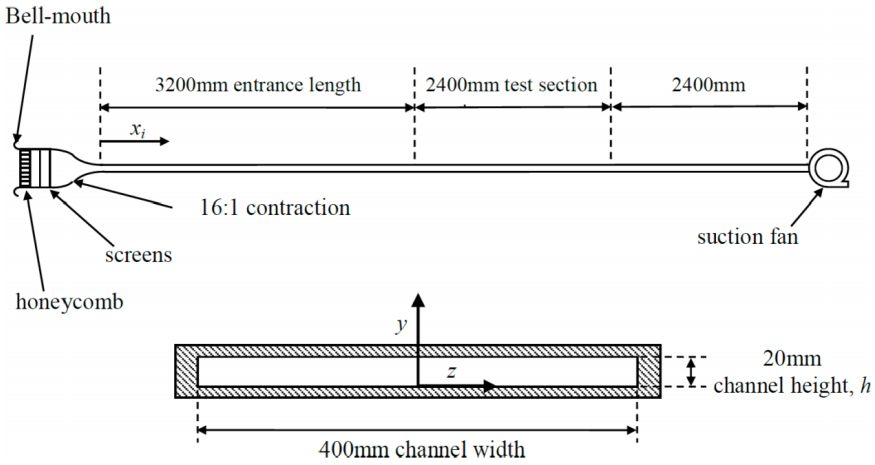

Figure 3.6: Side view test setup (up) and front view test setup (down) (Tay et al., 2015).

Earlier research indicated a setup with different dimensions. In the study of 2009, a test section of 450 mm in streamwise and spanwise direction is described, accompanied by an entrance section and exit section of the same spanwise dimension and streamwise dimensions of 1035 mm and 515 mm, respectively. While using this setup, the focus was not on drag reduction but rather on flow visualizations near the wall. Another research examining the flow visualization of various dimple types was conducted in 2014. This study measured the influence of two single dimples by the use of water flow instead of airflow. The test setup was submerged into a test domain with dimensions 750 mm x 1000 mm x 2250 mm, preceded by a re-circulating water tunnel with a 6:1 constriction. Similarly to Tay's article from 2009, this study also focused on flow visualization. Six different flow stages were observed that are depicted in Figure 3.9

Dimple geometry. The small indentations referred to as dimples are applied in various ways. Different factors influence the geometry of these indentations. Earlier research only refers to circular shapes (Tay (2011); Tay et al. (2015)). In later research elliptical, teardrop and diamond shapes were introduced (Tay and Lim (2018); Tay et al. (2019); Ng et al. (2020)). There are simple correlations between the circular dimple shapes and other dimple shapes, see Figure 3.7b. The ellipsoidal length is βD where $\beta = 1.5$. Equally, γ has a value of 2, and the diamond length is γD. As such, the dimple with the elliptical shape has a length of 75 mm in this case. The diamond-shaped dimple has a streamwise length of 100 mm and is made up of a circle and two triangles, one on each side. Considering that the teardrop shape involves one triangle combined with the circle, it has a streamwise length of 75 mm. The straight lines of the triangles are tangent with the circle. The angle of the isosceles triangle is 60°. The cross-sections of the dimples parallel to the x-z plane remain geometrically identical for different height y. As such, the angle of the triangle remains 60°at all depths in the dimple. The dimples' side view identifies that the slope of the ellipse and the diamond are more gradual than the slope of the circle. For the teardrop, this is valid for either the upstream or the downstream part of the dimple.

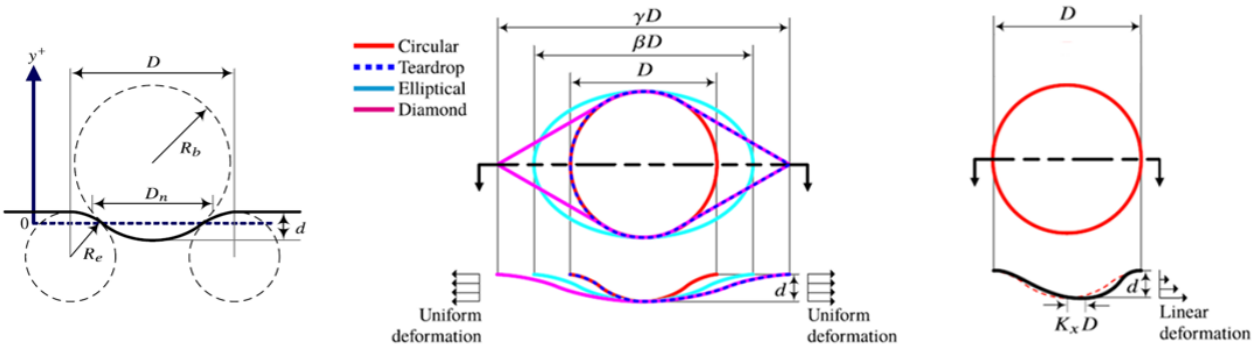

(a) Circular pattern. **(b)** Different patterns. **(c)** Shifted deepest point.

Figure 3.7: Dimple geometries (Ng et al., 2020).

Depth-diameter ratio. In studies performed at NUS, the ratio of dimple depth over dimple diameter is of major influence. As mentioned above, Mitsudharmadi et al. (2009) confirmed that with increasing d/D, flow separation would occur in an earlier stage, i.e., for relatively low Reynolds numbers. In order to emphasize this, Figures 3.8 and 3.9 illustrate how each stage can be identified and how the Reynolds number relates to the d/D ratio, respectively. Figure 3.9 shows that dimples with a low d/D ratio remain in stage I longer than dimples with a higher d/D ratio. As stage I indicates, the flow is fully attached, shallow dimples with a d/D ratio of no more than 10% encounter flow separation at higher Reynolds numbers. The smaller the d/D ratio, the lesser development stages are seen. Although for $d/D = 5\%$, some flow separation in the upstream half of the dimple might be observed (stage II), none of the vortical structures can be recognized for dimples $d/D < 10\%$. Moreover, Mitsudharmadi et al. observed that the flow over these shallow dimples eventually re-attaches. Veldhuis and Vervoort (2009) also observed that the d/D ratio should be less than 10% to obtain DR, which is in line with the patents filed by Yee (1992) and Vida (2004).

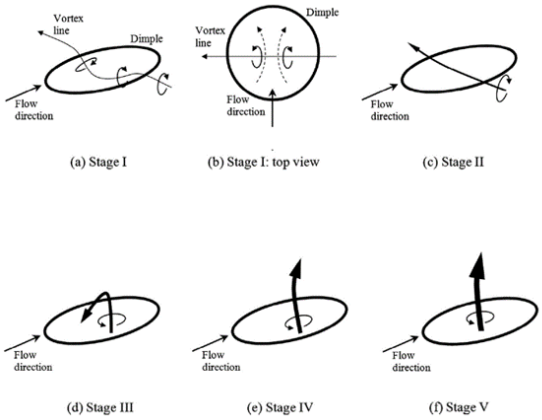

(a) Alignment of vortex line in various stages; bold arrow head shows vortex line given by the right hand rule, thickness of vortex line indicates its relative strength. The dashed lines in (b) show streamlines (Tay et al., 2014).

Stage	Characteristic of development stage
I	No vortices present, fully attached flow; streamlines curve towards the centerline at the upstream half and away from the centerline in the downstream half of the dimple; symmetric about centerline
II	Same as stage I, but with separation region present in the upstream half of the dimple
III	A pair of counter-rotating vortices connected by a vortex line forms a horseshoe vortex within the dimple depression; flow is symmetric about centerline
IV	Single dominant vortex within the dimple, axis of vortex is tilted from the vertical with spanwise and downstream components; no switching of rotational direction is observed; flow is asymmetric
V	Single dominant vortex within the dimple, axis of vortex is vertical and vortex may switch its rotational direction randomly; flow is asymmetric
VI	Mean flow is symmetric about centerline; a pair of counter-rotating vortices may be superimposed within the mean flow. No further large scale changes observed as the Reynolds number increases

(b) Flow development stages.

Figure 3.8: Stages visually and described.

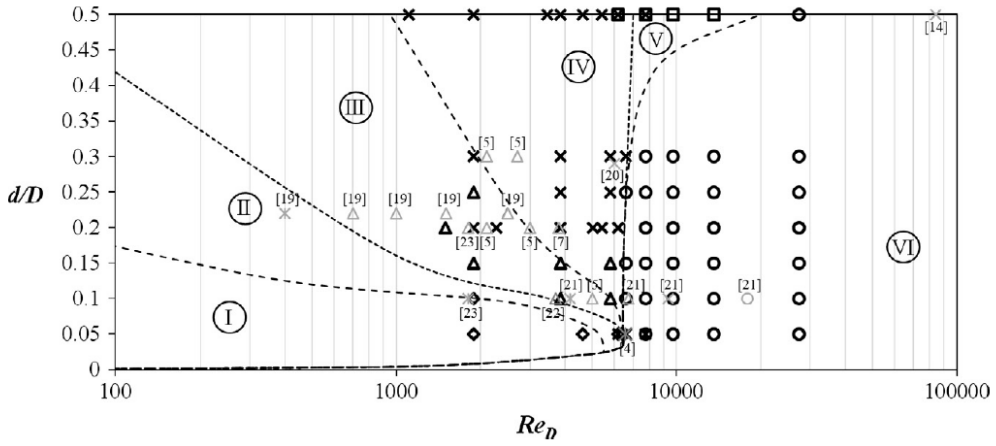

Figure 3.9: Different stages illustrated in terms of d/D ratio and Reynolds number (Tay et al., 2014).

In all researches published at NUS, dimples are expressed in dimensionless terms such as d/D. Hence, it might be worth noticing what diameters of the circular dimples are used. In 2009 the dimples had a diameter of 40 mm. Thereafter, Tay has been using dimples with a diameter of 50 mm. The cross section of the dimples used can be made up by three circles. In Figure 3.7a, $D = 5\delta$, $R_e = 4.21\delta$ (edge radius, not to be confused with Reynolds number), $R_b = 8.415\delta$ (base radius), $y = 0.05D$ and where $\delta = h/2$. In other papers, the ratio taken is precisely 1:2 in terms of circle radii (Tay et al., 2015). Bear in mind that these dimensions represent a d/D ratio of 5%. For deeper or more shallow dimples the correlation between the three circles changes.

Skewness. The dimples illustrated in Figure 3.7a and 3.7b all have their lowest point in the center of the circular part of the dimple. However, Ng et al. (2020) has also investigated the consequences of moving the lowest point of the dimple either upstream or downstream and hence skewing the dimples along the streamwise direction (Tay and Lim (2017); Ng et al. (2020)). To identify the x-coordinate of the dimpled surface after shearing, the following formula was used:

$$x_{asym} = x_{sym} + \frac{K_x D}{d} h \tag{3.1}$$

where x_{sym} is the x-coordinate before shearing and h is the channel height. K_x is the skewness parameter and is altered between -0.2 and 0.2 with an increment of 0.1, resulting in five steps. In Ng et al. (2020) there has been done a numerical simulation involving nine steps with increments of 0.05. A visual representation of the skewed center coordinate is depicted in Figure 3.7c.

Coverage Ratio. The coverage ratio (CR) for different dimple shapes is consistent over the years. For spherical dimples, CR's of 40% and 90% are applied in Tay et al. (2015). The 90% CR dimple plates resulted in more promising results. Hence, in researches following 2015, there was opted for a CR of 90% regarding spherical dimples. The CR can also be expressed in length between the centers of the spherical dimples. This is depicted in Figure 3.10a where β is 50 mm for a CR of 90% and 75 mm for a CR of 40%. In an earlier study, these distances measured 50.2 mm and 75.3 mm, respectively (Tay, 2011). As the angle between the individual dimples in the staggered pattern is 60°, the distance between each dimple in a triangular setup is β based on simple trigonometry.

All the setups portrayed in Figure 3.10 have dimple diameters of 50 mm. As the geometry of the teardrop- and diamond dimples is derived from the circular pattern, the distances β for Figures 3.10b and 3.10c are identical to β in Figure 3.10a, i.e. 50 mm. The maximum CR of the teardrop dimple is limited to 84.4% due to its asymmetric shapes. However, diamonds can reach almost a perfect CR reaching a maximum of 99.5% (Ng et al., 2020).

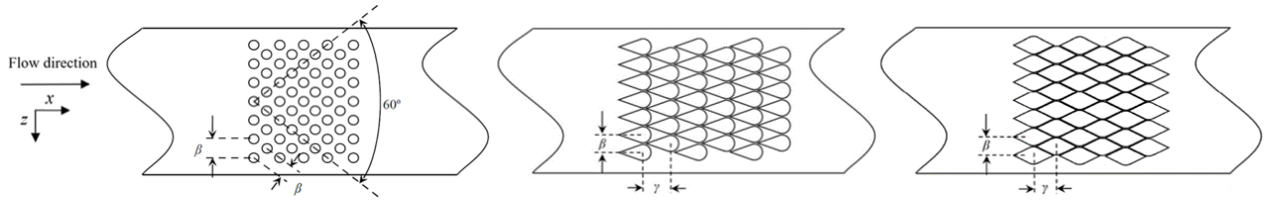

(a) Spherical pattern with theoretical CR of 40% .

(b) Teardrop pattern with theoretical CR of 84.4%.

(c) Diamond pattern with theoretical CR of 99.5%.

Figure 3.10: Different dimple patterns (top view).

Measurement techniques

Tay et al. used a couple of techniques to identify the consequences of dimpled surfaces regarding a change in drag with respect to flat surfaces. Pressure measurements are used to measure how the pressure changes. This is important to eventually quantify the change in drag. The hotwire technique analyzes flow patterns that occur over dimpled surfaces and helps validate that the BL is properly developed.

Pressure measurements. The publications of 2011 and 2015 best describe the experimental setup and results of the pressure measurements performed by Tay. The first streamwise pressure tap is drilled at $x/h = 27.5$, i.e., 550 mm downstream of the channel entrance. More taps are drilled in streamwise direction with an interval of $x/h = 10$ starting at $x/h = 27.5$. The last streamwise tap preceding the test section (there are no pressure taps between $x/h = 160$ and $x/h = 280$) is located at $x/h = 147.5$. There are two additional spanwise taps on each side of the centered tap with a 50 mm spacing at this location. Right after the test section at location $x/h = 297.5$, there are again five spanwise taps, each with a spacing of 50 mm. The pattern of a streamwise pressure tap each $x/h = 10$ is repeated up to $x/h = 367.5$. In conjunction with the last pressure tap, a pitot tube is placed to measure the total pressure. Tay et al. (2015) sampled at 1000 Hz for 33 s.

Hotwire Anemometry. For hotwire anemometry, the fixed roof in place for the pressure measurements is replaced by a sliding roof system above the test section. The 3-axis computer-controlled system lends itself for velocity measurements at any point in the 3D-space of this sliding roof by combining the rotating disc, an asymmetric vertical motion actuator on this disc, and a spanwise motion actuator. Due to the asymmetric location of the vertical actuator, measurements are possible at different streamwise and spanwise locations. In Figure 3.11) a Dantec 55P15 probe, specifically designed for measuring in boundary layers, is depicted that was used at NUS. As the prongs are under an angle, there should be no disturbance from the probe body to the flow. Based on Mitsudharmadi et al. (2009) where Constant Temperature Anemometry (CTA) was applied, it can be argued that this was also done by Tay et al. (2015). However, this is not described in the article from 2015.

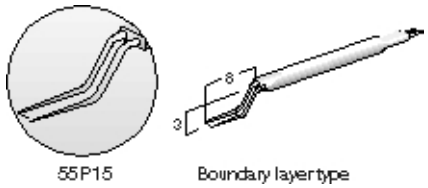

Figure 3.11: Hotwire probe used at NUS.

Results from NUS

Pressure measurements. A drag reduction for several dimple patterns at multiple Reynolds numbers was observed at NUS. Spherical dimples with a CR of 40% were studied in 2011 and 2015. Data indicated that a low 40% CR of spherical dimples yielded less DR than a large 90% coverage ratio. After 2015, only coverage ratios of 90% were used concerning spherical dimples. From 2011 and onward, the dimple geometry of the spherical dimples has not changed.

A clear overview of all maximum drag changes is depicted in Table 3.3. The affiliation between the coverage ratio and the drag reduction is striking in this table. As the CR of the test section increases, the drag reduction increases as well. The straightforward answer to this observation would be the volume increase of the channel by machining dimples on the flat channel floor. Whereas there seems to be a correction for this matter in one of the numerical studies assuming a constant flow rate (Ng et al., 2020), there is no correction for this in experimental work performed at NUS. In Tay et al. (2015) the mean channel height increases 3.8% for the spherical dimples that have a ratio $d/D = 0.05$ and 1.2% for dimple with $d/D = 0.015$. Based on data for Reynolds numbers lower than 20,000 where the DR is smaller for the deeper dimples, the possibility of volume increase dependency is neglected, see Figure 3.12a. In the DNS study from 2020, two teardrop designs with a different change in drag are used to argue that additional mechanisms are present which have influenced the eventual drag property.

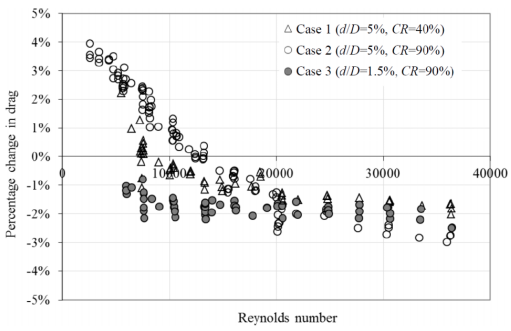

(a) Results of circular dimples (Tay et al., 2015).

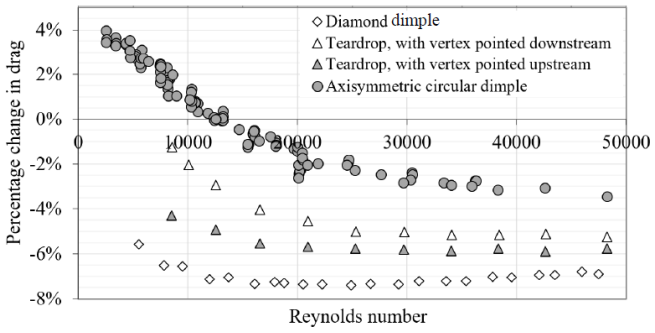

(b) Results of various dimple patterns (Tay et al., 2019).

Figure 3.12: Change in drag for various patterns, CR's and d/D ratios.

For $Re < 12,000$, the circular axisymmetric pattern (90% CR) leads to a drag increase. For the teardrop-shaped patterns and the diamond pattern, DR is observed for all measured Reynolds numbers. The diamond-shaped dimple pattern reaches the largest DR, depicted in Figure 3.12b. Even though there are no experimental

results (yet) for elliptical shaped dimples, numerical results indicated a drag reduction of -4.9% (Ng et al., 2020).

The presence of dimples activates a certain form drag in the channel as the flow is not passing a 2D surface but a 3D surface instead. Flow behavior near the surface and the effect of dimples on flow structures create opportunities for new analyses. Furthermore, a correction for the change in volume in experimental work has not been examined so far, which forms an interesting research question.

Hotwire anemometry. Despite all articles published about pressure measurements which resulted in a DR, studies from 2009 and 2015 seem to be the only articles where flow structures in the TBL are elaborated utilizing hotwire anemometry (HWA). In 2015, a 3D analysis using HWA was performed. The highest spatial resolution measurements were taken at $\Delta x \approx 0.043D$ and $\Delta z \approx 0.05D$, which is equivalent to a spacing of 2.15 and 2.5 mm, respectively. By taking measurements at various heights above the wall, two clear high-speed streaks could be identified. Counter-rotating vortices cause high and low-speed streaks. For the more shallow dimples ($d/D = 0.015$), merely one streakline was encountered. One of the key conclusions is that larger streamwise

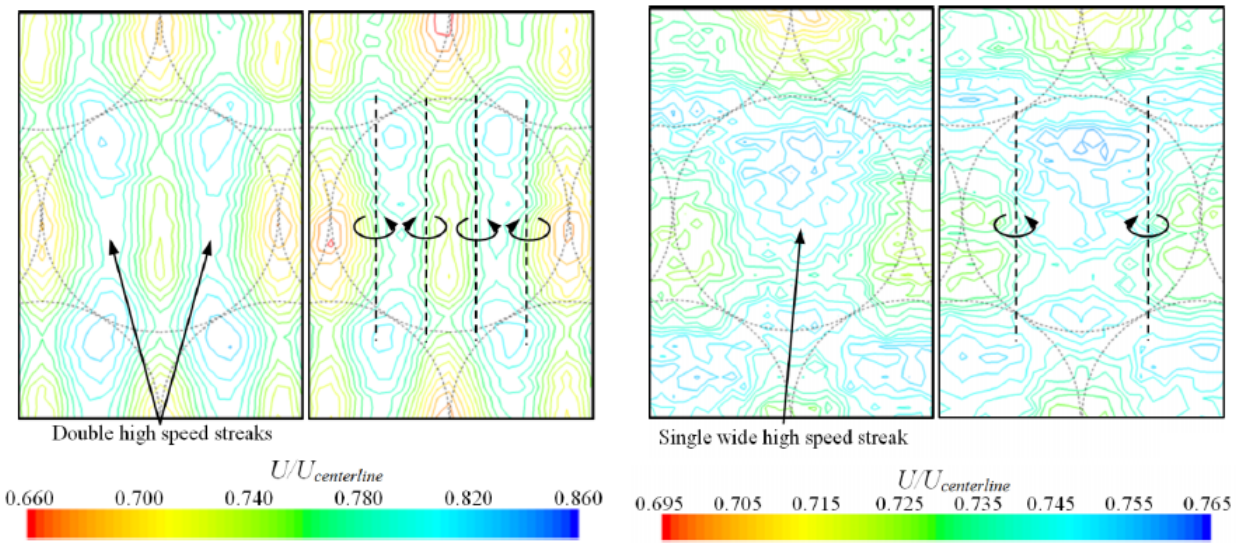

(a) Streaklines in deep dimples.

(b) Streakline in shallow dimples.

Figure 3.13: HWA results by Tay et al. (2015) indicating streaklines and vortices.

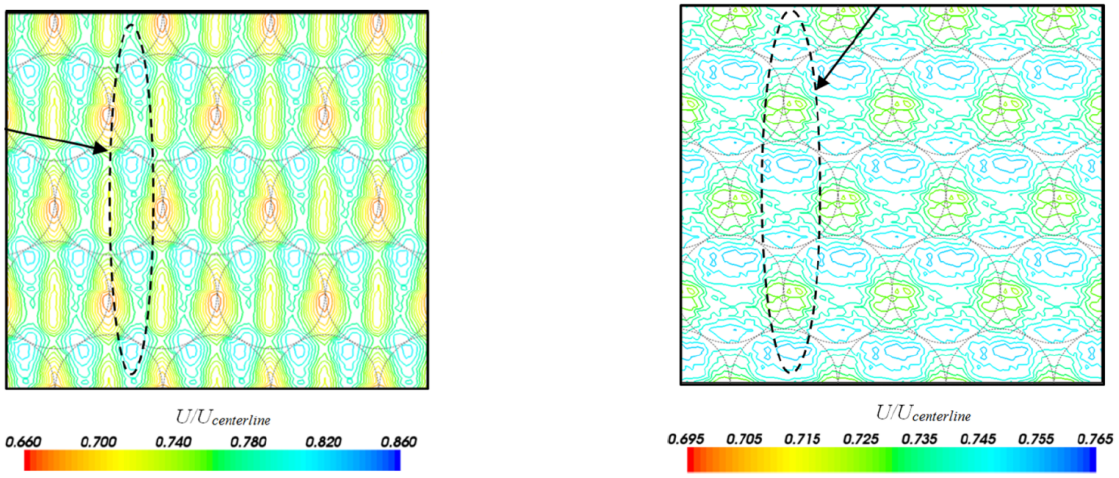

(a) Adjacent high speed regions in streamwise direction.

(b) Adjacent high speed regions in spanwise direction.

Figure 3.14: Continuous high speed regions for deep dimples (left) and discontinuous high speed regions for shallow dimples (right).

vorticity is caused by deeper dimples. Moreover, adjacent high speed regions are merged in single streamwise bands. Shallower dimples also form high speed regions but they remain separated. As a consequence spanwise high speed bands start to form, which is not conducive to the total resistance. Ideally, the HWA measurements are performed at constant wall units y^+. The wall units are dependent on Reynolds number and thereby on the kinematic viscosity. As such, for constant y^+-values similar flow structures should be visible at different physical heights above the wall.

The increased streamwise vorticity triggers an increase of spanwise flow components (Tay et al., 2015). As a result, wall-normal vorticity is dampened, turbulence operates at a larger scale, and high-speed streak lines retain energy dissipation at smaller scales. Moreover, near-wall flow is stabilized, which reduces the skin friction drag. Some sort of order is created in the chaos of turbulence.

To briefly summarize the research done at NUS:

- Researchers at NUS consistently use a narrow and long aluminum wind tunnel with dimensions 8000 mm by 20 mm by 400 mm (in x-, y- and z-direction, respectively). The test section area is located between $x/h = 160$ and $x/h = 280$ downstream from the inlet of the tunnel. One wall of the test section is covered with dimples. The dimple patterns used are spherical, teardrop (pointed upstream and pointed downstream), elliptical, and diamond. The geometry of spherical dimples is made up of three circles. The spherical dimple diameter is 50 mm, and the depth-diameter ratio d/D is 0.05, while the teardrop, ellipse, and diamond shape are simple variations of the spherical dimple shape.

- For the teardrop and diamond patterns, DR at all investigated Reynolds numbers is observed. Circular dimples show a DR only at $Re > 12,000$, based on $h/2$. No experimental data are available (yet) for elliptical dimples, although direct numerical simulation (DNS) data showed a DR of -4.9%. Evaluating all patterns, the maximum drag reduction obtained at NUS is -7.4% for the diamond-shaped dimple at a Reynolds number of 25,000 (Tay et al., 2019). On top of that, diamonds are the only pattern where the DNS result perfectly coincides with the experimental result.

- Earlier research neglected the gravity of volume increase of the channel. Later, in 2020, it is recognized that additional mechanisms are active near the dimpled surface. Nevertheless, the effect of an increased channel volume remains something that has not been investigated in experimental research.

- Hotwire results point out that two streamwise high-speed regions are formed for higher Reynolds numbers while only one high-speed streakline is observed for lower Reynolds numbers. Deeper dimples triggered a continuous high-speed region in the streamwise direction. Shallower dimples also triggered a continuous high-speed region but in the spanwise direction.

3.3 Conclusion DRT

The conclusion of this chapter is subdivided into two subsections. The first one concludes section 3.1, the second subsection summarizes section 3.2.

3.3.1 Active and passive flow control

- One of the more advanced active and passive drag-reducing technique were discussed. Both DRA and riblets give consistent drag reduction. The drag reduction of DRA's is 4-8 times higher than the DR of riblets in some cases (Abdulbari et al., 2013).

- Both techniques have several disadvantages. Macromolecules are prone to degradation, making them unsuitable for closed systems or systems with valves and fittings. SPS form residues and increases the risk of clogging. Riblet technology is a clean, scientifically proven technique. Nevertheless, degradation of the mini-structures, clogging of the narrow spaces between the ribs, and fabrication costs remain indisputable bottlenecks.

- A passive flow control technique is highly favored over an active DRT. The very reason that riblet technology has survived over the past decades is that it has proven to be working. It simply does not tick all the boxes, and the search for a working passive drag-reducing technique remains unfinished.

3.3.2 Studies on dimpled surfaces

Taking into account subsections 3.2.1 and 3.2.2 as well as consulting Table 3.2, the following conclusions can be drawn:

- Initially dimpled surfaces were implemented to achieve an increase in heat transfer. By accident, the potential of drag reduction was discovered. Researches can be divided into two categories: a group that focuses on the increase of heat transfer and a group that focuses on finding drag reduction.
- Various interesting articles concerning a change in drag of dimpled surfaces are published, e.g., Tay et al. (2015), Van Nesselrooij et al. (2016), and Spalart et al. (2019). However, the majority of the experiments are performed at relatively low Reynolds numbers, focus on heat transfer enhancement, or are carried out in wind tunnels with relatively large cross-sections.
- Although numerous researchers cite their colleagues, real cross-validations through reconstructing the same test setup and applying similar test conditions are limited. Researchers that have done cross-validations seem to have reached a consensus that dimpled surfaces result in a slight increase in drag. However, researchers at NUS have published various papers in the last ten years finding drag reduction utilizing dimpled surfaces in channel flow, and the arguments for opting for a more thorough investigation in their findings are threefold:
    1. Researchers at NUS are the only ones who continuously found drag reduction for different Reynolds numbers, multiple dimple patterns, and for experimental as wells as numerical experiments. The majority of the results have not been cross-validated yet as far as the author of this document is aware.
    2. Very little is written about the application of dimples on the inside of channels. In contrast, the first patents of dimples on transport devices and locomotive were already filed in the early '90s. This is strange since dimples aim to reduce skin friction drag. In smooth pipelines, the total drag is caused almost solely by skin friction drag, which forms a good opportunity to apply dimples (Yunqing et al., 2017).
    3. Based on Ng et al. (2020), NUS will continue doing research (numerical and experimental) on dimpled surfaces in channel flows. New developments from NUS most likely will find their way to existence in the near future.

Chapter 4

Experimental considerations

In the upcoming sections, experimental considerations are discussed. This involves measurement techniques used in this research, facilities available at TUD and, an introduction to the channel setup. Last but not least, the experimental models that were used in all experiments are discussed.

4.1 Experimental techniques

Three flow measurement techniques are discussed. First, the execution of static and total pressure measurements will be discussed. This is followed by HWA, used to analyze the BL. Thirdly, a relatively straightforward surface flow visualization technique involving oil will be discussed.

4.1.1 Pressure measurements

Two types of pressure measurements are performed. Static pressure taps are applied to measure the static pressure in the tunnel, allowing identification of the pressure gradient. A pitot tube is used to measure the total pressure from which the velocity can be deduced. Then, the velocity combined with the half-channel height and the kinematic viscosity is converted to a Reynolds number.

Static pressure tapping. A pressure measurement device at boundaries of fluids and solids is often referred to as 'pressure tapping' or 'wall tapping.' In an ideal situation, pressure taps are drilled normal to the wall with sharp edges, as shown in image (a) in Figure 4.1. An example of an anomaly could be a tap that is drilled under an angle. A selection of errors caused by skewed static pressure tapping is provided in the other images of Figure 4.1. In addition to this, the output may be over-or underestimated for rounded edges depending on which edge is rounded. The accuracy is made dimensionless by the dynamic velocity. More examples can be found in the study done by Chue (1975). Shaw (1960) pointed out that for a pipe with a ratio of $d_s/h = 0.1$, d_s being the diameter of the tap and h the diameter of the pipe, the resulting error of the mean dynamic pressure is approximately 1% for a pipe Reynolds number of $2 \cdot 10^5$. Based on this information, it is recommended to remain below this ratio.

Apart from the diameter, the depth of the orifice is also relevant. This is depicted as l_s in Figure 4.2a. This length has an impact on the extent of the eddy system, often called cavity vortices, that result from the flow deflecting into the orifice. Consequently, the measured pressure will be higher than the 'true' pressure at the wall. The orifice length is often expressed in the ratio l_s/d_s. A consensus seems to be taking a minimum ratio of $l_s/d_s \approx 2$ beyond which the error ceases to change (C. Tropea, A.L. Yarin (2007); McKeon and Smits (2002); Shaw (1960)).

The second point of attention is the height of potential dust, excess material of the drilling, or other undesired material close to the edge of an orifice. Burrs might influence the flow and the boundary layer close to the surface. For burrs at the downstream edge, the error is positive, while burrs at the upstream edge stimulate a negative error (Chue, 1975). The error of a burr height of $\epsilon_b/d_s = 1/127$ is approximately equal to the error caused by the hole size itself. An extensive overview of the influence of burrs on the flow is given by Shaw (1960).

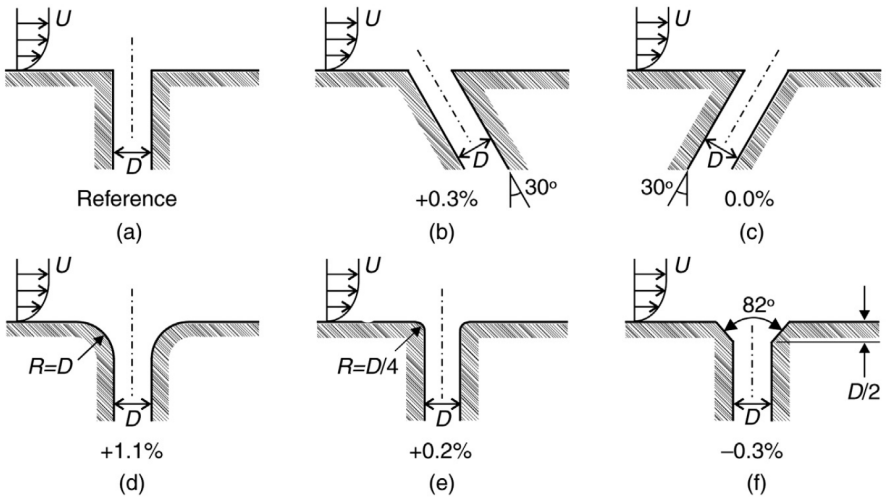

Figure 4.1: Configuration of static pressure taps and the influence of their geometry on the accuracy (Kim, 2016), non-dimensionalized by dynamic pressure.

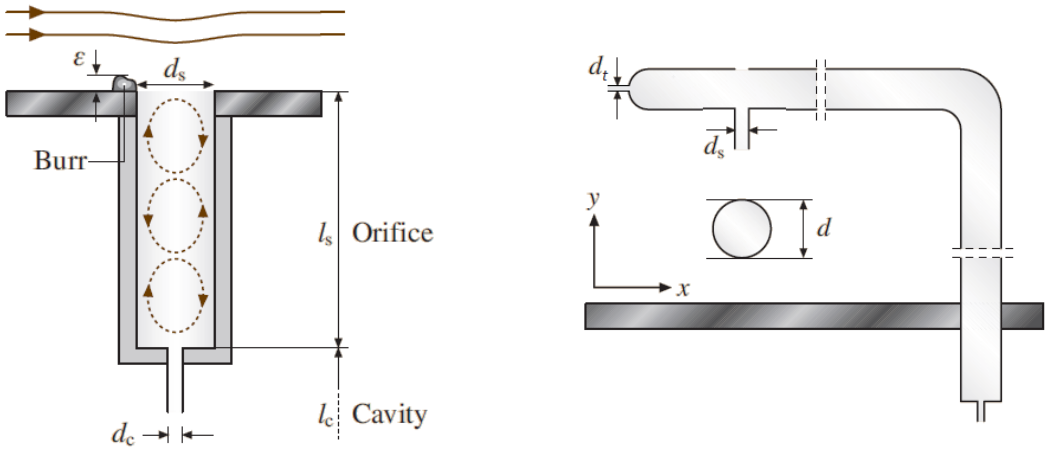

(a) Static wall tapping

(b) Pitot static tube

Figure 4.2: Cross-sections of static wall tapping and pitot static tube (C. Tropea, A.L. Yarin, 2007).

As mentioned in subsection 2.1.2, for turbulent flows, a distance of approximately 50 pipeline diameters is required for the flow to become fully developed. As such, it is recommended to drill the static pressure taps downstream of this distance.

Pitot-static tube. A pitot-static tube is a device used to measure the total pressure, which is the static- and dynamic pressure combined. Orifice with width d_t is the entrance for air that is used to measure total pressure. Orifices with width d_s are used to measure the static pressure, see Figure 4.2b. If static pressure taps are absent on the pitot-static tube, the measurement device is referred to as a simple pitot tube or pitot.

For subsonic flow velocities, the cone of the tube should be hemispherical. As the flow speed increases to supersonic velocities, a conical shape is advised to keep the bow shock attached to the probe and thereby to minimize the flow (C. Tropea, A.L. Yarin (2007); Chue (1975)). Two important factors have to be considered when using a tube with static taps. On the one hand, the distance from the nose to the static taps. For subsonic flow speeds, a distance of 6 pitot diameters rearward of the nose should suffice to neglect the error. On the other hand, a pitot tube has to be supported by a stem. This stem has a positive influence on the pressure readings of orifices ahead of the stem. For subsonic flow speeds, orifices located ten stem diameters upstream of the stem itself resulted in a dynamic pressure error of approximately 0.5% according to Chue (1975). This is an empirical rule that can be adapted for this research. The entrance of the orifice in the pitot is placed

perpendicular to the flow direction. Simultaneously, if present, the static pressure taps are parallel to the flow. In pipe flows, the tube is placed in the center of the channel to acquire the centerline velocity, which is the maximum velocity in the pipe.

4.1.2 Hotwire anemometry

A second important measurement technique, HWA, can provide insight into the velocity profile and the flow structures in the TBL. The name of the technology implies using a heated wire to carry out velocity measurements in air. A typical wire is made of tungsten or platinum and is 5 μm in diameter, which is approximately 16 times thinner than a human hair (Lomas, 1986). It is held in place by two support needles, often called prongs. The thin wire is electronically heated, causing the temperature of the wire to rise.

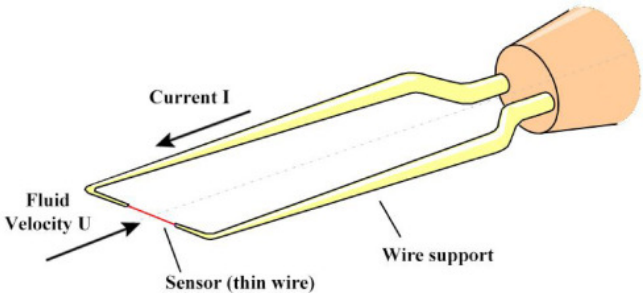

Figure 4.3: Hotwire structure (Stornelli et al., 2017).

As a flow passes around the wire, the wire is cooled. It can be assumed that only convective heat transfer occurs when the length of the wire is significantly larger than its diameter, i.e., $l/d > 200$ (Wilkinson et al., 1988). Two main modes of operation for HWA can be distinguished:

CCA. Constant current anemometry. For this mode, the circuit visible in Figure 4.4a applies. Here, the current passing through the wire is to be kept constant. A certain voltage is supplied that generates a current. This current heats the wire in such a way that its temperature is higher than its surroundings. A bridge is placed between the four resistances R_1, R_2, R_3 and R_{sens}, the resistance of the wire. V_{out} is in the state of equilibrium, i.e. $V_{out} = 0$. As soon as the resistance of the wire changes, the bridge is unbalanced, and the gauge indicates a non-zero value (Pawlowski, 2016). Following convective heat transfer, the resistance of the wire decreases as well as the voltage. With this, the temperature of the wire has to increase to maintain the constant current. Hence, the possibility of overheating the wire exists. In addition to that, as the voltage of the CCA mode decreases with increasing velocity, the output might interfere with the white noise spectrum (i.e., low voltage errors). This could make it harder to distinguish the signal from the noise. Therefore, the CCA mode is not applied very often.

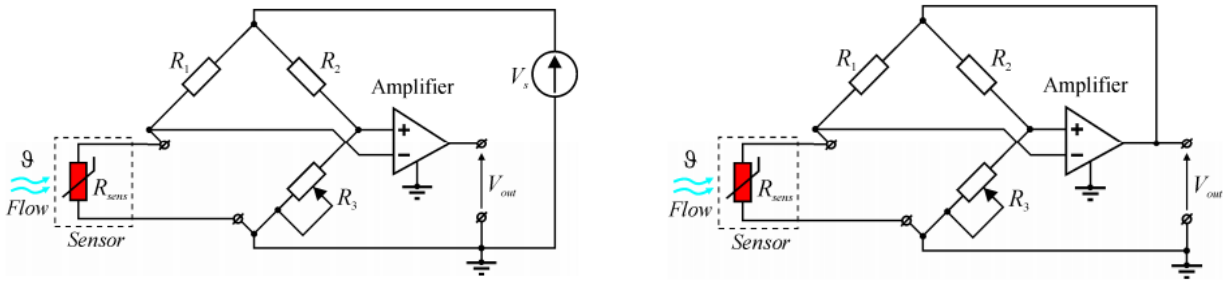

(a) CCA. **(b)** CTA.

Figure 4.4: Electrical circuits of two modes of operation for HWA (Pawlowski, 2016).

CTA. Constant temperature anemometry. Rather than the current, the temperature of the wire is maintained constant and thereby also its resistance. The CTA circuit is depicted in Figure 4.4b, which incorporates the feedback amplifier (Lomas, 1986). As the passing air cools the wire, feedback is received that a higher current is to be passed through the wire to bring the wire back to its reference temperature. The consequence is that the voltage also increases. For the CTA mode, King's law can be applied to describe the sensor's thermal

equilibrium concerning the moving fluid flow. Constants A_H and B_H have to be determined by calibration while constant n is often set to 0.5 (Pawlowski, 2016):

$$E^2 = A_H + B_H \cdot u^n \tag{4.1}$$

where u is the fluid velocity and E is the voltage. While using this equation, the sensitivity of the function should be considered. When the voltage increases, u increases exponentially. As a consequence, a slight error in the voltmeter might result in large errors in fluid velocity. This is elaborated further in subsection 6.1.1.

4.1.3 Surface flow visualization

As mentioned in chapter 1, Leonarda da Vinci was one of the first to sketch surface flow visualizations indicating complex vortex structures. Nowadays, surface flow visualization techniques are a significant asset for complex flow structures near the surface. Two factors that can hinder analyzing surface flow patterns are turbulence and gross time dependency. However, videography can be of use to indicate low-frequency oscillations (Schloemer, 1967).

SOFV. Surface oil flow visualization is one of the more common techniques used to observe flow structures such as lines of separation and reattachment near objects in a wind tunnel (Ristic, 2007). It involves the application of a paint mixture that is in contrast with the surface (Schloemer, 1967). Kerosene, diesel oil, or their mixtures form a common basis for paint applied on the surface. Once this coated surface is exposed to flow, the air exerts a force on the paint, causing it to deform since the inertial forces are significantly smaller than the viscous forces. Ideally, the oil's viscosity is high enough so that it is not carried away during the start-up phase of the wind tunnel but rather deforms at the desired wind tunnel speed (Mosharov et al., 2005). A clear image of flow around two cylinders on a plate is visible in Figures 4.5a and 4.5b.

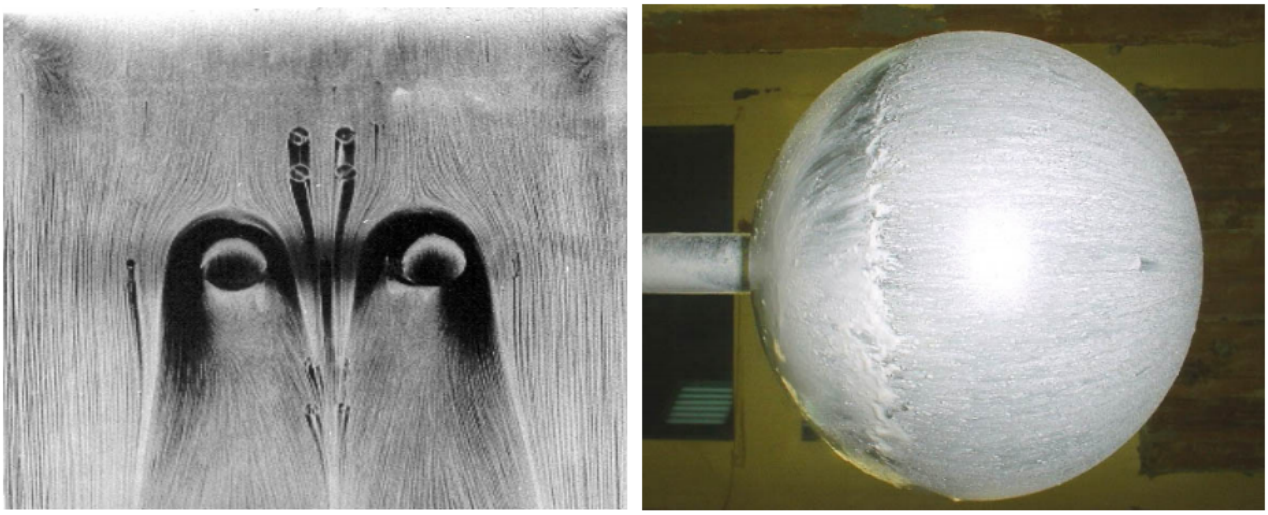

(a) Oil flow around two cylinders on a plate.

(b) Oil flow around a sphere.

Figure 4.5: Examples of surface oil flow visualizations (Ristic, 2007).

Tufts. Tufts are small pieces that indicate the instantaneous flow field. They often are used to identify if the flow is attached or separated (Yang, 2001). Ordinarily, tufts are made of silk cotton and have a diameter of less than 0.1 mm. The direction of the tufts has to be observed by their reflected light. For the small amount of light reflected, a long shutter response time and a wide aperture of the camera are required, which makes it challenging to capture the vibrating tufts (Ristic, 2007). Conventional tufts have a rather large degree of intrusiveness that contributes permanently to drag. As a response to this inconvenience, fluorescent mini-tufts were invented by Settles (1982). These tufts are of a small diameter (0.01-0.10 mm), causing less disturbance of the boundary layer. Using a UV light source, the tufts' fluorescent property increases the luminance of the tufts, making them appear thicker and brighter (Ristic, 2007). Furthermore, due to the small diameter and weight of the tufts, they can also easily be used to detect leakages. Even the smallest air flows can be detected by holding a strip of tufts close to a wind tunnel's outer surface.

4.2 Introduction to channel setup

Vacuum pumps. There are two identical pumps used to pass air through the wind tunnel. They are Leybold SV 750 50 Hz vacuum pumps from 1998. Both pumps include gas ballast to discharge oil aerosols in order to prevent contamination of the pump. Subsection 3.2.2 illuminates that Reynolds numbers in the order of tens of thousands are most interesting in terms of DR. Hence, a brief calculation of the pressure drop and maximum flow velocity was done in order to guarantee the feasibility of the aimed Reynolds numbers. Computations indicated that a theoretical Reynolds number of $3.47{\cdot}10^4$ could be reached and that underpressures would be in the range of 4.9 kPa. This is elaborated in Appendix B.

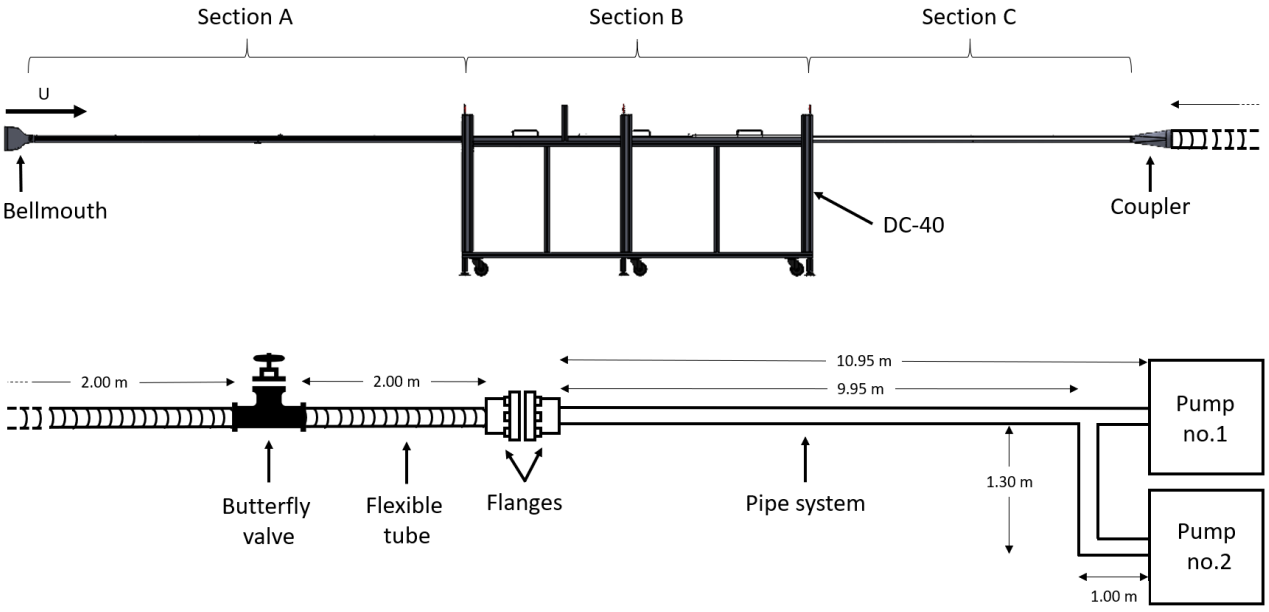

Figure 4.6: Full flow system from point of entrance at bellmouth to vacuum pumps no.1 and no.2. Images are not to scale.

(a) First part. The grey pipe is replaced by the flexible tubing system. The red arrow indicates the flange of the blue pipe system. Flow from bottom to top.

(b) Second part. Flow exists the wall, from bottom to top.

(c) Third part. Connected to pump no.1 (top) and pump no.2 (bottom). Flow from top to bottom.

Figure 4.7: Pipe system that connects flexible tube system to vacuum pumps.

Wind tunnel. For all experiments, a wind tunnel was built with the same dimensions as the wind tunnel used at NUS, 8000 mm long, 20 mm in height, and 400 mm wide. Appendix F contains a full description of the design and construction of the wind tunnel built at TUD. The tunnel was christened DC-40: Delft Channel 40 centimeters.

Flow system. The flow direction through the system is as follows: DC-40 $\longrightarrow$ flexible tube system $\longrightarrow$ piping system $\longrightarrow$ vacuum pumps. This is visualized in Figure 4.6. Once the flow exits the 'coupler', see Figure F.2b, it enters a 127 mm inner diameter tube of 2 m long. It makes a 90° turn towards the floor, where it makes a second 90° turn to the left. At this point, the flow enters a piece of pipe that has a T-shape with the stem points upwards. There is a butterfly valve in the stem that can be used to manage the flow velocity in the tunnel. When it is open, false air-leakage will cause the flow velocity to drop. The pressure valve is fastened to a pallet on the floor for stability. Once the flow exists the T-valve, it enters another 2 m flexible tube. This tube makes a 90° turn upwards. Approximately 1.5 m above the floor, the tube makes another 90° turn such that the tube is horizontal. The tube is connected to a piece of pipe that is welded to a flange. This flange is tightened to another flange, which is the beginning of the pipe system. Images of the pipe system are depicted in Figure 4.7. The pipe system connects the flexible tube system with the vacuum pumps. The flanges in Figure 4.6, are depicted by a red arrow in Figure 4.7a. The pipe system is 10.95 m long from the right flange to pump no.1 and 12.25 m long to pump no.2, see Figure 4.6 and 4.7c. It involves two 45° bends and four 90° bends.

4.3 Experimental setups

In the following subsections, experimental setups of three measurement techniques used in this research will be discussed in detail. To give an overview, Figure 4.8 illustrates where the three measurement techniques were performed in the wind tunnel. Black dots indicated the location of streamwise pressure taps, red dots the location of spanwise pressure taps, and blue dots where velocity profiles are measured. The red star illustrates the location of the pitot, used to measure the total pressure.

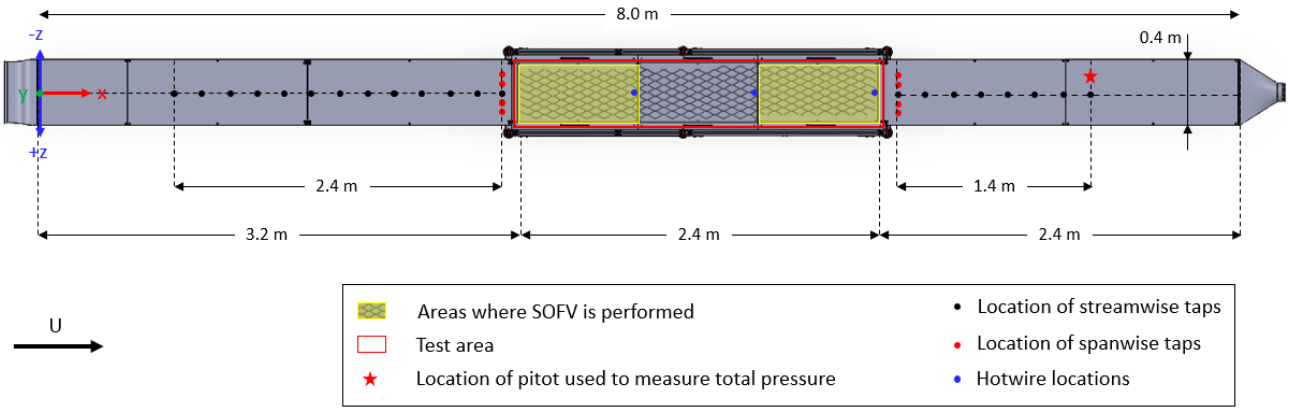

Figure 4.8: Top view of DC-40 with the location of three measurement techniques used in this research: pressure measurements, hotwire anemometry, and surface oil flow visualization (SOFV). Flow fltr. The red square marks the test area, which is amplified in Figure 4.17.

4.3.1 Pressure measurements

Pressure taps. The pressure taps are drilled manually on the channel wall floor and have a diameter of 1 mm. On the outside of the channel, the drilled pressure tap is enlarged to 1.1 mm to install a thin pressure tap of outer diameter equal to 1 mm. In total, there are 29 pressure taps. The first one is drilled at $x/h = 27.5$, where x is the streamwise distance from the entrance of the channel and h the height of the channel. From $x/h = 27.5$ to $x/h = 147.5$, 13 taps are drilled spaced $x/h = 10$ apart. All streamwise taps are drilled in the center of the bottom channel wall where the y-, and the z-coordinate are 0. Any spanwise movements are indicated by a negative or positive change in the z-direction. The x-, y-, and z-coordinate system is depicted in Figure 4.8. The last pressure tap upstream of the test section is drilled at $x/h = 147.5$. At this x-location, there is a total of five pressure taps spaced 50 mm apart with spanwise coordinates z/h = -5, -2.5, 0, 2.5, and 5. Right after the test section at $x/h = 297.5$, there is a second row of spanwise pressure taps with the same z/h-coordinates.

The spanwise pressure taps act to check the two-dimensionality of the flow right before and right after the test section (Tay et al., 2015). Between $x/h = 297.5$ and $x/h = 367.5$ there is another array of 8 pressure taps spaced $x/h = 10$ apart at the centerline of the channel.

There is a simple pitot tube of outer diameter 2.0 mm and inner diameter 1.0 mm in conjunction with the last pressure tap. The pitot is not placed in the centerline to prevent intervention with the static pressure tap at $x/h = 367.5$. Instead, it is placed at a quarter of the channel width at $z/h = -5$. The pitot entrance is at $x/h = 367.5$, and the stem enters the channel floor 20 mm downstream of this location. The entrance of the pitot is at $y/h = 0.5$ to measure the maximum centerline velocity.

(a) Single static pressure tap (50 cent for reference). **(b)** Pitot to measure total pressure.

Figure 4.9: Static and total pressure devices.

Pressure scanners. In order to measure the pressure drop, Nub pressure scanners are used. As the pressure drop in the upstream part of the tunnel will be considerably smaller than in the downstream part, various scanners will be used. After calibration, three scanners were selected with a maximum range of 600 Pa, 2.5 kPa, and 10 kPa. Each scanner has a frequency of 2000 Hz. For measurements performed with one pump, the first two scanners (600 Pa and 2.5 kPa) were used, while the latter two scanners (2.5 kPa and 10 kPa) are used for measurements performed with two vacuum pumps. Figure 4.10 depicts scanners connected to the pressure taps upstream and downstream of the test section. The scanners are placed on an object that is not in contact with the tunnel to prevent any disturbance caused by vibrations. The measured signals are transformed to raw data by LabVIEW 2018. This software is particularly suitable for data acquisition and communication with measurement devices. The raw data is analysed in Python. The full setup for the pressure measurements can be found in a block diagram depicted in Figure 4.11.

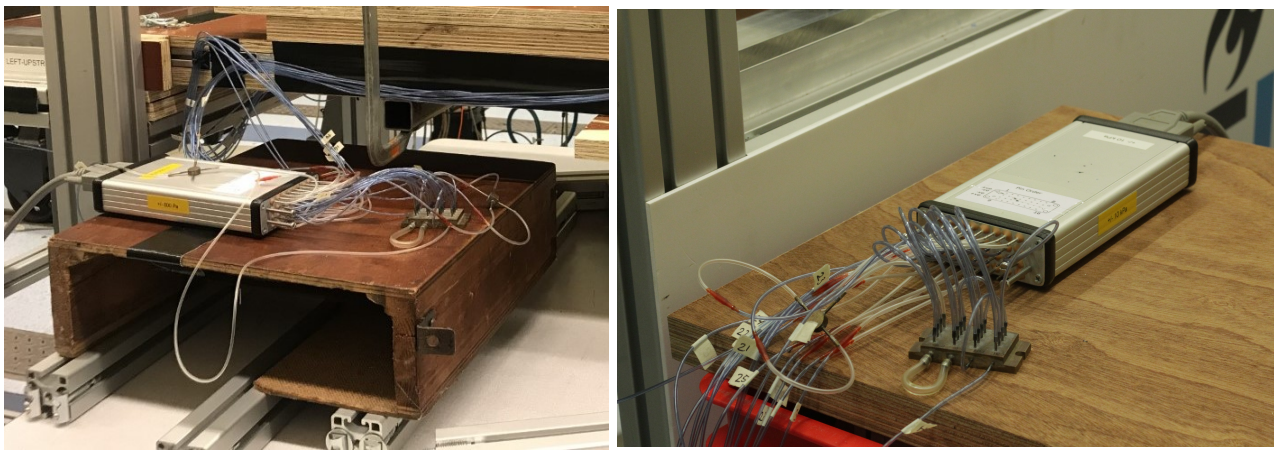

(a) Pressure scanner upstream of the test section. **(b)** Pressure scanner downstream of the test section.

Figure 4.10: Pressure scanners on separate tables, not in contact with the DC-40.

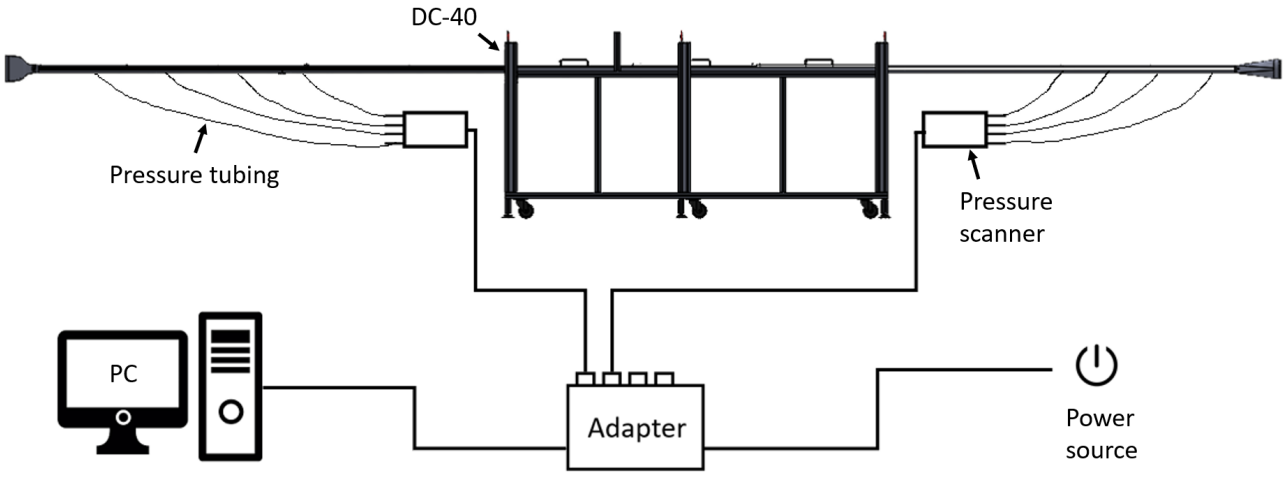

Figure 4.11: Block diagram of experimental setup for pressure measurements.

4.3.2 Hotwire anemometry

The hotwire setup used in research done at NUS involved a traverse system that is capable of acquiring data in a 3D-space. For simplicity, the hotwire measurements performed at TUD involved only one traverse in the y-direction. The traverse that was used is Dantec Dynamics traverse system. A broad overview of the experimental setup is illustrated in Figure 4.12. The adapter of the traverse and the traverse itself were mounted on two aluminium cross beams hovering over the test section, see Figure 4.13a. A hollow rod with inner diameter 10 mm and outer diameter 20 mm made of Polyoxymethylene (POM) was clamped vertically on the traverse. At the bottom of the rod, the outer diameter was reduced to 15 mm for a vertical distance of 25 mm, see Figure 4.15b. This was done to create less aerodynamical blockage in the tunnel. At the end of the hollow rod a 3D-printed probe support holder is inserted, see Figure 4.13c. The small Allen-screw at the back of the rod can be used to lock the probe support holder. A similar construction is used to hold the probe support in place within the 3D printed support holder. The probe support holds the probe itself which has prongs and a hotwire at the end which is visualized in Figure 4.15a. The probe that is used is a 55P15 probe which was illustrated in Figure 3.11 in section 4.1.

The adapter of the traverse is connected to a PC. The cable of the hotwire is guided through the hollow rod. It is connected with a control box that is linked to a laptop. Dimple Aerospace uses the control box to acquire i.a. hotwire data. In addition to that, it holds a Dantec MiniCTA 54T42 system to measure the voltage. LabVIEW is used to maneuver the traverse axis that is required for the HWA analysis.

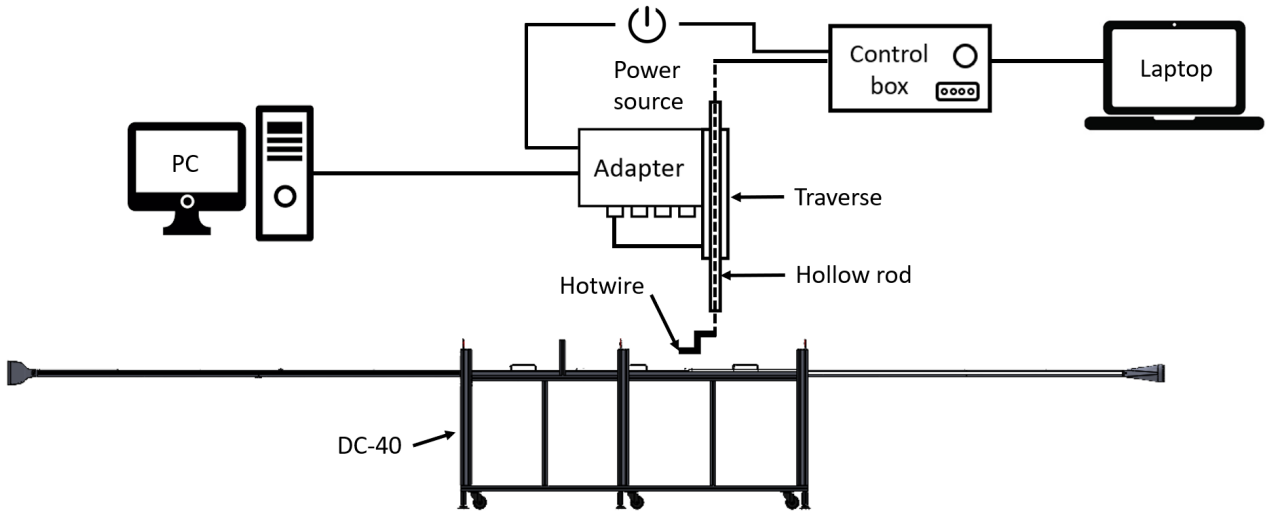

Figure 4.12: Block diagram of experimental setup for HWA. Aluminium cross beams are not illustrated.

(a) Traverse with hollow rod. Flow from bottom to top.

(b) Hotwire setup far away from the wall. Flow fltr.

(c) Hollow rod with 3D printed probe support holder.

Figure 4.13: HWA experimental setup. Photograph a and b are taken at test location 'downstream'.

Test locations. The measurement locations of hotwire have been stipulated based on two conditions. Firstly, the flow is desired to be as smooth as possible when it flows around the hotwire. Each transition between channel walls creates a certain step that possibly could interfere with the BL. As such, it is desired to keep transitions, hence potential steps, as far upstream of the hotwire as possible. By placing the hotwire slightly upstream of a transition of two top walls, it will have a long smooth part of the test section where the flow is undisturbed. This can be seen in Figures 4.14 and 4.15a. Secondly, the very narrow channel restricts access

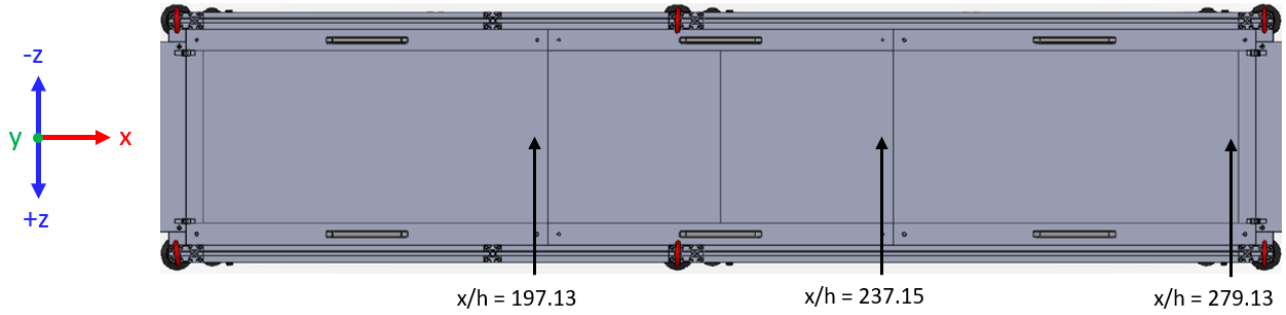

Figure 4.14: Upstream ($x/h = 197.13$), center ($x/h = 237.15$) and downstream ($x/h = 279.13$) test locations HWA. Flow fltr.

from all angles. To calibrate the hotwire position with respect to the wall, the experimental setup should be completely static except for the traverse. Therefore, the ceiling wall of the channel that is pierced with the hollow rod should be completely fastened. At this point, the only possible access to install the probe with the hotwire is when the hollow rod is placed close enough to the edge of the ceiling wall element such that the probe support holder sticks out. This is illustrated in Figure 4.15a. There were only three possible locations, taking the requirements mentioned above into account. The 'upstream' and 'downstream' locations are favored over the 'center' location considering they are the furthest apart.

The boundary layer is symmetric, presuming the channel has smooth walls on each side. Hence, the focus is on the bottom boundary layer that theoretically reaches from $y/h = 0$ to $y/h = 0.5$, where $y/h = 0$ is the floor of the flat channel wall. Furthermore, there is better access for the hotwire setup to be installed, and the TBL over dimpled plates, which are positioned at the bottom wall, can be examined. Unfortunately, the setup does not allow moving the traverse for the full 10 mm due to the limited space available for the probe support holder.

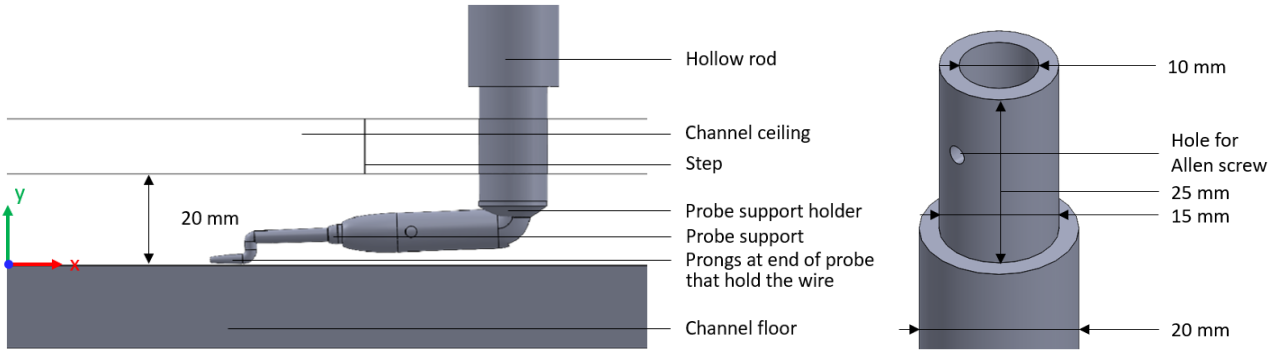

(a) Side view hotwire probe support holder. Flow fltr.

(b) Dimensions hollow rod.

Figure 4.15: Setup of hotwire rod including 3D hollow rod.

4.3.3 SOFV

For this measurement technique, only four things were needed: oil, fluorescent particles, a UV-light that can light up fluorescent particles mixed into the oil, and a photo camera to capture the movement of the oil and final flow structures. The oil is applied to the yellow areas depicted in Figure 4.8.

UV-light. The light was attached to an aluminum beam hovering over the test section; similar to the traverse in the HWA setup. For the upstream measurement, the light shined in the downstream direction. For the downstream measurement, the setup was mirrored, and the light shined in an upstream direction. It was challenging to position the UV-light in such a way that the reflection by the perspex and the aluminum dimpled test plates was minimal.

Photo camera. To capture the oil flow over the plates, a Nikon D7500 was used. The camera was mounted on an aluminum profile parallel to the test section. As such, it captures the flow movement from right to left. Ideally, the camera was positioned perfectly perpendicular to the test section. However, the oil measurements were performed on the last day of MC-4, and time management inhibited this. Nevertheless, the camera was already positioned well enough to capture good photographs, which can be found in section 7.2.

Oil. Shell Ondina Oil 927 was mixed with A-680 Plus fluorescent oil additives. By shining UV-light on the oil in a dark room, spectacular photographs can be taken, providing insight into flow behavior near the wall. The oil flow thickness was not measured. Nevertheless, it was mixed carefully, and a brush was used to spread it over the dimpled surface as smooth as possible.

(a) Setup at location 'upstream' including with top perplex wall. Flow fltr.

(b) Setup at location 'downstream' without perplex top wall. Flow fltr.

Figure 4.16: Oil flow setup.

4.4 Test plate geometries

Subsection 3.2.2 concludes that test plates covered with the diamond-shaped dimples result in the largest DR. Based on this conclusion, the selection of test plates with diamond-shaped dimples was obvious. The diamond-shaped dimples can theoretically reach a CR of 99.5% (Ng et al., 2020). However, it is preferred to only manufacture whole dimples in the test plates. In addition to that, space is required on the edge of every plate to fasten it on a 25 mm thick supporting plate.

The cross-section sketch of the diamond dimple was already portrayed in Figure 3.7b, subsection 3.2.2. The top view of the dimple is an assembly of a circle of $D = 50$ mm and two equilateral triangles. The length of the dimple is $2D$, i.e. 100 mm. The maximum depth of the dimple is 2.5 mm resulting in a d/D ratio of 5%. This only applies for $y = 0$, see Equation 4.2. The full geometry of the diamond dimple is more complex and described by the two equations below:

$$r = 25 - \sqrt{45.4^2 - (y - 45.4)^2} \quad \text{for } 0 \leq y < -0.899 \tag{4.2}$$

$$r = \sqrt{80.8^2 - (y + 78.3)^2} \quad \text{for } -0.899 \leq y \leq -2.5 \tag{4.3}$$

The 60°angle of the equilateral triangles is maintained as y drops to -2.5 mm and as the dimple cross-section becomes smaller, only the relative size of the dimple reduces (Tay et al., 2019).

In total, three plates were manufactured, of which the plate positioned most upstream, and the plate positioned most downstream are identical (803.1 in x-, 5 in y-, and 398 mm in the z-direction). The middle plate has dimensions of 793.8x5x398 mm. The odd dimensions ensure that the step between plates is located either halfway a dimple or between two dimples, considering the staggered pattern. The dimpled section used for this research is depicted in Figure 4.17, which is a scaled image of the real test plates. The 5 mm thick dimpled plates are molded out of aluminum and anodized afterward. The dimpled test plates are compared against flat plates, which have dimensions 1200x18x400 mm. These plates are made out of laminated plywood, which is also used for the entrance and exit sections. For further exact dimensions of the tunnel, test plates, and different sections, see Appendix F.

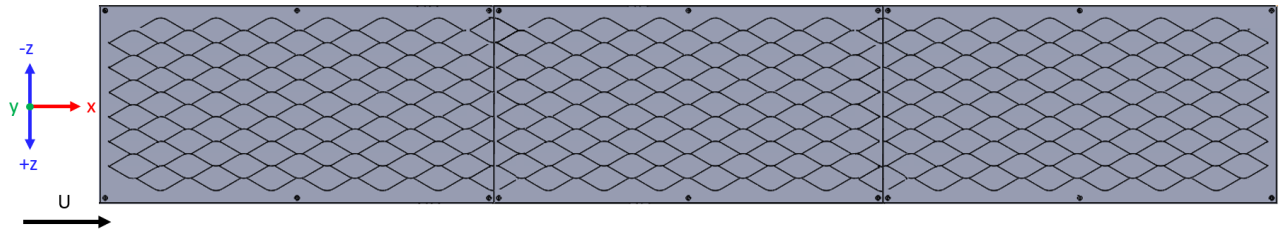

Figure 4.17: Scaled test plates with diamond-shaped dimples used at TUD. Flow fltr.

Chapter 5

Pressure based drag measurements

Chapter 5 involves a methodology, results, and a discussion for performed pressure measurements. The most important results can be found in section 5.3. Complementary graphs and charts can be found in Appendix E. Four measurement campaigns (MC's) of two weeks each have been performed. In the last two MC's, the final pressure, hotwire, and SOFV data was acquired. Between each MC, two or three off-weeks were scheduled to analyze the data and consider improvements for the setup.

Table 5.1: Measurement campaign schedule.

MC	Activities	Start campaign	End campaign
1	First test runs with DC-40	2020-09-29	2020-07-10
2	Second test runs with DC-40	2020-07-27	2020-08-07
3	Acquiring all pressure data - Acquiring pressure data with corrected volume	2020-08-24	2020-09-04
4	- HWA measurements - Surface oil flow visualization	2020-09-28	2020-10-09

5.1 Methodology

In the upcoming subsections, the methodology for pressure measurements is discussed. The calibration of the wind tunnel was quite challenging, and not all output data is probably as smooth as expected. Therefore, the methodology will also describe how corrections were applied to the raw data.

5.1.1 Measurement plan

Although the DC-40 has been calibrated and tested thoroughly prior to collecting data that is used for final analysis, there remains a chance that the tunnel experiences plastic deformation. In the worst-case scenario, the tunnel could implode should it be exposed to exceedingly large underpressures. For that reason, the first three days of measurements consisted of acquiring data using only one pump. After the measurements on day 1 were completed, the tunnel was dis- and re-assembled on day 2. New measurements were performed on the third day, which could be used to verify or deny the consistency of the wind tunnel. On the fourth day of data acquisition, two pumps were used to obtain higher flow velocities. The measurement plan for MC-3 is depicted in Table 5.2. Every day is started with a creep run. It is a test run to check if everything runs smoothly, and to see if no unexpected changes in results are observed with respect to earlier performed measurements. During a creep run, no data is acquired yet. On day 1, 3 and 4, 'sandwich' measurements are done. The sandwich-method describes an alternation of flat- and dimpled plates. The dimpled result can be referenced against the average of the two adjacent flat plate results. Eventually, three pressure delta's proceed from the 'sandwich' method. The delta's are averaged which leads to the final change in drag value. The method allows to check for any inconsistencies during a flat-dimpled-flat sequence by comparing the flat plate data. There might be reason to omit the data or correct for it in case it is not consistent enough.

Table 5.2: Sandwich method planned for MC3.

Day 1 (1 pump)	Day 2	Day 3 (1 pump)	Day 4 (2 pumps)
Creep run	*Disassemble and re-assemble DC-40*	Creep run	Creep run
Flat plates		Flat plates	Flat plates
Dimpled plates		Dimpled plates	Dimpled plates
Flat plates		Flat plates	Flat plates
Dimpled plates		Dimpled plates	Dimpled plates
Flat plates		Flat plates	Flat plates
Dimpled plates		Dimpled plates	Dimpled plates
Flat plates		Flat plates	Flat plates

Minimizing human error. During the acquisition of the pressure data, two strict routines were followed to minimize human errors. The first routine describes how flat test plates were swapped for dimpled test plates during the pump-off time. The second sequence helped to maintain a consistent routine during the pump-on time. Both routines can be found in Appendix D.

5.1.2 Data corrections.

There are several corrections applied that help to draw an unbiased verdict on the pressure results. Furthermore, various verifications are performed, which will be discussed separately in section 5.2.

Mean gradient. In an ideal world, the pressure data resembles the chart in Figure 5.1. For dimpled plates in section B, see Figure F.1, the gradient of the pressure drop per meter is more shallow compared to the flat plate gradient. Thereby, it indicates a smaller pressure drop. After the dimpled section, the plates are flat again, and the gradient is parallel to the gradient before the test section. Would the red dotted gradient have been steeper than the black line in section B, a drag increase could be concluded. As discussed earlier in chapter 1, drag in pipelines is (almost) fully caused by skin friction drag. Put concretely, the pressure drop is a direct consequence of skin friction drag.

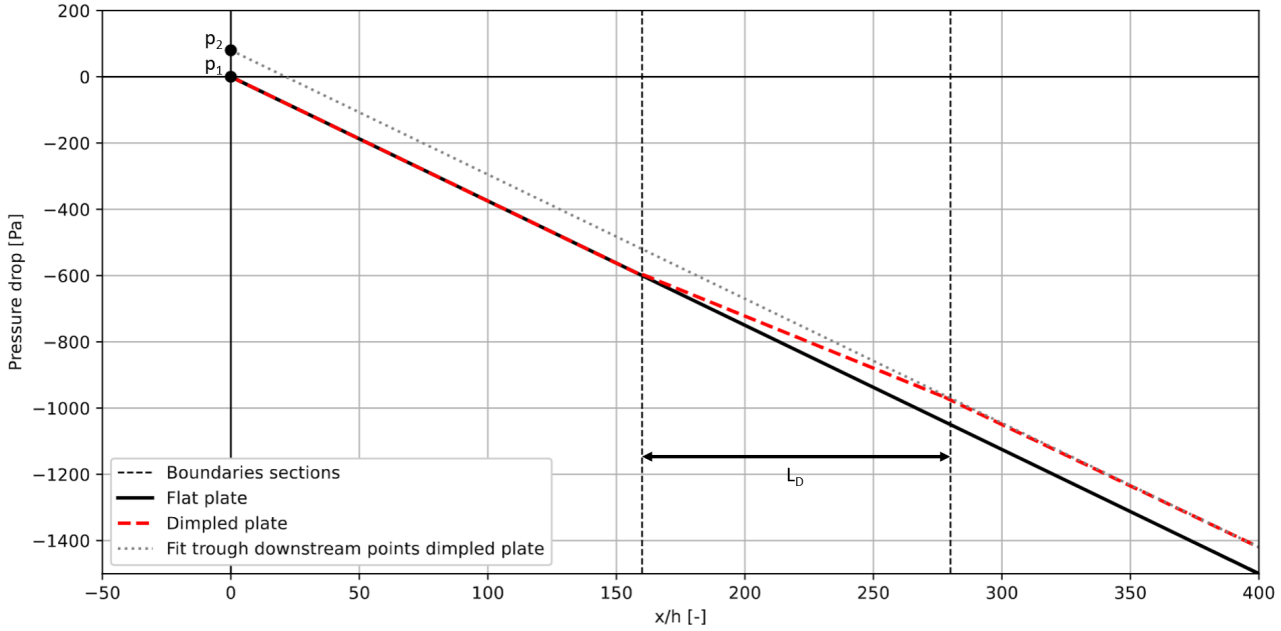

Figure 5.1: Hypothetical DR of dimpled plates with respect to flat plates.

The difference between p_1 and p_2 can be used to determine the change in drag. The following formula is applied where p_g is the pressure gradient, L_D the length of the dimple array, and Δ_d the change in drag:

$$\Delta_d = \frac{(p_1 - p_2)}{L_D p_g} \tag{5.1}$$

In other words, assuming that the gradient in section A and section C are the same, a vertical upward shift of p_1 to p_2 indicates a drag reduction.

In theory, a linear fit through the pressure data points upstream of section B should have the same gradient as a linear fit through the pressure data points downstream of the test section. In practice, however, this is challenging. The sensitivity of the measured static pressures is really high, which results in upstream- and downstream gradients that are not identical. The slightest offset in gradient would have a major impact on the difference between p_1 and p_2 and consequently on the change in drag. Therefore, the gradient upstream and the gradient downstream of the test section must be identical.

As an alternative, a mean gradient of a linear fit through all data points is established. The values of the spanwise taps are averaged to one value for taps at locations $x/h = 147.5$ and $x/h = 297.5$. Considering there are more data points upstream (13) than downstream (8) of section B, the mean gradient is based on a weighted average. The new mean is expressed by Equation 5.2 below:

$$p_{g,new} = \frac{13\left(\frac{dp}{dx}\right)_{up} + 8\left(\frac{dp}{dx}\right)_{down}}{13+8} \tag{5.2}$$

Data points both upstream and downstream of the test section are interpolated separately with this new mean, which theoretically would result in the black line and the dotted line in Figure 5.1 when dimpled plates are tested.

Subtracted fit. Data shows a drag reduction for flat plates (see section 5.3), which is in contradiction with the theory that expects a zero change in drag for flat plates. Therefore, a correction is applied that subtracts a linear fit from the change in drag to calibrate a new zero point. This is elaborated in Appendix E.

Cutoff data. During the last dimple measurement on day 4, listed in Table 5.2, the pressure scanner downstream of the test section seemed to have experienced some kind of failure. The pressure entered a downward trend rather than staying constant. For this measurement, the average data of the first 18 seconds is used as there is no clear indication that something interfered with the flow. This will be discussed further in section 5.4.

5.1.3 Corrected test volume.

The DC-40 is designed in such a way that the 'peaks' of the dimpled surfaces are at $y = 0$ mm. Considering that the dimples are $d = 2.5$ mm deep, the deepest point of a dimple is 22.5 mm distanced from the upper wall, see Figure 5.2. Hence, by machining dimples in the testing surface, the hydraulic diameter and volume of the test section are increased. The width and height for the tunnel in Figure 5.2 are scaled. However, be aware that the exact geometry of the dimples (described in subsection 3.2.2) is more smooth at the 'peaks' of the dimples. Basic physics indicates that a pipeline with an enlarged cross-sectional area and a constant flow rate has to withstand less viscous forces. To clarify this, consider a pipe with the entrance of fluid at location 1 and the exit of the fluid at location 2. To Bernoulli, $u_1 A_1 = u_2 A_2$. Now if $A_2 > A_1$ then $u_2 < u_1$ which is a drop in velocity. Consulting Equation 2.1, it can be concluded that a drop in velocity will result in a decrease in shear stress of a fluid against the wall. This is equivalent to a reduction of skin friction drag. The Darcy Weisbach equation is suggested, Equation 2.17, where the Darcy friction factor for the *turbulent* regime can be expressed as:

$$f_D = \frac{8\tau_w}{\rho u^2} \tag{5.3}$$

Considering a constant Darcy friction factor and constant fluid density, a drop in velocity due to the increase in cross-sectional area resonates with a drop in shear stress at the pipe wall as well. This can be observed as DR. However, by enlarging the cross-sectional area, no true DR can be identified. In total, the plates used for this research contain 266 dimples. Each dimple removes 2.42 cm^3 with respect to a flat plate. Subsequently, the dimples increase the channel volume by 3.35% with respect to a wind tunnel that has dimensions 2400x20x400

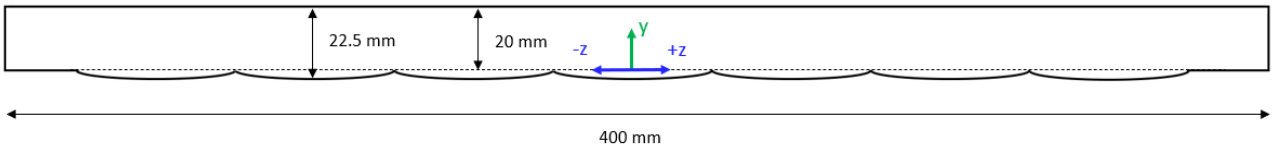

Figure 5.2: Cross section test section with dimples.

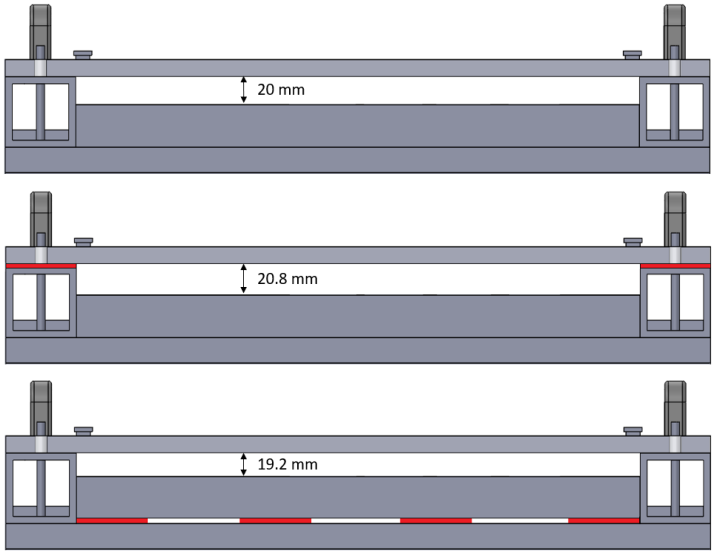

(a) Front view of test section with different volumes.

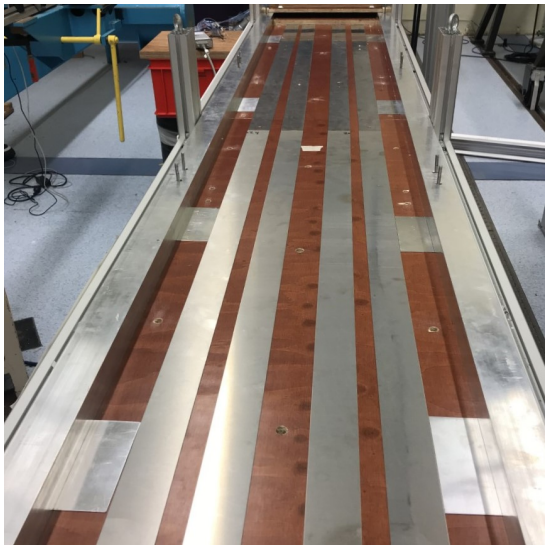

(b) Aluminium shims to lift test plates.

Figure 5.3: Left image from top to bottom: normal volume, increased volume, decreased volume. The red rectangles indicate the shims that were used to change the volume. Real shims visible in the right image.

mm, which is significant for a DR in the order of 4-7%. To verify the hypothesis that dimpled surfaces can be held accountable for drag reduction due to an increase in volume, a correction was made for the increased volume by heightening the dimpled test plates. Moreover, tests with increasing and decreasing the testing volume for both flat and dimpled surfaces were done, which should point out the relevance of change in volume in terms of DR. To increase the volume, thin 0.8 mm aluminum shims were placed on the aluminum 50x50 mm cross-section bars. Thereby, the transparent ceiling walls were heightened, and the volume was increased. The aluminum shims were placed between the foundation plates (see Appendix F) and the supporting plates

Table 5.3: Pressure measurement plan MC-4. F = flat plate, D = dimpled plate.

Day 1	Notes	Day 2	Notes
F	Creep run	D	Creep run
F	Normal volume	D	Normal volume
F	Increased volume	D	Increased volume
F	Decreased volume	D	Decreased volume
F	Normal volume	D	Normal volume
D	Normal volume	F	Normal volume
D	Increased volume	F	Increased volume
D	Decreased volume	F	Decreased volume
D	Normal volume	F	Normal volume

to decrease the volume. This resulted in a lift of the test plates. The steps at the transitions on the bottom wall that were created due to the lift of the test plates could be covered with duct tape. Physical access limited the application of duct tape for the steps that, most likely, were formed at the top wall when the transparent ceiling walls were heightened to increase the volume. The measurement plan for these volume corrected pressure measurements is depicted in Table 5.3. Similar to MC-3, MC-4 was again started with creep runs. The second day was started with dimpled plates as replacing flat plates for dimpled plates is a time consuming operation.

5.2 Verifications

The various corrections described above are applied to help to determine the DR as objectively as possible. However, to confirm that these analyses are valid, a number of verifications are carried out. Each verification is immediately followed by its result. Reynolds numbers, used in figures illustrated in this section, are based on $h/2$ and the centerline velocity. Some figures are supported by additional graphs that are available in Appendix E. Verifications described in subsections 5.2.1-5.2.4 were done with data acquired during the 'sandwich' sequence described in Table 5.2. Verifications described in subsections 5.2.5-5.2.9 required additional measurements. These measurements involve different measurement times or a slightly different experimental setup. The final measurement plan for MC-3, including the additional measurements, is depicted in Table 5.4.

Table 5.4: Measurement plan MC-3. F = flat plates, D = dimpled plates.

Day 1	Notes	Day 2	Notes	Day 3	Notes	Day 4	Notes
F	Creep run	F	Creep run	F	Creep run	F	Creep run
F	Sandwich	F	Long measurement	F	Sandwich	F	Long measurement
F	Repeatability test	D	Long measurement	D	Sandwich	D	Long measurement
F	Use pump 1	F	Error scanners	F	Sandwich	D	Bending of tunnel
D	Sandwich	-	*Disassemble and re-assemble DC-40*	D	Sandwich	F	Bending of tunnel
F	Sandwich			F	Sandwich	F	Sandwich
D	Sandwich			D	Sandwich	D	Sandwich
F	Sandwich			F	Sandwich	F	Sandwich
D	Sandwich			F	Starting with scanner on	D	Sandwich
F	Sandwich			F	Ref. pressure at atm pressure	F	Sandwich
				F	Error scanners	D	Sandwich
				F	Bending of tunnel	F	Sandwich
				D	Bending of tunnel	F	Ref pressure at atm. pressure

5.2.1 Two dimensionality

As described in subsection 4.3.1, five spanwise pressure taps upstream of section B and five pressure taps downstream of section B are used to demonstrate that the flow is 2D. Each spanwise tap can be expressed as a percentage of their respective dynamic pressure. In the study performed by Tay (2011), all spanwise taps are within a threshold of 1% with respect to the mean static pressure.

As it is rather hard to identify the consistency with the unaided eye, the error of each spanwise pressure tap is depicted in Figures 5.4a and 5.4b, referenced against the mean of the pressure taps. The 1% threshold line is plotted for reference in both figures. For the pressure taps upstream of section B, the error is well within the 1% error range for most velocities. Only at the lower velocities, the error is slightly higher. The spanwise taps downstream of the test section, on the other hand, return a significantly higher error. The error for two pumps is more consistent than the error for one pump, i.e., for lower velocities, the error is the same as for higher velocities ($\approx 1\%$ at $x/h = 147.5$ and $\approx 3\%$ at $x/h = 297.5$). In Appendix E the actual spanwise pressures are depicted in Figure E.6.

5.2.2 Variation of difference in measured static pressures from a least-square fit

This method identifies the difference between the actual data points with respect to their least-square fit: the expected data points. A linear fit through all 21 (13 upstream and 8 downstream) data points is drawn to make

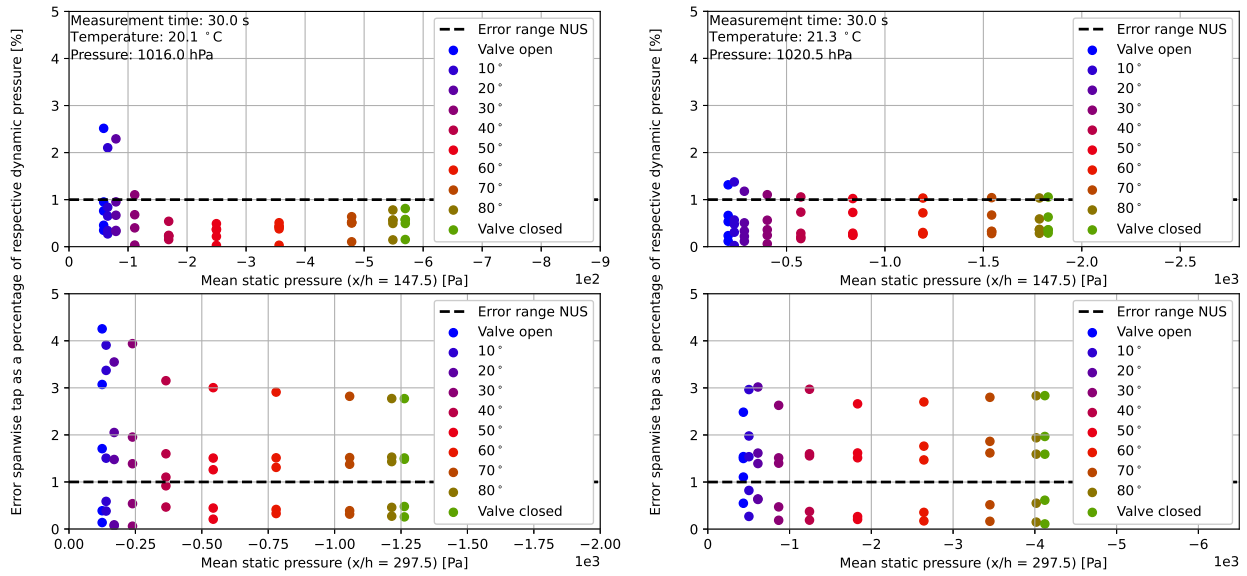

(a) 1 pump. Top image is upstream ($x/h = 147.5$) of test section, bottom is downstream ($x/h = 297.5$) of test section. Valve fully open corresponds to $Re \approx 5.80 \cdot 10^3$, valve closed corresponds to $Re \approx 2.06 \cdot 10^4$.

(b) 2 pumps. Top image is upstream ($x/h = 147.5$) of test section, bottom is downstream ($x/h = 297.5$) of test section. Valve fully open corresponds to $Re \approx 1.17 \cdot 10^4$, valve closed corresponds to $Re \approx 4.02 \cdot 10^4$.

Figure 5.4: Error spanwise pressure tap with respect to mean of all spanwise pressure taps non-dimensionalized by dynamic pressure.

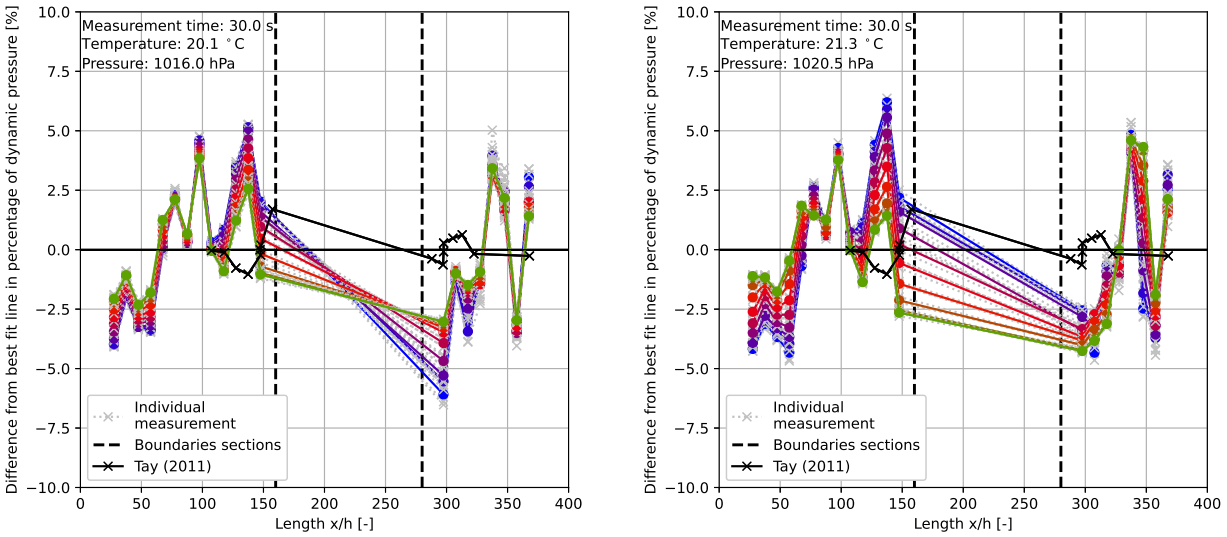

(a) 1 pump.

(b) 2 pumps.

Figure 5.5: Variation of difference in measured static pressures from weighted average least squares fit over all data points for flat plates. Green lines are data points acquired with valve closed (i.e. highest velocity), blue lines are data points acquired with valve open (i.e. lowest velocity).

this analysis. The spanwise data points at location $x/h = 147.5$ and $x/h = 297.5$ are averaged to two streamwise data points. The differences in static pressure are divided by their respective dynamic pressure allowing to express the variance in a percentage. The colored lines with data points in Figure 5.5 are averages from four flat plate measurements acquired during the 'sandwich' sequence. Each individual measurement is designated by a silver dashed line. The maximum difference is approximately 5-6% from its mean for one and for two pumps.

The consistency for different Reynolds numbers is less for measurements performed with two pumps. I.e., for two pumps, the plotted lines overlap less than for one pump. It is unknown why x/h-coordinate of the measurement points by Tay (2011) deviate from the data points acquired at TUD considering the setup, and therefore the location of the pressure taps, was reconstructed, see Figure 5.5.

Furthermore, a least-square fit through merely the upstream data points theoretically would suffice to find a difference between the actual and the predicted values. However, as $p_{g,up}$ and $p_{g,down}$ are not identical, this method cannot be used. To still be able to see how the difference varies for flat plates and dimpled plates, it is chosen to interpolate the upstream data points with the new pressure gradient that was defined earlier in Equation 5.2. The result will point out how much the downstream data points deviate from this mean. The result of this analysis can be found in section 5.4.

5.2.3 Colebrook-White

The Colebrook-White equation is an acknowledged formula for flow through conduits as mentioned in subsection 2.1.2. It can be used in combination with the Darcy Weisbach equation as a verification tool for linear pressure drop per meter versus the Reynolds number. The Darcy friction factor is computed by iterating Equation 2.4, an implicit formula. Consulting the Moody diagram in Figure 2.2 and White (2006), it is concluded that perspex, anodized aluminum, and plywood can be classified as smooth pipe surfaces. As a result, the Colebrook-White equation is simplified to Equation 5.4. The linear pressure drop per meter is analyzed theoretically as well as experimentally.

$$\frac{1}{\sqrt{f_D}} = -2\log\left(\frac{2.51}{\mathrm{Re}\sqrt{f_D}}\right) \tag{5.4}$$

Figure 5.6 depicts the linear pressure drop per meter. A Reynolds number of 21,000 corresponds to the maximum capacity of one pump. The dashed line indicates the theoretical relation of linear pressure drop per meter computed with the Colebrook-White relation. Furthermore, experimental data from Tay et al. (2015) is depicted for reference. The theoretical line that Tay et al. used for reference intersected perfectly with their experimental data. Hence, this theoretical line is not plotted. The experimental pressure drop per meter is visualized by a linear fit through the upstream data points, through the downstream data points, and an average of the upstream and downstream fits. After a Reynolds number of approximately 21,000, the difference between the linear pressure drop per meter for a fit through the upstream data points and a fit through the downstream data points is apparent. Furthermore, the theoretical pressure drop per meter used in this research decreases relatively to data from Tay et al. (2015). Moreover, the pressure drop per meter from Tay et al. (2015) becomes smaller than the experimental pressure drop per meter acquired in this research. A vertical dashed line in Figure 5.6b designates the maximum capacity of one pump.

5.2.4 Skin-friction coefficient

Based on the pressure data, the wall shear stress and skin-friction coefficient can be determined through the formulas below (Lienhart et al., 2008):

$$\tau_{\mathrm{w}} = -\frac{h}{2}\frac{\mathrm{d}p}{\mathrm{d}x} \tag{5.5}$$

$$C_{f,e} = \frac{2\tau_{\mathrm{w}}}{\rho U_{\mathrm{b}}^2} \tag{5.6}$$

where τ_w is the shear stress, dp/dx the pressure gradient, U_b the bulk velocity and $C_{f,e}$ the experimental friction coefficient. The bulk velocity is taken as 87% of the centerline velocity (Tay, 2011). The skin-friction coefficient can also be expressed by Blasius' curve fit to the turbulent part of the Moody diagram (White, 2006):

$$C_{f,t} \approx \frac{0.0791}{Re_h^{\frac{1}{4}}} \tag{5.7}$$

where $C_{f,t}$ is a theoretical skin friction coefficient. The results of the experimental and practical skin friction coefficients are depicted in section 5.3.

Figure 5.7 shows the theoretical and experimental skin friction coefficient, plotted for one pump and for two pumps. The lines coincide rather well. The experimental skin friction coefficient is higher than the theoretical

skin friction coefficient for higher Reynolds numbers, see Figure 5.7b. This can be related to Figure 5.6. The linear pressure drop per meter increases, which means the shear stress increases as well as experimental skin friction coefficient $C_{f,e}$.

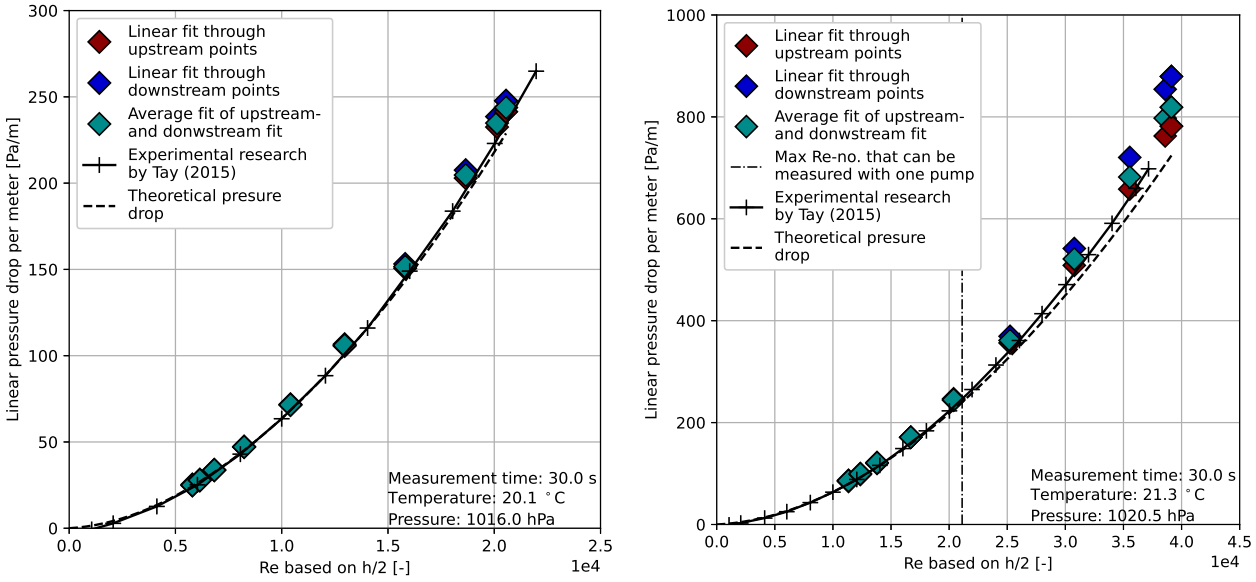

(a) 1 pump. **(b)** 2 pumps.

Figure 5.6: Colebrook White equation for flat plates. Be aware of different y-axis values.

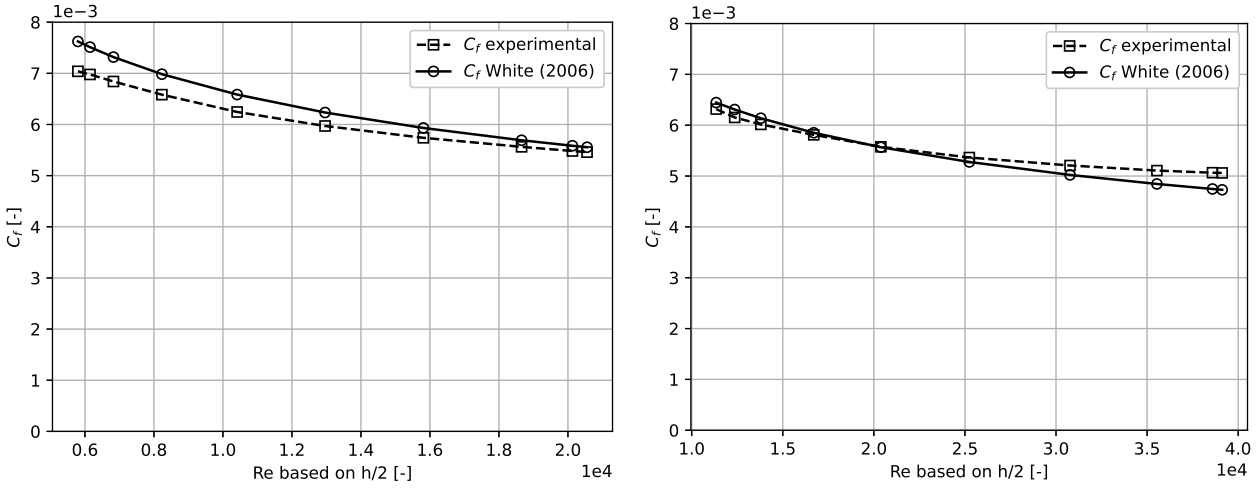

(a) 1 pump. **(b)** 2 pumps.

Figure 5.7: Theoretical and experimental skin friction coefficients for flat plates.

5.2.5 Repeatability

There are two tests done to ensure that the wind tunnel is consistent. The first check was done on day 1, when two consecutive flat plate measurements were done. During pump-off time, the plates were taken out and put back, and the results were compared. The second test is on a larger scale. On day 2, the tunnel was disassembled and re-assembled. Figure F.10 captures the disassembled DC-40. The results of day 1 were compared to day 3 by examining the mean absolute percentage error (MAPE) of the pressure drop to a linear fit. One measurement of 30 seconds at a certain valve angle yields an array of data points. Ten straight lines are fitted through the data points. Then, the MAPE is computed for each valve angle (i.e., each of the ten

linear fits) according to Equation 5.8 where N is the number of data points, and the linear fitted lines are used to find the predicted value for each data point.

$$\text{MAPE} = \frac{1}{N}\sum_{t=1}^{N}\left|\frac{\text{predicted value} - \text{actual value}}{\text{predicted value}}\right| \tag{5.8}$$

Figure 5.8 shows the MAPE of the pressure drop versus the non-dimensional lengthscale x/h for different flow velocities (i.e. different valve angles). Results of the flat plate data are depicted in 5.8a while dimpled plate data is illustrated in Figure 5.8b. The error for dimpled plates is about 1% larger than the error for flat plates on average. The MAPE is higher on day 3 in comparison with day 1 although the difference is minimal.

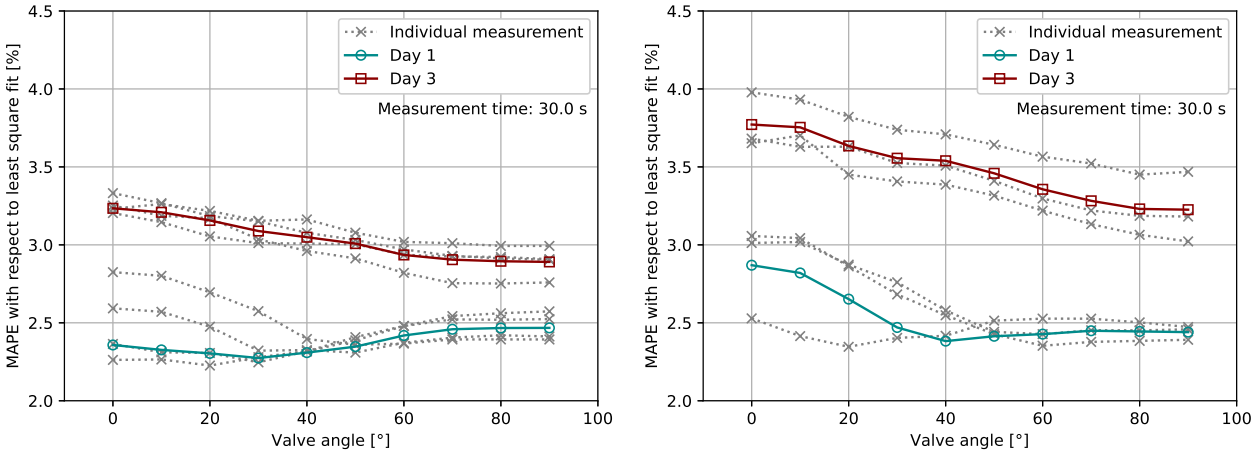

(a) Flat plates.

(b) Dimpled plates.

Figure 5.8: Consistency of the wind tunnel for different experimental models (1 pump).

5.2.6 Instantaneous pressure variation

The frequency of the scanners is 2000 Hz. The measurement time is 30 seconds per valve angle for the 'sandwich' sequence measurements. This means there are $6 \cdot 10^4$ data points for every pressure tap. To analyze this data for the pressure gradient and the change in drag, the mean of $6 \cdot 10^4$ data points for each pressure tap is taken. However, it is not guaranteed that the flow continuously denotes a constant value. As a response to this, measurements of 60 seconds involving $1.2 \cdot 10^5$ data points are carried out at three different valve angles. This is denoted as 'Long measurement' in Table 5.4. It allows for an analysis of the raw data over a more extended period. In addition to this, the errors of each pressure scanners are considered to determine if they have a significant impact on the measured values.

For the instantaneous pressure data, the static pressure at $x/h = 376.5$ is analyzed. Three runs were done (i.e., one at valve open, one at valve half-open, and a third measurement with the valve closed) for one pump and for two pumps. In Figure 5.9, pressure scanners of 600 Pa and 2.5 kPa were used while scanners of 2.5 kPa and 10 kPa were used for data obtained in Figure 5.10. For this measurement, a longer measurement time of 60 seconds was preferred.

The errors of the scanners are approximately 0.5 Pa, 1.2 Pa, and 8 Pa for scanners of 600 Pa, 2.5 kPa, and 10 kPa, respectively. Figure E.5 illustrates how the errors for the pressure scanners were determined. Figures 5.9 and 5.10 depict $1.2 \cdot 10^5$ data points for each colored line that was obtained. The data that was acquired with one pump is rather consistent. The range for one pump is 25 Pa at low velocities and 60 Pa for higher velocities. For data acquired with two pumps, an oscillation can be observed that is repeated every 12-15 seconds. On top of that, the error range of the maximum amplitude is between 150-250 Pa, which is larger than than the amplitude of measurements that were performed with one pump. Possibly, the fluctuations are caused by the false air leakage in the pressure valve as the data of most downstream pressure tap is used to perform the instantaneous pressure measurements.

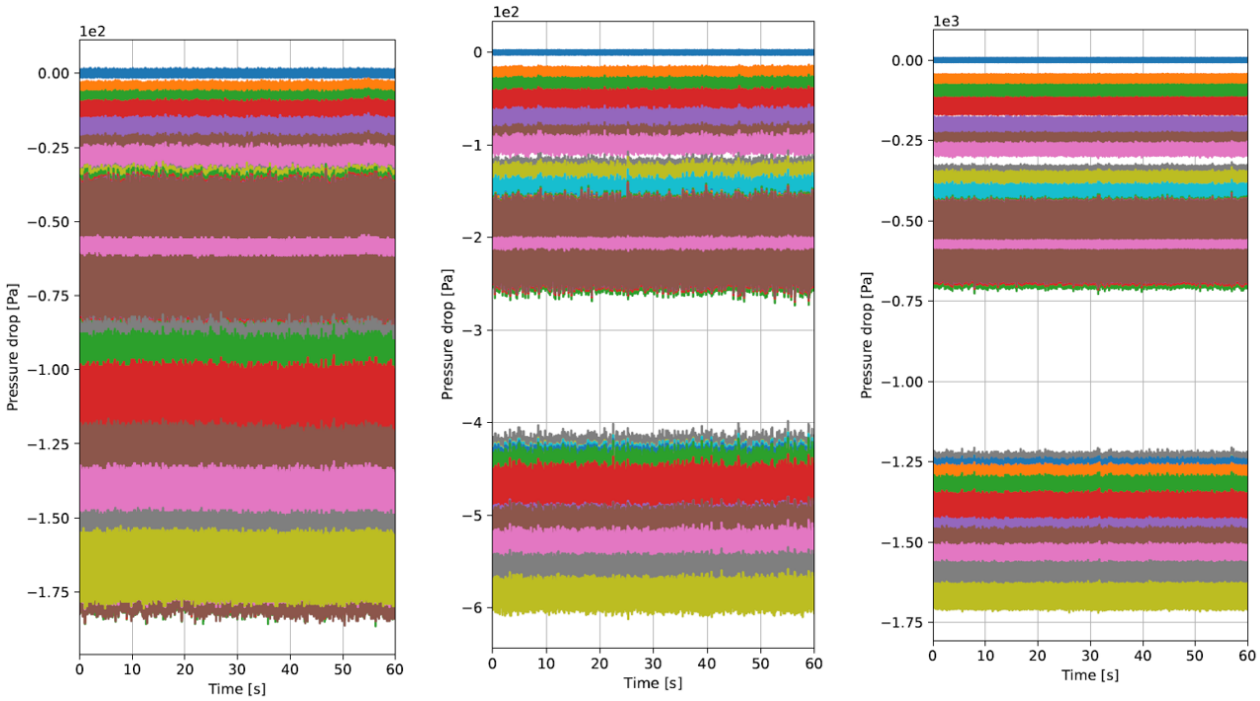

(a) Valve open. Reynolds number ≈ 5,900. **(b)** Valve half open. Reynolds number ≈ 11,800. **(c)** Valve closed. Reynolds number ≈ 20,900.

Figure 5.9: Instantaneous pressure over a 60 second measurement using one pump. First horizontal blue line at the top denotes the pressure drop at tap 1, the green line at the bottom denotes the pressure drop at tap 29. The valve is opened, 45° open and closed for Figures 5.10a, 5.10b and 5.10c, respectively. Note: y-axis has a different range for each figure.

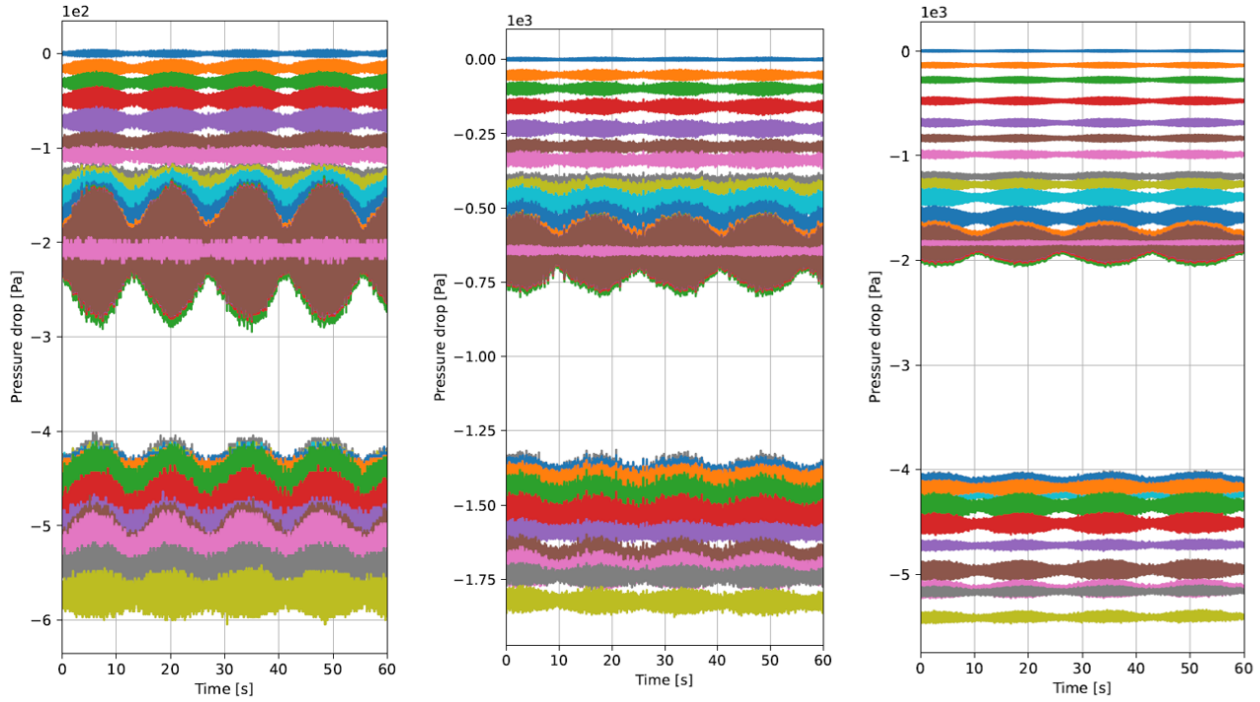

(a) Valve open. Reynolds number ≈ 11,900. **(b)** Valve half open. Reynolds number ≈ 22,600. **(c)** Valve closed. Reynolds number ≈ 40,600.

Figure 5.10: Instantaneous pressure over a 60 second measurement using two pumps. First horizontal blue line at the top denotes the pressure drop at tap 1, the green line at the bottom denotes the pressure drop at tap 29. The valve is open, 45°open and closed for Figures 5.10a, 5.10b and 5.10c, respectively. Note: y-axis has a different range for each figure.

5.2.7 Start with valve closed

The pumps are almost instantly at their maximum capacity. The normal routine is to start with the measurement that involves the lowest underpressure. This way, the instantaneous underpressure on the channel walls is minimized. In order to achieve this, the valve needs to be open before the pump is started. Even though this is considered the most logical procedure, the measurement routine is also performed in reversed order. The first measurement is done with the valve closed (highest underpressure), and the valve is opened in 9 consecutive steps. Equation 5.8 is used to make the analysis.

One measurement run includes ten measurements at ten different valve angles of 30 seconds each. The difference between starting with the valve closed or with the valve open is depicted in Figure 5.11. Individual measurements from the 'sandwich' sequence that were performed with the valve open are depicted as well. The MAPE is expressed as the deviation of the pressure data from its linear fit in a percentage from its corresponding dynamic pressure. The MAPE for starting with the valve closed is slightly less than when a measurement is started with the valve open. It is preferred to start with the valve closed as this results in less instantaneous underpressures on the channel walls, considering the minimal difference.

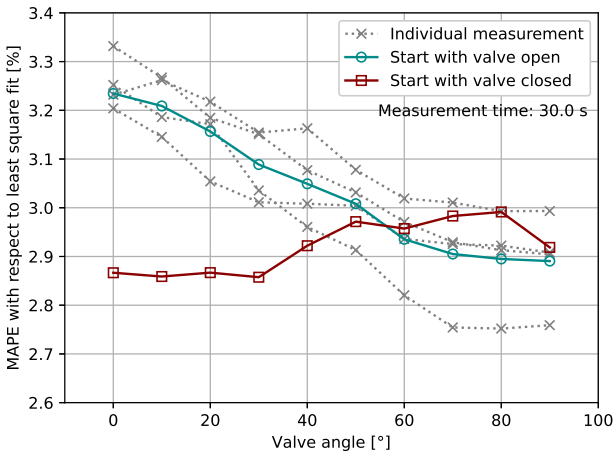

Figure 5.11: MAPE versus valve angle. Difference starting sequence with valve closed and with valve open.

5.2.8 Pump usage and an ambient reference pressure

Approximately half of all the tests are done with one pump. As there might be differences between the two pumps, the same pump was used consistently such that no debate was possible about data that was acquired with different pumps. Both pumps are run individually and compared to determine which pump was more accurate. Equation 5.8 was also used to determine which pump was preferred for measurements with a single pump. The errors are in the same order of magnitude. Pump no.2 has a 0.1% larger error than pump no.1 at higher velocities. However, pump no.2 was selected as the better pump considering its error was up to 0.3% smaller at lower velocities than pump no.1.

Furthermore, the pressure drop measured by the Nub scanners is referenced against the measured pressure of the first pressure tap at $x/h = 27.5$. This way, no local flow movements near the reference taps of the scanner can interfere. One measurement is done with the reference pressure set to atmospheric pressure to ensure that this is the right method. Again, Equation 5.8 is applied to identify the difference in accuracy.

The measurements that have an ambient reference pressure show a larger inconsistent MAPE of pressure drop in comparison with the measurements that have the underpressure measured at tap 1 as reference pressure. It should be noted that the MAPE with tap 1 pressure as reference pressure depicted in Figure 5.12b, is an average of four measurements. The ambient reference pressure data points on the other hand, are obtained from one single measurement. Nevertheless, an irregular pattern is observed when ambient pressure is used as reference pressure. For measurements with reference pressure set to the pressure at tap 1, the MAPE is much more consistent.

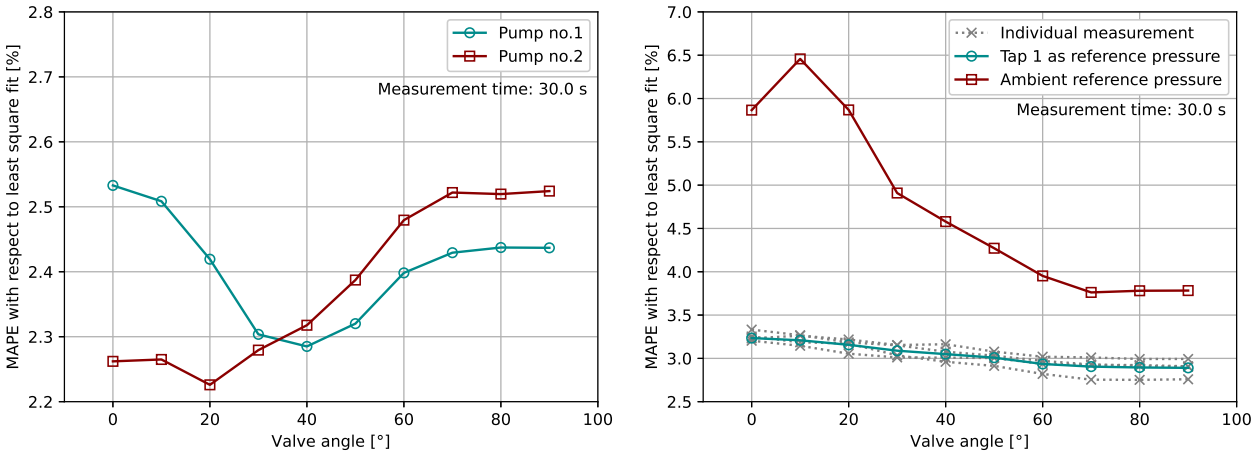

(a) Valve angle versus MAPE for pump no.1 and pump no.2. Valve is open for valve angle =0°and closed for valve angle = 90°. **(b)** Ambient reference pressure and reference pressure equal to the pressure measured at pressure tap 1 for two pumps.

Figure 5.12: MAPE for pump usage and ambient reference pressure.

5.2.9 Bending of the tunnel

As mentioned in Appendix B, the pressure drop and maximum velocity were predicted rather accurately. However, the severity of the channel walls' deflection due to large underpressure caused by the pressure drop was underestimated. Initially, the tunnel was too weak to sustain large underpressures caused by two vacuum pumps. Tangible proof can be found in Appendix C where it is observed that especially the ceiling of the channel, which is thinner than the floor, was prone to deflection. It initially bent over 5 mm, which is visible in Figure C.1a.

Three upgrades were done to tackle this issue. First, a small airfoil was placed in the channel at the end of

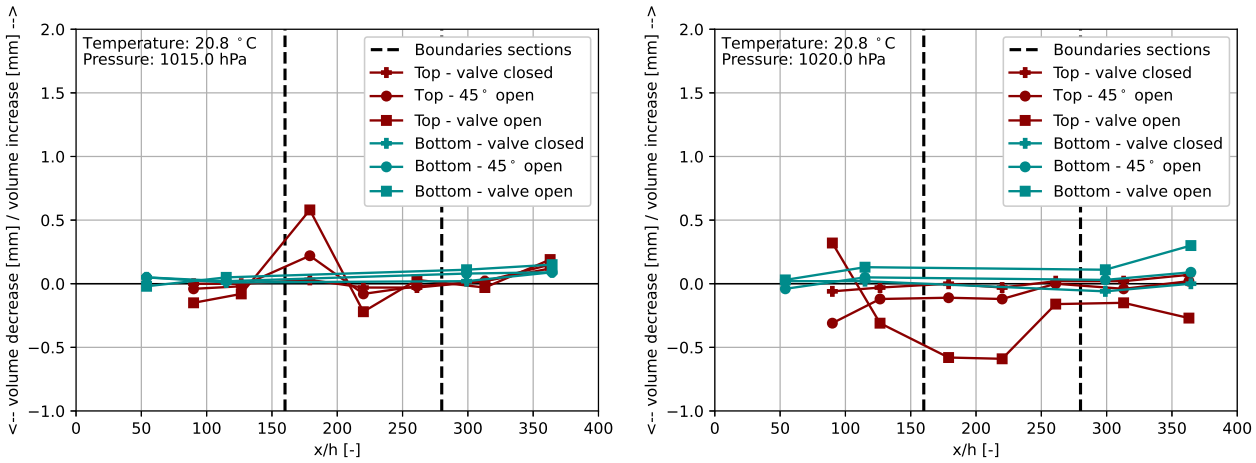

(a) 1 pump. **(b)** 2 pumps.

Figure 5.13: Bending of wall elements for flat plates.

part C2 (see Figure F.1 for explanation of each part) that acts as a stut, se Figure 5.15b. This is downstream of all pressure taps and will not have influence on the pressure data. Secondly, thick 25 mm wooden plates were mounted on the top wall of section C considering the underpressure and bending will be the largest in that area, see Figure 5.15c. After this improvement, the bending of the top wall elements of the tunnel without having reinforced every section was measured. This was done with a caliper as well as a measuring clock (Figure 5.15a) which has a smaller error. The result of this bending can be found in Figure C.1b. Due to the thick plate, the bending of the wall is significantly less after section B. Following this observation, a third improvement was made. The tunnel was reinforced with steel O-profiles of 30 by 30 mm in cross-section. These steel ribs were glued on the ceiling elements as well as the floor elements. An example of such a beam is depicted in Figure 5.15d.

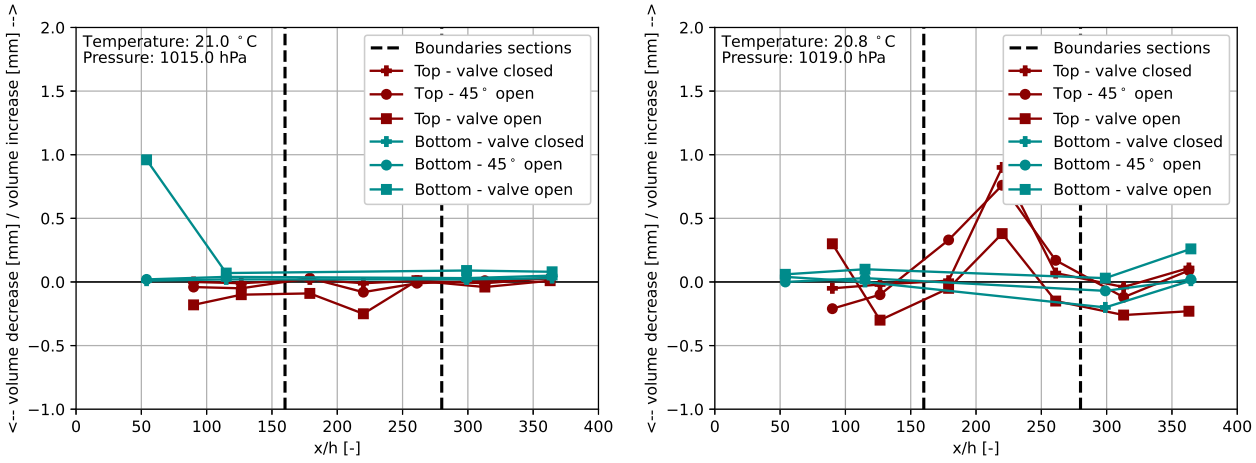

(a) 1 pump. **(b)** 2 pumps.

Figure 5.14: Bending of wall elements for dimpled plates.

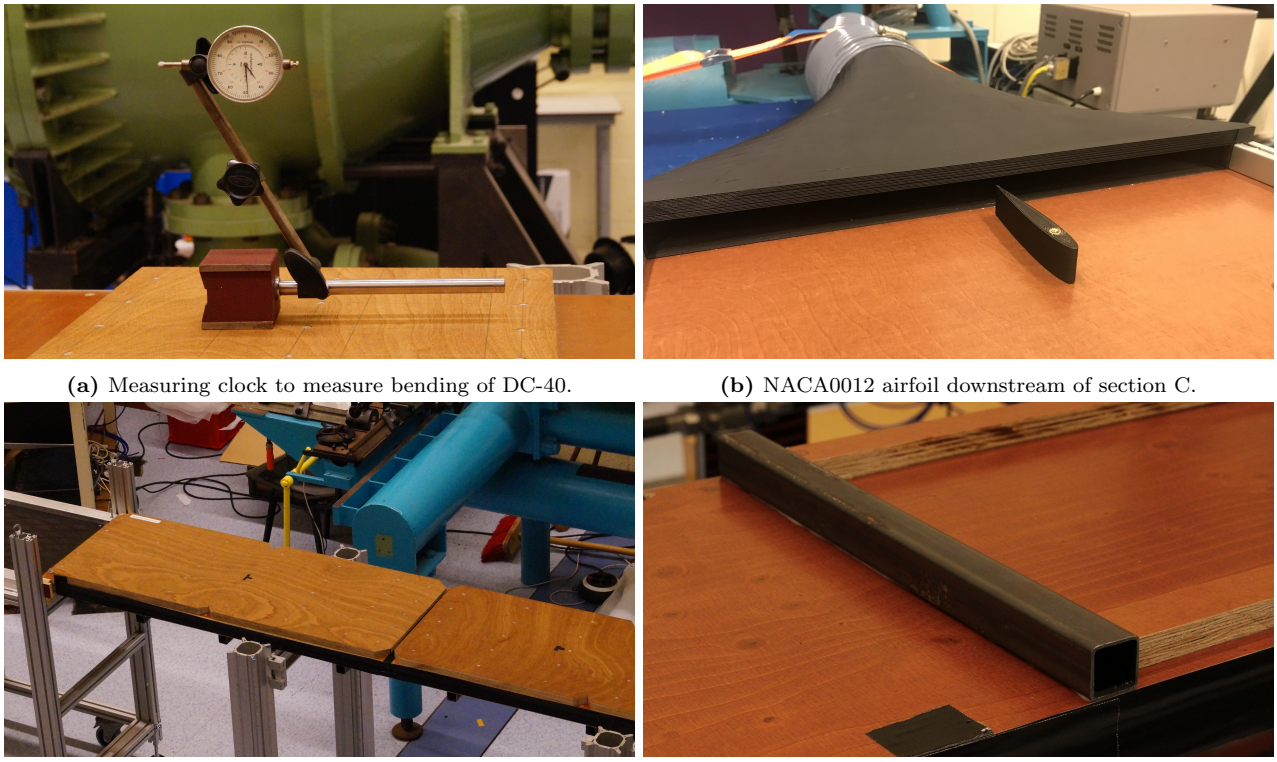

(a) Measuring clock to measure bending of DC-40. **(b)** NACA0012 airfoil downstream of section C.

(c) Reinforced top section C. **(d)** Reinforced wall by cross beam.

Figure 5.15: Measuring clock and reinforcements DC-40.

After these improvements, the bending tests were done a second time to determine the efficiency of the reinforcements. This time, only the measuring clock was used. The clock was secured with a magnet to a very thick and straight steel beam. The beam with the measuring clock was placed on the top wall. For the measurements of the bottom wall, the measuring clock was secured to the steel O-profiles that were applied for reinforcement.

Once the steel profiles were applied perpendicular to the streamwise direction, the bending was significantly less. In fact, it is rather difficult to pinpoint if the encountered bending is a result of underpressure or if it is caused by inaccuracies of the measuring clock. The red lines in Figures 5.13 and 5.14 are bending tests performed at the top wall of the tunnel. The dark cyan lines indicate the bending of the bottom wall of the

tunnel. As there is no good access on the bottom wall of the tunnel in section B, no bending tests are performed in this section. On top of that, the bottom wall in section B is a thick pack of multiple plates firmly held together by a plurality of screws. As such, no significant bending of the bottom wall of the test section is expected.

Figure 5.13 portrays the bending of the walls while testing flat plates. When the valve is open, the underpressures are the smallest, which would imply the least bending. Hence, the red peaks at 0.6 mm in Figure 5.13a and -0.6 mm in Figure 5.13b are, most likely, false data points. In Figure 5.14a, a sudden compression of the bottom wall is observed at $x/h = 54$. This will probably be an outlier, considering the bottom plate is the thicker plate, and the underpressure is minimal at section A. The red peaks in Figure 5.14b are peculiar, especially considering the deformation is positive, indicating an expansion of the top wall. The wall expands as the wind tunnel speed increases. There is no clear indication of what might have caused this outward bending of the top wall except for errors in the measurement tool.

5.3 Results

The pressure measurement data is categorized into two parts. Firstly, the final change in drag versus Reynolds number is displayed. Secondly, the change in drag versus Reynolds number, including a correction for volume, is illustrated. Reynolds numbers, used in figures illustrated in this section, are based on $h/2$ and the centerline velocity.

5.3.1 Change in drag versus Reynolds number

Figures 5.16a and 5.16b are established with data from the sandwich sequence (Table 5.2 day 3 and 4). The average of three measurements is displayed in each figure supported by the three individual measurements themselves. An individual measurement marks the delta in drag of a dimpled plate with respect to the average of its two adjacent flat plates. Furthermore, for a channel with flat test plates, a linear pressure gradient is expected, which, to Equation 5.1, would result in a zero change in drag. However, tests with flat plates returned a DR between 8-15%, this is depicted in Figure E.1a and E.2a. A linear fit is taken through the flat data points to correct this error. For each measurement, this linear fit is subtracted. Hence, changes in drag depicted in Figure 5.16 are absolute. Raw data without the subtraction is visible in Appendix E.

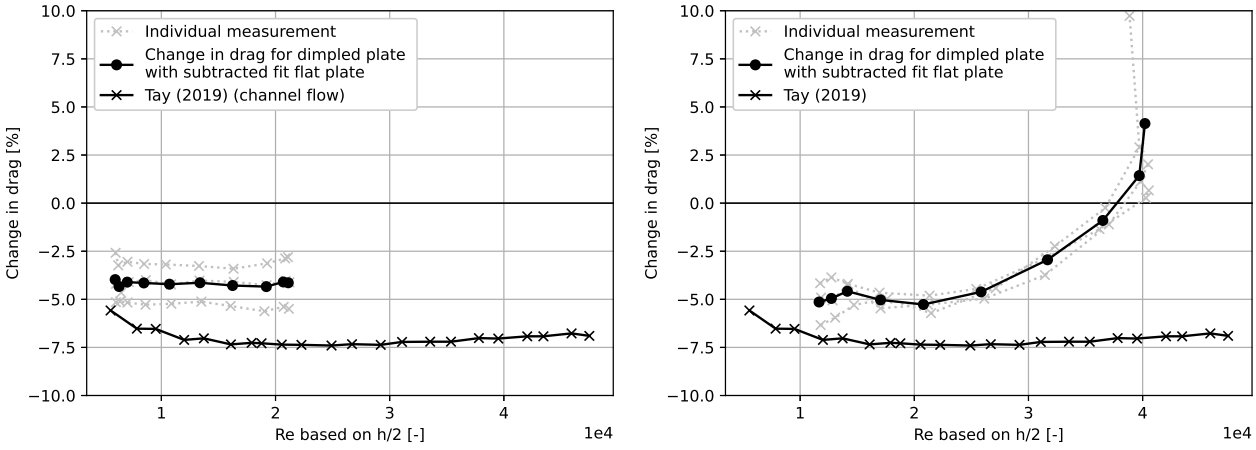

(a) 1 pump.

(b) 2 pumps.

Figure 5.16: Change in drag with flat subtracted fit vs Reynolds number including data of NUS (Tay et al., 2019).

The drag reduction is rather consistent up to a Reynolds number of approximately 21,000, comparing the change in drag for one pump and for two pumps. Remarkably, this is the threshold of using one pump or two pumps. Figure 5.16b shows a steep increase after a Reynolds number of 21,000 with an outlier that shows a drag increase of approximately 10%. Results by Tay et al. (2019) are depicted for reference. Researchers at NUS measured a slightly larger DR as well as more consistent for higher Reynolds numbers.

The pressure drop versus dimensionless length scale x/h is illustrated in Figure 5.17. When the valve is open, there is a lot of false air leakage at the valve, which results in a lower flow velocity. Once the valve is

closed, higher velocities and underpressures are generated. The data points are an average of four measurements obtained with flat plates performed in the 'sandwich' sequence on day 3 and 4 of MC-3. The data points are interpolated with a least-square fit which is denoted by a dashed line for each valve angle. Note that the y-axis values are different for Figures 5.17a and 5.17b. The black vertical dashed lines denote the transition of section A to section B and section B to section C, respectively. No data points were gathered in test section B.

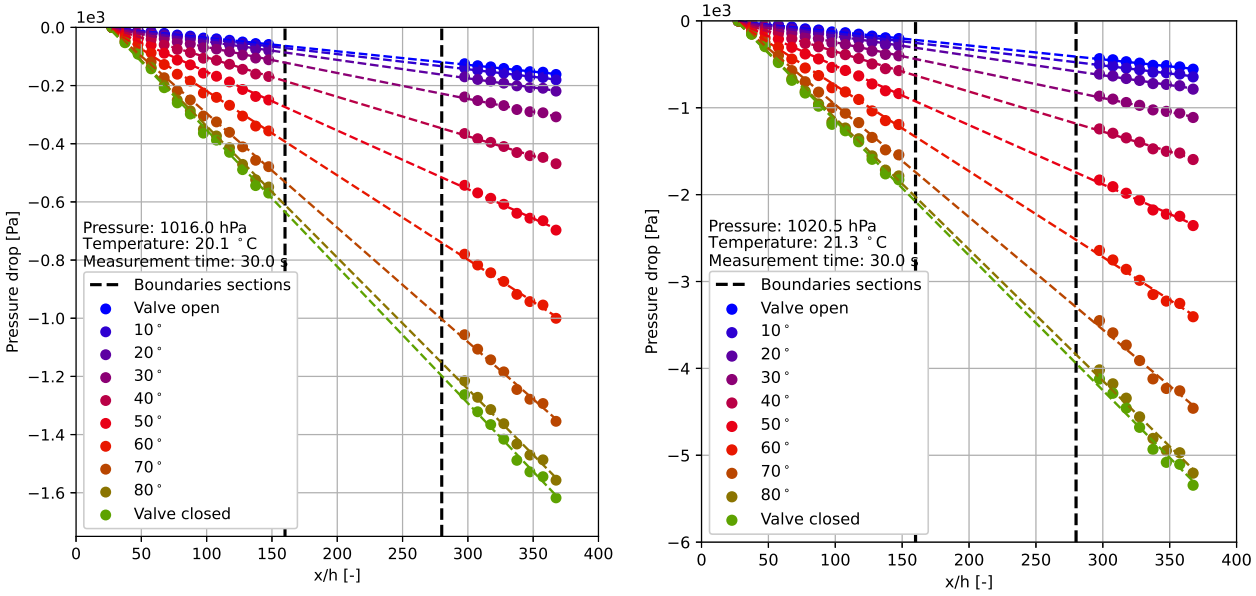

(a) 1 pump. Valve fully open corresponds to $Re \approx 5.80 \cdot 10^3$, valve closed corresponds to $Re \approx 2.06 \cdot 10^4$.

(b) 2 pumps. Valve fully open corresponds to $Re \approx 1.17 \cdot 10^4$, valve closed corresponds to $Re \approx 4.02 \cdot 10^4$.

Figure 5.17: Static pressure versus dimensionless lengthscale x/h.

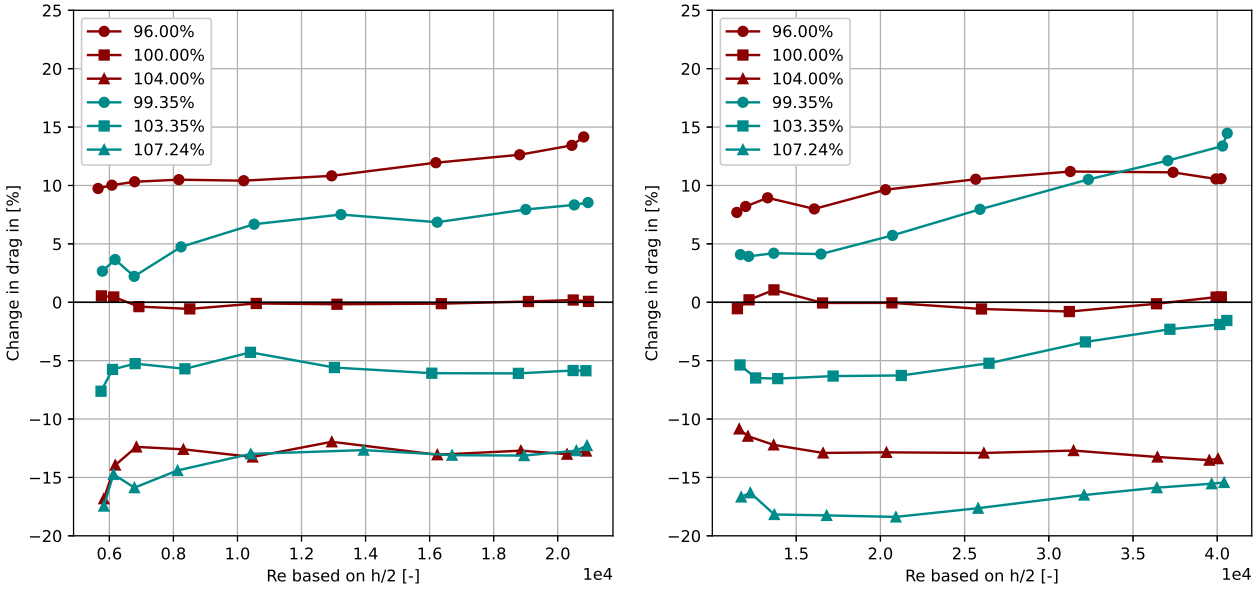

(a) 1 pump.

(b) 2 pumps.

Figure 5.18: Change in drag versus Reynolds number for different volumes. The red lines denote flat plates, the dark cyan lines dimpled plates. The percentages represent the volume. A volume of 100% is the volume of the test section at original dimensions.

5.3.2 Corrected test volume

A clear correlation between the test section volume of the wind tunnel and the change in drag is found as depicted in Figure 5.18. The volume in this figure is expressed in a percentage referenced against the original test volume (2400x20x400 mm). The red line with the square marker is the original volume when testing flat plates and is therefore 100%. This volume is increased as well as decreased, which is denoted by the triangle and the round markers, respectively. The computation volume change for dimpled plates includes a second parameter, the extruded volume due to dimples. On top of the change in volume caused by the aluminum shims, the dimples positively influence the volume. The measurements performed with dimpled plates are illustrated by the dark cyan lines where similar markers apply as the flat plates.

Figure 5.19a depicts the change in drag for each volume at the highest Reynolds number that was measured with one pump. Figure 5.19b indicates the same but in the form of a line plot. The dimpled test plates encounter less drag than the flat plates when the volume change due to dimples is left out of the equation. When both the volume change due to the aluminum shims and the volume change due to dimples are considered, the dimpled test plates return a larger drag.

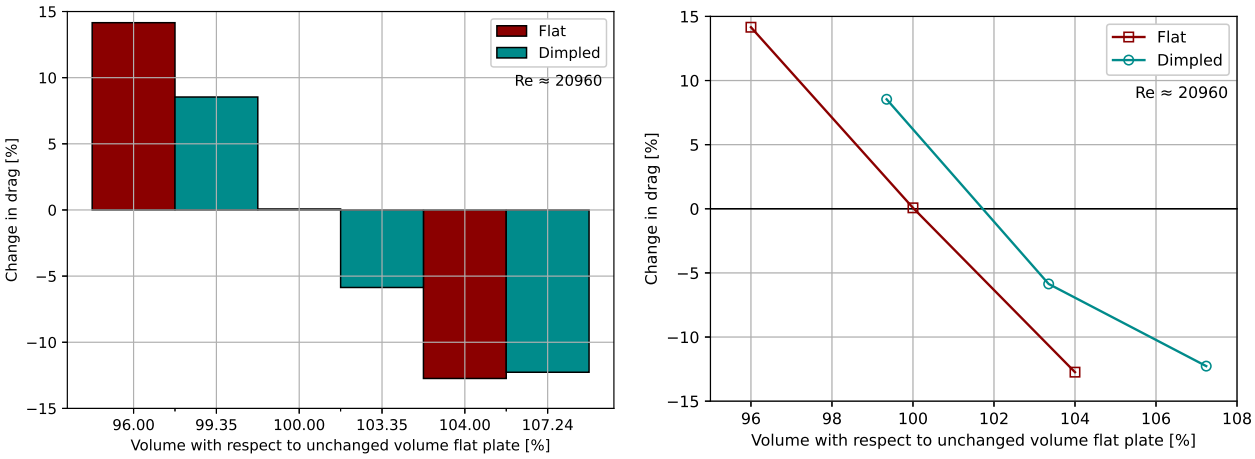

(a) Bar plot.

(b) Line plot.

Figure 5.19: Change in drag versus Reynolds number, indicating the effect of varying the test volume.

5.4 Discussion

Various verification tools supported the final pressure results. The main results are discussed first, followed by analyses of some verifications.

The drag reduction that is measured with the dimpled plates in the current study is less than the DR measured at NUS. There are several explanations for this outcome.

- The wind tunnel constructed at TUD is not as perfect as was aspired. Although a lot of effort and care was put into the design and construction of the DC-40, the majority of the tunnel parts were crafted by hand. The errors that remain are inevitable, considering high accuracy and precision of the wind tunnel are required. The flat plate measurements already indicated a negative error of 8-15%. Considering the dimpled test plates returned an absolute DR of 5% compared to the flat test plates, the magnitude of the wind tunnel error is significant.
- The stiffness of the tunnel is directly related to the materials that were used. Albeit the reinforcements that were necessary to perform wind tunnel tests at higher Reynolds numbers lead to more accurate measurements, the fact that reinforcements are mandatory to operate at higher underpressures does not contribute to forming an unbiased opinion on the results.
- The volume increase that is formed due to the dimples generates a drag reduction. Based on Figures 5.19a and 5.19b, the volume of the 'decreased test volume' for dimpled plates (99.35%) is close to the unchanged

flat plate volume (100.00%). A similar conclusion can be drawn for an increased test volume when the flat plates are used (104.00%) and a 'normal' volume when the dimpled plates are tested (103.35%). Merely focusing on the test volume, it is assumed that the change in drag should be approximately the same. If dimples would induce DR, the drag of the dimpled plates should be less than the drag for flat plates for approximately the same volume. Interestingly, the opposite is true, which means the dimples generate an increase in drag. To visualize this, Figure 5.20 depicts data from NUS, data from ongoing results performed at TUD in a wind tunnel with a 400x400 mm cross-section, and results of the current study with and without a correction for volume increase of the dimples. Tay et al. (2015) do recognize the enlarged channel volume due to the high CR of dimples. Despite this recognition, it is argued that other flow structures are at play as shallow dimples registered a larger DR than deeper dimples. Additionally, Ng et al. (2020) documented that teardrop-shaped dimples with tips pointing in opposite directions return different DR. This is evident as the form drag and flow structures within the teardrop dimples will be different when positioned in the opposite direction.

To bring DR versus volume change into perspective, Figure 5.21 depicts all the numerical and experimental results obtained at NUS and sets out the drag reduction to the volume increase. Based on this figure, a clear correlation can be derived between the volume increase caused by the dimples and the DR that is found. The average DR up to a Reynolds number of 21,000 found in this research is depicted by the green diamond. The small table in Figure 5.21b illustrates the CR of each dimple pattern. For the studies at NUS, theoretical CR's are considered that cover the full test area as it is unknown if the actual CR is lower, as is the case for this research. However, a fundamental note is that in numerical research done at NUS, a constant flow rate for flat and dimpled test plates is considered to correct for the test section volume increase caused by the dimples. Despite this correction, there is still observed a large DR of -7.4% (Ng et al., 2020).

- The dimpled test plates that were used at TUD did not cover the full area of the plates. The sides of each plate and the front and end of respectively the first and the third plate did not contain dimples (see Figure 4.17). In fact, the test plates used at TUD reach an actual CR of 78.1% for the 2400x400 mm test area. The reason for this is that it was preferred to manufacture only whole dimples in the plate. Tay et al. (2019) describe that diamond-shaped dimples can reach a CR of 99%. However, it is not mentioned if the full plate is covered with dimples or if only part of the test plate reaches the CR of 99%. This could partially explain a difference in encountered DR at NUS and in the current research at TUD.

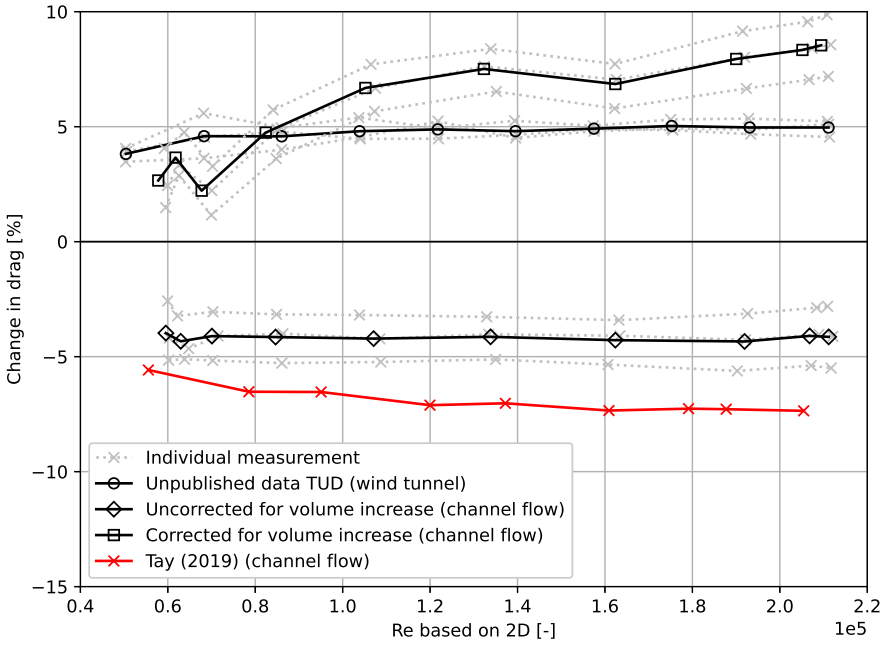

Figure 5.20: Different tests with diamond-shaped dimples. The wind tunnel has dimensions 881x400x400 mm. Channel flow is the DC-40 channel with dimensions 8000x20x400 mm.

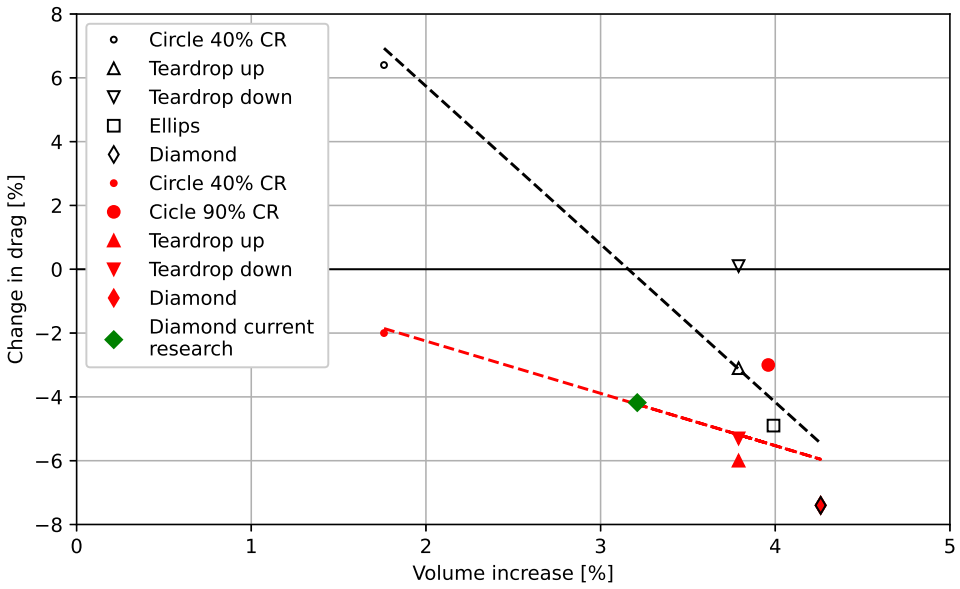

(a) Volume increase versus drag reduction for different patterns.

Pattern	Coverage ratio
Circular	40 and 90%
Teardrop (downstream)	84,4%
Teardrop (upstream)	84,4%
Elliptical	90,7%
Diamond	99,5%

(b) CR of each dimple pattern.

Figure 5.21: Relation between CR, the volume increase of the channel, and drag reduction (Tay et al. (2015); Ng et al. (2020)). Red markers illustrate numerical research; black markers illustrate experimental research. The depicted dotted lines are linear fits for each method.

The dimples form a consistent drag reduction up to a Reynolds number of approximately 21,000, as can be seen in Figure 5.16. After this Reynolds number threshold, the change in drag experiences an almost exponential boost upwards. The explanation for this behavior is twofold. Firstly, Re = 21,000 marks the exact threshold of using one pump or two pumps. From Figure 5.10 it is deduced that the instantaneous pressure is not consistent when two pumps are used, although it is not believed this plays a major role. Secondly, during the calibration phase of the wind tunnel, it was already concluded that the tunnel is operating past its maximum capacity. Reinforcements were necessary to operate with two pumps. Despite their positive impact, pushing the tunnel to a new maximum after the reinforcements is not ideal. It is plausible that there is still some bending of walls at higher Reynolds numbers, which would result in lower channel volume and hence a biased drag increase.

However, Figure 5.16 does show consistent absolute drag reduction up to $Re \approx 21,000$. In reality, the flat plate measurements also showed a drag reduction which points to errors in the wind tunnel. Figures E.1-E.4 prove that accuracy is far from perfect but that the precision is relatively good. Considering the high consistency of the measurements, the author feels confident to correct for this inaccuracy.

To pinpoint where the inaccuracy is formed, it is relevant to analyse the variation of difference in measured static pressure from its best fit line. Figure 5.5 shows the variation with respect to the line fitted through all points. To understand where the unexpected drag reduction is achieved, a line is fitted through the upstream data points only. The fitted line through upstream data points has the gradient of the new weighted average mean, see subsection 5.1.2. Theoretically, the downstream data points would also intersect with this fit. Based on Figure 5.22 it can be deduced that this is not the case for the measurements performed with the DC-40. The variation for upstream as well as downstream data points is within a range ±7-7.5%. The actual deviation with respect to the fit takes place between $x/h = 147.5$ and $x/h = 297.5$, in the test section. A first theory is that section B has a larger volume, also for flat plates, in comparison with volumes of section A and section C. The cross-section at the inlet and outlet of each section is measured to challenge this theory. In addition to that, the average cross-section of section B when dimpled plates are tested is computed. All cross-sections are represented in Figure 5.23 delta percentage with respect to the theoretical cross-section (20x400 mm). No clear indication of a volume increase in section B can be related to the error observed in Figure 5.22.
A second theory is that the error is the result of leakage. While duct tape was applied at all sides of section A and section C, see Figure F.8b, this was not done for section B. Furthermore, at high velocities, the underpressure is large. This means that the channel walls are pressed firmly in contact with adjacent material, reducing

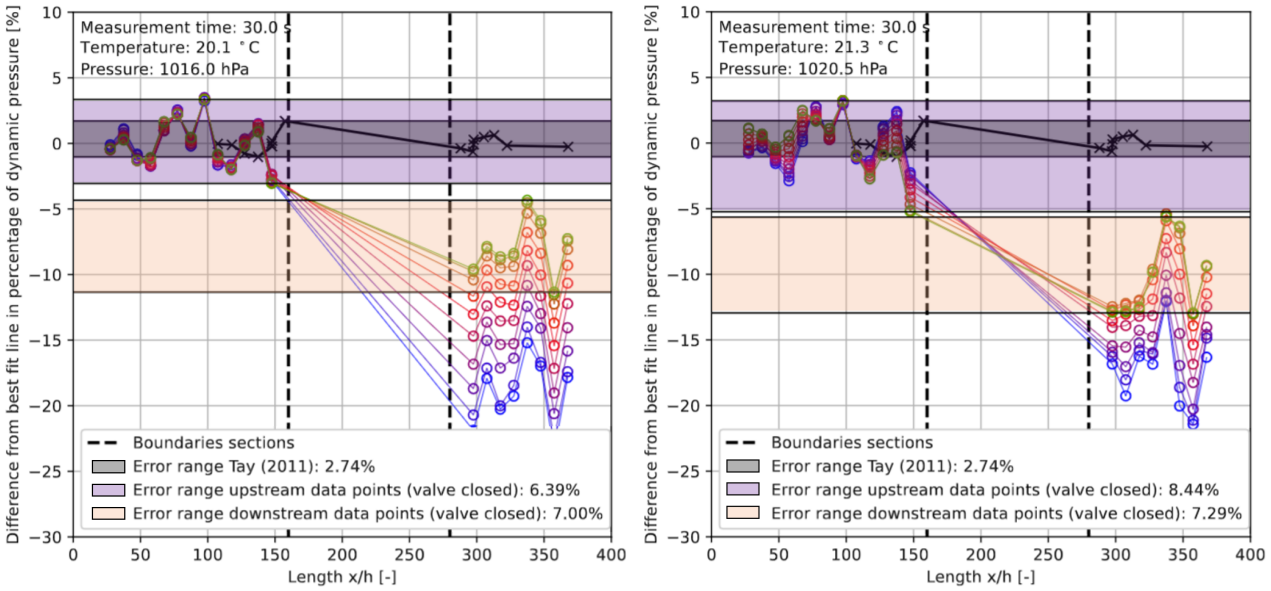

(a) 1 pump. Valve fully open corresponds to $Re \approx 5.80 \cdot 10^3$, valve closed corresponds to $Re \approx 2.06 \cdot 10^4$.

(b) 2 pumps. Valve fully open corresponds to $Re \approx 1.17 \cdot 10^4$, valve closed corresponds to $Re \approx 4.02 \cdot 10^4$.

Figure 5.22: Error range for upstream and downstream pressure taps with respect to new gradient. Flat plates are used. The green markers indicate the highest velocity (valve closed), the blue the lowest velocity (valve open).

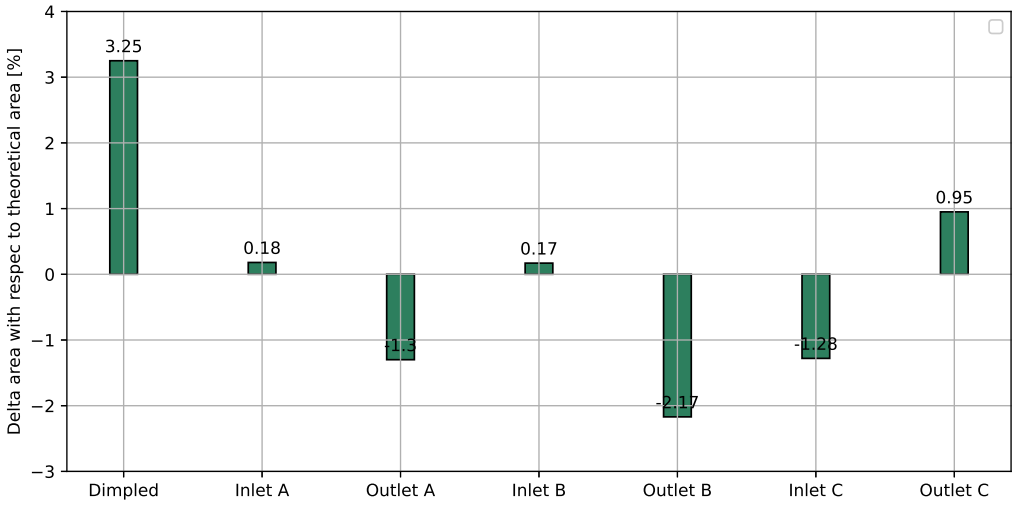

Figure 5.23: Delta cross-section with dimpled plates and delta cross-section at inlet and outlet of each section as a percentage of the theoretical cross-section (20x400 mm).

possible leakage. However, at low velocities, the walls might have some degree of freedom with respect to the sides, resulting in more leakage and higher errors. Last but not least, in section B, the ceiling wall is made out of perplex and the sides out of aluminum. Both materials are smooth and do not indent much, which leaves room for leakage. The laminated plywood walls in sections A and C likely allow for more local deformation, which helps to seal possible gaps between the sidewalls and the top- and bottom walls. Figure 5.22 clearly illustrates that the error is dependent on the Reynolds number, which makes this a plausible theory.

5.4.1 Verification measurements

The error of the pressure taps that is larger for the pressure taps at $x/h = 297.5$ can be explained by a single pressure tap. The tap at location $x/h = 297.5$ and $z/h = 2.5$ consistently returned a lower value than the other taps. It is probable this tap is partially clogged. When it was connected to another sensor, a similar result was obtained. If this tap had been neglected, the maximum error for the remaining pressure taps would have

been in the range of 2% instead of ±3-4%. The first values of taps downstream are not within the 1%-range for measurements with one pump, see Figure 5.4a. In section F.3 it was already explained that screw clamps were applied to reduce vibration. If there is a vibration of the wall with respect to the sides of the tunnel, there is room for leakage. As mentioned above, there may be more leakage at lower velocities resulting in vibrations and larger errors. At higher velocities, the underpressure would surpass a certain threshold where vibration is absent, and the errors are smaller than for lower velocities.

The experimental linear pressure drop per meter for this research and research done at NUS, computed with the Colebrook White equation, overlap reasonably well. In addition to that, the measurement's theoretical pressure drop is also in line with these two curves. The current results deviate at a Reynolds number higher than 21,000, indicating a larger pressure drop per meter. This is in perfect harmony with the drag results depicted in Figure 5.16. Furthermore, the difference between the linear pressure drop per meter based on the fit through the upstream data points and the fit through the downstream data points starts to increase as well. Everything suggests that the accuracy of the tunnel drops when Reynolds numbers >21,000 are reached.

The instantaneous pressure can be a good analyzing tool if anything seems off with the obtained data. For example, in the last dimple run with one pump, an outlier that has a 10% drag increase is found while the other measurements fluctuate between 0% and 2.5% drag increase, see Figure 5.16b. It could be concluded that the pressure tumbled significantly after approximately 18 seconds in the test run, analyzing the instantaneous pressure. Most likely, an issue with the scanner of 10 kPa downstream caused this anomaly as the data of the pressure taps upstream remains consistent while the downstream data deflects, see Figure 5.24. Nevertheless, there is no clear indication of the nature of this issue. For all other measurements, this was not encountered.

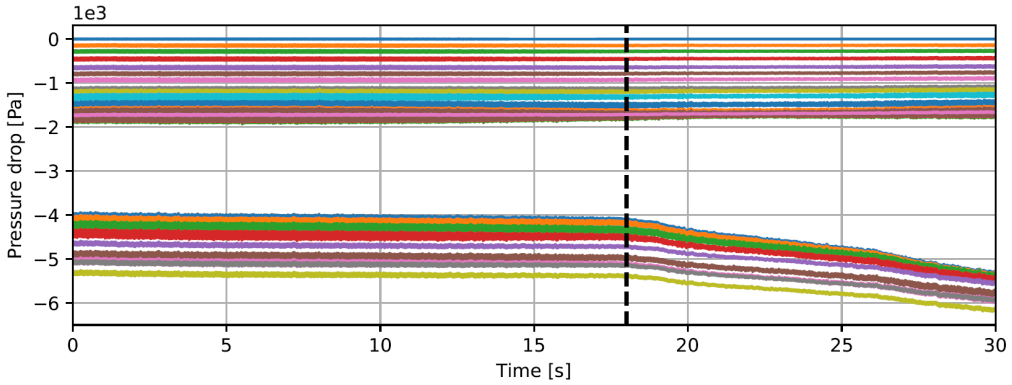

Figure 5.24: Malfunctioning of pressure scanner after 18 seconds. Colored lines depict the pressure drop at static pressure taps in streamwise direction.

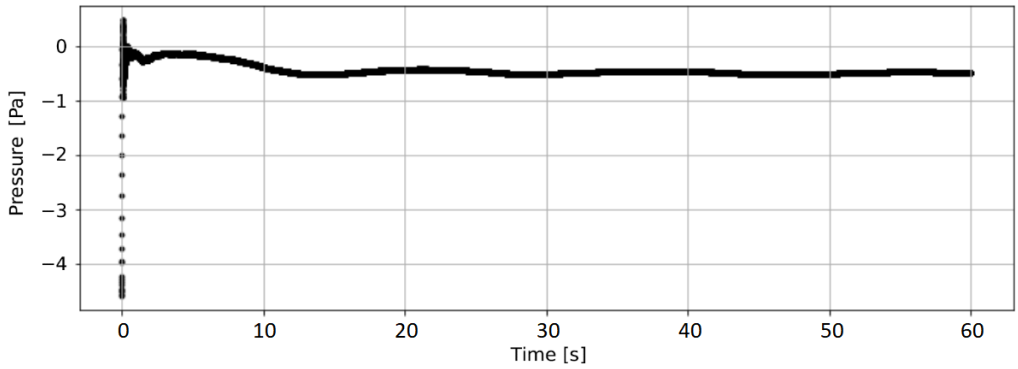

Figure 5.25: Converging instantaneous pressure. After each data point, the new average pressure is plotted. Measurement for pressure tap at $x/h = 27.5$. Flat plates and two pumps were used with the valve closed.

Furthermore, in section 5.3, an odd oscillation in amplitude was observed for the measurements with two pumps. The oscillation has nothing to do with the error of the pressure scanners, as the maximum error is 8 Pa for the scanner of 10 kPa. The amplitude is almost up to 250 Pa at a maximum Reynolds number of ≈ 40,600. On

top of that, any error caused by the scanners would be heterogeneous and not show awkward oscillations. The instantaneous pressure of the measurement performed with pump no.1 has also been investigated, although no irregularity could be found. Although the awkward oscillation is not desired, the impact on the instantaneous pressure is insignificant. Based on Figure 5.25, it can be concluded that the mean of the instantaneous pressure is found after about 12 s. However, within the first second, the largest part of the fluctuation is already averaged out.

Finally, as for the bending of the wall, Figures 5.13 and 5.14 are analyzed. The relatively large bending at low flow velocities can be explained as follows. The measuring clock works with a spring that pushes a pin to the surface that is examined. Once this surface moves down, the pin is pushed out further, indicating a negative bending. The spring can be somewhat rigid, which means it might not expand smoothly at minimal movements of the wall. Switching the pumps from off to on with the valve open has only minimal impact on the wall movement. At this point, the rigidness of the spring could cause it to be slightly stuck. Once the movement is significant, the spring will compress or expand accordingly.

Chapter 6

Velocity profiles by use of HWA

Hotwire anemometry is the second measurement technique that is used in this research. It allows mapping the TBL within the channel. The chapter is subdivided into a methodology, results, and a discussion.

6.1 Methodology

In this section, the methodology applied for the hotwire measurements is touched upon. The hotwire measurements should allow for the second sub-research question to be answered.

6.1.1 Measurement plan

In total, ten tests have been done to acquire boundary layer data. This is denoted in Table 6.1. Both days were started with a creep run, similar to the pressure measurements. On day 1, two test runs were done with flat plates at location $x/h = 237.15$, denoted as the 'center' location. The first run was with one pump, the second run with two pumps. Ideally, there would have been done two additional runs with dimpled plates. Unfortunately, this could not be done due to lack of time. Two complete datasets were acquired at the 'upstream' and the 'downstream' location on day 2. The boundary layer data of the second day is visualized in section 6.2. Considering the modest height, the flow within the channel is fully composed of boundary layer that has its

Table 6.1: Hotwire measurement plan MC-4. F = flat plate, D = dimpled plate. Upstream: $x/h = 197.13$; Center = $x/h = 237.15$; Downstream: $x/h = 279.13$.

Day 1	Notes	Pumps	ID	Day 2	Notes	Pumps	ID
F	Creep run	2	N-10	F	Creep run	2	N-10
F	Calibration	1+2	N-20a	F	Calibration	1+2	N-20b
F	Center (test run)	2	N-21	F	Upstream	2	N-23
F	Center (test run)	1+2	N-22	F	Upstream	1+2	N-24
				F	Downstream	2	N-25
				F	Downstream	1+2	N-26
				D	Downstream	2	N-27
				D	Downstream	1+2	N-28
				D	Upstream	2	N-29
				D	Upstream	1+2	N-30

highest velocity at $y/h = 0.5$. Consequently, the full height of the test section forms a field of interest. However, due to physical limitations of the setup, it is challenging to measure the full 20 mm of the test channel. Instead boundary layers of 6-8 mm in BL thickness were acquired.

The frequency of the data acquisition system is 10 kHz, and each measurement takes 5 seconds. Such a measurement is started on the laptop. As soon as the five seconds have passed, the traverse is moved to the next measurement point. The control of the traverse is on the PC. This sequence is alternated for 101 steps.

It is essential that the distance to the wall, visible on the PC, is monitored closely to ensure the wire is not compromised. During experiments, the distance of the last step to the wall typically had to be reduced to 90% of the original step size to prevent breaking the wire. This deficit was built up during the 100 steps that were taken before the last step.

Calibration. The minimum distance of the wire to the wall was calibrated prior to testing. A photo camera is used to zoom in on the hotwire. Based on the wire itself and its reflection on the wall, it is positioned as close as possible to the wall. This position is marked as height 0. From here, the traverse moves a multiple of millimeters upwards. The maximum location of the wire with respect to the wall varied between 6 and 8 mm. The wire is positioned at its maximum distance from the wall at the start of a test. The boundary layer is divided into 101 steps. E.g., when the maximum distance is 6 mm, each step is 0.06 mm, and each step is 0.08 mm when the maximum distance from the wall is 8 mm. The author is aware that a non-linear step size with a higher spatial resolution close to the wall would have been preferred. This could give more information about the viscous sublayer. Nevertheless, there was opted for a single step size in light of simplicity.

Table 6.1 denotes a calibration at the beginning of each day. The ambient temperature might change over time. The HWA is calibrated by measuring the difference in temperature of the wire and the ambient temperature. A higher ambient temperature results in an upward shift of the voltage curves depicted in Figure 6.1. Ideally, calibration is done prior to each measurement to reduce the error to a minimum. This is very time consuming, and the calibration is done only once at the beginning of each measurement day. The CTA output for calibrations of day 1 and day 2 can be found in Figures 6.1a and 6.1b.

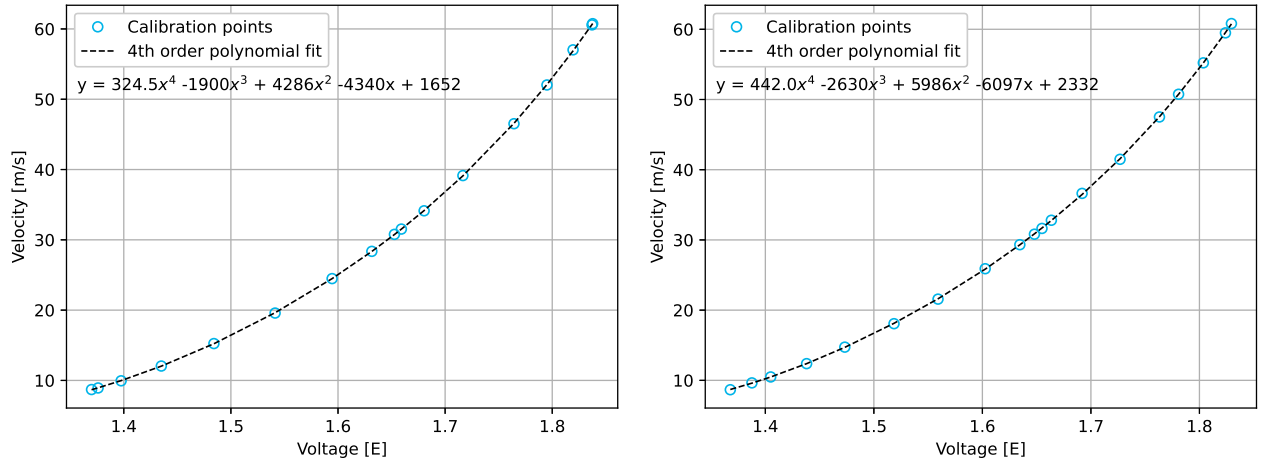

(a) Day 1.

(b) Day 2.

Figure 6.1: Calibration curves according King's Law for day 1 and day 2. The corresponding equation of the 4th order polynomial fit is given in the charts.

6.1.2 Data processing and corrections

Processing. The output data of each 5 second hotwire measurement is threefold: $50 \cdot 10^4$ data points, the velocity at that location, and the temperature. Unfortunately, the distance to the wall had to be written down and could not be logged simultaneously with voltage, temperature, and maximum velocity. Analysis of the hotwire data is done with the assistance of a code provided by Dimple Aerospace B.v. This code was slightly adjusted, considering that the corresponding y-coordinates of the wire with respect to the wall had to be imported from another data file. The code is based on research done by Rodríguez-López, E., Bruce, P. J., & Buxton (2015) and is further elaborated in section 6.2.

Data corrections. Some factors could influence the hotwire data. The high-tech hotwire system is very delicate, and if not treated with care, the hardware and the output data, might be compromised. Only the correction described by the first bullet point was applied.

- The hotwire has its first measurement point calibrated as close to the wall as possible. Taking into account that the wire is never to touch the wall itself, there is space between the wall and the wire at its null

location. Thus, the boundary layer that has $y^+ = 0$ when the wire is at its first measurement point should be corrected with an upward shift considering that the dimensionless wall unit and the dimensionless velocity are not equal to zero at the first measurement location.

- For some boundary layers, data points closest to the wall show an increase in velocity. Considering the no-slip condition at the wall always applies, this is not possible. There are three explanations for this phenomenon. Firstly, the prongs that hold the hotwire touch the wall. Subsequently, the hotwire is moved upwards where the flow velocity is higher than close to the wall, see Figure 6.2. Secondly, close to the wall, there is an increasing aerodynamic blockage effect due to the close distance of the probe and thongs to the wall (Hutchins and Choi, 2002). Thirdly, if the wire comes into contact with the wall, the heat loss through conduction increases significantly. The wire will lose heat, which is translated into an increase in voltage and velocity. Although the increased velocity close to the wall likely has another nature for the TBL's over dimpled plates, which is discussed in section 6.3, the explanations above are very plausible in case compromised data of a zero pressure gradient boundary layer.

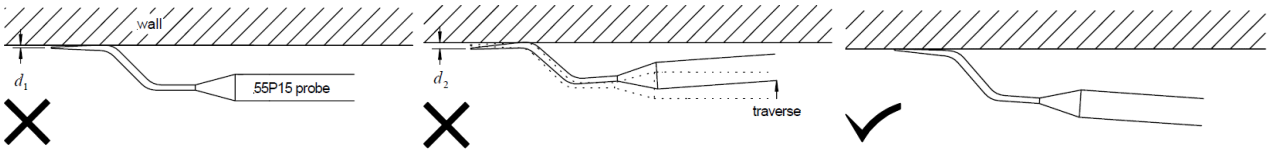

(a) Probe in contact will wall; movement of wire.

(b) Probe traversed further into the wall; deformation of prongs.

(c) Correct HWA probe setup; probe support holder under an angle.

Figure 6.2: Correct and wrong experimental setups of hotwire close to the wall (Hutchins and Choi, 2002).

6.2 Results

In this section, the results of the HWA measurements are presented. There are eight dimensional velocity profiles used for assessment. Four velocity profiles are examined for the flat plates and four for the dimpled plates. The height of the BL is not constant throughout the results. At certain test locations, the vertical range of the hotwire was more limited than at other locations. Reynolds numbers, used in figures illustrated in this section, are based on $h/2$ and the maximum measured velocity in the velocity profile. Figure 6.3-6.6 present the flat plate data which also include non-dimensional velocity profiles. Figure 6.7 and 6.8 represent the dimpled plate data.

The non-dimensional profiles are fitted through an optimization method based on a study performed by Rodríguez-López, E., Bruce, P. J., & Buxton (2015). Five parameters are used to fit the non-dimensional profile: the friction velocity u_τ, the position with respect to the wall Δy, the wake parameter Π, the boundary layer thickness δ, and the Von Kármán constant κ. The study concludes that the best optimization method involves an overshoot over the logarithmic law in the buffer layer and gives more weight (i.e., applies a mean relative error) to the points closer to the wall where the velocity is smaller than further away from the wall. The residual error of these five parameters is minimized to find the optimal solution.

Flat plates. An overview of eight BL properties for flat plates is provided in Table 6.2. The boundary layer thickness is fixed at 10 mm for all plotted boundary layers during the optimization process. The shape factors H for N-23 to N-26 are 1.322, 1.263, 1.489, and 1.301. This is close to the theoretical shape factor value of 1.3-1.4 for TBL's. The BL's measured at two locations for flat plate data coincide fairly well. At the 'upstream' location, the acquired BL for flat plates returned an average velocity number that is approximately 95% of the average velocity at location 'downstream'. The comparison is made for velocities in the same y-range as the measured BL's are not of equal height. In the upper left corner of each subfigure b (for Figures 6.3-6.6), the length of one wall unit is expressed according $l_* = \nu/u_\tau$. The length of one wall unit is identical for two pumps (4.7 μm) and very similar for one pump (8.0 μm and 8.3 μm). Data points by Tay et al. (2015) and Johansson and Alfredsson (1982) are plotted for reference in the non-dimensional velocity profile. Tay et al. applied values of $\kappa = 0.41$ and $B = 5.5$ while Johansson and Alfredsson used $\kappa = 0.41$ and $B = 5.0 - 5.8$ for the overlap layer. The non-dimensional optimized velocity profile only coincides with other studies such as Johansson and Alfredsson (1982) in the viscous sublayer. Unfortunately, no data was acquired in this region. The reason for this is the proximity of the wire with respect to the wall. In the logarithmic layer, the data of

Table 6.2: All properties HWA measurements. Up = Upstream, Down = Downstream, F = Flat, D = Dimpled.

Description	ID / Parameter	N-23	N-24	N-25	N-26
	Pumps	2	1+2	2	1+2
	Location	Up	Up	Down	Down
	Test plate	F	F	F	F
Friction velocity	u_τ [m/s]	1.810	3.231	1.878	3.182
Boundary layer thickness	δ [mm]	10.00	10.00	10.00	10.00
Displacement thickness	δ^* [mm]	1.053	0.964	0.693	1.247
Momentum thickness	θ [mm]	0.796	0.763	0.465	0.958
Shape factor	H [-]	1.322	1.263	1.489	1.301
Wake parameter	Π [-]	0.220	0.223	0.150	0.094
Von Kármán constant	κ [-]	0.597	0.557	0.573	0.467
Law of the wall constant	B [-]	4.879	4.475	4.638	3.415

this research does not show overlap with data from the other studies.

Dimpled plates. The results for N-29 and N-30 are in line with the expectation. One point has a higher velocity near the wall for N-29 and 2 points that are shifted to a higher velocity near the wall for N-30. Figure 6.8, including N-27 and N-28, present more extreme BL's that reach a lower velocity near the wall. However, For Figure 6.8a a cluster of points can be observed near the wall, and for Figure 6.8b as many as 18 points are shifted to a higher velocity near the wall.

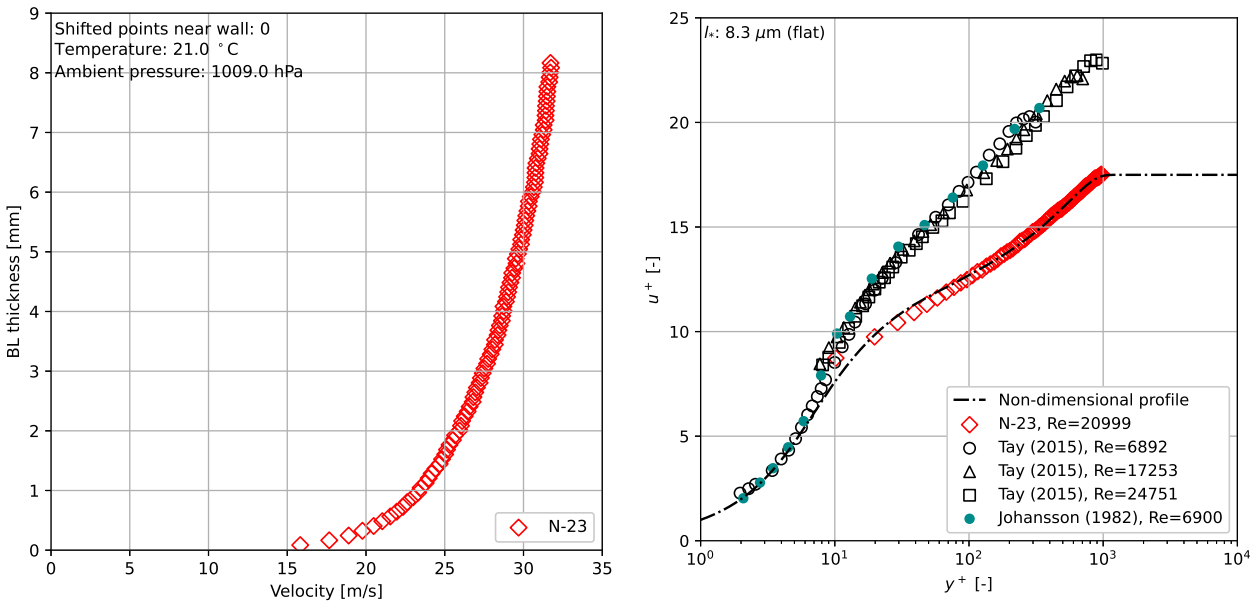

(a) Dimensional BL.

(b) Fitted velocity profile.

(c) BL properties

Name	u_τ [m/s]	δ [mm]	δ^* [mm]	θ [mm]	H [-]	Π [-]	κ [-]	B [-]
Value	1.810	10.0	1.053	0.796	1.322	0.220	0.597	4.8795

Figure 6.3: Boundary layer over a flat plate for one pump. Location: upstream.

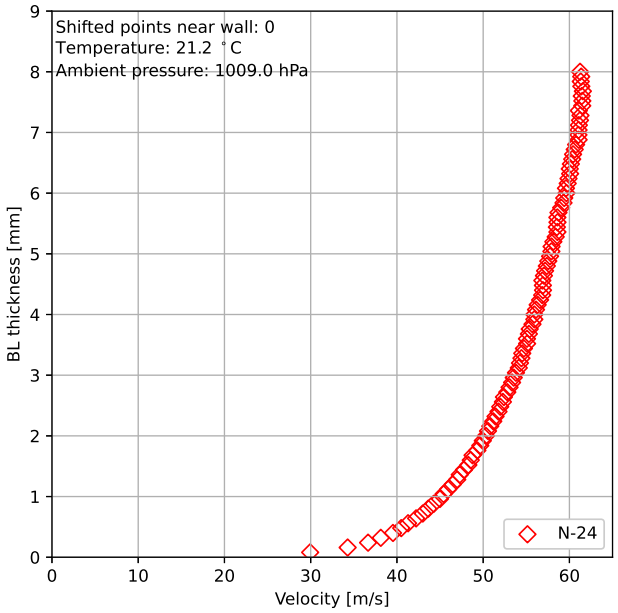

(a) Dimensional BL.

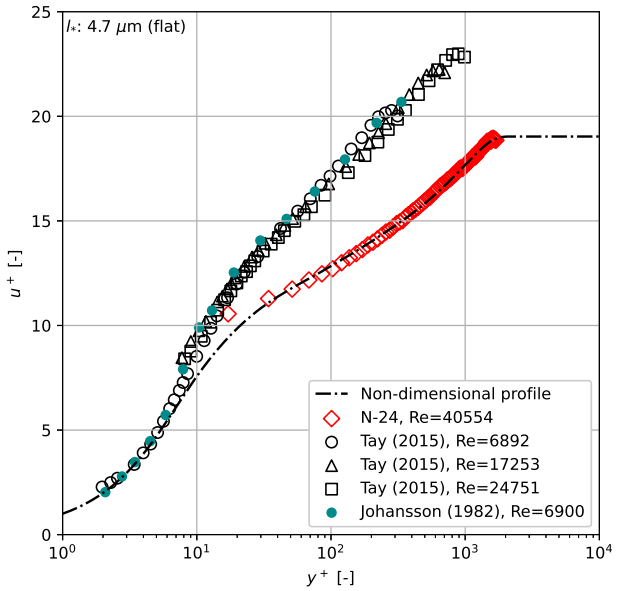

(b) Fitted velocity profile.

(c) BL properties

Name	u_τ [m/s]	δ [mm]	δ^* [mm]	θ [mm]	H [-]	Π [-]	κ [-]	B [-]
Value	3.231	10.0	0.964	0.763	1.263	0.223	0.557	4.475

Figure 6.4: Boundary layer over a flat plate for two pumps. Location: upstream.

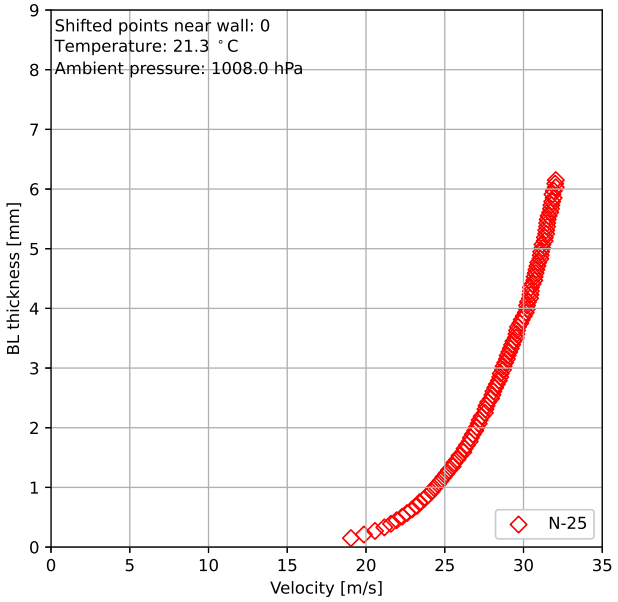

(a) Dimensional BL.

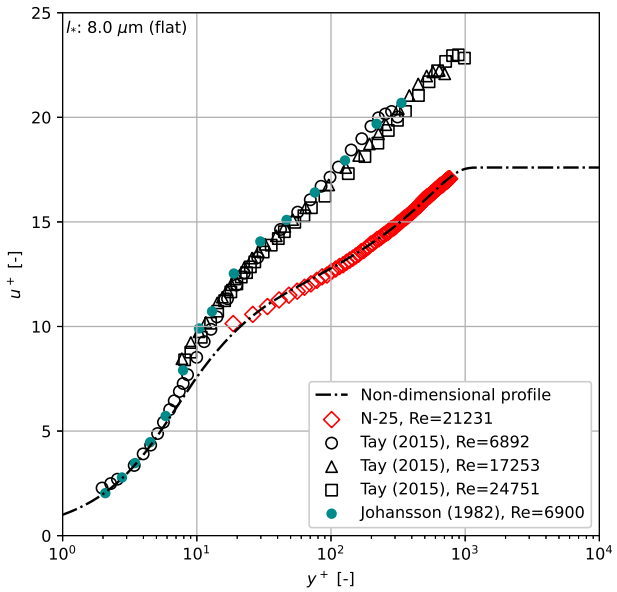

(b) Fitted velocity profile.

(c) BL properties

Name	u_τ [m/s]	δ [mm]	δ^* [mm]	θ [mm]	H [-]	Π [-]	κ [-]	B [-]
Value	1.878	10.0	0.693	0.465	1.489	0.15	0.573	4.6388

Figure 6.5: Boundary layer over a flat plate for one pump. Location: downstream.

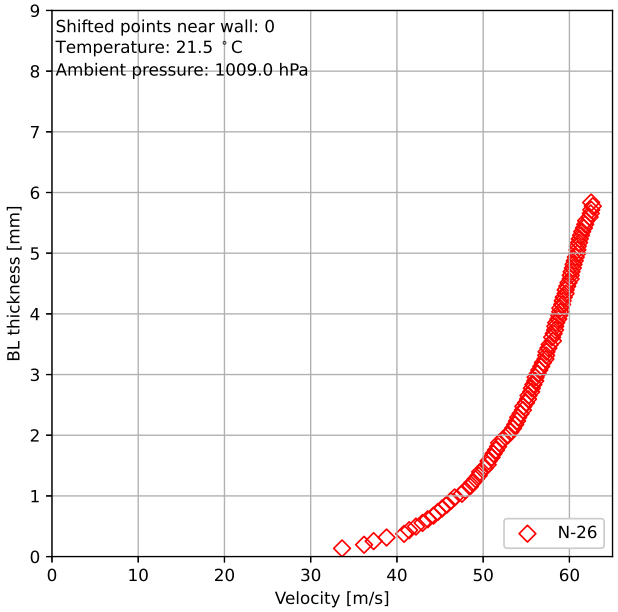

(a) Dimensional BL.

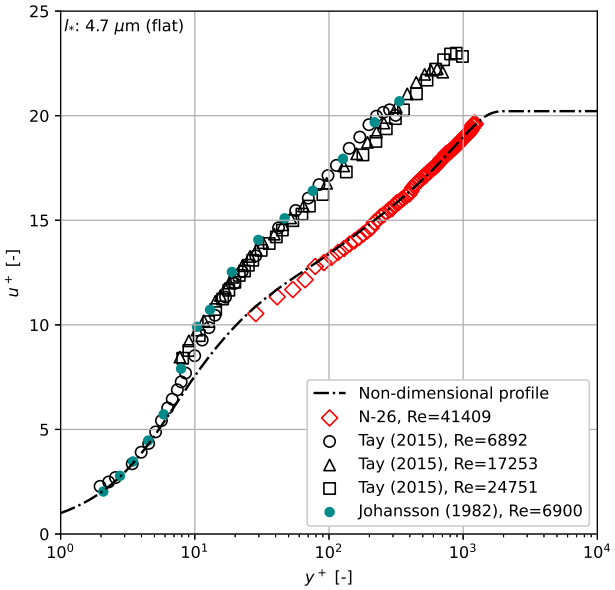

(b) Fitted velocity profile.

(c) BL properties

Name	u_τ [m/s]	δ [mm]	δ^* [mm]	θ [mm]	H [-]	Π [-]	κ [-]	B [-]
Value	3.182	10.0	1.247	0.958	1.301	0.094	0.467	3.415

Figure 6.6: Boundary layer over a flat plate for two pumps. Location: downstream.

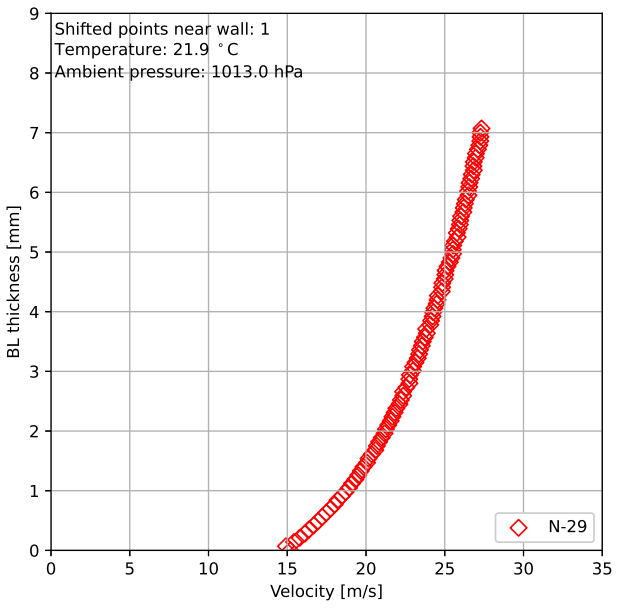

(a) One pump.

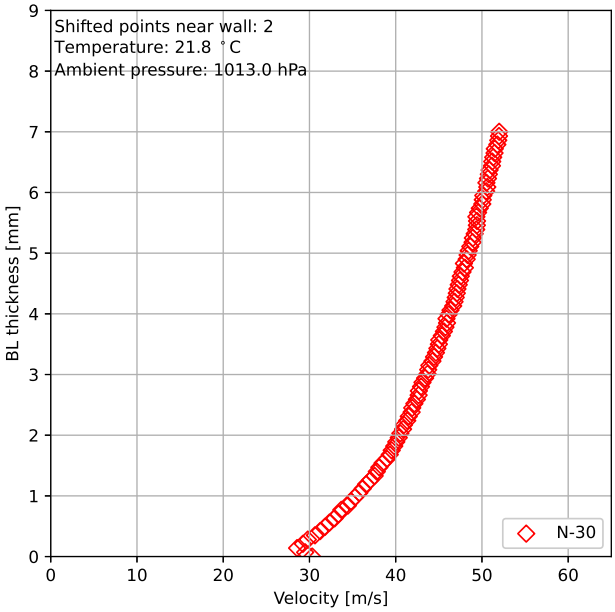

(b) Two pumps.

Figure 6.7: Dimensional boundary layers over a dimpled plate. Location: upstream.

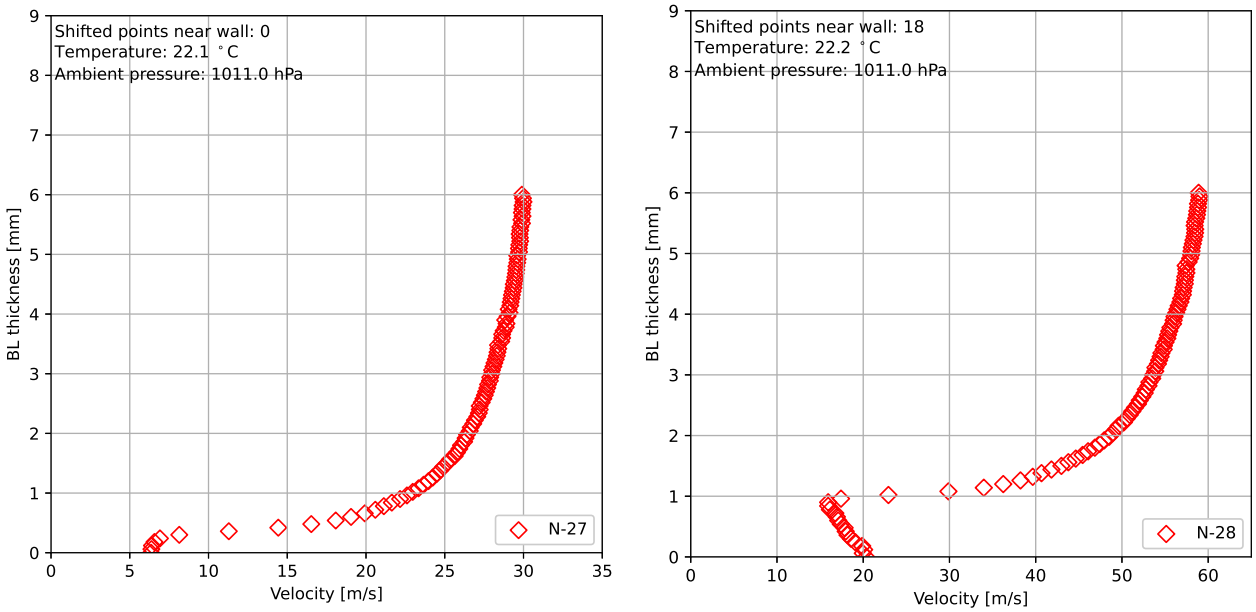

(a) One pump.

(b) Two pumps

Figure 6.8: Dimensional boundary layers over a dimpled plate. Location: downstream.

6.3 Discussion

In this section, the HWA results will be discussed. For flat plate flow, the non-dimensional velocity profiles could be computed by use of an optimizer tool, which is dependent on Spaldings law of the wall. For dimpled plates however, the optimizer could not be used considering it has a non-flat surface. Several challenges during the hotwire data acquisition are discussed below.

- Considering the slim channel height, it is assumed that the BL has a parabolic shape, see chapter 2. Unfortunately, the movement in the y-direction is minimal. Moreover, the 10 mm half channel width could not be fully covered. This limited the possibility of confirming the theory that the BL is indeed symmetric and mirrored to the center of the channel. The maximum velocity could be reached at a distance less than 10 mm from the wall, which would result in a skewed BL due to a difference in wall properties.

- The flat test plate is made out of laminated plywood. Although the material is finished with a smooth surface, there remain some irregularities on the channel wall. Also, the DC-40 is composed of handcrafted parts. In other words, during the construction of the wind tunnel, some steps, distances, and material properties might slightly deviate from the design. This consequently has a negative impact on the hotwire data.

- The irregularities of the tunnel and the wall prevented to acquire data in the viscous boundary layer. Chapter 2 describes that the viscous boundary layer is between 0-5 wall units. The closest obtained data point with respect to the wall is at a distance of 10-30 wall units, depending on the boundary layer.

- While acquiring the hotwire data, the traverse had to be moved manually and each hotwire measurement of 5 seconds had to be started manually. In these 5 seconds, one data set is acquired, consisting of 50,000 voltage values, the velocity, and the temperature. Due to human errors, the acquired data did not consist of 101 data sets for each BL. Deviated velocity profiles are N-26, consisting of 96 data sets, N-23, N-25, and N-29, which consisted of 102 data sets. It could not be determined at which point an extra set of data points was acquired. Neither was this detectable indisputably in the plotted boundary layers. As such, N-26 was measured from 0 mm (almost at the wall) up to 5.70 mm from the wall, and N-23, N-25, and N-27 were measured from 0 mm to respectively 8.08, 6.06, and 7.07 mm from the wall. Self evidently, this is not ideal, and it creates a deviated BL.

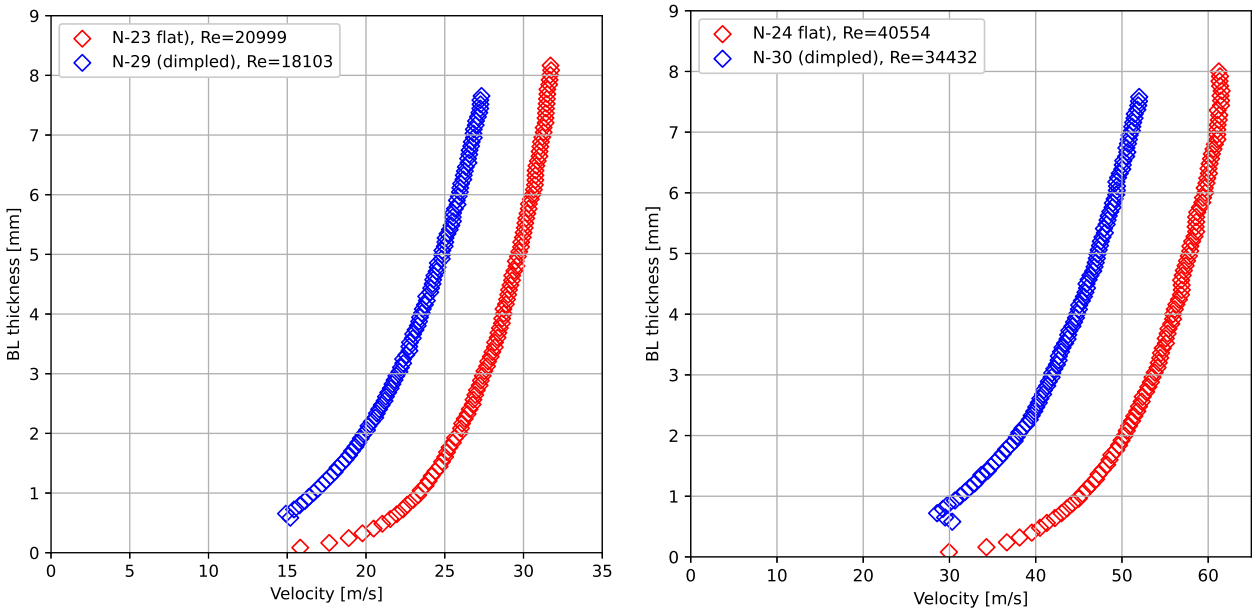

(a) 1 pump.

(b) 2 pumps.

Figure 6.9: Comparison of dimensional TBL of dimpled and flat test plates at location 'upstream'.

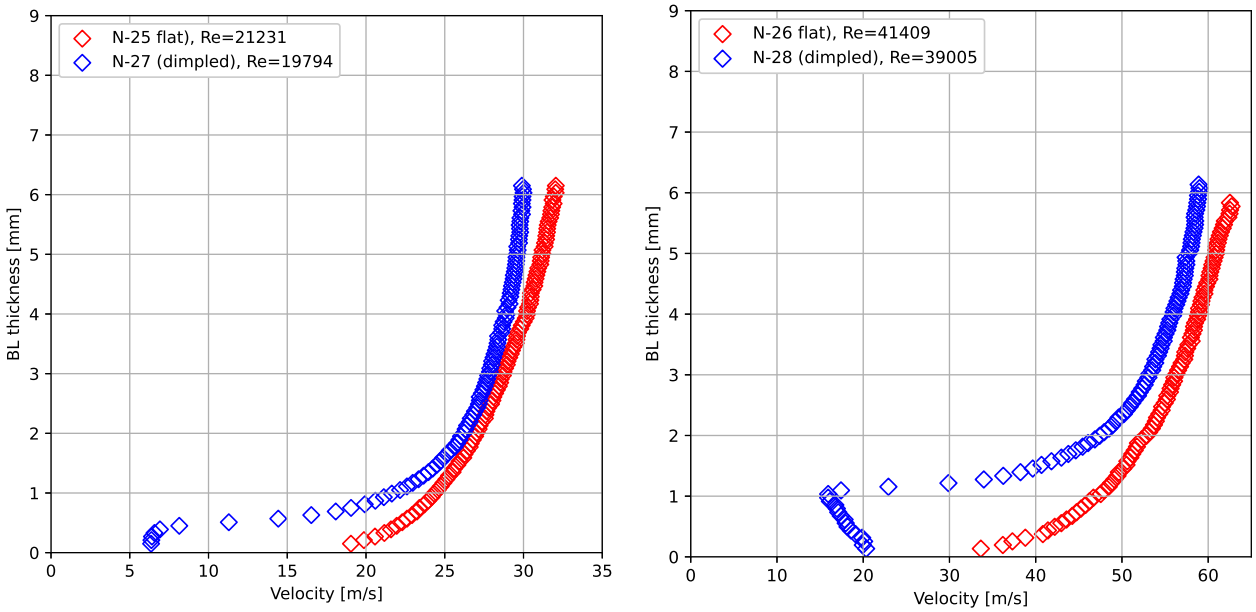

(a) 1 pump.

(b) 2 pumps.

Figure 6.10: Comparison of dimensional TBL of dimpled and flat test plates at location 'downstream'.

Ideally, an integral momentum equation is established to determine the change in momentum, and therefrom the change in drag, for flat plates in the test section and for dimpled plates in the test section. The change in drag computed through velocity profiles could be compared to the change in drag measured with the pressure measurements. However, from the discussion in chapter 5, it was concluded that the test section, section B, includes a large error, possibly formed due to leakage. Secondly, the position of the hotwire is not identical with respect to the dimple geometry in streamwise direction, depicted in Figure 6.11. It is likely that higher or lower local flow velocities are present at different points in or above the dimple. Thirdly, no full boundary (10 mm) neither the viscous sublayer was captured. Concluding, no BL's are compared between the 'upstream' and the 'downstream' location.

Nevertheless, dimensional BL's of flat- and dimples plates at the same test location are compared in a single graph. For location 'upstream', this is depicted in Figure 6.9 and the BL's at location 'downstream' are depicted in Figure 6.10. A clear shift of the velocity profile between the two types of test plates can be observed for tests conducted with one pump and with two pumps, especially at location 'upstream'. A drop in velocity directly relates to less shear stress and a reduction in skin friction drag.

As the hotwire is never to touch the wall, there is a 'gap' between the wall and the first measurement point location. This distance, Δy, was computed with the optimizer for flat plates and is also visualized in Figure 6.11b. For location 'downstream', the hotwire was downstream of the last dimple, see Figure 6.11b. For that reason, it is assumed that Δy for dimpled plates is identical to Δy for flat plates. However, for the 'upstream' location, the hotwire was positioned approximately 10 mm into the dimple, see Figure 6.11a. Consequently, the Δy is larger than the Δy for flat plates. The deepest point of the 100 mm long dimple with respect to the flat surface is 2.5 mm. The geometry of the dimple is simplified to an isosceles triangle. As the hotwire was placed about 10 mm from the edge of the dimple, 500 μm is added. This is illustrated in Figure 6.11a.

An overview of the closest distance of the wire with respect to the wall for each BL is depicted in Table 6.3. In this overview, it can be observed that Δy is about twice as large for location 'downstream' in comparison with location 'upstream'. The reason for this is duct tape, which covers a step of the transition between section B and section C. The tape is located straight under the prongs, limiting the to move the wire closer to the wall, which is depicted in Figure 4.13b.

Table 6.3: Different Δy's: distance between wall and first measurement location of the TBL.

	1 pump		2 pumps	
	Flat (μm)	Dimpled (μm)	Flat (μm)	Dimpled (μm)
Upstream	80	80 + 500	84	84 + 500
Downstream	135	135	150	150

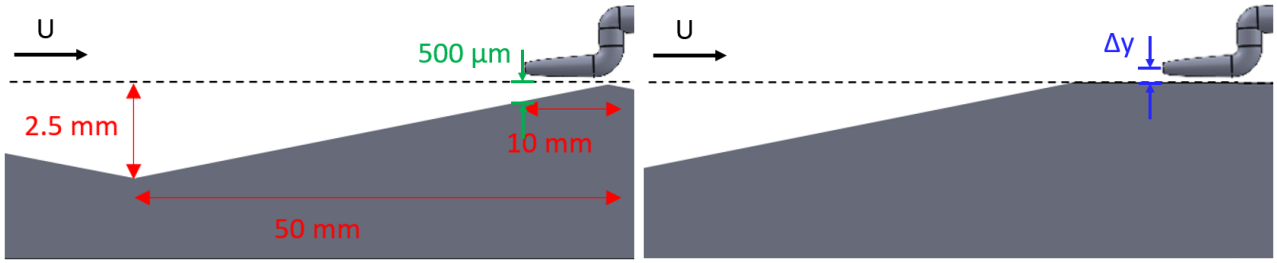

(a) Position of hotwire at location 'upstream'.

(b) Position of hotwire at location 'downstream'.

Figure 6.11: Location of the hotwire at location 'upstream' and 'downstream'. Added distance of 500 μm between wire and wall in Figure 6.11a. Dimensions are not scaled.

Measurements performed with dimpled test plates do not return a zero pressure gradient boundary layer. Several points near the wall indicate a higher velocity than locations further away from the wall. For N-27, this was as much as 18/101 data points. A probable reason for this anomaly is the location of the hotwire near the edge of the test plate, see Figure 4.13b. The duct tape is approximately 230 μm in thickness. The wall units for N-25 and N-26 are 8.0 and 4.7 μm, respectively. As mentioned in subsection 2.1.3, the thickness of the viscous sublayers is around five wall units. In other words, the duct tape is six times as thick as the viscous sublayer of N-25 and 12 times as thick as the viscous sublayer of N-26. On top of that, the duct tape covers a clear step between the section B and section C, which is located just downstream of the hotwire location. This could be a reason for higher flow velocities near the wall, i.e., flow reversal that is caused by the step.

A second explanation could be that the prongs touch the wall resulting in an upward movement of the wire illustrated earlier in Figure 6.2b. A third possibility is that the wire is in contact with the wall, which leads to an increase in conduction, which also stimulates the voltage and hence velocity. The last two explanations do not seem very probable, considering the amount of ignored points for some measurements. The prongs, and especially the wire itself, are able to withstand only tiny forces. Subsequently, they most certainly would have

been deformed or broken by the time several points returned an increased velocity.

A more convincing explanation of the increased velocity near the wall is provided by Beratlis et al. (2014). They performed a DNS study over a flat surface, which included two rows of dimples at the beginning. The side view of the plate with two rows of dimples can be found in image IV of Figure 6.12. Images I-III depict dimensional velocity profiles, normalized by the free stream velocity, at the locations where the arrows are pointed. A clear correlation between the velocity profiles by Beratlis et al. and the profiles of this research can be observed, especially for the dimensional velocity profile of N-28, depicted in Figure 6.8b. However, it should be noted that the study by Beratlis et al. (2014) involves a Reynolds number of 1,000, based on the boundary layer thickness δ, and the flow is laminar over flat plates. The study does conclude that dimples are effective in tripping the laminar flow to a turbulent state.

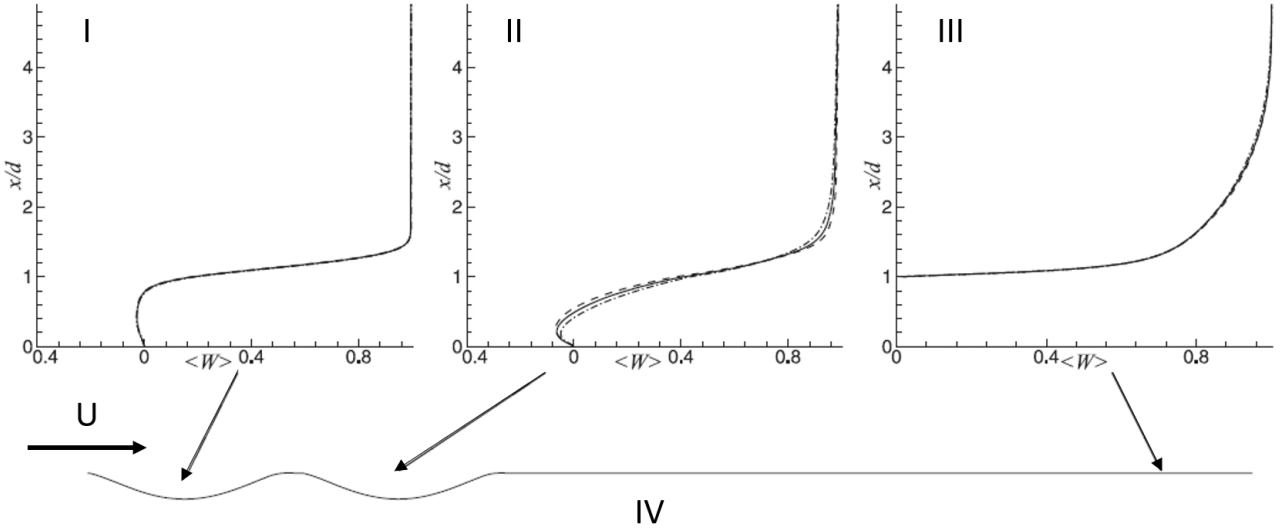

Figure 6.12: Dimensional boundary layers according to the DNS study done by Beratlis et al. (2014) over a dimpled surface.

Lastly, Figure 6.13 depicts the friction velocity for all measured flat plates BL's. For measurements with two pumps, u_τ is larger than for one pump. The theoretical u_τ is computed with equations 5.6 and 5.7. The u_τ found by the optimizer is larger than the theoretical shear velocity, which is related to the average velocity of the measured BL. The average velocity of the full boundary layer, which is 10 mm, will be larger and therefore also induce a larger friction velocity. The friction velocity does not change much between the two measurement locations.

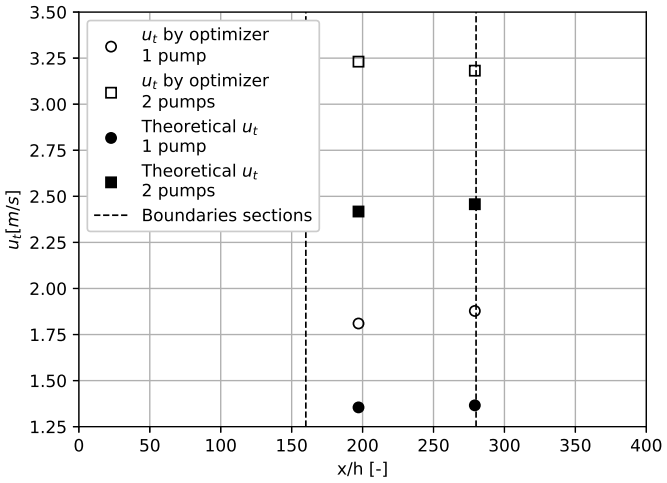

Figure 6.13: Friction velocity u_τ for flat plates at location 'upstream' and location 'downstream', computed by the optimizer and theoretically. Theoretical values are computed with formulas by White (2006).

Chapter 7

Surface oil flow visualization

The last measurement technique that was used in this research is surface oil flow visualization. Similar to the previous two chapters, a methodology, results, and a discussion can be found in this chapter.

7.1 Methodology

While HWA accurately portrays flow behavior near the wall and has a high spatial resolution, it is time-consuming to investigate a large area or 3D-space. Surface flow visualization utilizing oil flow, on the other hand, provides insight for a large test area within a relatively short amount of time. Although only substantial flow structures such as flow reversal can be recognized when using oil flow, it is a rather straightforward method that does not require as much expertise to perform HWA.

7.1.1 Measurement plan

The oil flow measurements were performed at the end of MC-4. Two oil flow measurements for dimpled plates were done, one measurement at the upstream part of section B and a second measurement at the downstream part of section B. This is depicted by yellow areas in Figure 4.8. The purpose of the oil flow measurements was to check for any irregular obvious flow structures such as separation or flow reversal. Secondly, the movement of the air through the dimples close to the surface could be visualized. In an earlier stage during calibration of the DC-40, a more viscous type of oil was used to identify unexpected flow structures near the spanwise dimples at location $x/h = 147.5$. This did not yield any useful data as the oil was too viscous.

7.2 Results

In Figure 7.1, the part of the test section that was covered with oil is illustrated for location 'upstream'. In Figure 7.2, the oil flow visualization at the downstream location is depicted. There are some reflections of the UV-light on caused by the anodized aluminum. Figure 7.3 illustrates the black square from Figure 7.2. The crisscross of streaklines can be subdivided into two categories: straight lines and oscillation lines. There are straight lines where oil particles enter and exit the dimple at the tips. Considering the fact that the triangle tips of the dimples are adjacent two each other in the streamwise direction, the oil moves straight into the next dimple. The straight lines are alternated with lines that oscillate through the staggered dimples.

7.3 Discussion

Although the fluorescent oil particles heavily light up the dimpled test plate, the streaklines are identifiable. All lines were uninterrupted, such that there is no reason to believe that flow reversal or flow separation is present. The flow converges when it enters the dimple and diverges when it exits. This type of oscillation has been observed in earlier studies (Van Nesselrooij et al. (2016); Van Campenhout et al. (2018)). However, this oil flow measurement also shows straight streaklines, which are explained easily by the adjacent dimples.

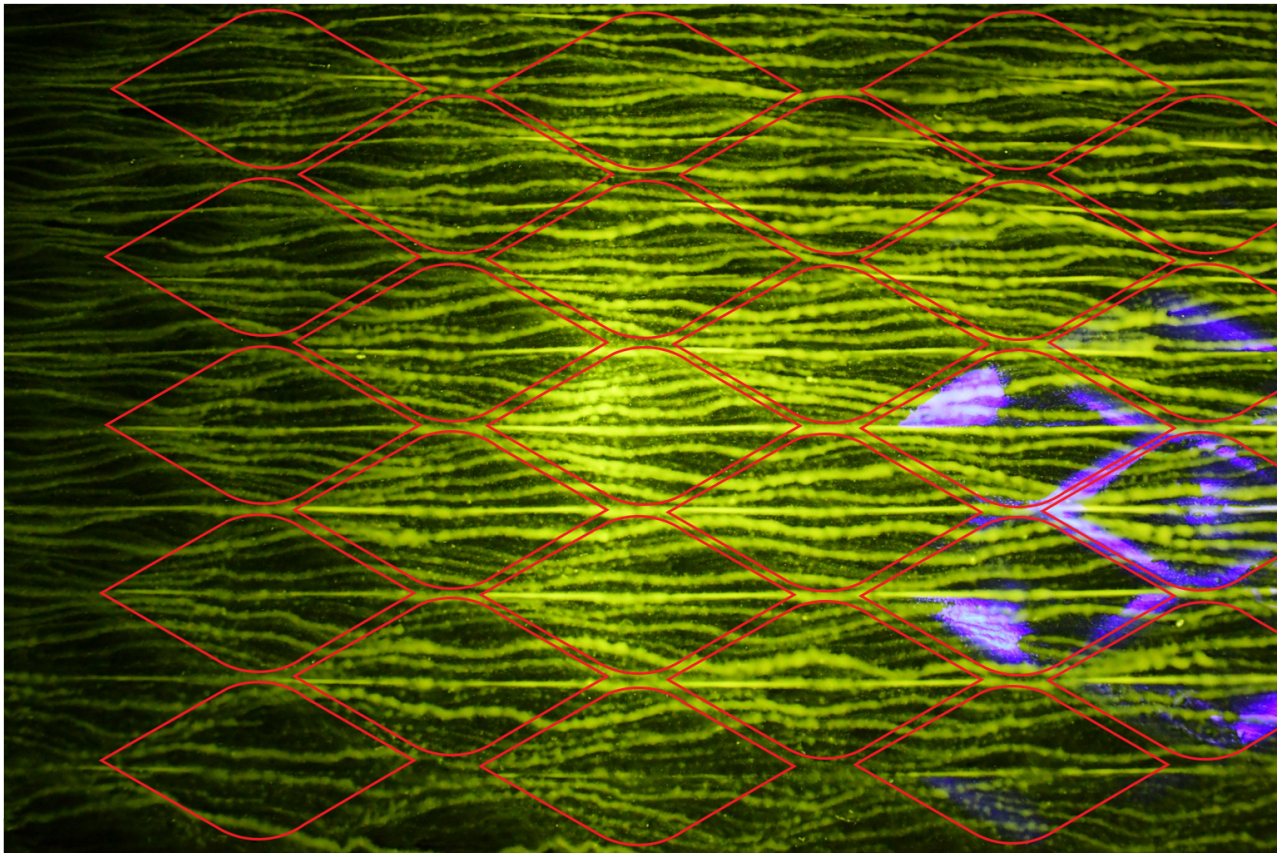

Figure 7.1: SOFV at location upstream. Flow fltr.

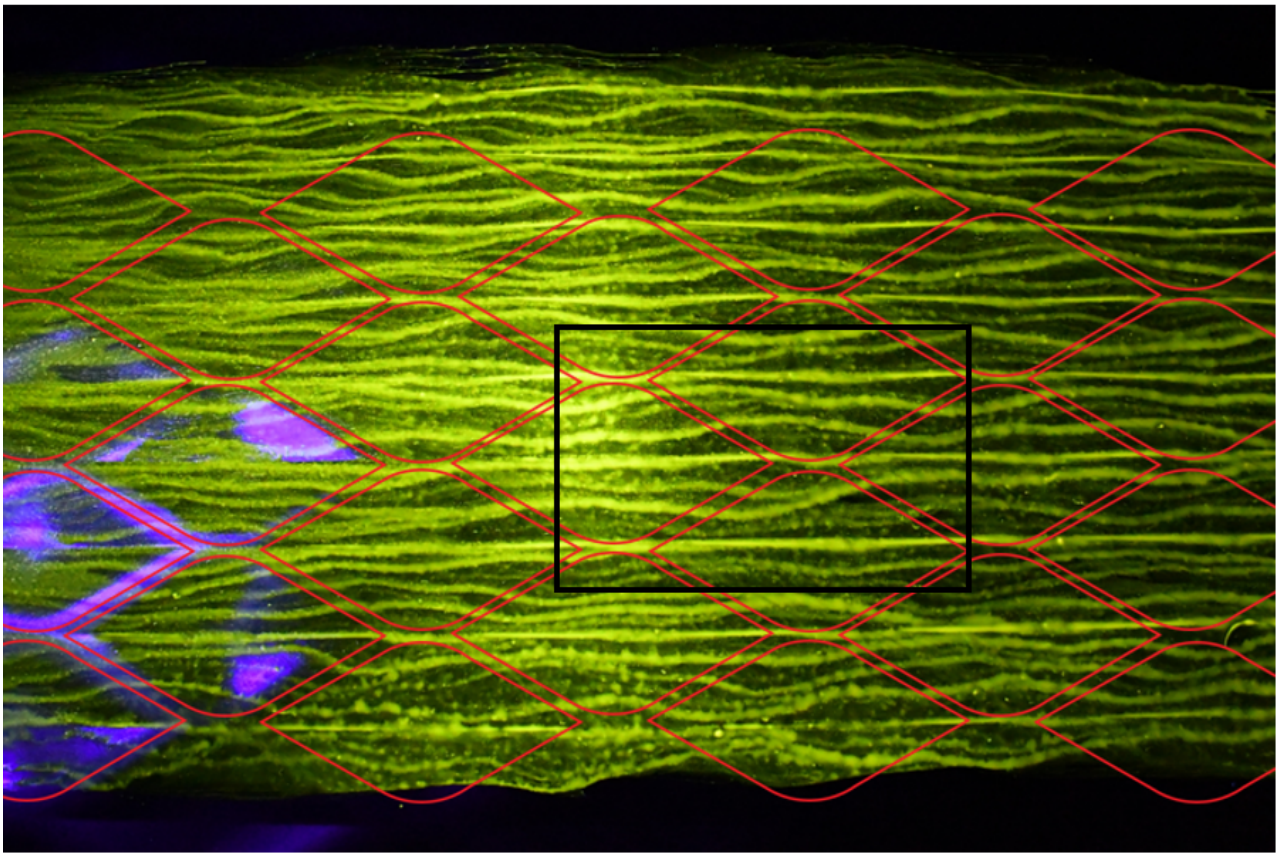

Figure 7.2: SOFV at location downstream. Black square is magnified in Figure 7.3. Flow fltr.

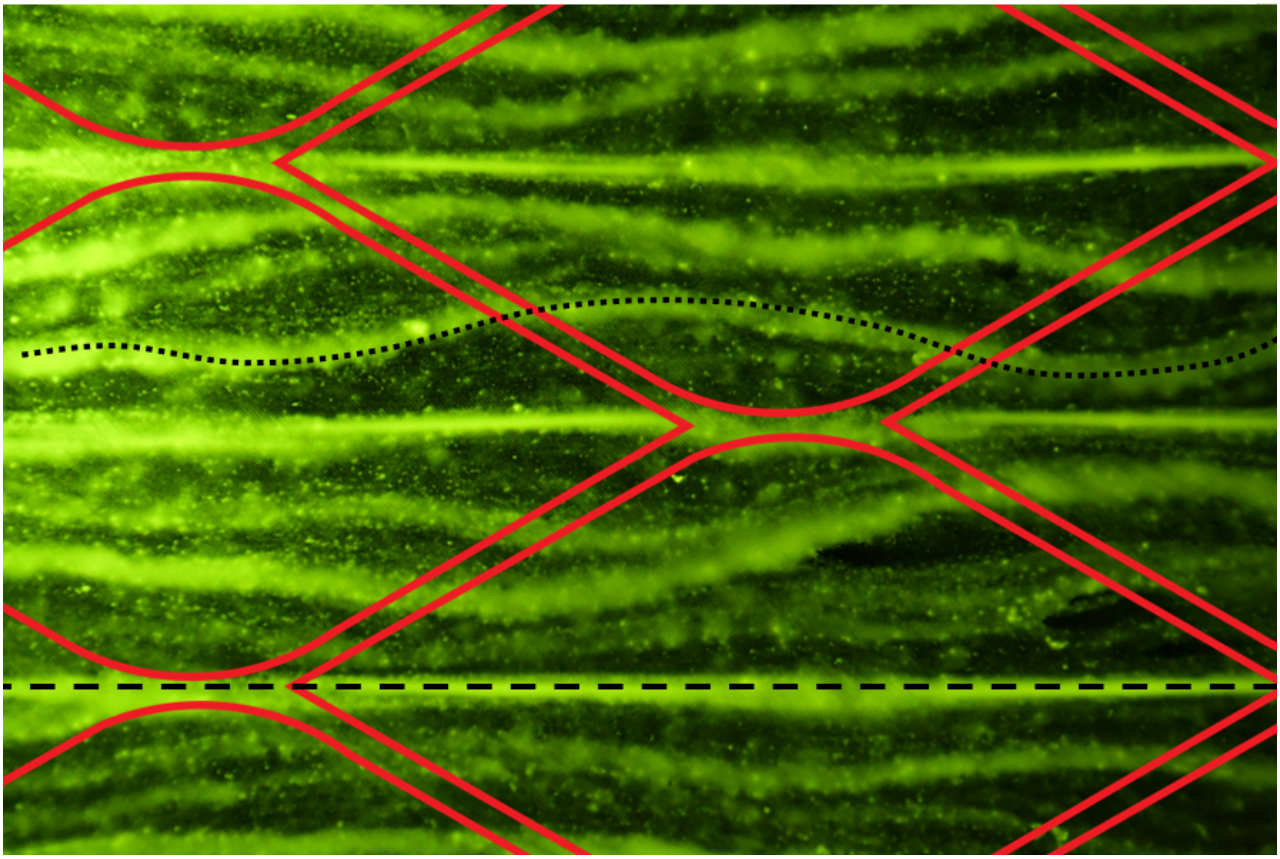

Figure 7.3: Oil flow surface visualization. Dashed lines represent straight streaklines; dotted line is an oscillating streakline. Flow fltr.

Preferably, the camera should be positioned more orthogonal, although the current setup does not limit the possibility to identify the flow structures. Furthermore, the steel beams used for reinforcement limited optical access for videography. In addition to that, the perspex demonstrated strong reflections of the UV-light. If time-dependent flow behavior is to be monitored in the future, optical access should be improved.

During the calibration of the DC-40 at the beginning of this research, there were some unexpected deviations in the pressure measurements. SOFV was used to see if awkward flow structures could explain the deviation. However, the applied oil was too thick, resulting in minimal movement of the particles and an unsuccessful measurement.

Chapter 8

Conclusions

In this chapter, the research questions posed at the beginning of this report are answered. Each bullet point represents a conclusion of the research question, which will be rephrased for convenience.

- *Can drag reduction be observed for turbulent channel flows employing a dimpled surface?* The wind tunnel used at NUS was designed and reconstructed at TUD. After calibration, pressure measurements of the DC-40 returned a consistent absolute drag reduction of approximately 5% up to a Reynolds number of 21,000. This percentage is in the same order of magnitude of the results by Tay et al. (2019). They found DR up to 7.4% for Reynolds numbers between 5,000 and 50,000. However, the volume caused by the dimples is not considered for the 5% DR. Results of this research pointed out that drag started to increase significantly beyond a Reynolds number of 21,000. Consequently, an objective analysis was not possible anymore beyond this threshold.

- *Can a zero pressure gradient boundary layer with a linear pressure gradient be obtained? Which verifications are required to confirm this?* A linear pressure gradient was found, although the error is significant. The flat plate data indicates a substantial DR in the range of 8-15%, which is formed in the test area of the channel. A new benchmark is set by subtraction of a linear fit from the raw data. Verifications are needed to estimate the precision and accuracy of the pressure-based drag results and the linear pressure gradients. Examples are a two-dimensionality check, a comparison of theoretical and experimental skin friction coefficients, and differences between the pressure drop per meter of this research and other researches. It can be concluded that the precision of the results is relatively high but that the DC-40 lacks accuracy. The lack in stiffness of the DC-40, likely one of the factors that contributed to an insufficient accuracy, could have been foreseen by performing a priori stiffness computations, as is described in Appendix C.

- *What momentum difference in the turbulent boundary layer can be observed between flat- and dimpled test plates?* No quantitative momentum analysis was performed to determine the change in drag based on the velocity profiles. Nevertheless, a clear shift of the velocity profiles over the dimpled plates was observed with respect to the velocity profiles over the flat plates at the 'upstream' test location. At the 'downstream' test location, the shape of the velocity profiles over the two types of test plates deviated. In the boundary layer for dimpled plates, lower velocities were reached. However, an increased velocity near the wall was observed, which resembles the velocity profiles encountered by Beratlis et al. (2014). Last but not least, the near-wall flow structures recorded at NUS were not investigated. Hence, it cannot be confirmed nor denied whether the nature of the change in drag is related to near-wall flow structures or not.

- *Does a correction for the increased channel volume abate encountered drag reduction? If so, by how much?* The change in drag, including a correction for volume increase caused by the dimples, is in line with data from unpublished ongoing tests at TUD. The unpublished ongoing TUD data was obtained in a wind tunnel with a larger cross-section (400x400 mm) where a free stream velocity could be reached rather than a centerline velocity. For measurements with the DC-40, a correction for volume increase transformed the change in drag from negative to positive. In other words, there is a strong belief that the 5% DR is a response to the volume increase caused by the dimples rather than near-wall flow mechanisms.

- *Does flow reversal occur in the diamond-shaped dimples used at NUS?* Based on the oil flow measurements, no flow separation or flow reversal could be identified. The streaklines of the oil flow measurements are continuous and no unexpected flow structures were observed.
- *Do dimpled surfaces have the potential to be applied in existing pipelines?* Based on this research, it can be concluded that dimples do not have a positive effect on the drag reduction in channel flows. Shortly translated, dimples are inadequate to be used as a drag-reducing mechanism in pipelines. Nevertheless, it should be mentioned that follow-up research is required to confirm current results. In addition to that, other DRT's could be further investigated to search for drag reduction.

Chapter 9

Recommendations

The desired true drag reduction was not found. Nevertheless, the results are interesting from an academic point of view. The volume dependency seems indisputable, yet there are several improvements required to fully validate this theory. Some recommendations for further research are provided below.

- **Channel and valve improvements.** Firstly, various improvements can be made on the DC-40, creating a more confident test channel. This should contribute to validate the volume dependency theory with more certainty. Recommendations on the channel are discussed in Appendix F. Furthermore, the butterfly valve that is used to run tests under different flow velocities is currently operated manually. For future measurements, this valve should be replaced by a remotely operated valve. This will increase the repeatability of wind tunnel tests, and measurements could be performed at more precise velocities. It is also preferred to have a butterfly valve that does not require false air leakage to lower the flow velocity, which should contribute to the accuracy of the output data. Instead, the valve should be placed in the tube itself, which would minimize the number of elbows.

- **HWA with multiple traverses.** Future HWA measurements should be performed at the same orientation with respect to individual dimples on the test plate. A second recommendation on the hotwire setup is to create a mechanism that allows to map the full BL (half channel width), including the viscous sublayer. Thirdly, Tay et al. (2015) used a 3D traverse system to acquire HWA data. Subsequently, the boundary layer could be examined at a larger spatial resolution (in a 3D space instead of a 1D space). Taking the SOFV data into account, it is expected that the high-speed streaks are formed in the center with oscillating streaklines on the side. Two high-speed streaks that oscillate were also identified at NUS. Unfortunately, a thorough investigation of the flow structures could not be performed during this research. However, for future research, this is highly recommended considering that DR found at NUS is based on the near-wall flow structures. All HWA recommendations require an upgraded test design with higher accuracy.

- **Merging of data processors.** For HWA, the y-position from the wall had to be acquired on a separate computer (PC). The 101 steps required 202 manual clicks (101 at the PC and 101 at the laptop). During the acquisition of the data, some human errors were made. The traverse movement should be integrated into the system that measures the voltage such that the data is absent from human errors and data acquiring is automated for one run. Last but not least, this would help to generate the output data as a single file.

- **DNS study.** At NUS, a DNS study for various dimple patterns is performed (Ng et al., 2020). Both DNS and experimental research for diamond-shaped dimples returned a DR of 7.4%. A numerical study concerning diamond-shaped dimples is something that is also recommended for research at TUD. Considering that DNS results obtained at NUS involve a correction for volume increase by using a constant flow rate, it would be exciting to see what change in drag DNS experiments return involving the same correction at TUD.

Bibliography

S. T. A. Kartushinsky, A. Mulgi and E. E. Michaelides. An experimental study of the effect of particles on the shear stress in particulate turbulent pipe flow. *Proceedings of the Estonian Academy of Sciences, Engineering*, 11(2):161–168, 2005. URL https://books.google.nl/books?hl=nl{&}lr={&}id=qhsQfdw2{_}EsC{&}oi=fnd{&}pg=PA161{&}dq=A.+Kartushinsky,+A.+Mulgi,+S.+Tisler,+and+E.+E.+Michaelides,+\OT1\textquotedblleftAn+experimental+study+of+the+effect+of+particles+on+the+shear+stress+in+particulate+turbulent+pipe+flow,\OT1\textquotedblright+Proc.+Estoni.

K. K. A.A.B. Hayder, A.H. Nour and A. Abdalia. Investigating the effect of solid particle addition on the turbulent multiphase flow in pipelines. *International Journal of the Physical Sciences*, 6(15):3672–3679, 2011. doi: https://doi.org/10.5897/IJPS11.647.

H. Abdulbari. Introducing slag powder as drag reduction agent in pipeline: An experimental approach. *Scientific Research and Essays*, 7(18):1768–1776, 2012. ISSN 1992-2248. doi: 10.5897/sre11.1483.

H. A. Abdulbari, R. M. Yunus, N. H. Abdurahman, and A. Charles. Going against the flow — A review of non-additive means of drag reduction. *Journal of Industrial and Engineering Chemistry*, 19(1):27–36, 2013. ISSN 1226086X. doi: 10.1016/j.jiec.2012.07.023.

H. A. Abdulbari, B. Ainoon Shabirin, and H. N. Abdurrahman. Bio-polymers for improving liquid flow in pipelines—A review and future work opportunities. *Journal of Industrial and Engineering Chemistry*, 20: 1157–1170, 2014. doi: https://doi.org/10.1016/j.jiec.2013.07.050.

H. A. Abdulbari, H. D. Mahammed, and Z. B. Y. Hassan. Bio-Inspired Passive Drag Reduction Techniques: A Review. *ChemBioEng Reviews*, 2(3):185–203, 2015. doi: https://doi.org/10.1002/cben.201400033. URL https://onlinelibrary.wiley.com/doi/abs/10.1002/cben.201400033.

S. H. Agarwal and R. S. Porter. Shear degradation of poly(vinyl acetate) in toluene solutions by high-speed stirring. *Journal of Applied Polymer Science*, 25(2):173–185, 1980. ISSN 0021-8995. doi: 10.1002/app.1980.070250205. URL https://onlinelibrary.wiley.com/doi/abs/10.1002/app.1980.070250205.

G. I. K. Alekseev, I. A. Gachechiladze, V. G. Oleinikov, and V. V. Mechanisms of the Self-Organization of Tornado-Like Jets Flowing Past Three-Dimensional Concave Reliefs. *Heat Transfer Research*, 37(6): 467—-494, 2006. doi: 10.1615/HeatTransRes.v37.i6.10. URL http://www.dl.begellhouse.com/journals/46784ef93dddff27,7927a22050399ec2,71e4d0ce5f3969f0.html.

J. D. Anderson. *A History of Aerodynamics and Its Impact on Flying Machines*. Press Syndicate of the University of Cambridge, 1997. URL https://books.google.nl/books?hl=nl{&}lr={&}id=1OeCJFJY3ZYC{&}oi=fnd{&}pg=PR11{&}dq=aristotle+and+archimedes+drag+aerodynamic{&}ots=WiIA2W{_}DDr{&}sig=WaPjT236OibsltJBhSOOHDUoRzY{&}redir{_}esc=y{#}v=onepage{&}q{&}f=false.

I. I. Azubuike and S. S. Ikiensikimama. Forecasting Oil Formation Volume Factor for API Gravity Ranges Using Artificial Neural Network. *Advances in Petroleum Exploration and Development*, 5(1):14–21, 2013. ISSN 1925-5438. doi: http://dx.doi.org/10.3968/j.aped.1925543820130501.996.

C. Beal. The Viscosity of Air, Water, Natural Gas, Crude Oil and Its Associated Gases at Oil Field Temperatures and Pressures. *Transactions of the AIME*, 165(01):94–115, 1946. ISSN 0081-1696. doi: 10.2118/946094-G. URL https://doi.org/10.2118/946094-G.

P. Beider and N. Tawil. *Future investment in drinking water and wastewater infrastructure*. Congress, 2002. ISBN 9780160512438.

N. Beratlis, E. Balaras, and K. Squires. Effects of dimples on laminar boundary layers. *Journal of Turbulence*, 15(9):611–627, sep 2014. doi: 10.1080/14685248.2014.918270. URL https://doi.org/10.1080/14685248.2014.918270.

B. Bhushan. Biomimetics: lessons from nature - an overview. *Philos Trans A Math Phys Eng Sci*, 367(1893): 1445–1486, 2009. ISSN 1364-503X (Print) 1364-503X (Linking). doi: 10.1098/rsta.2009.0011. URL https://www.ncbi.nlm.nih.gov/pubmed/19324719.

H. Bilinksky. Riblet Microfabrication Method for Drag Reduction. In *55th AIAA Aerospace Sciences Meeting*, Grapevine, Texas, 2017. doi: https://doi.org/10.2514/6.2017-0047.

E. C. Bingham. An Investigation of the Laws of Plastic Flow. *Bulletin of the Bureau of Standards*, 13:309–353, 1916.

R. B. Bird, W. E. Stewart, and E. N. Lightfoot. *Transport Phenomena*. Revised Second Edition. John Wiley & Sons, Inc., 2006. ISBN 978-0-470-11539-8. URL https://www.academia.edu/37707900/Transport{_}Phenomena{_}Bird{_}Stewart{_}Lightfoot{_}Second{_}Edition{_}pdf.

G. D. Bixler and B. Bhushan. Fluid Drag Reduction with Shark-Skin Riblet Inspired Microstructured Surfaces. *Advanced Functional Materials*, 23(36):4507–4528, sep 2013a. ISSN 1616-301X. doi: https://doi.org/10.1002/adfm.201203683. URL https://doi.org/10.1002/adfm.201203683.

G. D. Bixler and B. Bhushan. Shark skin inspired low-drag microstructured surfaces in closed channel flow. *Journal of Colloid and Interface Science*, 393:384–396, 2013b. ISSN 0021-9797. doi: https://doi.org/10.1016/j.jcis.2012.10.061. URL http://www.sciencedirect.com/science/article/pii/S0021979712012568.

G. D. Bixler and B. Bhushan. Bioinspired micro/nanostructured surfaces for oil drag reduction in closed channel flow. *Soft Matter*, 9(5):1620–1635, 2013c. ISSN 1744-683X. doi: 10.1039/C2SM27070F. URL http://dx.doi.org/10.1039/C2SM27070F.

D. Brkic. Review of explicit approximations to the Colebrook relation for flow friction. *Journal of Petroleum Science and Engineering*, 77(1):34–48, 2011. doi: https://doi.org/10.1016/j.petrol.2011.02.006.

D. Brkic et al. Unified Friction Formulation from Laminar to Fully Rough Turbulent Flow. *Applied Sciences*, 8(11):20136, 2018. doi: https://doi.org/10.3390/app8112036.

W. Brostow. Drag reduction and mechanical degradation in polymer solutions in flow. *Polymer*, 24(5):631–638, 1983. ISSN 0032-3861. doi: https://doi.org/10.1016/0032-3861(83)90119-2.

O. M. M. Burgess N. K. and P. M. Ligrani. Nusselt Number Behavior on Deep Dimpled Surfaces Within a Channel. *Journal of Heat Transfer*, 125(1):11–18, 2003. doi: https://doi.org/10.1115/1.1527904.

J. F. C. Tropea, A.L. Yarin. *Springer Handbook of Experimental Fluid Mechanics*. Springer, Berlin, Heidelberg, 2007. doi: https://doi.org/10.1007/978-3-540-30299-5.

CEPA. Discover interesting facts about the pipeline industry, 2015. URL https://cepa.com/en/resources/infographics/.

M. Chaczykowski. Transient flow in natural gas pipeline – The effect of pipeline thermal model. *Applied Mathematical Modelling*, 34(4):1051–1067, 2010. ISSN 0307-904X. doi: https://doi.org/10.1016/j.apm.2009.07.017. URL http://www.sciencedirect.com/science/article/pii/S0307904X09002133.

Y. P. Charron, P. Sagaut, and Y. Pressure loss reduction in hydrogen pipelines by surface restructuring. *International Journal of Hydrogen Energy*, 34:8964–8973, 2009. ISSN 0360-3199. doi: https://doi.org/10.1016/j.ijhydene.2009.08.035. URL http://www.sciencedirect.com/science/article/pii/S036031990901307X.

K.-S. Choi. Near-wall structure of a turbulent boundary layer with riblets. *Journal of Fluid Mechanics*, 208: 417–458, 1989. ISSN 0022-1120 1469-7645. doi: 10.1017/s0022112089002892.

S. H. Chue. Pressure probes for fluid measurement. *Progress in Aerospace Sciences*, 16:147–223, 1975. doi: https://doi.org/10.1016/0376-0421(75)90014-7.

F. Civan. Review of Methods for Measurement of Natural Gas Specific Gravity, 1989. URL https://doi.org/10.2118/19073-MS.

J. Clint. *Surfactant Aggregation*. Springer, Dordrecht, 1992. doi: ttps://doi.org/10.1007/978-94-011-2272-6.

R. Costantini, J.-P. Mollicone, and F. Battista. Drag reduction induced by superhydrophobic surfaces in turbulent pipe flow. *Physics of Fluids*, 30(2):25102, feb 2018. ISSN 1070-6631. doi: 10.1063/1.5011805. URL https://doi.org/10.1063/1.5011805.

L. Da Vinci. Codex Atlanticus. In B. Ambrosiana, editor, *Codex Atlanticus*. Unknown, Milan, 1509.

A. G. Darbyshire and T. Mullin. Transition to turbulence in constant-mass-flux pipe flow. *Journal of Fluid Mechanics*, 289:83–114, 1995. doi: https://doi.org/10.1017/S0022112095001248.

A. P. Davis and E. E. Michaelides. Geothermal power production from abandoned oil wells. *Energy*, 34 (7):866–872, 2009. ISSN 0360-5442. doi: https://doi.org/10.1016/j.energy.2009.03.017. URL http://www.sciencedirect.com/science/article/pii/S0360544209000607.

B. Dean and B. Bhushan. Shark-skin surfaces for fluid-drag reduction in turbulent flow: a review. *Philosophical Transactions: Mathematical, Physical and Engineering Sciences*, 368(1929):4775–4806, 2010. ISSN 1364503X. doi: 10.2307/25753440. URL http://www.jstor.org/stable/25753440.

R. Dean. *An investigation of shear layer interaction in ducts and diffusers*. PhD thesis, Imperial College London, 1974. URL https://spiral.imperial.ac.uk/bitstream/10044/1/20693/2/Dean-RB-1974-PhD-Thesis.pdf.

R. B. Dean. Reynolds Number Dependence of Skin Friction and Other Bulk Flow Variables in Two-Dimensional Rectangular Duct Flow. *Journal of Fluids Engineering*, 100(2):215–223, jun 1978. ISSN 0098-2202. doi: 10.1115/1.3448633. URL https://doi.org/10.1115/1.3448633.

A. Dinklelacker. Preliminary experiments on the influence of flexible walls on boundary layer turbulence. *Journal of Sound and Virbration*, 4(2):187–204, 1966. doi: https://doi.org/10.1016/0022-460X(66)90121-0.

Enerpac. Types Of Pipeline Every Oil and Gas Engineer Should Know About, 2017. URL https://blog.enerpac.com/types-of-pipeline-every-oil-and-gas-engineer-should-know-about/.

G. Enyutin et al. Drag reduction in riblet-lined pipes. *Fluid Dynamics*, 30(1):45—-48, 1995. URL https://link.springer.com/content/pdf/10.1007/BF02029926.pdf.

R. et al. Martinez-Palou. Transportation of heavy and extra-heavy crude oil by pipeline: A review. *Journal of Petroleum Science and Engineering*, 75(3-4):274–282, 2011. doi: https://doi.org/10.1016/j.petrol.2010.11.020.

A. A. Fontaine, H. L. Petrie, and T. A. Brungart. Velocity profile statistics in a turbulent boundary layer with slot-injected polymer. *Journal of Fluid Mechanics*, 238:435–466, 1992. doi: 10.1017/S0022112092001770.

X. Gao and L. Jiang. Water-repellent legs of water striders. *Nature*, 432(7013):36, 2004. ISSN 1476-4687. doi: 10.1038/432036a. URL https://doi.org/10.1038/432036a.

R. García-Mayoral and J. Jiménez. Drag reduction by riblets. *Philos Trans A Math Phys Eng Sci*, 369 (1940):1412–1427, 2011. ISSN 1364-503X (Print) 1364-503X (Linking). doi: 10.1098/rsta.2010.0359. URL https://www.ncbi.nlm.nih.gov/pubmed/21382822.

J. M. Gerez and A. R. Pick. Heavy Oil Transportation by Pipeline. In *International Pipeline Conference*, volume 2, pages 699–710, 1996. URL https://watermark.silverchair.com.

Y. Gu, W. Zhang, J. Mou, S. Zheng, L. Jiang, Z. Sun, and E. Wang. Research progress of biomimetic superhydrophobic surface characteristics, fabrication, and application. *Advances in Mechanical Engineering*, 9: 168781401774685, dec 2017. doi: 10.1177/1687814017746859.

B. Guo. Chapter 4 - Wellbore performance. In B. B. T. W. P. H. S. E. Guo, editor, *Well Productivity Handbook*, pages 93–122. Gulf Professional Publishing, 2019. ISBN 978-0-12-818264-2. doi: https://doi.org/10.1016/B978-0-12-818264-2.00004-X. URL http://www.sciencedirect.com/science/article/pii/B978012818264200004X.

B. Guo, W. C. Lyons, and A. Ghalambor. 10 - Separation Systems. pages 117–132. Gulf Professional Publishing, Burlington, 2007. ISBN 978-0-7506-8270-1. doi: https://doi.org/10.1016/B978-075068270-1/50015-3. URL http://www.sciencedirect.com/science/article/pii/B9780750682701500153.

N. Hutchins and K.-S. Choi. Accurate measurements of local skin friction coefficient using hot-wire anemometry. *Progress in Aerospace Sciences*, 38(4):421–446, 2002. ISSN 0376-0421. doi: https://doi.org/10.1016/S0376-0421(02)00027-1. URL http://www.sciencedirect.com/science/article/pii/S0376042102000271.

INTECH GmbH. Pipeline Design and Selection. Optimum Pipeline Diameter, 2020. URL https://intech-gmbh.com/pipelines{_}calc{_}and{_}select/{#}optimal{_}flow{_}rate{_}for{_}different{_}pipe{_}systems.

C. Ishiyama and Y. Higo. Effects of humidity on Young's modulus in poly(methyl methacrylate). *Journal of Polymer Science Part B: Polymer Physics*, 40(5):460–465, mar 2002. ISSN 0887-6266. doi: https://doi.org/10.1002/polb.10107. URL https://doi.org/10.1002/polb.10107.

C. Jin and R. Randall. The Estimation of Production and Location of Pumps for a Cutter Suction Dredge using a Long Distance Pipeline. *Journal of Dredging*, 16, apr 2018.

A. V. Johansson and P. H. Alfredsson. On the structure of turbulent channel flow. *Journal of Fluid Mechanics*, 122:295–314, 1982. doi: 10.1017/S0022112082002225.

Y. C. Jung and B. Bhushan. Biomimetic structures for fluid drag reduction in laminar and turbulent flows. *Journal of Physics: Condensed Matter*, 22(3):35104, 2009. ISSN 0953-8984. doi: 10.1088/0953-8984/22/3/035104. URL http://dx.doi.org/10.1088/0953-8984/22/3/035104.

G. I. Kiknadze, Y. K. Krasnov, and Y. V. Chushkin. Investigation of the Enhancement of Heat Transfer due to Self-Organization of Ordered Dynamic Twisted Heat-Carrier Structures on a Heat-Transfer Surface. Report, I. V. Kurchatov Institute of Atomic Energy, 1984.

K. Kim. *Application of Thermo-Fluidic Measurement Techniques*. Elsevier Inc., 2016. ISBN 978-0-12-809731-1. doi: https://doi.org/10.1016/C2015-0-01881-0.

L. Kong, Y. Wang, B. Wu, and Z. Wang. Simulation and Experimental Study on Cuttings-Carrying for Reverse Circulation Horizontal Directional Drilling with Dual Drill Pipes. *Advances in Civil Engineering*, 2019:6262308, 2019. ISSN 1687-8086. doi: 10.1155/2019/6262308. URL https://doi.org/10.1155/2019/6262308.

M. O. Kramer. Boundary-layer stabilization by distributed damping. *Journal of the Aerospace Sciences*, 27(1):69, 1960. ISSN 1936-9999.

V. Kulik. Influence of the Velocity of Turbulent Flow on Its Interaction with a Viscoelastic Coating. *Journal of Engineering Physics and Thermophysics*, 76(6):1266–1270, 2003. doi: https://doi.org/10.1023/B:JOEP.0000012030.25141.10.

V. Kulik, A. Boiko, and I. Lee. Influence of the thickness of monolithic compliant coatings on the skin friction drag. In *MATEC Web of Conferences*, volume 115, page 2024. EDP Sciences, 2017. ISBN 2261-236X.

P. K. Kundu, I. M. Cohen, D. R. Dowling, and G. Tryggvason. *Fluid dynamics*. 2016. ISBN 978-0-12-405935-1.

H. Lienhart, M. Breuer, and C. Köksoy. Drag reduction by dimples? — A complementary experimental/numerical investigation. *International Journal of Heat and Fluid Flow*, 29(3):783–791, 2008. ISSN 0142727X. doi: 10.1016/j.ijheatfluidflow.2008.02.001.

P. M. Ligrani, N. K. Burgess, and S. Y. Won. Nusselt Numbers and Flow Structure on and Above a Shallow Dimpled Surface Within a Channel Including Effects of Inlet Turbulence Intensity Level. *Journal of Turbomachinery*, 127(2):321–330, 2005. ISSN 0889-504X. doi: 10.1115/1.1861913. URL http://dx.doi.org/10.1115/1.1861913.

M. Liravi, H. Pakzad, A. Moosavi, and A. Nouri-Borujerdi. A comprehensive review on recent advances in superhydrophobic surfaces and their applications for drag reduction. *Progress in Organic Coatings*, 140:105537, 2020. ISSN 0300-9440. doi: https://doi.org/10.1016/j.porgcoat.2019.105537. URL http://www.sciencedirect.com/science/article/pii/S0300944019311737.

K. N. Liu, C. Christodoulou, O. Riccius, and D. D. Joseph. Drag reduction in pipes lined with riblets. *AIAA Journal*, 28(10):1697–1698, oct 1990. ISSN 0001-1452. doi: 10.2514/3.10459. URL https://doi.org/10.2514/3.10459.

Y. Liu, H. Gu, Y. Jia, J. Liu, H. Zhang, R. Wang, B. Zhang, H. Zhang, and Q. Zhang. Design and preparation of biomimetic polydimethylsiloxane (PDMS) films with superhydrophobic, self-healing and drag reduction properties via replication of shark skin and SI-ATRP. *Chemical Engineering Journal*, 356:318–328, 2019. ISSN 1385-8947. doi: https://doi.org/10.1016/j.cej.2018.09.022. URL http://www.sciencedirect.com/science/article/pii/S1385894718317303.

C. G. Lomas. *Fundamentals of Hotwire Anemometry*. Cambridge University Press, New York, 1986. ISBN 978-0-521-30340. URL https://books.google.nl/books?hl=nl{&}lr={&}id=g17qbt1YEXAC{&}oi=fnd{&}pg=PR7{&}dq=lomas+1986+hotwire+oil+hair+thin{&}ots=NGe1Lm6Nub{&}sig=T-V8WMhdBClqGOpXwTmGzXbzVG4{&}redir{_}esc=y{#}v=onepage{&}q{&}f=false.

P. Luong. Pipeline: The Worst Transportation Method of Oil, Except for All the Rest. 2019.

G. I. Mahmood and P. M. Ligrani. Heat transfer in a dimpled channel: Combined influences of aspect ratio, temperature ratio, Reynolds number, and flow structure. *International Journal of Heat and Mass Transfer*, 45(10):2011–2020, 2002. URL http://www.scopus.com/inward/record.url?eid=2-s2.0-0037128920{&}partnerID=40{&}md5=786662e06129ba30601be4ddf91d6f58.

G. I. Mahmood, M. L. Hill, D. L. Nelson, P. M. Ligrani, H. K. Moon, and B. Glezer. Local Heat Transfer and Flow Structure on and Above a Dimpled Surface in a Channel. *Journal of Turbomachinery*, 123(1):115, 2001. ISSN 0889504X. doi: 10.1115/1.1333694.

N. Makwashi et al. Investigation of the Severity of Wax Deposition in Bend Pipes Under Subcooled Pipelines Conditions. In *Society of Petroleum Engineers*. Society of Petroleum Engineers, 2019. doi: https://doi.org/10.2118/195559-MS.

B. J. McKeon and A. J. Smits. Static pressure correction in high Reynolds number fully developed turbulent pipe flow. *Measurement Science and Technology*, 13(10):1608–1614, 2002. ISSN 0957-0233. doi: 10.1088/0957-0233/13/10/314. URL http://dx.doi.org/10.1088/0957-0233/13/10/314.

H. Mitsudharmadi, C. M. J. Tay, and H. M. Tsai. Effect of rounded edged dimple arrays on the boundary layer development. *Journal of Visualization*, 12(1):17–25, 2009. URL http://www.scopus.com/inward/record.url?eid=2-s2.0-60449119081{&}partnerID=40{&}md5=f837b674d753474aa8c7bf5765e9fd21.

S. Mohsenabadi. Comparison of Explicit Relations of Darcy Friction Measurement with Colebrook-White Equation. *Applied mathematics in Engineering, Management and Technology*, 2(4):570–578, 2014. URL https://d1wqtxts1xzle7.cloudfront.net/62063906/7120200211-129617-1cbkqii.pdf?1581424395={&}response-content-disposition=inline{%}3B+filename{%}3DComparison{_}of{_}Explicit{_}Relations{_}of{_}Darc.pdf{&}Expires=1605971379{&}Signature=Q95KMlSv1TnrlHpLNxaw6HxNvWXwtiltgYwL93vyqd.

H. K. Moon, T. O'Connell, and B. Glezer. Channel height effect on heat transfer and friction in a dimpled passage. *Journal of Engineering for Gas Turbines and Power-Transactions of the Asme*, 122(2):307–313, 2000. ISSN 0742-4795. doi: Doi10.1115/1.483208. URL {%}3CGoto.

K. J. Moser R.D. and N. N. Mansour. Direct numerical simulation of turbulent channel flow up to Reτ=590. *Physics of Fluids*, 11, 1999. doi: https://doi.org/10.1063/1.869966.

V. Mosharov, A. Orlov, and V. Radchenko. New Approach to Surface Oil-Flow Visualization. In *Instrumentation in Aerospace Simulation Facilities, 2005. iciasf '05. 21st International Congress on*, pages 176–180, 2005. doi: 10.1109/ICIASF.2005.1569920.

K. Mysels. Flow of Thickened Fluids, 1949.

J. H. Ng, R. K. Jaiman, T. T. Lim, C. M. Tay, and B. C. Khoo. Geometric Effects of Shallow Dimples in Turbulent Channel Flows at Re = 180 : A Vorticity Transport Perspective. *Flow, Turbulence and Combustion*, 2020. ISSN 1573-1987. doi: https://doi.org/10.1007/s10494-020-00112-6.

P. Nitschke. Experimental investigation of turbulent flow in smooth and longitudinal grooved tubes. *Materials Science, Physics*, 1983. URL https://www.semanticscholar.org/paper/Experimental-investigation-of-turbulent-flow-in-and-Nitschke/f550e3fa0cb1ce0cca258a5e1508e38050212e8f.

Offshore Technology. North America has the highest oil and gas pipeline length globally, 2020. URL https://www.offshore-technology.com/comment/north-america-has-the-highest-oil-and-gas-pipeline-length-globally/{#}:{~}:text=Thetotallengthofthe,accordingtoGlobalData'slatestreport.

D. Ohlendorf, W. Interthal, and H. Hoffmann. Surfactant systems for drag reduction: Physico-chemical properties and rheological behaviour. *Rheologica Acta*, 25(5):468–486, 1986. ISSN 1435-1528. doi: 10.1007/BF01774397. URL https://doi.org/10.1007/BF01774397.

S. Papavinasam. *Corrosion Control in the Oil and Gas Industry*, book section 1,2, pages 41–131. Gulf Professional Publishing, Boston, 2014. ISBN 9780123970220. doi: https://doi.org/10.1016/B978-0-12-397022-0.00002-9.

R. W. Paterson and F. H. Abernathy. Turbulent flow drag reduction and degradation with dilute polymer solutions. *Journal of Fluid Mechanics*, 43(4):689–710, 1970. doi: https://doi.org/10.1017/S0022112070002677.

E. Pawlowski. Thermal heat-balance mode flow-to-frequency converter. In *International Conference on Optical and Electronic Sensors*, 2016. doi: https://doi.org/10.1117/12.2243598.

H. L. Petrie et al. Polymer drag reduction with surface roughness in flat-plate turbulent boundary layer flow. *Experiments in Fluids*, 35:8–23, 2003. doi: https://doi.org/10.1007/s00348-003-0589-x.

PHMSA. U.S. Department of Transportation, 2020. URL https://www.phmsa.dot.gov/data-and-statistics/phmsa-data-and-statistics.

PST. Pipeline Basics \& Specifics About Natural Gas Pipelines, 2015. URL http://pstrust.org/wp-content/uploads/2015/09/2015-PST-Briefing-Paper-02-NatGasBasics.pdf.

P. K. Ptasinski, F. T. M. Nieuwstadt, B. van den Brule, and M. A. Hulsen. Experiments in Turbulent Pipe Flow with Polymer Additives at Maximum Drag Reduction. *Flow, Turbulence and Combustion*, 66(2):159–182, 2001. ISSN 1573-1987. doi: 10.1023/A:1017985826227. URL https://doi.org/10.1023/A:1017985826227.

L. W. Reidy and G. W. Anderson. Drag Reduction for External and Internal Boundary Layers Using Riblets and Polymers. In *26th Aerospace Sciences Reidy, L. W. and Anderson, G. W. (1988). Drag Reduction for External and Internal Boundary Layers Using Riblets and Polymers. 26th Aerospace Sciences Meeting, 138. https://arc.aiaa.org/doi/pdf/10.2514/6.1988-138Meeting*, page 138, Reno, Nevada, 1988. URL https://arc.aiaa.org/doi/pdf/10.2514/6.1988-138.

W. Renpu. Chapter 2 - Well Completion Mode Selection. In W. B. T. A. W. C. E. T. E. Renpu, editor, *Advanced Well Completion Engineering*, pages 75–116. Gulf Professional Publishing, 2011. ISBN 978-0-12-385868-9. doi: https://doi.org/10.1016/B978-0-12-385868-9.00002-6. URL http://www.sciencedirect.com/science/article/pii/B9780123858689000026.

S. Ristic. Flow Visualisation Techniques in Wind Tunnels Part I – Non optical Methods. *Scientific Technical Review LVII N.*, 17, 2007. URL https://www.researchgate.net/publication/267296233{_}Flow{_}Visualisation{_}Techniques{_}in{_}Wind{_}Tunnels{_}Part{_}I{_}-{_}Non{_}optical{_}Methods.

J. P. Robert. Drag Reduction: An Industrial Challenge. Report, AGARD, 1992.

O. R. Rodríguez-López, E., Bruce, P. J., & Buxton. A robust post-processing method to determine skin friction in turbulent boundary layers from the velocity profile. *Experiments in Fluids*, 56(4):68, 2015. doi: 10.1007/s00348-015-1935-5.

J. Rohr et al. A comparison of the drag-reducing benefits of riblets in internal and external flows. *Experiments in fluids*, 13(6):361—-368, 1992. URL https://link.springer.com/content/pdf/10.1007/BF00223243.pdf.

H. H. Schloemer. Effects of Pressure Gradients on Turbulent-Boundary-Layer Wall-Pressure Fluctuations. *The Journal of the Acoustical Society of America*, 42(1):93–113, 1967. doi: doi:http://dx.doi.org/10.1121/1.1910581. URL http://scitation.aip.org/content/asa/journal/jasa/42/1/10.1121/1.1910581.

G. S. Settles. No TitleThe state of the art of conventional flow visualization techniques for wind tunnel testing, 1982. URL https://ntrs.nasa.gov/citations/19820024789.

E. Shashi Menon. Chapter Five - Fluid Flow in Pipes. In E. B. T. T. P. C. Shashi Menon and S. Manual, editors, *Transmission Pipeline Calculations and Simulations Manual*, pages 149–234. Gulf Professional Publishing, Boston, 2015. ISBN 978-1-85617-830-3. doi: https://doi.org/10.1016/B978-1-85617-830-3.00005-5. URL http://www.sciencedirect.com/science/article/pii/B9781856178303000055.

R. Shaw. The influence of hole dimensions on static pressure measurements. *Journal of Fluid Mechanics*, 7(4): 550–564, 1960. doi: https://doi.org/10.1017/S0022112060000281.

A. Shenoy. *Drag Reducing Agents: A Historical Perspective*, pages 1–38. Springer International Publishing, Cham, 2020. ISBN 978-3-030-40045-3. doi: 10.1007/978-3-030-40045-3_1. URL https://doi.org/10.1007/978-3-030-40045-3{_}1.

A. V. Shenoy. A review on drag reduction with special reference to micellar systems. *Colloid and Polymer Science*, 262(4):319–337, 1984. ISSN 1435-1536. doi: 10.1007/BF01410471. URL https://doi.org/10.1007/BF01410471.

P. R. Spalart, M. Shur, M. Strelets, A. Travin, K. B. Paschal, and S. P. Wilkinson. Experimental and numerical study of the turbulent boundary layer over shallow dimples. *International Journal of Heat and Fluid Flow*, 78:108438, 2019. ISSN 0142-727X. doi: https://doi.org/10.1016/j.ijheatfluidflow.2019.108438. URL http://www.sciencedirect.com/science/article/pii/S0142727X19302176.

V. . Stornelli et al. The assessment of wind conditions by means of hot wire sensors anda modifed Wheatstone bridge architecture. *Sensors and Actuators A: Physical*, 262:130–139, 2017. doi: https://doi.org/10.1016/j.sna.2017.05.005.

C. M. Tay. Determining the Effect of Dimples on Drag in a Turbulent Channel Flow. In *49th AIAA Aerospace Sciences Meeting*. AIAA, 2011. doi: 10.2514/6.2011-682.

C. M. Tay and T. T. Lim. Drag reduction with non-axisymmetric dimples. In *35th AIAA Applied Aerodynamics Conference, 2017*, 2017. doi: 10.2514/6.2017-3569. URL https://www.scopus.com/inward/record.uri?eid=2-s2.0-85067317370{&}doi=10.2514{%}2F6.2017-3569{&}partnerID=40{&}md5=763fc264cc2843dda63f4f09976ebe0d.

C. M. Tay, Y. T. Chew, B. C. Khoo, and J. B. Zhao. Development of flow structures over dimples. *Experimental Thermal and Fluid Science*, 52:278–287, 2014. ISSN 08941777. doi: 10.1016/j.expthermflusci.2013.10.001.

C. M. J. Tay, B. C. Khoo, and Y. T. Chew. Mechanics of drag reduction by shallow dimples in channel flow. *Physics of Fluids (1994-present)*, 27(3):35109, 2015. ISSN 1070-6631.

C. M. J. Tay, T. T. Lim, B. C. Khoo, and R. K. Jaiman. Effectiveness of triangular depressions and asymmetric circular dimples for drag reduction. In *Proceedings of the 20th Australasian Fluid Mechanics Conference, AFMC 2016*, 2016. URL https://www.scopus.com/inward/record.uri?eid=2-s2.0-85084013356{&}partnerID=40{&}md5=ff74be1b1c7e7eacd62c9c56866630d7.

J. Tay and T. T. Lim. Drag reduction with teardrop-shaped dimples. In *2018 Flow Control Conference*, page 3528, 2018.

J. Tay, T. T. Lim, and B. C. Khoo. Drag Reduction with Diamond-shaped Dimples. In *AIAA Aviation 2019 Forum*, page 3296, 2019.

D. G. Thomas. Transport characteristics of suspension: VIII. A note on the viscosity of Newtonian suspensions of uniform spherical particles. *Journal of Colloid Science*, 20(3):267–277, 1965. ISSN 0095-8522. doi: https://doi.org/10.1016/0095-8522(65)90016-4. URL http://www.sciencedirect.com/science/article/pii/0095852265900164.

B. A. Toms. Some observations on the flow of linear polymer solutions through straight tubes at large Reynolds numbers. *First International Congress on Rheology*, 2:135–141, 1948.

TUD OCW. Dredge Pumps and Slurry Transport, 2016. URL https://ocw.tudelft.nl/course-readings/pump-and-pipeline-characteristics/?course{_}id=7862.

U.S. Energy Information Administration. International Energy Outlook 2019. Technical report, EIA, 2019.

USDA Forest Service. Mechanical Properties of Wood-Based Composite Materials. In R. Ross, editor, *Wood Handbook - Wood as an Engineering Material*, pages 12–1 – 12–12. General Technical Report (GTR), 2010.

O. Van Campenhout et al. An experimental investigation into the flow mechanics of dimpled surfaces in turbulent boundary layers. In *Kissimmee, Florida*, 2018. doi: https://doi.org/10.2514/6.2018-2062.

M. Van Eeten. *Radio-frequency slurry-density measurement for dredging pipelines*. PhD thesis, Technical University Eindhoven, 2011.

M. Van Nesselrooij et al. Drag reduction by means of dimpled surfaces in turbulent boundary layers. *Experiments in Fluids*, 57(142), 2016. doi: https://doi.org/10.1007/s00348-016-2230-9.

L. L. M. Veldhuis and E. Vervoort. *Drag Effect of a Dented Surface in a Turbulent Flow*, pages 1–12. Fluid Dynamics and Co-located Conferences. American Institute of Aeronautics and Astronautics, 2009. doi: doi: 10.2514/6.2009-395010.2514/6.2009-3950. URL http://dx.doi.org/10.2514/6.2009-3950.

N. Vida. Three dimensional surface structure for reduced friction resistance and improved heat exchange, 2004. URL https://patents.google.com/patent/WO2004083651A1/en.

P. Virk, E. Merrill, H. Mickley, K. Smith, and E. Mollo-Christensen. The Toms phenomenon: Turbulent pipe flow of dilute polymer solutions. *Journal of Fluid Mechanics*, 30(2):305–328, 1967. doi: 10.1017/S0022112067001442.

P. S. Virk. Drag reduction in rough pipes. *Journal of Fluid Mechanics*, 45(2):225–246, 1971. doi: 10.1017/S0022112071000028.

P. S. Virk. Drag reduction fundamentals. *AIChE Journal*, 21(4):625–656, 1975. ISSN 0001-1541. doi: 10.1002/aic.690210402. URL https://aiche.onlinelibrary.wiley.com/doi/abs/10.1002/aic.690210402.

M. Walsh. Turbulent boundary layer drag reduction using riblets. In *20th Aerospace Sciences Meeting*, 1982. doi: 10.2514/6.1982-169.

M. Walsh and A. Lindemann. Optimization and application of riblets for turbulent drag reduction. In *22nd Aerospace Sciences Meeting*, 1984. doi: 10.2514/6.1984-347.

M. Walsh, W. Sellers, and C. McGinley. Riblet drag reduction at flight conditions. In *6th Applied Aerodynamics Conference*, 1988. doi: 10.2514/6.1988-2554.

M. J. Walsh. Riblets for Aircraft Skin-friction Reduction. Report, NASA Langley Research Center, 1986.

C. M. White and M. G. Mungal. Mechanics and Prediction of Turbulent Drag Reduction with Polymer Additives. *Annual Review of Fluid Mechanics*, 40(1):235–256, jan 2008. ISSN 0066-4189. doi: 10.1146/annurev.fluid.40.111406.102156. URL https://doi.org/10.1146/annurev.fluid.40.111406.102156.

F. M. White. *Viscous fluid flow*, volume 3. McGraw-Hill New York, 2006.

M. Widden. *Fluid Mechanics*. Foundations of engineering. Macmillan, 1996. ISBN 9780333517994.

S. P. Wilkinson, J. B. Anders, B. S. Lazos, and D. M. Bushnell. Turbulent drag reduction research at NASA Langley: progress and plans. *International journal of heat and fluid flow*, 9(3):266–277, 1988. ISSN 0142-727X.

W. J. Yang. *Handbook of Flow Visualization*. Tayler & Francis, 2 edition, 2001. ISBN 1-56032-417-1. URL https://books.google.nl/books?id=pMuCDwAAQBAJ{&}pg=PA136{&}dq=tufts+fluorescent{&}hl=nl{&}sa=X{&}ved=2ahUKEwiBlbfIkubrAhWB{_}KQKHShBBE4Q6AEwAHoECAYQAg{#}v=onepage{&}q=tuftsfluorescent{&}f=false.

D. Yee. Drag reduction surface depressions, 1992.

G. Yunqing et al. Analysis of Drag Reduction Methods and Mechanisms of Turbulent. *Applied Bionics and Biomechanics*, 2017, 2017. doi: https://doi.org/10.1155/2017/6858720.

E.-S. Zanoun, F. Durst, and H. Nagib. Evaluating the law of the wall in two-dimensional fully developed turbulent channel flows. *Physics of Fluids*, 15(10):3079–3089, sep 2003. ISSN 1070-6631. doi: 10.1063/1.1608010. URL https://aip.scitation.org/doi/abs/10.1063/1.1608010.

L. H. Zhao, H. I. Andersson, and J. J. J. Gillissen. Turbulence modulation and drag reduction by spherical particles. *Physics of Fluids*, 22(8):81702, aug 2010. ISSN 1070-6631. doi: 10.1063/1.3478308. URL https://doi.org/10.1063/1.3478308.

Appendix A

Other passive DRT

Compliant coatings

Bio-mimetics, i.e., applying characteristic structures and designs of animal species or plants on human-made systems, is a popular method to search for drag reduction (Dean and Bhushan, 2010). Besides riblets, another first example is DR through compliant coatings, which is analogous to dolphins' skin. First actual tests were done by Kramer (1960) who towed a slender shaped body behind a motorboat. Due to the fact that the surface is flexible, the coating can react to forces normal to the wall. The more the surface oscillation interacts with the turbulent forces, the more the viscous drag reduces (Kulik; 2003, 2017).

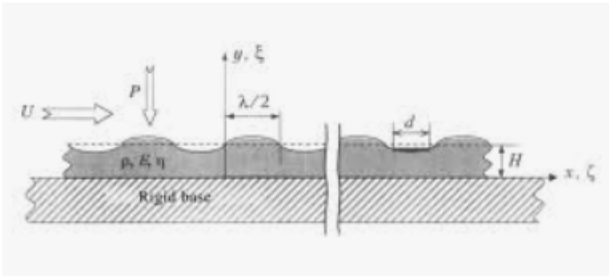

Figure A.1: Deformation of a compliant coating (Kulik, 2003).

An important detail is that throughout research of compliant coatings done by Kramer, the goal has mainly been to delay the transition point from laminar to turbulent flow (Abdulbari et al., 2013). Nevertheless, compliant coatings were able to reduce skin friction drag for both laminar as well as turbulent flow. As a response to Kramer's research, Dinklelacker (1966) did experiments with vertical water pipe flow. He measured a DR, but his results do not seem very convincing. One of his conclusions is that the question of whether compliant coatings can reduce drag 'remains entirely open'.

Another disadvantage is that compliant coatings are sensitive to pressure gradients and have different responses under varying flow conditions (Abdulbari et al., 2013). Taking into account that pipelines can operate under an extensive range of pressures (see Table 2.1), compliant coatings do not seem the most optimal solution at this point in time to reduce the viscous drag of pipe flows.

Super-hydrophobic surfaces

A recent overview of the latest progress concerning superhydrophobic surfaces is given by Liravi et al. (2020). The most important property of a superhydrophobic surface is the angle of contact (CA). When this angle surpasses 150°, the surface can be classified as superhydrophobic. The antonym for a superhydrophobic is superhydrophyllic. The water is appealed to the surface instead of being repelled by it; both types of surface are depicted in Figure A.2a. The effect of the super-hydrophobic surfaces does not function though without micro- or even nanostructures on the surface. The amount of superhydrophic surfaces in nature are present in large numbers. A classic example that has been thoroughly researched is the lotus leaf which is able to cleanse

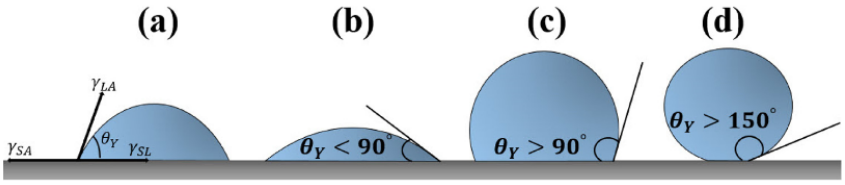

(a) (a) Schematic of contact angle for a water droplet on a smooth surface, (b) hydrophyllic, (c) hydrophobic, (d) super-hydrophobic surfaces (Liravi et al., 2020).

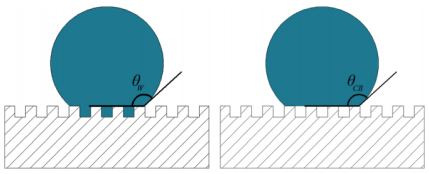

(b) Wenzel model (left) and Cassie-Baxter model (right) (Gu et al., 2017).

Figure A.2: Different CA's of super-hydrophobic surfaces

Figure A.3: Hydrophobic legs of a Water Strider (Liravi et al., 2020)

itself due to its microstructures (Liu et al., 2019). Another example is the water strider which is depicted in Figure A.3. This fascinating insect has tiny hairs on its legs that are seperated in the order of nanometers. Due to this property the legs do not pierce the water surface until a dimple of >4.4 mm has been formed. Moreover, one leg is capable of carrying 15 times the body weight of the water strider (Gao and Jiang, 2004). There are two theories of water droplets resting on these microstructures. The first model is postulated by Wenzel. He proposed a droplet that is completely in contact with a rough surface. The Cassie-Baxter model, on the other hand, proposes that the water droplet is only in contact with the peaks of the rough surface, see Figure A.2b. As a consequence, small pockets of air can form below the water droplet. The angle of the droplet with the surface for both theories can be determined by the following two formulas:

$$\cos\theta_W = R_f \cos\theta_Y \quad \text{(Wenzel)} \tag{A.1}$$

$$\cos\theta_{CB} = f_1 (\cos\theta_1 + 1) - 1 \quad \text{(Cassie-Baxter)} \tag{A.2}$$

where θ_W is the angle of the droplet with the surface for Wenzel's theory, R_f the roughening factor, θ_Y the CA of a smooth surface, θ_{CB} the CA of Cassie-Baxter, and f_1 the fraction of the solid surface that is in contact with the droplet. By applying the second equation, a higher CA can be reached theoretically.

Costantini et al. (2018) did a DNS study to applying a superhydrophobic surface on the inside of pipelines, which resulted in a total drag reduction. In a sense, superhydrophobic surfaces are related to riblets as the structures are similar. However, riblets can also be used for aerodynamical purposes, while superhydrophobic surfaces require a liquid for the air pockets to be seized. Liu et al. (2019) did research on hydrophobic surfaces in comparison with riblets and found a DR of 21.7% while the sharkskin surface only was able to push the DR to 5.4%. It offers excellent opportunities for the marine industry. Liravi et al. (2020) mentions the potential of superhydrophobic surfaces on vessels and submarines as well as within pipelines.

Variations on superhydrophobic surfaces are superaerophobic (air repelling) and superoleophobic (oil repelling) surfaces. Although this technology has a large potential, it has not been applied yet in large industries. Similar to riblets, superhydrophobic surfaces also involve high production costs. On top of that, instabilities of the air pockets, which are crucial for the technology to work, form a significant challenge.

Appendix B

Power of vacuum pumps

Leybold SV750 B vacuum pumps are used for the measurements. The operation of building a wind tunnel is a complex and expensive operation. Prior to starting this procedure, a brief calculation was done to determine the pressure loss generated in the channel and the maximum centerline velocity that could be reached. For this calculation, an extended version of the Darcy Weisbach equation is applied:

$$\Delta P = f_D \cdot \rho \cdot \left(\frac{L_{ch}}{D_{h,ch}} \cdot \frac{1}{2} \left(\frac{Q}{A_{ch} * 3600} \right)^2 + \frac{L_{vt}}{D_{h,vt}} \cdot \frac{1}{2} \left(\frac{Q}{A_{vt} * 3600} \right)^2 \right) \tag{B.1}$$

where the subscript 'ch' refers to channel and 'vt' to vacuum tube. Flow rate Q is given in m^3/hr. A regressive calculation with the results from Tay et al. (2015) is performed to obtain the Darcy friction factor f_D. An iterative computation is used to find the pressure loss. The maximum capacity of the vacuum pumps is used to find the theoretical maximum velocity, followed by the pressure loss. The new capacity of the vacuum pump, including the pressure loss, is then used to set a new maximum velocity. The iteration process ended after iteration 'n+1' did not deviate more than 0.1% from iteration 'n'. It can be concluded that the vacuum pumps

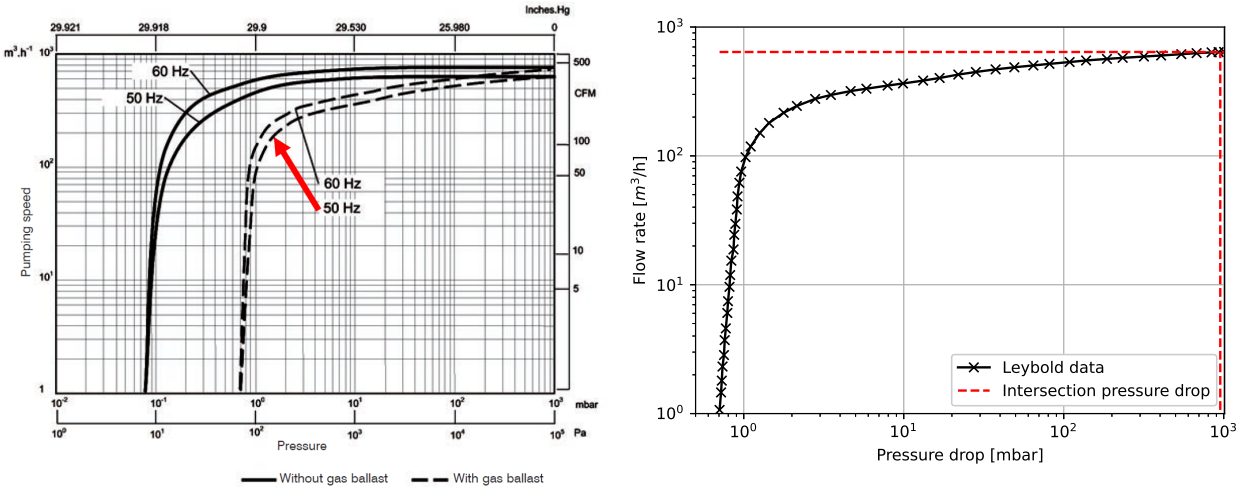

(a) Pumping speeds SV750 B.

(b) Pressure loss for SV750 B.

Figure B.1: Leybold max pumping speed and pressure loss.

when used in series should be able to reach theoretical velocities of up to 51.1 m/s in spite of the larges friction forces present. This results in a maximum $Re \approx 3.47 \cdot 10^4$. The theoretical pressure loss with respect to atmospheric pressure is approximately 4.89 kPa. The calculation regarding the capacity of the vacuum pumps turned out to be rather accurate. However, the underpressure was underestimated and it was not realized that this could have a significant impact on bending of the tunnel walls. This is addressed further in Appendix C.

Appendix C

Bending of channel walls

The deformation of the tunnel walls was underestimated in the design. In the photograph in Figure C.1a, the NACA0012 airfoil was not placed yet. Figure C.1b depicts the bending when the thick plates and the NACA0012 airfoil were installed, see Figures 5.15b and 5.15c. The steel O-profiles were not yet glued to the walls of the channel. At its peak, the measuring clock identified a negative bending of more than 5 mm. This is over 25% of the initial channel height.

(a) Bending of wall at $x/h = 400$ without reinforcements.

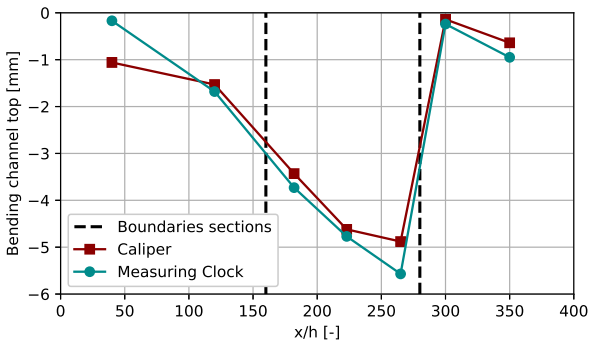

(b) Bending of tunnel measured with different tools.

Figure C.1: Consequence of large underpressures. In the graph, the bending of section C was already resolved by thick plates and the NACA0012 airfoil.

Strain calculation. Estimation of strain on beforehand would have saved much time. Nevertheless, it is still relevant to see the expected deformation based on measured underpressures. This can be done by assuming a uniformly loaded beam according to Equation C.1:

$$u_d = \frac{5qw^4}{384E_Y I} \quad \text{with} \quad I = \frac{1}{12}lh^3 \tag{C.1}$$

where u_d denotes the deflection of a channel wall, q is the load which can be obtained by using the underpressure, w is the width of the channel, l the length, and h the thickness. The parameters E_Y and I are Young's modulus and the area moment of inertia. The maximum underpressure at the end of the 8 m long test channel is -6.2 kPa. Dividing the underpressure by an area results in a load q. Ishiyama and Higo (2002) tested how Young's modulus of PMMA changed with humidity. He found values between approximately 2.8 and 3.8 GPa. For plywood that was used (laminated veneer lumber), the elasticity modulus is in the order of 9-19 GPa (USDA Forest Service, 2010). Subsequently, the estimated deflection of the 12 mm PMMA plates and 12 mm plywood plates is between 1.51-2.08 mm and 0.30-0.64 mm, respectively. Bear in mind that this is for the maximum underpressure at the end of the wind tunnel. Experiments pointed out that the deflection of the wall was up to 5 mm. Likely, the Young's modulus was overestimated for the calculation above, which would result in less strain.

Appendix D

Routines pressure measurements

The first sequence was followed during the pump-off time. Considering a 'sandwich'-technique where test plates had to be swapped repeatedly, no anomalies were desired. Forgetting to tighten one knob or leaving one clamp unfastened could significantly affect the results, which would mean the measurement had to be done a second time. In this sequence, flat plates are swapped for dimpled plates. The valve must always be open when the pumps are turned on as the underpressure is generated instantly. Subsequently, the valve can be closed in steps to increase the underpressure gradually. Furthermore, it was regularly checked if the tapes that were applied were still smooth or if they need to be replaced.

Table D.1: Sequence followed for swapping plates during pump-off time.

Step	Description
1	Remove pieces of tape used to seal the removable transparent ceiling walls of section B.
2	Loosen the clamps that are used to connect sections A and C to section B.
3	Loosen the knobs on the top that hold the transparent ceiling walls in place.
4	Remove plate B3.
5	Remove plate B1 and B2 simultaneously.
6	Remove tapes used to cover up any steps in transitions on the inside of the tunnel.
7	Loosen knobs at the bottom side of the tunnel.
8	Remove one of the tapes that cover holes in the foundation plate.
9	Push out the test plates.
10	Replace flat plates with dimpled plates.
11	Remove the ring and one nut from the threaded end glued to the knobs on the bottom side of the tunnel. Place ring back on the threaded end.
12	Fasten the dimpled plates from below with the knobs.
13	Put the tape back to cover a large hole in the foundation plate.
14	Put tapes on the inner side of the wall back.
15	Place ceiling walls B1 and B2 simultaneously, followed by B3.
16	Fasten all knobs on the top side of the tunnel.
17	Connect all sections using the clamps.
18	Put tape on the outer side of the tunnel at the transitions between plates.

The second sequence used during the pump-on time. While the pump was running, the valve that regulates the velocity in the tunnel had to be adjusted ten times for the majority of the measurements. The vacuum pumps normally run with certain backpressure. As was described in subsection 4.3.1, in this setup, the atmospheric pressure acts as the backpressure for the pumps. Consequently, the pumps might get overheated if they are turned on for a long time or if consecutive measurements are performed without sufficient downtime to allow the oil in the pumps to cool off. Before every measurement, the temperature was checked by feeling the temperature of the pumps.

Table D.2: Sequence followed during pump-on time.

Step	Description	Time [s]
1	Set valve open.	
2	Check if all knobs are tightened.	
3	Write down the temperature.	
4	Write down pressure.	
5	Zero the pressure scanners.	
6	Make sure settings in Labview are correct.	
7	Walk to pump (check the temperature by feeling pumps) and turn it on.	
8	Walk back to the desktop.	15
9	Start the first measurement and walk to the valve.	30
10	Rotate the necessary amount of degrees and walk back to the desktop.	15
11	Repeat steps 9 and 10 nine more times.	390
11	Walk to pumps and turn off.	15
12	Walk back to PC and check if all data is acquired correctly.	
	Total wind tunnel operating time	7m45s

Appendix E

All pressure results

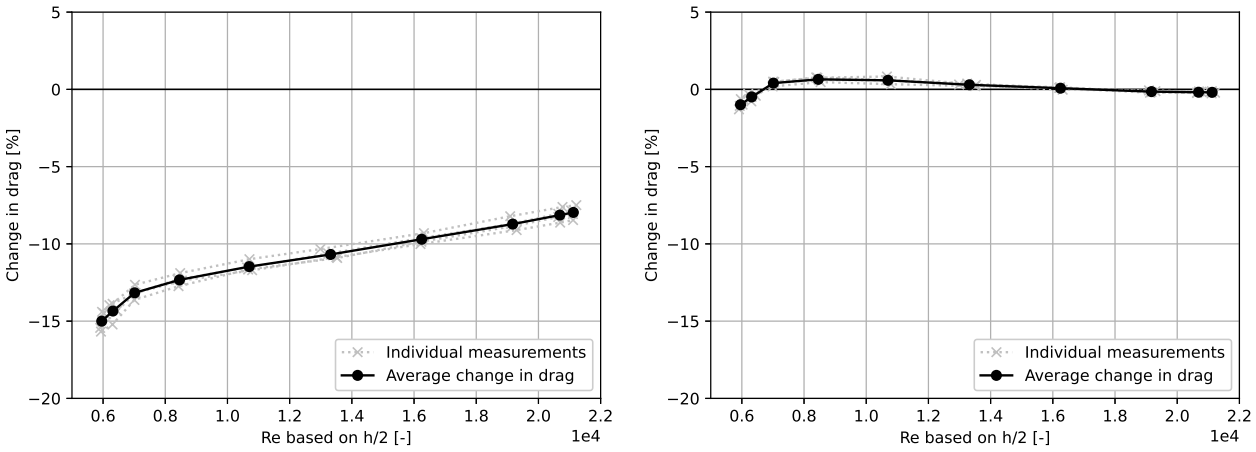

(a) Reynolds number versus change in drag. **(b)** Reynolds number versus change in drag with subtracted fit.

Figure E.1: Flat plate data for 1 pump.

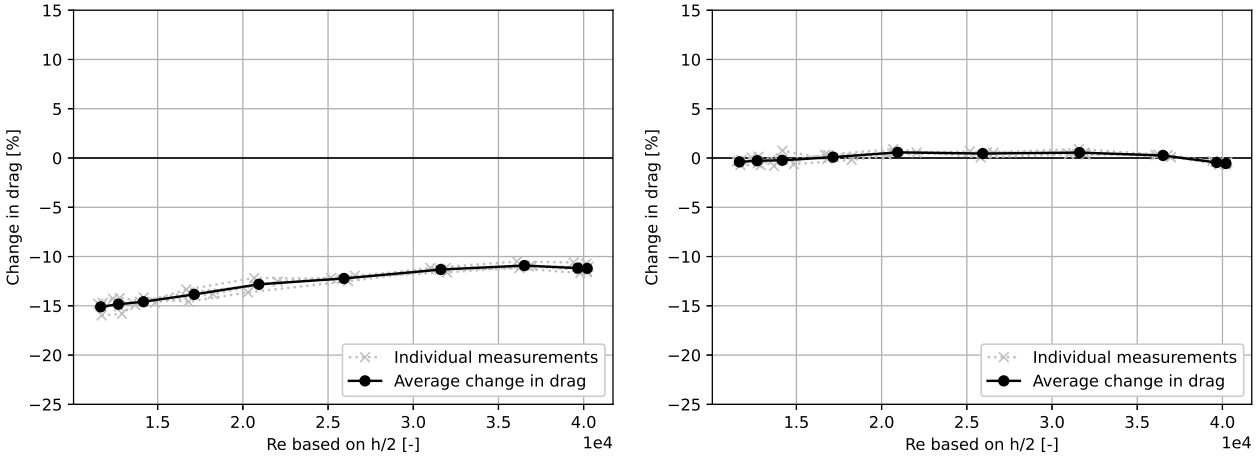

(a) Reynolds number versus change in drag. **(b)** Reynolds number versus change in drag with subtracted fit.

Figure E.2: Flat plate data for 2 pumps.

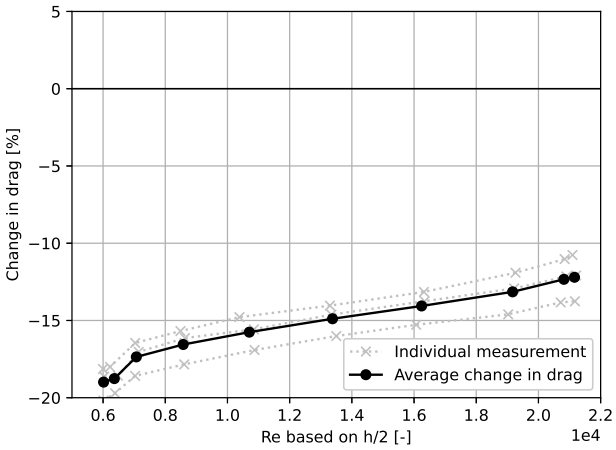

(a) Reynolds number versus change in drag.

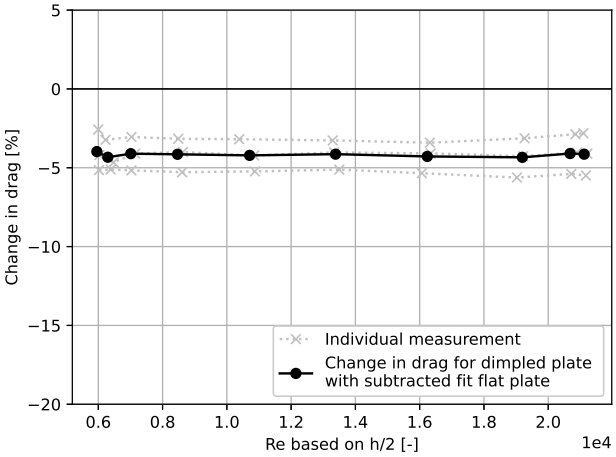

(b) Reynolds number versus change in drag with subtracted fit.

Figure E.3: Dimpled plate data for 1 pump.

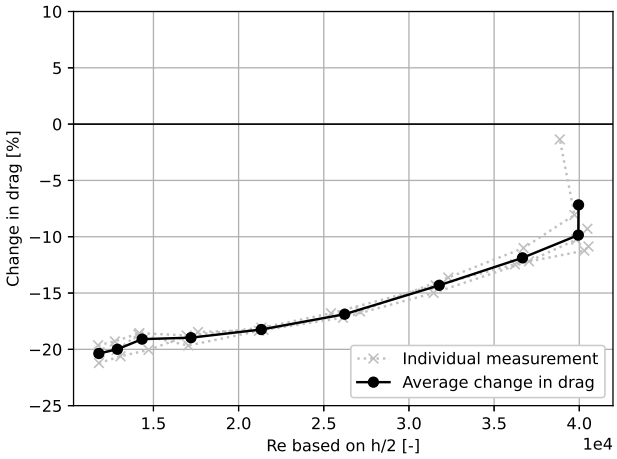

(a) Reynolds number versus change in drag.

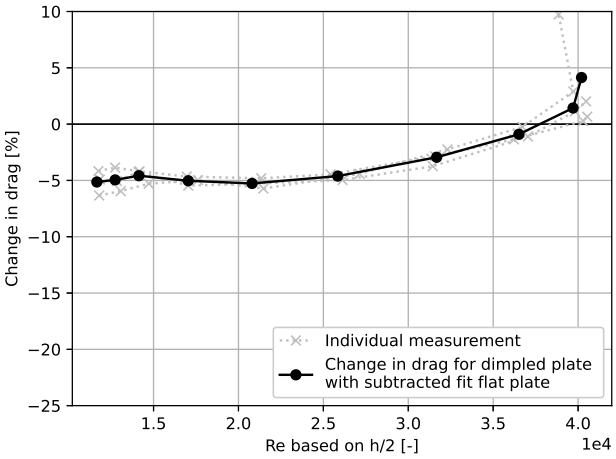

(b) Reynolds number versus change in drag with subtracted fit.

Figure E.4: Dimpled plate data for 2 pumps.

The flat plate data is an average of the four measurements performed in the sandwich sequence. The individual measurements are illustrated as well. The dimpled plate data is an average of three intermediary measurements acquired in the same sandwich sequence. Subfigure a) in Figures E.1-E.4 represents the raw change in drag. Subfigure b) for the same figures represent the raw data with a subtraction of a linear fit of the raw flat plate data. The precision of the measurements is rather good. The accuracy, on the other hand, is significantly off. For flat plate data, a 0% change in drag is expected. However, a drag reduction between 8-15% is observed. Figure E.4 has a data point that is not in line with the expectation. This most likely is caused by an error in the pressure scanner. This is discussed in subsection 5.4.1. Furthermore, the clean change in drag of the wind tunnel decreases with increasing Reynolds number. The dimpled plate data returns a constant change in drag up to a $Re \approx 21,000$. After that, it starts deviating.

In Figure E.5, the errors of the pressure scanners are depicted. There were done three measurements of 30 seconds each. The circles illustrate three standard deviations of each measurement. The squares depicts the average of these three measurements for each pressure tap. Subsequently, the average of all pressure taps is computed, which is marked by the red horizontal line. Figures E.6a and E.6b depict the spanwise pressure measured just upstream of test section and right after the test section for one pump and for two pumps. The top figures represent the pressure drop upstream of the test section ($x/h = 147.5$) while the bottom figures illustrate the pressure drop after the test section ($x/h = 297.5$).

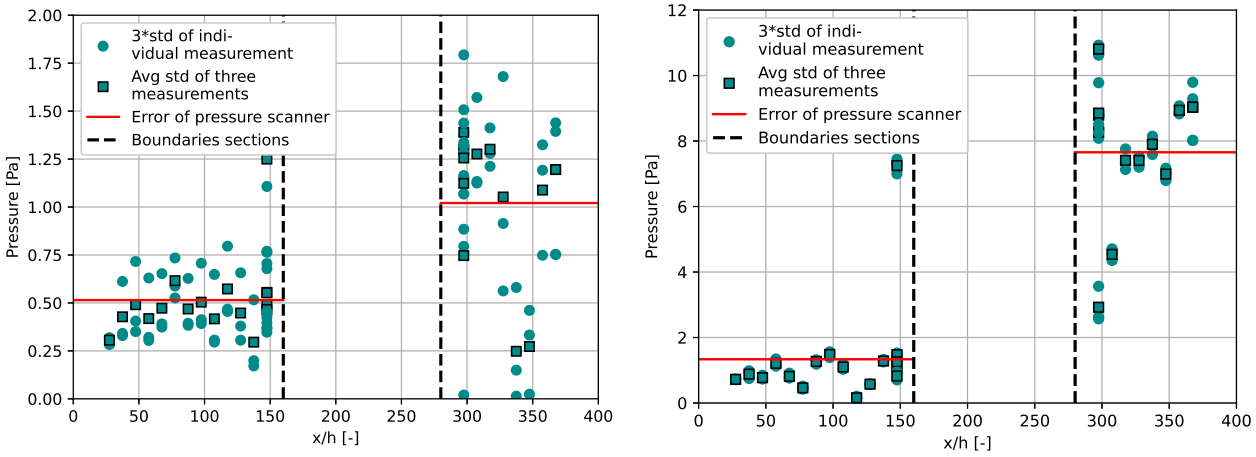

(a) Error for 600 Pa-scanner ≈0.5 Pa; error for 2.5 kPa-scanner ≈ 1.0 Pa.

(b) Error for 2.5 kPa-scanner ≈ 1.3 Pa; error for 10.0 kPa-scanner ≈ 7.9 Pa.

Figure E.5: Circles are 3 standard deviations of an individual measurement. Squares indicate the average of these three individual measurements. The red bar is the average of the squares, which indicates the scanners' error.

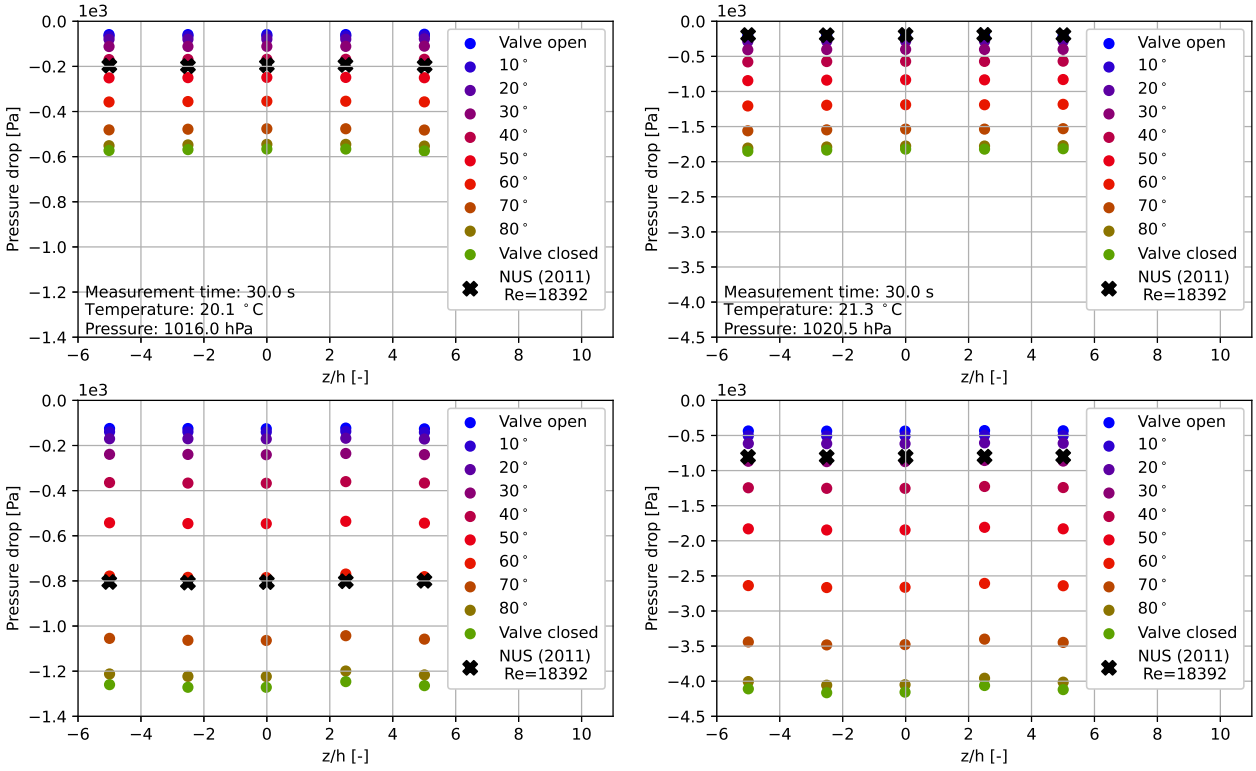

(a) 1 pump. Top figure is upstream of the test section (x/h = 147.5), bottom figure is downstream of the test section (x/h = 297.5).

(b) 2 pumps. Top figure is upstream of the test section (x/h = 147.5), bottom figure is downstream of the test section (x/h = 297.5).

Figure E.6: Spanwise variation for one pump and for two pumps.

In Figures E.7 and E.8, the variation of difference in measured static pressure from the least square fit is depicted for flat- and dimpled plates, respectively. It can be observed that the flat plates measured with two pumps (Figure E.8a) return more consistent values than the other three measurements downstream of the test section. The dimpled plates measured with two pumps on the other hand, seem to be depending the most on the velocity. Measurements performed with one pump show a higher consistency, i.e., they show much overlap, upstream of the test section in comparison with measurements performed with two pumps. Furthermore, it is

obvious that all deflections from the linear square fit follow the same pattern, independent on the amount of pumps or the type of test plates. Lastly, the largest difference is formed in the test section, for flat plates as well as dimpled plates.

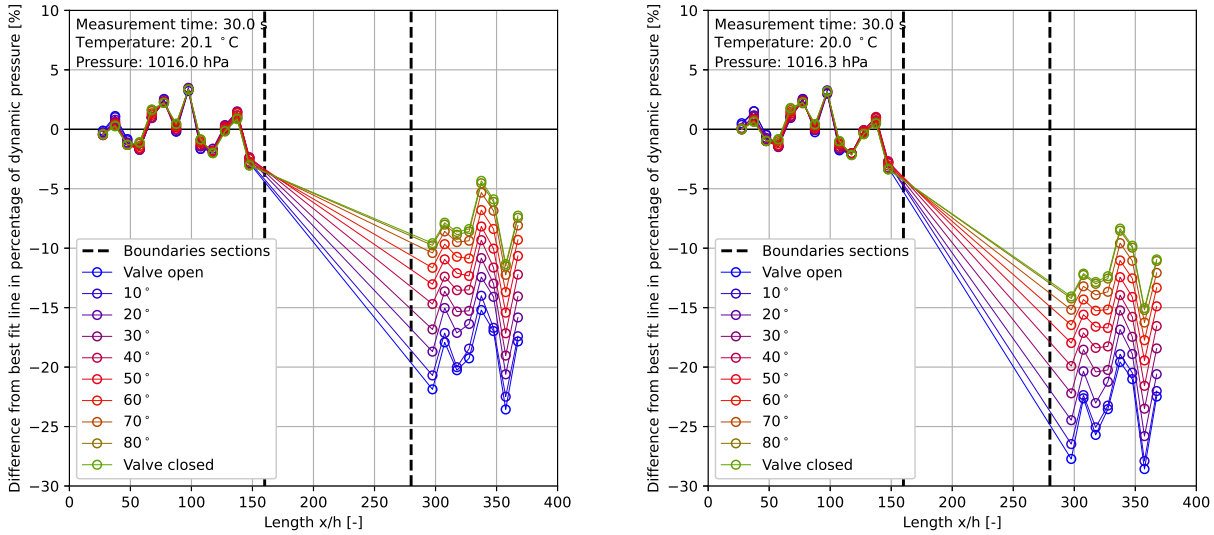

(a) Flat plates **(b)** Dimpled plates.

Figure E.7: Variation of difference in measured static pressures from least square fit for flat plates. Result from Tay (2011) is shown for reference. One pump is used; valve open and closed denote a Reynolds number of ≈6,000 and ≈21,000, respectively.

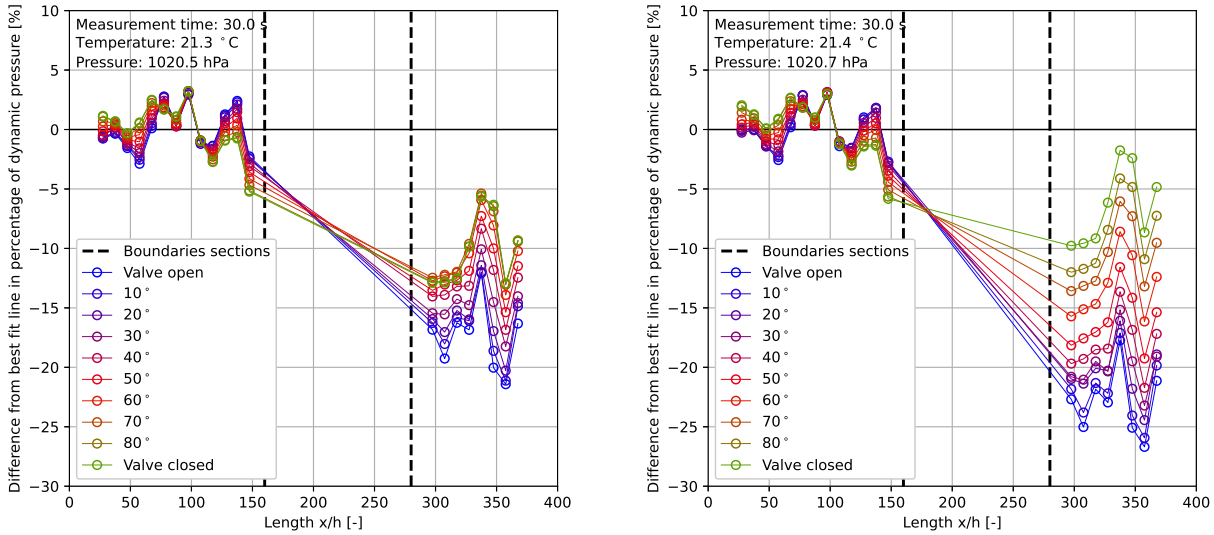

(a) Flat plates. **(b)** Dimpled plates.

Figure E.8: Variation of difference in measured static pressures from least square fit for flat plates. Result from Tay (2011) is shown for reference. Two pumps used; valve open and closed denote a Reynolds number of ≈11,800 and ≈40,000, respectively.

Appendix F

Windtunnel

This appendix describes everything about the wind tunnel (DC-40) that was built at TUD. In light of answering the main research question, there can be distinguished three phases that need to be completed before actual tests can be performed. Phase one marks the wind tunnel design that is a replica of the wind tunnel used by NUS as aforementioned in subsection 3.2.2 (Tay et al., 2015). The second phase involves constructing the designed wind tunnel, followed by the third and final phase: calibrating the wind tunnel. The first two phases are attended prior to the MC's. During the first and second MC, the tunnel was calibrated. Each phase will be discussed in the sections below.

F.1 Phase 1: Design

By designing the DC-40 before constructing it, certain obstacles could be prevented, and the most prominent flaws were removed. The entire wind tunnel is designed by use of Computer Automated Design (CAD) software. For this project, SolidWorks 2020 was used. Due to the size of the DC-40 and limited space available at TUD, the idea of constructing a mobile wind tunnel was developed. The tunnel either is in operational mode to perform wind tunnel tests or in storage mode. Both modes are discussed below.

Operational mode. The tunnel is subdivided into three sections: A, B, and C. Each section contains two or three parts: A1 and A2 for sections A, B1, B2, and B3 for section B and C1 and C2 for section C. Section A forms the tunnel entrance, B the test section of the tunnel, and C the exit section. A1 is the part most upstream, C2 the part most downstream of the tunnel. In operational mode, all parts are connected and secured by clamps. The DC-40 then reaches over 9 meters in length, see Figure F.1. A permanent framework supports section B. Sections A and C are supported by aluminum profiles referred to as x-beams due to their shape. As the x-beams are borrowed from TUD, they are left out of the design made in CAD. The tunnel is an open system and the vacuum pumps suck atmospheric pressure.

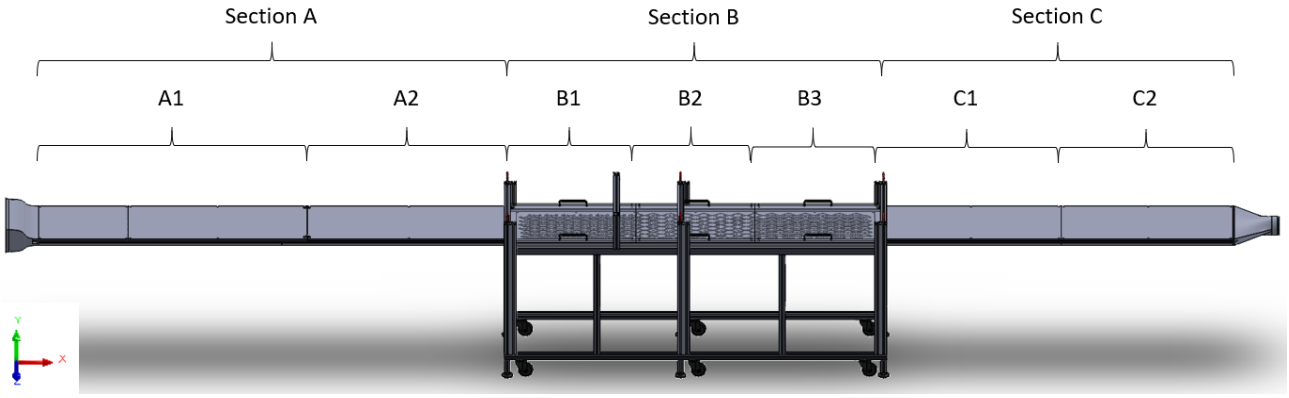

Figure F.1: DC-40: operational mode. Flow fltr.

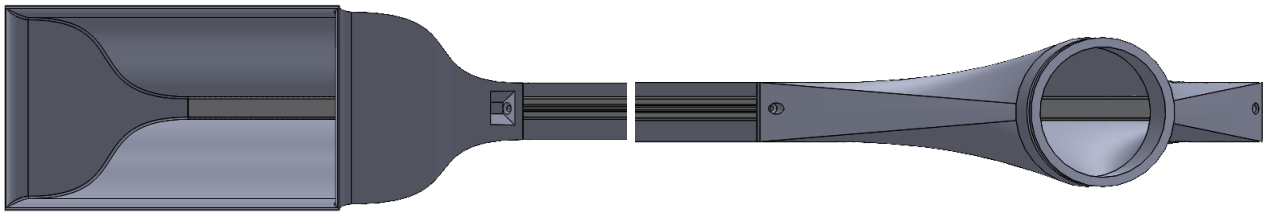

(a) Transition bell-mouth to A1. **(b)** Transition C2 to coupler.

Figure F.2: Transitions bell-mouth-A1 and C2-coupler. Flow fltr.

Figure F.2a depicts how the air enters the bell-mouth that converges the flow to the dimensions of the DC-40: 40 cm in width and 2 cm in height.

For parts A1 and A2, the ceiling, sides and floor are staggered to improve the robustness of the connection. Four clamps are installed at the bottom and the top of the tunnel on each side to merge parts A1 and A2. This is depicted in Figure F.3a.

Section C is almost identical to section A, with the exception that C1 and C2 are merged. The floors and ceilings can be removed individually, but the sides are designed as a one-piece aluminum. Downstream of part C2, there is another single 3D-printed piece that transforms the rectangular cross-section into a circular cross-section, which is compatible with a flexible tube system (depicted in Figure 4.6). This part will be referred to as the 'coupler' from now on. Similar to the bellmouth, the 'coupler' is secured to the front of the sidepieces of the channel with screws (Figure F.2b). Section B is more complex than sections A and C considering its appli-

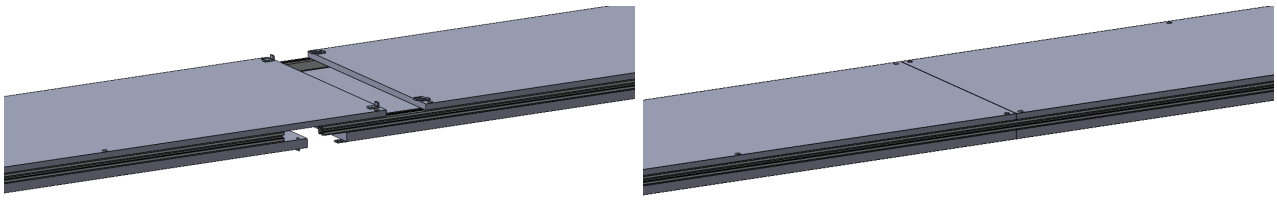

(a) Staggered transition A1-A2 with two clamps at the ceiling wall and two clamps at the bottom wall. **(b)** Aligned transition C1-C2 (fixed).

Figure F.3: Transitions A1-A2 and C1-C2. Flow fltr.

cability to multiple test plates. Figure F.4 depicts an exploded view of the different layers involved in section B from bottom to top. It starts with the foundation plate. This plate contains multiple holes in the bottom that have a twofold purpose. Firstly, Dimple Aerospace B.V. has constructed an advanced mold for test plates called 'The Hill'. In this research, no tests were performed with the Hill, but the option to do that in future research is still open. The Hill contains various sensors that can be connected to a monitor using cables. These cables need to be locked away through the bottom of the foundation plate. Secondly, once test plates are in place, it is hard to remove them from above. Instead, one can push the test plates upwards through the holes in the bottom.

The dimpled test plates that are used for this research are 5 mm in thickness. However, taking into account the possibility of placing 'The Hill' (which has a thickness of 30 mm) into the DC-40, the depth of the test section area was lowered to 30 mm. Consequently, the test plates used for this research had to be mounted on an additional plate of 25 mm in thickness. Despite requiring additional material, the thicker test plates have a substantial advantage over thinner test plates, which will be touched upon in section F.3. The Achilles heel of the entire design are transitions A2-B1 and B2-C1. The complexity is formed by the absence of staggered connections and transition between different materials. These transitions can be found in Figure F.5. The construction of this part of the tunnel will be explained in further in section F.2.

Storage mode. In storage mode, parts A1 and A2 are disconnected from section B, and the bellmouth is detached from part A1. Contrarily to section A, section C is disconnected as a whole, leaving parts C1 and C2 unseparated. The reason for this is the length of each section. The framework supporting section B simultaneously forms a storage area for sections A and C. As section A ($x/h = 160$) is longer than section B ($x/h = 120$), it had to be stored in two parts. Section C, however, is equally long as section B and can be stored as a

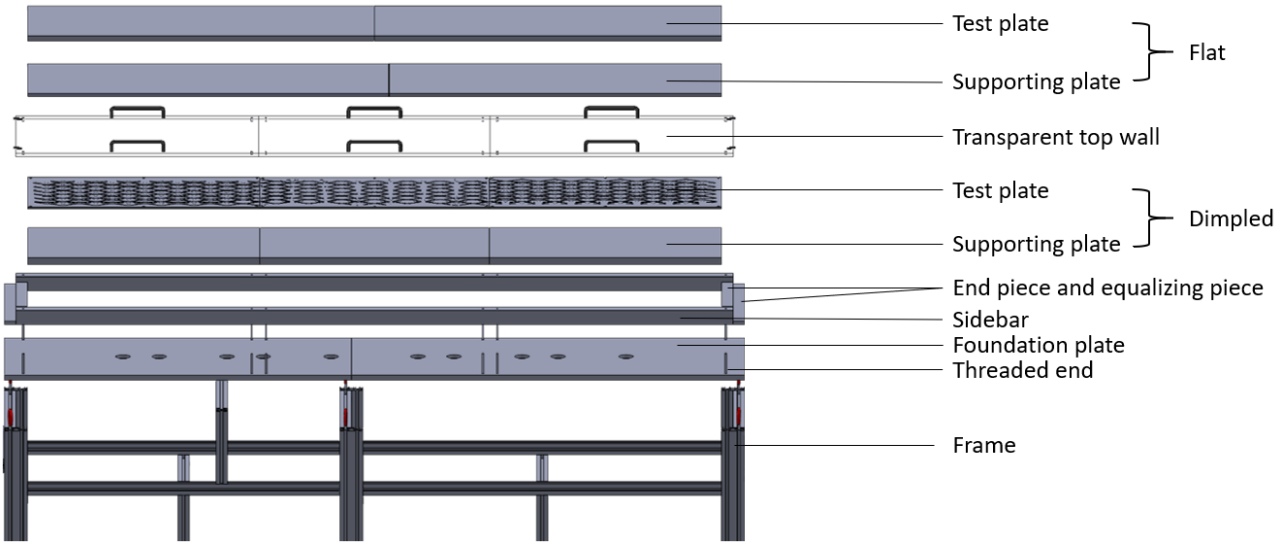

Figure F.4: Exploded view section B.

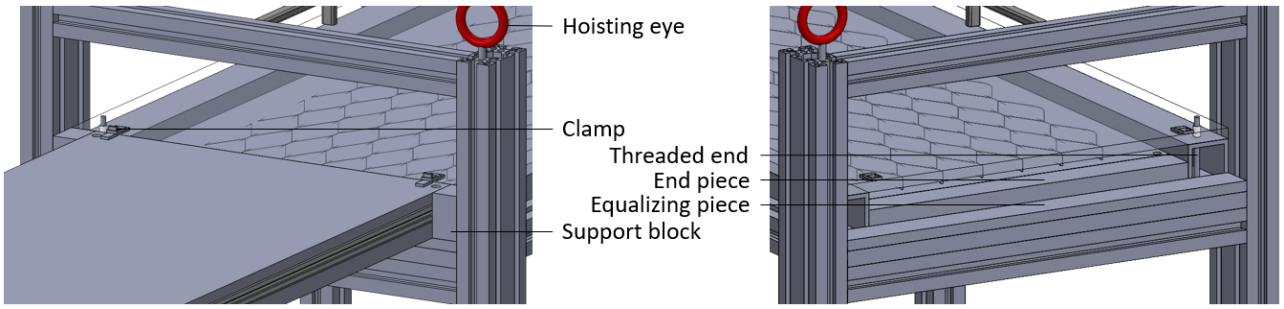

Figure F.5: Transitions of A2-B1 and B3-C1. Left: the section A is installed. Supporting blocks are used to prevent it from shearing. Right: section C is removed.

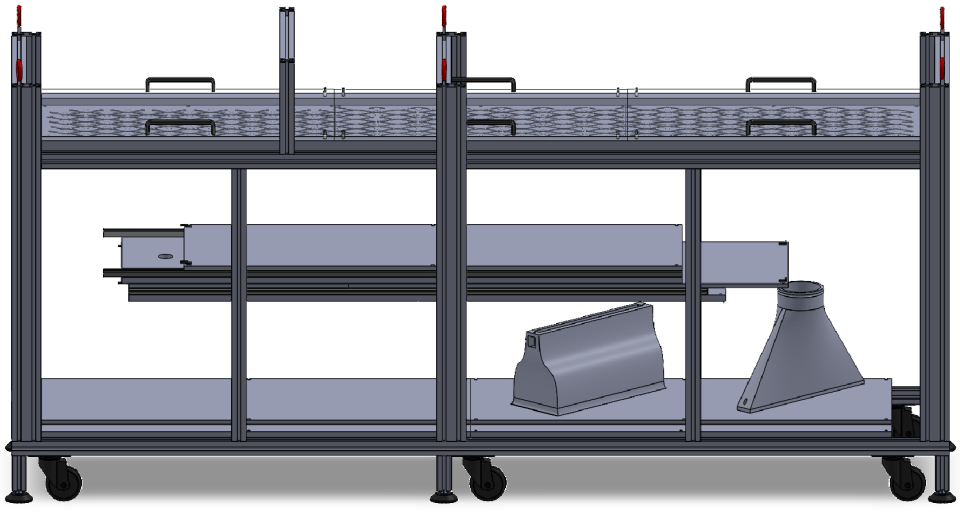

Figure F.6: DC-40: storage mode.

whole. Like the bellmouth, the 'coupler' at the end of part C2 was uncoupled and stored individually to prevent any damage during the storing process. The storage mode design is depicted in Figure F.6. The framework supporting section B contains six swivel castors at the bottom, allowing the DC-40 to be maneuvered with ease from its storage location to the test location. In conjunction with the wheels, six supporting feet are installed,

which are adjustable in height. When switching to operational mode, the feet can be lowered to lift the entire frame causing it to be irremovable. Furthermore, the DC-40 can be tilted using the adjustable feet until it is completely leveled. At the top of the frame, six lifting eyes were implemented to hoist the entire DC-40 to its storage location.

F.2 Phase 2: Construction

The core of the tunnel is formed by the frame that supports the test section. Hence, the construction phase commenced by assembling aluminum profiles to a frame. The majority of the aluminum profiles were recycled from old experimental setups used at TUD. The frame has outer dimensions 2560 mm by 1040 mm by 580 mm in length (streamwise direction), height (wall-normal direction), and width (spanwise direction). From here on, all dimensions are given as streamwise x wall-normal x spanwise direction in mm. The frame dimensions do not involve wheels or lifting eyes. Once the frame was assembled, the three sections were built.

Section A. The bellmouth was designed in SolidWorks and 3D printed at Dimple Aerospace B.V. in a single piece. The curve of the bellmouth that converges the flow is a 5th order polynomial allowing for a smooth constriction of the flow. At the very beginning of section A, a trip is glued on the floor as well as on the ceiling wall to trigger turbulent flow and accelerate the evolution to its fully developed state (Lienhart et al., 2008).

The wind tunnel floor is 18 mm thick, while the ceiling is 12 mm in thickness. The reason for the difference in thickness is twofold: the financial budget and the continuity of the wind tunnel ceiling. The ceilings of section B are made of perspex allowing optical access. This material is rather expensive, especially when required in a significant thickness. The perspex used was 12 mm in thickness. As such, ceilings of sections A and C were also designed and constructed 12 mm thick. This way, the top of the wind tunnel is continuous and can be fastened easily using clamps.

Both floor and top are made of laminated plywood. This material was selected for its smooth and workable properties as well as its considerable financial advantage over materials such as steel and aluminum. Although no aluminum was used for the floor and top walls, the sides of sections A and C were built from aluminum profiles. They are 20 by 20 mm in cross-section with one smooth side, which self evidently faces the inside of the channel. The other three sides have grooves that can hold T-slots. The plywood walls are secured to the aluminum sides by screws that go through the walls into the T-slots placed in the grooves of the aluminum profiles.

Section B. First, the foundation plate (2560x18x500) was installed. Large holes were drilled in the center along the streamwise direction to lock away cables and provide access to the test plates. On each side of the foundation plate, multiple helicoils were placed with threaded ends pointing upwards. Hollow aluminum profiles (50x50 mm cross-section) with holes on the locations of the threaded ends were placed on each side of the foundation plate. These aluminum profiles have dimensions 2480x50x50 and serve as the sides of the wind tunnel for section B. At both ends, between the aluminum profiles, wooden end pieces (40x400x30) were mounted on the foundation plate. This resulted in a perfect mold of 2400 mm long, 30mm deep, and 400 mm wide: the test section's exact dimensions. The wooden end pieces upstream and downstream of the test section form the last 40 mm of section A and the first 40 mm of section C, respectively.

The test section mold is filled with either test plates (5 mm thick anodized aluminum dimpled plate mounted on a 25 mm thick wooden supporting plate) or flat plates (18 mm thick plywood test plate mounted on 12 mm plywood supporting plate). The test- and supporting plates are depicted in Figure F.4.

There are 40 mm left upstream as well as downstream from the test section mold. These edges allow space to support sections A and C. However, as the floors of section A and C are merely 18 mm thick, an additional 12 mm of material (referred to as the equalizing piece) is required to even the floors of section A and C with the floor of section B.

On top of the aluminum 50x50 cross-section profiles, perspex plates were placed to seal the wind tunnel. Similar to the aluminum 50x50 profiles, holes were drilled in the perspex allowing for the threaded ends to pass through. By using knobs on the threaded ends, the perspex plates can be tightened to the aluminum profile preventing as much leakage as possible.

Section C. Section C is identical to section A apart from its length and the fact that it is stored as a whole. The 'coupler' is a single piece and also 3D-printed at Dimple Aerospace B.V. In the floor of sections A and C, a total of 29 pressure taps and a hole for a simple pitot were drilled. This is explained further in subsection 4.3.1. In Figures F.11a and F.11b the photographs of the operational mode and storage mode are depicted.

F.3 Phase 3: Calibration

The most challenging part of the wind tunnel process is phase 3, the calibration. Due to its modest height of 20 mm, the smallest movements of the wall elements will have a significant impact on the accuracy of the measurements. The objective of the third phase was to reach a linear pressure drop over the entire test channel. In this phase, various wind tunnel improvements have been made.

1: Fastening the test plates. Due to the underpressure generated by the vacuum pumps, the test plates were lifted as their gravity was not sufficient to keep them in place. As a reaction to this, helicoil screws were inserted on the downside of the test plates. Through holes in the foundation plate, the test plates could be tightened by knobs on threaded ends, similar to the knobs that secured the ceilings of section B.

2: Vibration. During the assembling of the tunnel, there were not used enough T-slots to attach the channel walls sufficiently to the side. Consequently, the channel walls had a certain degree of freedom, which resulted in an audible vibration. This only occurred in part A2. The underpressure in section C was most likely sufficient to keep the walls attached to the sides of the channel. In addition to that, the thick plate on section C also contributes to keeping the wall from vibrating was already installed. For section A, screw clamps (see Figure F.8a) were applied to hold the walls attached to the sides. This silenced the vibration, which was also visible in the results during calibration.

Figure F.7: Knobs that hold the test plate in place when underpressures are active.

3: Leakage. Although it was hard to notice, it is very likely that leakage occurs along the tunnel. The transitions A2-B1 and B3-C1 are prone to leakage, considering they were not as swift as they were designed. To solve this issue as much as possible, all sides of sections A and C were sealed with duct tape. Furthermore, weather strips were placed between every transition to provide for better sealing. During pump-on time, there is carefully checked for leakage by using fingertips. No clear indication of leakage was observed. Also, the gap between the hole in the ceiling that is filled the hollow rod used for hotwire measurements did not yield noticeable air flows. For future research, however, it is recommended to use tufts as was already briefly touched upon in chapter 4.

F.4 Recommendations DC-40 version 2

In this section, recommendations for an improved DC-40 are listed. It should be mentioned that no financial assessment was made yet on any of the proposed solutions.

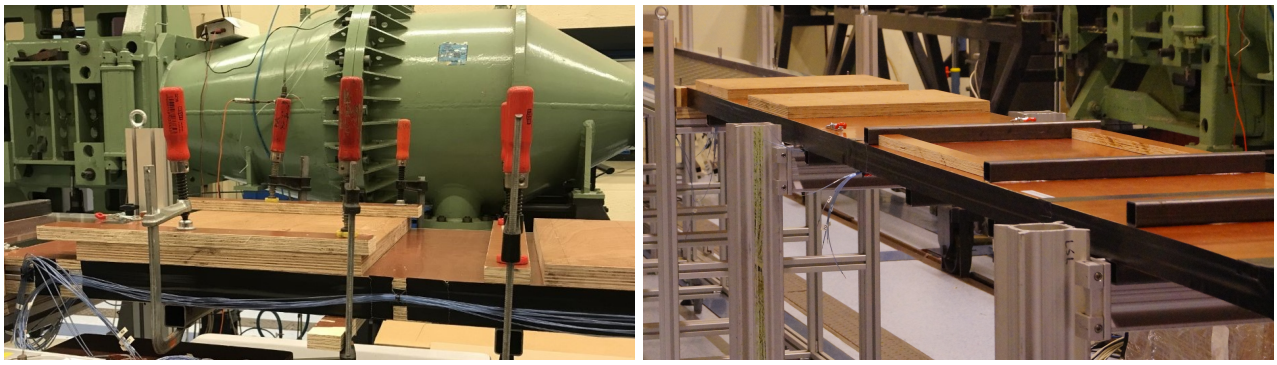

(a) Screw clamps to reduce vibration. **(b)** Taped sides to prevent leakage.

Figure F.8: Improvements on the DC-40.

- First and foremost, the channel walls should be increased in thickness. Also, both walls should be identical in thickness as there is no reason to assume that the underpressure is different at the floor wall and the top wall. It is recommended to use a material for the channel walls that has a higher stiffness than the plywood. Aluminum seems a logical choice considering the additional weight of steel walls would be a disadvantage. By consulting equation C.1 in Appendix C, the bending of new aluminium thicker plates can be estimated. The Young's modulus of pure aluminum is about 70 Gpa. Assuming a plate of dimensions 800x20x400 exposed to the 6 kPa underpressure would result in a theoretical deformation of 0.024 mm. An aluminum plate of 12 mm thick with the same stream- and spanwise dimensions would result in a deformation of 0.082 mm. This would be an error of 0.4% with respect to the channel height, which seems acceptable. Another benefit of aluminum is that its surface is more smooth than the plywood used in this research.

- For a second version, all wind tunnel parts that contain holes, strange dimensions, or other properties that otherwise would require human interaction should be milled by a machine. This most certainly will result in a higher precision of the DC-40. Also, it reduces fitting difficulties while assembling parts.

- Currently, the channel walls are reinforced with steel cross beams. In addition to that, the aluminum taps (denoted as 'pressure tap' in Figure F.9) stick out from the channel wall in the current design. Due to their small diameter of 1 mm, they are prone to deformation. In other words, there are multiple things on the outside of the channel wall. This made it impossible to slide a channel wall into the frame of the DC-40 to store it. Instead, three people had to lift it to place it in the framework with care such that no pressure taps were damaged. For the next version, it is recommended to make flush pressure taps covered with a safety part. This is visible in Figure F.9.

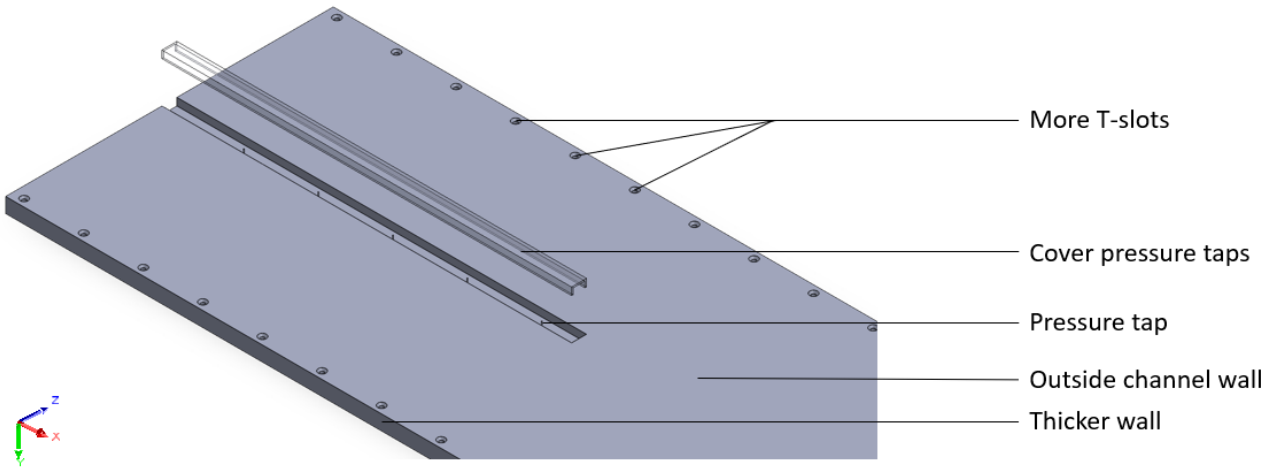

Figure F.9: Suggestion for a new channel wall design.

- To tackle the leakage issue, a rubber sealing between sidewalls and bottom- and top walls is required. In addition to that, more T-slots are recommended. A design of the increased amount of T-slots can already be found in Figure F.9. The aluminum side profiles of 20x20 mm can be recycled. If some rubber sealing is used between the sides and the channel walls, it is important that the channel height does not increase. Solving leakage is primarily necessary in section B, where a large error is formed, most likely because of leakage. Measurements with tufts could be performed for the next design to visualize leakage.
- The error acquired in section B, depicted in Figures 5.22b and 5.22a, likely is not only caused due to leakage. Test section B is composed of too many different parts. Each part has a tolerance, and considering all tolerances have to be taken into account, the final tolerance (or error) is significant. Although challenging, it is recommended to reduce the number of parts of section B. It is very plausible that simplifying and improving this part of the tunnel will reduce errors.
- As a final recommendation, the author suggests to create a staggered construction at all transitions as is done at transition A1-A2, illustrated in Figure F.3a. At the current setup, it is possible that one channel wall creates a step with the adjacent channel wall considering walls are not flush in y-direction.

For future research it is convenient to consider the 3D models that were designed and built during this research. Therefore, several SolidWorks files involving parts as well as full assemblies are attached to this document, A guide with a description for each file is provided in Table F.1:

Table F.1: Assemblies and parts that were designed in SolidWorks and used during this research.

Assembly no.	Description	File name
1	Full wind tunnel - operational mode. Including flat plates as well as dimpled plates.	SW_assembly1.STEP
2	Full wind tunnel - storage mode.	SW_assembly2.STEP
3	Aluminium frame.	SW_assembly3.STEP
4	Hotwire setup including the hollow rod and the probe support holder near the wall.	SW_assembly4.STEP
5	Proposed channel wall for version 2 of DC-40.	SW_assembly5.STEP
Part no.		
1	Bellmouth.	SW_part1.STEP
2	Coupler.	SW_part2.STEP
3	Probe support holder.	SW_part3.STEP

(a) Frame is moved from its position. **(b)** Wall elements of the wind tunnel. **(c)** More wall elements.

Figure F.10: Photographs of disassembled DC-40.

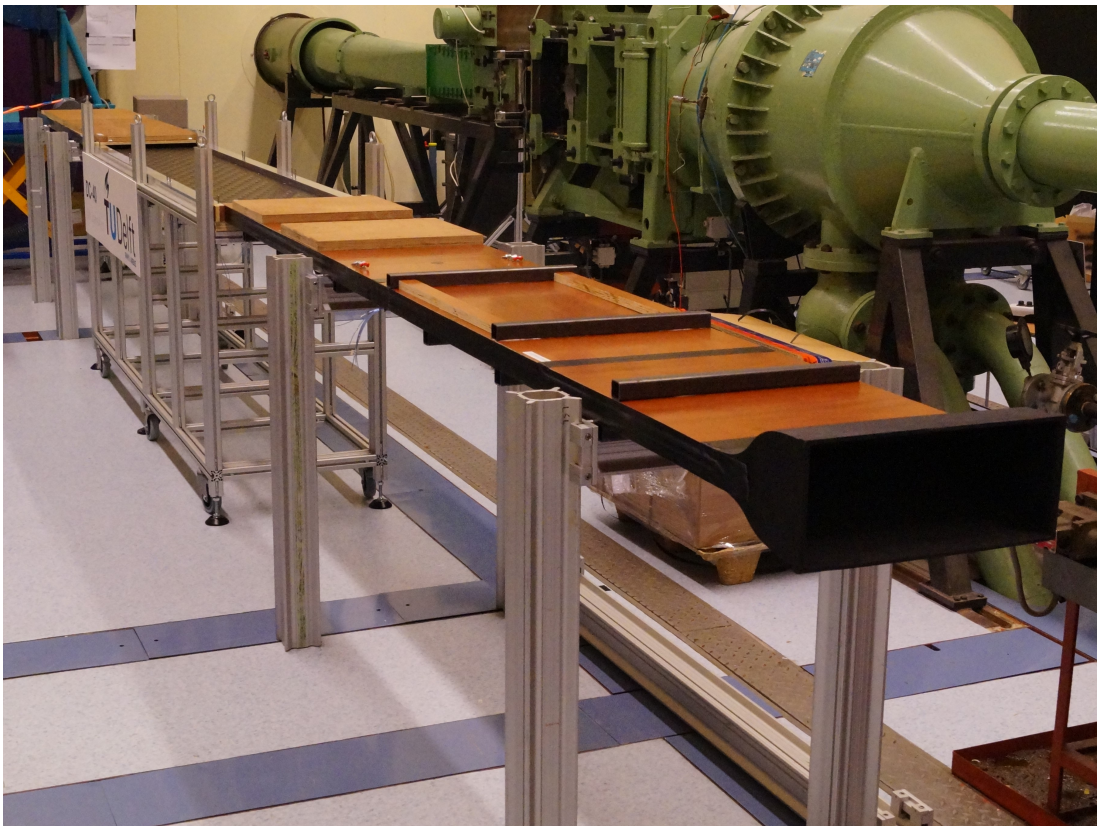

(a) Operational mode

(b) Storage mode.

Figure F.11: DC-40 in different modes.